Appendix C

HYDRODYNAMIC STUDIES

Technical Report

Hydrodynamic and Sediment Transport Study

Calcasieu River and Pass, Louisiana
Dredged Material Management Plan
Phase II

Contract No. DACW27-03-D-0005
Deliver Order No. CZ03
GEC Project No. 27321CZ03

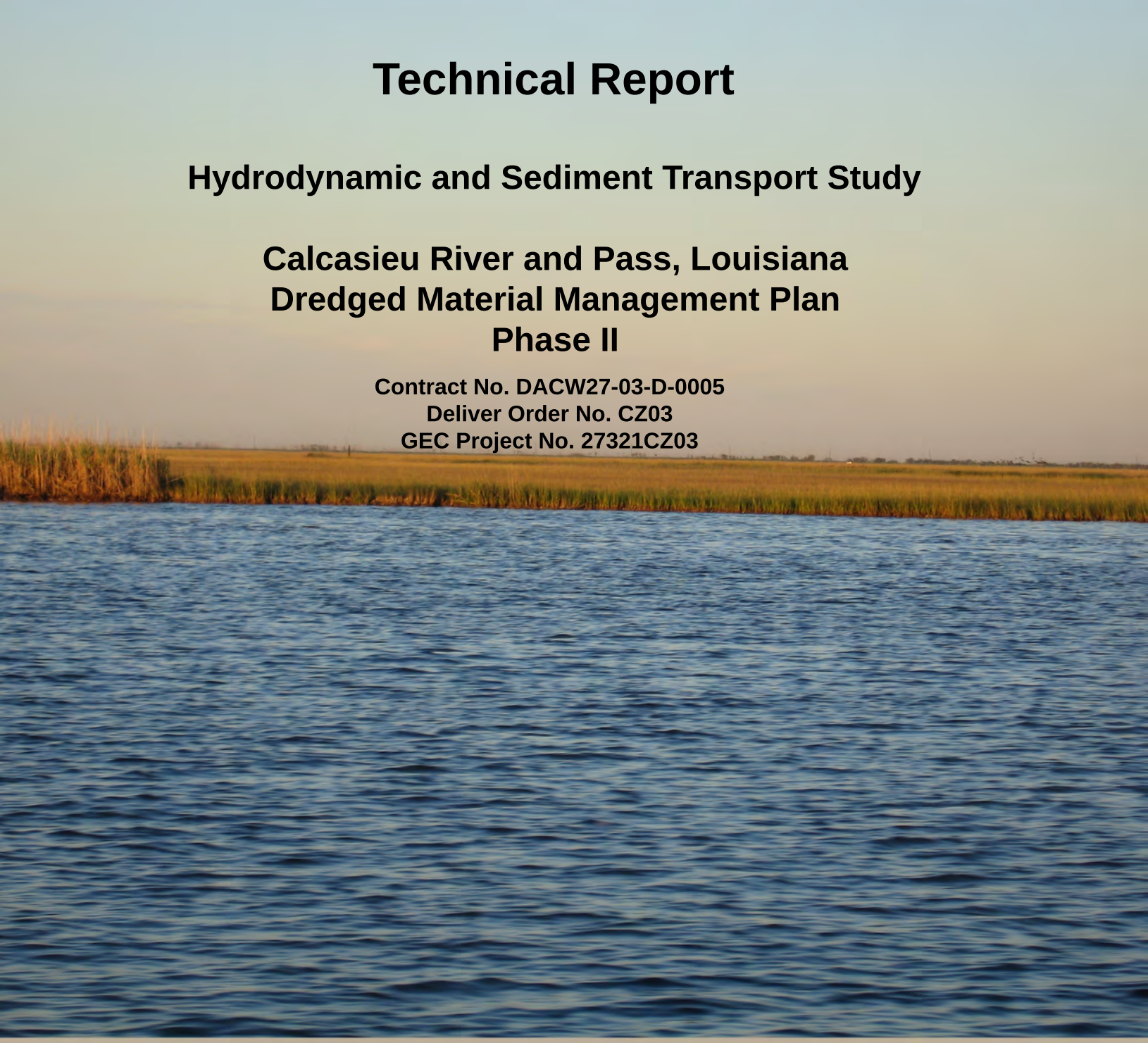

Prepared For:

U.S. Army Corps of Engineer
New Orleans District
New Orleans, LA

Prepared by:

Applied Coastal
Research and Engineering, Inc.
766 Falmouth Road, Suite A-1
Mashpee, MA 02649
508-539-3737
www.appliedcoastal.com

TABLE OF CONTENTS

I. INTRODUCTION 1

II. BACKGROUND 3

III. DATA COLLECTION AND ANALYSIS 12

III.1 WATER ELEVATION MEASUREMENTS 12
III.2 CURRENT MEASUREMENTS 21
III.3 WIND SPEED AND DIRECTION MEASUREMENTS 26
III.4 BATHYMETRY 30
III.5 FRESH WATER INFLOW MEASUREMENTS 32
III.6 WATER ELEVATION DATA 32

IV. HYDRODYNAMIC MODELING 35

IV.1 MODEL THEORY 37
IV.2 MODEL SETUP 37
IV.2.1 Grid Generation 37
IV.2.2 Boundary Condition Specification 38
IV.3 CALIBRATION 43
IV.3.1 Friction Coefficients 43
IV.3.2 Eddy Viscosity Coefficients and Density 45
IV.3.3 Comparison of Modeled Tides and Measured Tide Data 45
IV.4 ADCP VERIFICATION OF THE LAKE CALCASIEU SYSTEM 57
IV.5 MODEL CIRCULATION CHARACTERISTICS 60

V. SEDIMENT TRANSPORT MODELING 63

V.1 SEDIMENT CHARACTERISTICS AND DOMINANT PROCESSES 63
V.2 MODEL DESCRIPTION 72
V.3 MODEL INPUT PARAMETERS 74
V.4 MODEL RESULTS 76
V.4.1 Shear Stress 76
V.4.2 Total Suspended Sediments 79
V.4.3 Bed Change 89

VI. INFLUENCE OF VESSEL PASSAGE ON SEDIMENT SUSPENSION 95

VI.1 DATA COLLECTION 95
VI.2 CURRENT OBSERVATIONS 97
VI.3 HYDRODYNAMIC RESPONSE TO VESSEL PASSAGE 99
VI.4 SEDIMENT SUSPENSION 107

VII. EVALUATION OF PROPOSED DMMP ALTERNATIVES 109

VII.1 MODEL SETUP 109
VII.2 HYDRODYNAMIC MODEL RESULTS 114
VII.3 SEDIMENT TRANSPORT MODEL RESULTS 120

VIII. SUMMARY AND CONCLUSIONS 126

VIII.1 OVERVIEW 126
VIII.2 DATA COLLECTION 127
VIII.3 HYDRODYNAMIC MODELING 128
VIII.4 SEDIMENT TRANSPORT MODELING 130

VIII.5 INFLUENCE OF VESSEL PASSAGE ON SEDIMENT SUSPENSION 133
VIII.6 EVALUATION OF SEDIMENT MANAGEMENT OPTIONS 133

IX REFERENCES 135

LIST OF FIGURES

Figure I-1. Overview of the region covered by the hydrodynamic model, where the green line illustrates the land boundary utilized in the modeling effort. 2

Figure II-1. Historical channel dimensions of the Calcasieu Ship Channel as depicted in a report prepared by the Louisiana Department of Natural Resources (Louisiana DNR, 2002). 5

Figure II-2. Summary of observed significant wave height data between 1993 and 2001 collected at the National Data Buoy Center Station #42035 located 22 Nautical Miles east of Galveston. The red bands illustrate the standard deviation centered about the mean wave height for each month and the maximum significant wave heights for each month are shown in meters. 6

Figure II-3. Storm surge and wind observations during Hurricane Rita in 2005 (Source: National Weather Service). Loss of data from the Cameron, Mermentua, and Hackberry gages likely was a result of the substantial storm surge and wind associated with Hurricane Rita. 7

Figure II-4. Maximum measured flows since the USGS streamflow gage was installed near Kinder, Louisiana (Source: USGS) 8

Figure II-5. Distribution of (A) relative energy, (B) morphological components, and (C) sedimentary facies in a longitudinal section with an idealized wave-dominated (microtidal) estuary (Source: Dalrymple *et al*., 1992). 10

Figure II-6. Wetland and salinity shifts in the Calcasieu-Sabine Basin based on historical vegetative surveys between 1949 and 1997 (Source: Louisiana DNR, 2002). 11

Figure III-1. Tide gage locations in the northern portion of Lake Calcasieu. Yellow points are tide gage locations. 13

Figure III-2. Tide gage and ADCP transect locations in the southern portion of Lake Calcasieu. Yellow points are tide gage locations and red is the ADCP transect location. 14

Figure III-3. Tidal elevation observations for Gulf of Mexico (10066), Marker 60 (9507), East Bay (9487), and West Cove (9506). 15

Figure III-4. Tidal elevation observations for Hackberry (10064), Marker 88 (9488), GIWW (9515), and Lake Charles (9514). 16

Figure III-5. Example of an observed astronomical tide as the sum of its primary constituents. 19

Figure III-6. Water elevation variations for a 4-day period in the Lake Calcasieu. Notice the reduced amplitude as well as the delay in times of high- and low- tide relative to Gulf of Mexico due to frictional damping through the estuary. 21

Figure III-7. Color contour plot of velocity magnitude across the main channel measured at 12:35 EDT on October 25, 2006 during the ebb tide. Colors variations indicate the magnitude of flow moving in each measurement bin. 23

Figure III-8. Color contour plot of velocity magnitude across the main channel measured at 14:59 EDT on October 25, 2006 during the transition from ebb tide to flood tide. Colors variations indicate the magnitude of flow moving in each measurement bin. 24

Figure III-9. Color contour plot of velocity magnitude across the main channel measured at 19:55 EDT on October 25, 2006 at the peak measured flood

tide. Colors variations indicate the magnitude of flow moving in each measurement bin. 24
Figure III-10. Color contour plot of velocity magnitude across the main channel measured at 17:56 EDT on October 25, 2006. Transect measured prior to the passage of LNG tanker. Colors variations indicate the magnitude of flow moving in each measurement bin. 25
Figure III-11. Color contour plot of velocity magnitude across the main channel measured at 18:26 EDT on October 25, 2006 immediately after the passage of LNG tanker heading northbound on the flood tide. Colors variations indicate the magnitude of flow moving in each measurement bin. 25
Figure III-12. Measured flow rates for the ADCP transect in the inlet of Lake Calcasieu, Cameron, LA. Positive flow indicated flooding tide, while negative flow indicates ebbing tide. Bottom plot represents the tidal elevation observations for Gulf of Mexico (Gage 10066). 26
Figure III-13. Time series graphs for the wind measurement program. Wind speeds are depicted in the top plot; wind direction as the middle plot, followed by internal temperature as the bottom plot. 29
Figure III-14. Directional distribution (rose plot) and scatterplot of winds speeds during the measurement program. 30
Figure III-15. Bathymetry points gathered within Lake Calcasieu. Color contours indicate depth relative to the MLG vertical datum in meters. X-Y horizontal positions along the axes are in Louisiana South State Plane Coordinates, NAD 1983, meters. 31
Figure III-16. Daily mean discharge from salt water barrier in Lake Charles. Recorded at Lake Charles Calcasieu River Salt Water Barrier measurement station. 33
Figure III-17. Tidal elevation observations for NOAA Stations Cameron (8768094) and Lake Charles (8767816). 34
Figure IV-1. A site map showing the study area around Lake Calcasieu. 36
Figure IV-2. The model finite element mesh developed for Lake Calcasieu system. X-Y horizontal positions along the axes are in Louisiana South State Plane Coordinates, NAD 1983. (meters) 39
Figure IV-3. Details of the finite element mesh along the jettied entrance channel to Lake Calcasieu, Cameron, LA. X-Y horizontal positions along the axes are in Louisiana South State Plane Coordinates, NAD 1983. (meters) 40
Figure IV-4. Details of the finite element mesh around Texaco Pass, Hackberry, LA. X-Y horizontal positions along the axes are in Louisiana South State Plane Coordinates, NAD 1983. (meters) 40
Figure IV-5. Details of the finite element mesh at the junction of GIWW and Devils' Elbow. X-Y horizontal positions along the axes are in Louisiana South State Plane Coordinates, NAD 1983. (meters) 41
Figure IV-6. Bathymetric data interpolated to the finite element mesh of hydrodynamic model. Depth contours are in meters referenced to MLG. X-Y horizontal positions along the axes are in Louisiana South State Plane Coordinates, NAD 1983. (meters) 42
Figure IV-7. Final calibrated Manning's friction coefficients. X-Y horizontal positions along the axes are in Louisiana South State Plane Coordinates, NAD 1983 (meters). The Manning number used in MIKE21 is the reciprocal value of the Manning number typically used. 44

Figure IV-8. Comparison of water surface variations simulated by the model (solid blue line) to those measured within the system (solid black line) for the calibration time period, for the offshore gauging station. 46
Figure IV-9. Comparison of water surface variations simulated by the model (solid blue line) to those measured within the system (solid black line) for the verification time period at the Marker 60 gauging station (9507). 47
Figure IV-10. Comparison of water surface variations simulated by the model (solid blue line) to those measured within the system (solid black line) for the verification time period at the Sweetheart East Bay gauging station (9487). 48
Figure IV-11. Comparison of water surface variations simulated by the model (solid blue line) to those measured within the system (solid black line) for the verification time period at the West Cove gauging station (9506). 49
Figure IV-12. Comparison of water surface variations simulated by the model (solid blue line) to those measured within the system (solid black line) for the verification time period at the Hackberry gauging station (10064). 50
Figure IV-13. Comparison of water surface variations simulated by the model (solid blue line) to those measured within the system (solid black line) for the verification time period for the Marker 88 gauging station (9488). 51
Figure IV-14. Comparison of water surface variations simulated by the model (solid blue line) to those measured within the system (solid black line) for the verification time period at the GIWW gauging station (9515). 52
Figure IV-15. Comparison of water surface variations simulated by the model (solid blue line) to those measured within the system (solid black line) for the verification time period at the Lake Charles gauging station (9514). 53
Figure IV-16. Comparison of water surface variations simulated by the model (solid blue line) to those measured within the system (solid black line) for the verification time period at the NOAA's Cameron gauging station (NOAA 8768094). 54
Figure IV-17. Comparison of water surface variations simulated by the model (solid blue line) to those measured within the system (solid black line) for the verification time period at the NOAA's Lake Charles gauging station (NOAA 8767816). 55
Figure IV-18. ADCP transect location in the southern portion of Lake Calcasieu, the red line indicates the ADCP transect location. 58
Figure IV-19. Comparison of measured volume flow rates versus modeled flow rates (top plot) across the entrance to channel to Lake Calcasieu, over a 12.5 hours on October 25, 2006 (R^2 = 0.96). Flood flows into the inlet are positive (+), and ebb flows out of the inlet are negative (-). 59
Figure IV-20. Example of hydrodynamic model output in channel between the Gulf of Mexico and Lake Calcasieu for a single time step where maximum flood velocities occur for this tide cycle. Color contours indicate flow velocity, and vectors indicate the direction and magnitude of flow. 60
Figure IV-21. Example of hydrodynamic model output in channel along Lake Calcasieu for a single time step where maximum ebb velocities occur for this tide cycle. Color contours indicate flow velocity, and vectors indicate the direction and magnitude of flow. 61
Figure IV-22. Example of hydrodynamic model output along Calcasieu Ship Channel for a single time step where maximum flood velocities occur for this tide cycle. Color contours indicate flow velocity, and vectors indicate the direction and magnitude of flow. 62

Figure V-1. Lake Calcasieu Ship Channel location map. Mile markers are labeled every 5 miles. 66
Figure V-2. Average dredging quantities (CY/year/mile) along the Calcasieu Ship Channel for the period of 1994 to 2005. 67
Figure V-3. Maximum velocities observed during average tidal conditions. These hydrodynamic results are from the calibration run. Channel miles also provided as black dots. 69
Figure V-4. Sediment sampling locations within the CSC from Mile 6 to 23.5. 71
Figure V-5. Sediment physical characteristics within the CSC from Mile 5.5 to 23.5. 72
Figure V-6. A schematic diagram (DHI, 2007) showing how sediment layers and transport processes are included in the MT module of the MIKE 21 modeling suite. 73
Figure V-7. Map showing distribution of specified critical shear stress for second sediment layer. Light blue (main body of the Lake) indicates areas specified as 0.5 Pa, and the pale green (below mile 9 of the CSC) indicates area specified as 0.9 Pa. 75
Figure V-8. Average shear stress in the upper navigation channel computed during 8 day calibration period. 77
Figure V-9. Average shear stress in the lower navigation channel computed during 8 day calibration period. 78
Figure V-10. Maximum shear stress in the upper navigation channel computed during 8 day calibration period. 80
Figure V-11. Maximum shear stress in the lower navigation channel computed during 8 day calibration period. 81
Figure V-12. Average total suspended solids (TSS) computed for each model element over four tide cycles. 82
Figure V-13. Maximum total suspended solids (TSS) computed for each model element over four tide cycles. 83
Figure V-14. Total suspended solids (TSS) in the upper CSC (miles 13.5 to 20) computed for a single model time step, representative of maximum flood tide excursion. 85
Figure V-15. Total suspended solids (TSS) in the lower CSC (miles 9 to 16) computed for a single model time step, representative of maximum flood tide excursion. 86
Figure V-16. Total suspended solids (TSS) in the upper CSC (miles 13.5 to 20) computed for a single model time step, representative of maximum ebb tide excursion. 87
Figure V-17. Total suspended solids (TSS) in the lower CSC (miles 9 to 16) computed for a single model time step, representative of maximum ebb tide excursion. 88
Figure V-18. Bed change potential computed from mud transport model results, showing areas of erosional and depositional potential. 91
Figure V-19. Bed change potential in the upper portion of navigation channel computed from mud transport model results, showing areas of erosional and depositional potential. 92
Figure V-20. Bed change potential in the lower portion of navigation channel computed from mud transport model results, showing areas of erosional and depositional potential. 93
Figure V-21. Surveyed cross-sections at selected locations with the confined portion of the CSC. 94

Figure VI-1. Location of the two Nortek Acoustic Wave and Current profiler (AWAC) deployment locations. 96
Figure VI-2. Schematic of AWAC mounting relative to channel marker piling. AWAC was mounted approximately 3.4 meters below the surface, and offset 1 meter from the piling. 97
Figure VI-3. Averaged velocity and surface elevation time series at channel Marker 85. 98
Figure VI-4. Averaged velocity and surface elevation time series at channel Marker 69. 99
Figure VI-5. Events statistics at channel Marker 85 (north) and channel Marker 69 (south). Marker 85 event values are shown in the light line; Marker 69 values shown as the heavy line. 105
Figure VI-6. Maximum measured drawdown versus vessel size (length x beam x draft). 106
Figure VI-7. Maximum measured velocity versus vessel size (length x beam x draft). 107
Figure VI-8. Maximum calculated shear stress versus vessel size (length x beam x draft). 108
Figure VII-1. The model finite element mesh developed for Alternative 1. X-Y horizontal positions along the axes are in Louisiana South State Plane Coordinates, NAD 1983 (meters). 110
Figure VII-2. The model finite element mesh developed for Alternative 1. X-Y horizontal positions along the axes are in Louisiana South State Plane Coordinates, NAD 1983 (meters). 111
Figure VII-3. The model finite element mesh developed for Alternative 1. X-Y horizontal positions along the axes are in Louisiana South State Plane Coordinates, NAD 1983 (meters). 112
Figure VII-4. Bathymetric data interpolated to the finite element mesh of hydrodynamic model. Depth contours are in meters referenced to MLG. X-Y horizontal positions along the axes are in Louisiana South State Plane Coordinates, NAD 1983 (meters). 113
Figure VII-5. Comparison of water surface variations along the CSC between existing conditions and proposed Alternative 1. The existing conditions are represented by the dashed red line, and Alternative 1 by dashed blue line. The figures represent conditions during the calibration period, for the Hackberry and Marker 88 gauging stations. 115
Figure VII-6. Example of hydrodynamic model output in channel along Lake Calcasieu for a single time step where maximum ebb velocities occur for this tide cycle. Color contours indicate flow velocity, and vectors indicate the direction and magnitude of flow. 116
Figure VII-7. Example of hydrodynamic model output along Calcasieu Ship Channel for a single time step where maximum flood velocities occur for this tide cycle. Color contours indicate flow velocity, and vectors indicate the direction and magnitude of flow. 117
Figure VII-8. Difference in mean velocities observed during average tidal conditions between the hydrodynamic results from the Alternatives run and the calibration run. The grid is in LA state plane meters south 118
Figure VII-9. Difference in maximum velocities observed during average tidal conditions between the hydrodynamic results from the Alternatives run and the calibration run. The grid is in LA state plane meters south 119
Figure VII-10. Average shear stress in the upper navigation channel computed during 8 day calibration period. 121

Figure VII-11. Difference in maximum bed shear stress observed during average tidal conditions between the hydrodynamic results from the Alternatives run and the calibration run. The grid is in LA state plane meters south.....122
Figure VII-12. Average total suspended solids (TSS) computed at for each model element.....124
Figure VII-13. Maximum total suspended solids (TSS) computed at for each model element.....125
Figure VIII-1. Lake Calcasieu Ship Channel location map. Mile markers are labeled every 5 miles. 131

LIST OF TABLES

Table III-1. Tide datums computed from 12-day records collected in Lake Calcasieu in Dec 2006. Datum elevations are given relative to MLG in meters.....18
Table III-2. Tidal Constituents, Lake Calcasieu, Cameron, LA, Oct-Dec 2006.....18
Table III-3. M_2 Tidal Attenuation, Centerville Lake Calcasieu, Oct-Dec 2006 (Delay in hours relative to the Gulf of Mexico).....19
Table III-4. Percentages of Tidal versus Non-Tidal Energy, Lake Calcasieu, Oct to Dec 2006. 20
Table III-5. Wind Statistics (All speed units in meters/second, All times EDT). 28
Table III-6. Wind Statistics by Directional Quadrant *(All speed units in meters/second).*.....29
Table IV-1. Comparison of tidal constituent amplitudes calibrated MIKE21 model versus measured tidal data for the period November 17 to November 25, 2006. 56
Table IV-2. Comparison of tidal constituent phase calibrated MIKE21 model versus measured tidal data for the period November 17 to November 25, 2006.....57
Table V-1. Dredging Quantities (in cubic yards) on the Calcasieu Ship Channel by Mile (1994-2005). 68
Table V-2. Sediment fractions characteristics used for the Lake Calcasieu cohesive transport model. 76
Table VI-1. Matching Vessel Passage Events. 101
Table VI-2. Vessel Passage Event Statistics. 102
Table VI-3. Vessel Specifications per Event. 104

I. INTRODUCTION

To support the development of the Calcasieu Ship Channel Dredged Material Management Plan (DMMP), a hydrodynamic and sediment transport model was developed for the Lake Calcasieu estuarine system. The objective of this modeling effort was to identify and quantify, where possible, flow regimes, sediment sources and sinks, and the sediment processes within the Calcasieu Ship Channel, Lake, and Pass. The results of the study will provide information required to support and verify plan formulation and alternative analysis regarding sediment placement and management within the system to minimize dredging and placement impacts to the channel and ecosystem resources. An overview of the study area is provided in Figure I-1.

Based on information from the U.S. Army Corps of Engineers (USACE), approximately 4 million cubic yards of material is dredged from the Calcasieu Ship Channel and Pass between river miles 5 and 34. Most of this material has been placed in Confined Disposal Facilities (CDFs) adjacent to the ship channel. Since containment dikes are constructed of *in situ* materials, erosion caused by tidal and wind-generated currents, as well as the influence of ship wakes, have caused a significant volume of material within the CDFs to be reintroduced to the ship channel limits.

Prior to developing long-term solutions for dredged materials management, an understanding of the physical processes governing circulation and sediment transport are required. Due to the relatively modest tide range offshore of Calcasieu Pass (approximately 2 to 3 feet) and the shallow nature of Calcasieu Lake, wind stress on the surface of the estuary also plays an important roll in overall circulation patterns governing sediment transport. Appropriate hydrodynamic analyses of the Lake Calcasieu required a two-dimensional (vertically-averaged) modeling package that incorporated the influence of temporally varying wind fields associated with the range of conditions typical to the system. In addition, a field data collection effort was required to augment the available information including water elevation measurements and current measurements at key locations within the system. The dataset developed formed the basis for model boundary conditions, as well as calibration and validation data.

Following development of the calibrated/validated hydrodynamic model, a sediment transport model was incorporated into the two-dimensional circulation model. Since the dredged sediments are predominantly fine-grained (silts and clays), the analysis approach required evaluation of bottom sediment characteristics of the Calcasieu Ship Channel and surrounding areas. Sediment information including grain size distribution, relative shear strength of sediments, and fine-grained sediment mobilization criteria provided critical input parameters to the sediment transport model. A majority of this information was derived from existing local USACE studies (e.g. Calcasieu River and Pass Dredged Material Sedimentation Study) or regional evaluations that addressed similar estuarine morphology. The transport model incorporated these local and regional sediment characteristics, as well as results from the hydrodynamics analysis, to determine potential sediment transport pathways causing shoaling problems within the Calcasieu Ship Channel.

Figure I-1. Overview of the region covered by the hydrodynamic model, where the green line illustrates the land boundary utilized in the modeling effort.

The primary goal of the combined hydrodynamic and sediment transport modeling effort was to identify sediment sources and sinks, as well as the associated sediment transport pathways. Once developed, the model suite can be utilized to assess the effects of alternative dredge disposal sites (e.g. larger upland disposal sites or marsh islands) on circulation and sediment transport patterns.

In addition to the influence of natural hydrodynamic processes, anthropogenic factors potentially increase maintenance dredging frequency and/or accelerate erosion of the CDFs. Due to the heavy marine traffic utilizing the Ship Channel and the confined nature of the channel between Calcasieu Pass and Lake Charles, ship wakes and/or surge can significantly influence erosion of the CDFs adjacent to the channel. The USACE has estimated that nearly 15% of the material shoaling the Ship Channel may be derived from eroding banks associated with existing CDFs. Due to the significance of this potential sediment source responsible for channel shoaling, an analysis of ship-generated waves and currents was performed. Although a substantial amount of research has been compiled regarding ship wake and surge generation, site-specific information remains the most proven technique for evaluating the influence of ship-generated waves and currents on local sediment transport processes. To assess the potential influence of ships traveling along the Calcasieu Ship Channel, a wave and current monitoring program has been performed at key locations along the shipping channel. Information derived from this monitoring effort was utilized to determine the potential magnitude of ship wakes on sediment re-suspension and transport.

The hydrodynamic and sediment transport modeling effort for Lake Calcasieu consists of several components to support the overall goals of the project:

- *Background* – a general overview of the Lake Calcasieu estuarine system.
- *Data Collection and Analysis* – Presentation of data collected to calibrate and validate the modeling effort. The data sources evaluated include information from outside sources.
- *Hydrodynamic Modeling* – Description of the two-dimensional depth-averaged hydrodynamic model set-up, calibration, and validation.
- *Sediment Transport Modeling* – Description of the two-dimensional depth-averaged model of fine-grained sediment transport processes including a discussion of input parameters and limitations.
- *Influence of Vessel Passage on Sediment Suspension* – An evaluation of ship wake processes and their relative contribution to sediment transport within the central portion of the Calcasieu Ship Channel.

II. BACKGROUND

The Calcasieu River system drains an upland area of approximately 3,800 square miles (Nichol, *et al*., 1992). The upper portion of the system consists of a river channel that is characterized by a strong meandering morphology flanked by both cedar swamps and marshlands. The geology of the riverine portion of system consists of Pleistocene Terrace deposits. South of this region, the estuarine portion of Lake Calcasieu widens to a maximum width of approximately 14 miles behind the chenier plain that separates the lake from the Gulf of Mexico. The estuary is fringed by extensive salt marsh, as well as diked freshwater marshes that are managed via a series of control structures. An artificially straightened and deepened tidal inlet connects Lake Calcasieu to the Gulf of Mexico.

Extensive alterations to the natural channel system of Lake Calcasieu have taken place over the past ~130 years. Prior to the initial dredging of the Calcasieu Ship Channel (CSC), there was a 3.5-ft-deep shoal at the mouth of the Calcasieu River (War Department, 1897). This natural bar acted as a constriction, limiting saltwater and tidal inflow into the basin. Removal of the channel mouth bar, coupled with subsequent widening and deepening of the

CSC, allowed increased salinity levels and tidal intrusion into the estuary, resulting in substantial marsh loss, tidal export of significant quantities of organic marsh substrate, and an overall shift to more saline habitats in the region (USDA, 1994). In addition, the CSC permits the upriver flow of denser, more saline water as a saltwater wedge during certain freshwater inflow conditions.

The lower Calcasieu River and the Calcasieu Ship Channel (CSC) have been maintained for navigation since 1874, when the U.S. Army Corps of Engineers (USACE) first constructed a 5-ft-deep x 80-ft-wide x 7,500-ft-long navigation channel through the outer bar of Calcasieu Pass, between Calcasieu Lake and the Gulf of Mexico. In 1903, the CSC was deepened to 13 ft, and between 1937 and 1940, the channel was enlarged to 250 ft wide and 30 ft deep. Finally, in 1968 the ship channel was substantially widened again to 400 ft and dredged to its current depth of 40 ft. Figure II-1 graphically illustrates the timeline associated with anthropogenic changes to the cross-section of the CSC.

In 1968, the USACE completed construction of the Calcasieu River Saltwater Barrier on the Calcasieu River north of the city of Lake Charles. This barrier prohibited the flow of the saltwater into the upper reaches of the Calcasieu River to protect agricultural water supplies. The structure consists of a lock and a flood control barrier with adjustable gates.

The primary saltwater barrier in the lower Calcasieu Basin is the Calcasieu Lock maintained by the USACE, located approximately two miles east of the CSC. This sector-gated lock, which opened in 1950, was designed to prevent saltwater intrusion into the Mermentau Basin. The lock has a 75-ft-wide by ~1,200-ft long chamber with a 13-ft sill (Louisiana DNR, 2002). During upland flood events, the structure is often operated for drainage of the Mermentau Basin to the east. Operating the structure for drainage often becomes problematic for lock operators because of delays incurred to navigation during this time, when the lock is draining and the current through the structure is too swift for traffic to safely navigate through the gates. Therefore, the USACE is continually required to balance lock operation for flood control with the needs of waterborne commerce utilizing the Gulf Intracoastal Waterway (GIWW).

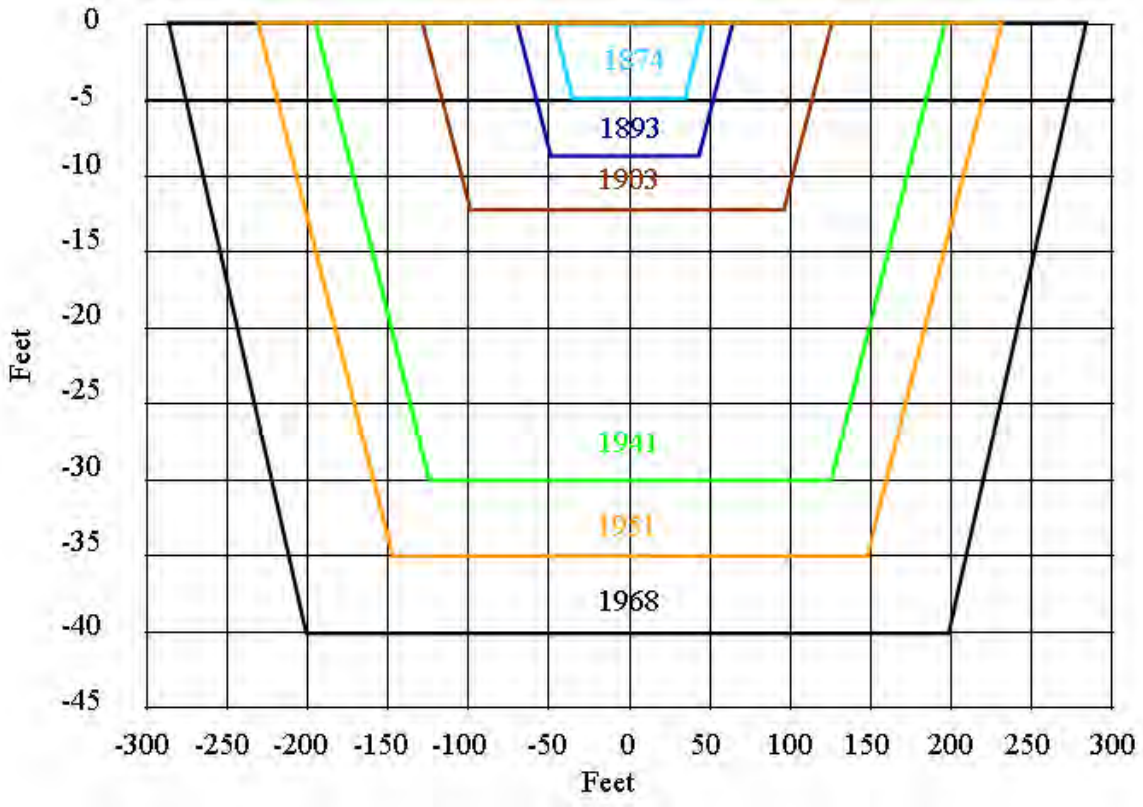

Figure II-1. Historical channel dimensions of the Calcasieu Ship Channel as depicted in a report prepared by the Louisiana Department of Natural Resources (Louisiana DNR, 2002).

According to a recent report prepared by the Louisiana Department of Natural Resources (Louisiana DNR, 2002), only portions of the CSC are dredged annually. Approximately 75% of the dredged material is placed in upland and offshore disposal sites, but the remaining 25% is used for beneficial means, to create marsh. From 1975 to 2002, records of the Louisiana Department of Natural Resources (DNR) Coastal Management Division and the Sabine National Wildlife Refuge indicate that approximately 1,400 acres of marsh had been restored through this beneficial use. The report also estimated that potentially 50% of the dredged material could be used for this purpose. A summary of U.S. Army Corps of Engineers estimates of the CSC shoaling, as well as the associated dredging volumes, can be found in the Shoaling Study: Calcasieu River and Pass, Louisiana, Dredged Material Management Plan – Phase II (Gahagan & Bryant Associates, 2007).

Tides

The offshore tide signal in the Gulf of Mexico can be characterized as a microtidal (tide range < 2 meters), storm influenced region. The mean spring tide range at the mouth of Lake Calcasieu is approximately 2.0 feet and can display either a diurnal or semi-diurnal pattern, also referred to as a mixed tide signal. The primary attenuation of the tide signal occurs through the entrance channel between the seaward tip of the jetties and the main basin of the lake. According to Forbes (1988), between Cameron and Hackberry (a distance of ~14 miles), measured a decrease in tide range from 0.47 meters to 0.20 meters during a semi-diurnal cycle. North of Hackberry, the data showed a negligible reduction in tide range.

Wave and Wind Climate

The wave climate affecting the barrier beach coast fronting the Lake Calcasieu region is relatively mild, with a mean wave height of approximately 1 meter and a mean period of 5-6 seconds from the south-southeast. Tropical storms and hurricanes, as well as passage of winter cold fronts, produce higher water levels and substantially higher energy wave activity than is observed in typical conditions. Figure II-2 illustrates offshore wave conditions typical of the Lake Calcasieu area.

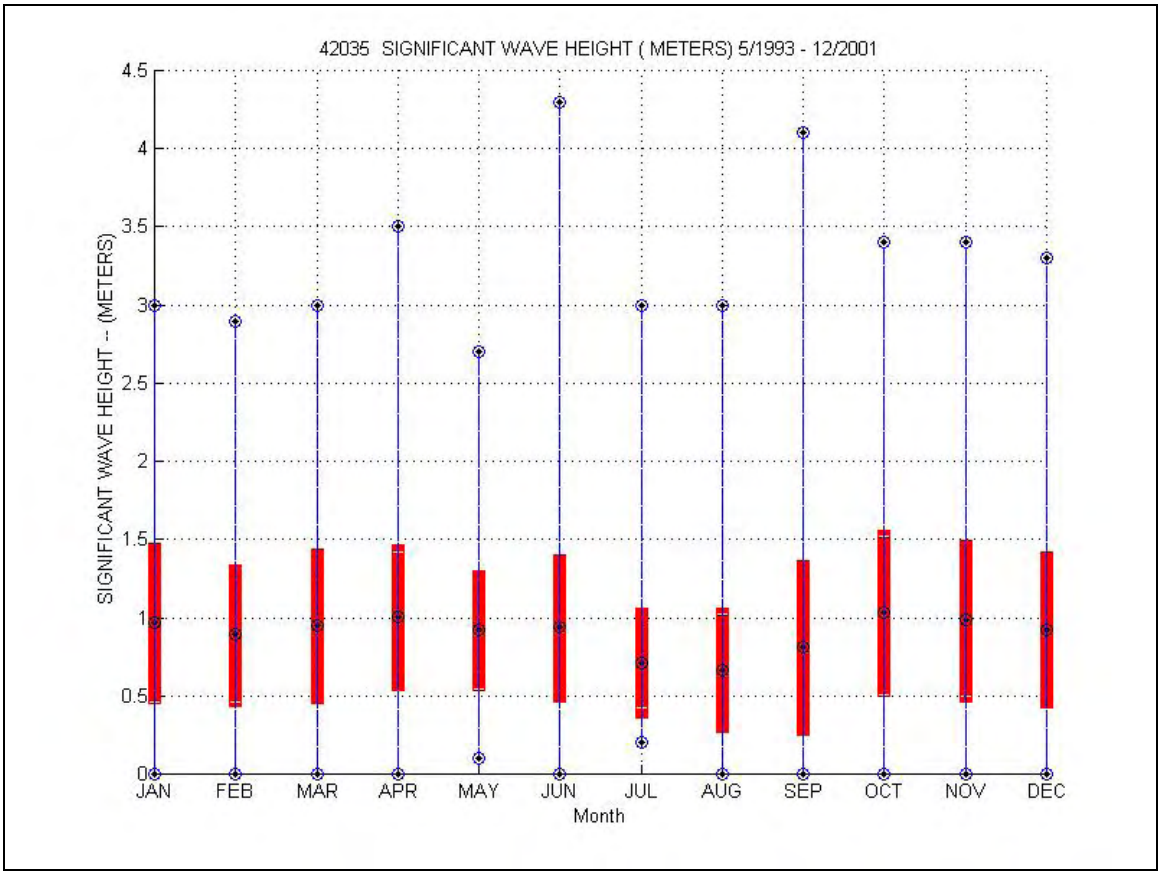

Figure II-2. Summary of observed significant wave height data between 1993 and 2001 collected at the National Data Buoy Center Station #42035 located 22 Nautical Miles east of Galveston. The red bands illustrate the standard deviation centered about the mean wave height for each month and the maximum significant wave heights for each month are shown in meters.

The most severe storms impacting the Lake Calcasieu area are hurricanes. On September 24, 2005, the Lake Calcasieu region experienced Hurricane Rita that had weakened from a Category 5 Hurricane to a strong Category 3 Hurricane at landfall. In Lake Charles, a storm surge elevation of 10 feet above mean sea-level was recorded, representing the second highest measured water level at this location. Figure II-3 provides available water elevation and wind information during Hurricane Rita. As expected, the storm surge elevations in the upper portions of the Lake Calcasieu estuarine system lagged behind the highest wind speeds. In addition, the large surge generated by this major hurricane event overtopped the barrier beach and chenier plain; therefore, the rise in water levels within the system was much more rapid than the subsequent draining. Similar storm surge elevations were observed during Hurricane Audrey on June 27, 1957. Conversely, persistent strong northerly winds can force water

downstream, depressing the water level in Lake Calcasieu by as much as 4 feet below sea level (Forbes, 1988).

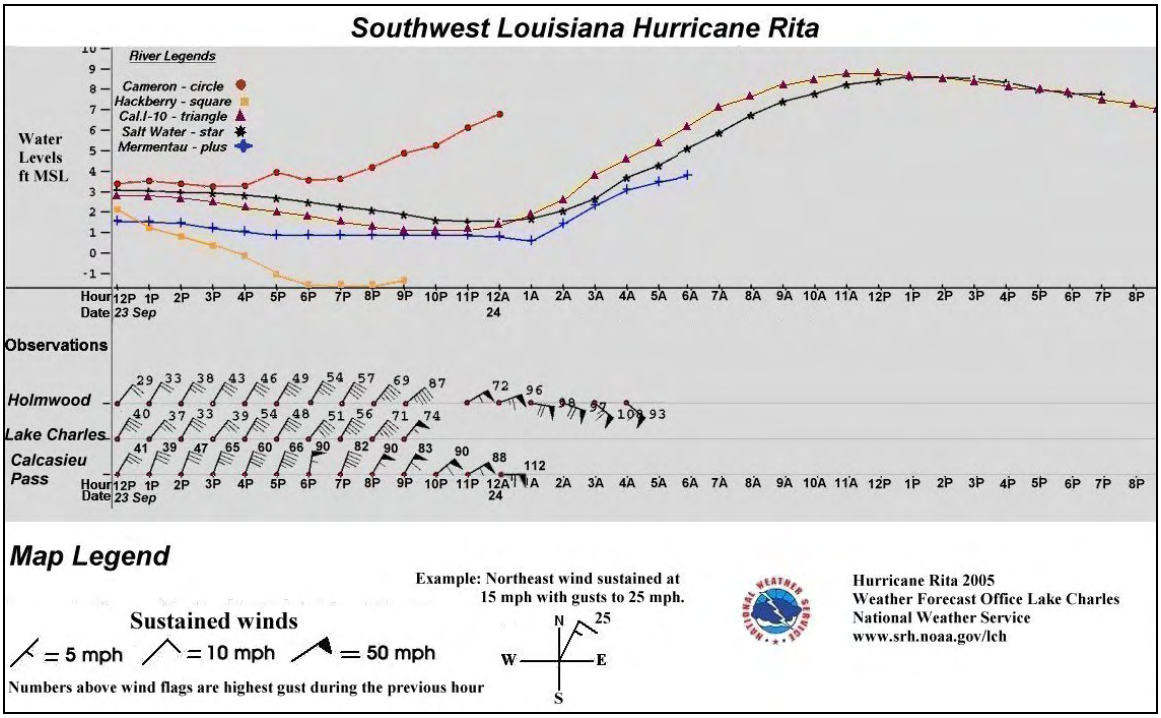

Figure II-3. Storm surge and wind observations during Hurricane Rita in 2005 (Source: National Weather Service). Loss of data from the Cameron, Mermentua, and Hackberry gages likely was a result of the substantial storm surge and wind associated with Hurricane Rita.

River Flow

The Calcasieu River varies from a small fast flowing stream in the headwaters to a broad, sluggish estuary from the latitude of Lake Charles to its entrance into the gulf. Flows in the upper basin may range from a high of 180,000 cubic feet per second in the winter and spring to only slightly over 100 cubic feet per second during the dry summer and fall months. These discharge rates represent instantaneous measurements and may be slightly higher or lower than average daily discharge values. Figure II-4 illustrates the maximum measured flows since the USGS streamflow gage was installed near Kinder. The maximum recorded daily discharge was 166,000 cubic feet per second on May 20, 1953 which raised the water level by about 5.8 feet above sea level (Nichol *et al*., 1992). Based upon available data from McCorquodale and Georgiou (2007),suspended sediment loads are at a maximum during these high freshwater inflow events. The average river inflow is more modest, where the mean daily average flow is ~2,600 cubic feet per second at Kinder. Although this gaging station is several miles upstream of the saltwater barrier in Lake Charles, Forbes (1988) determined that only 20% of the total drainage area and 18% of the discharge is not accounted for due to the stream gage location.

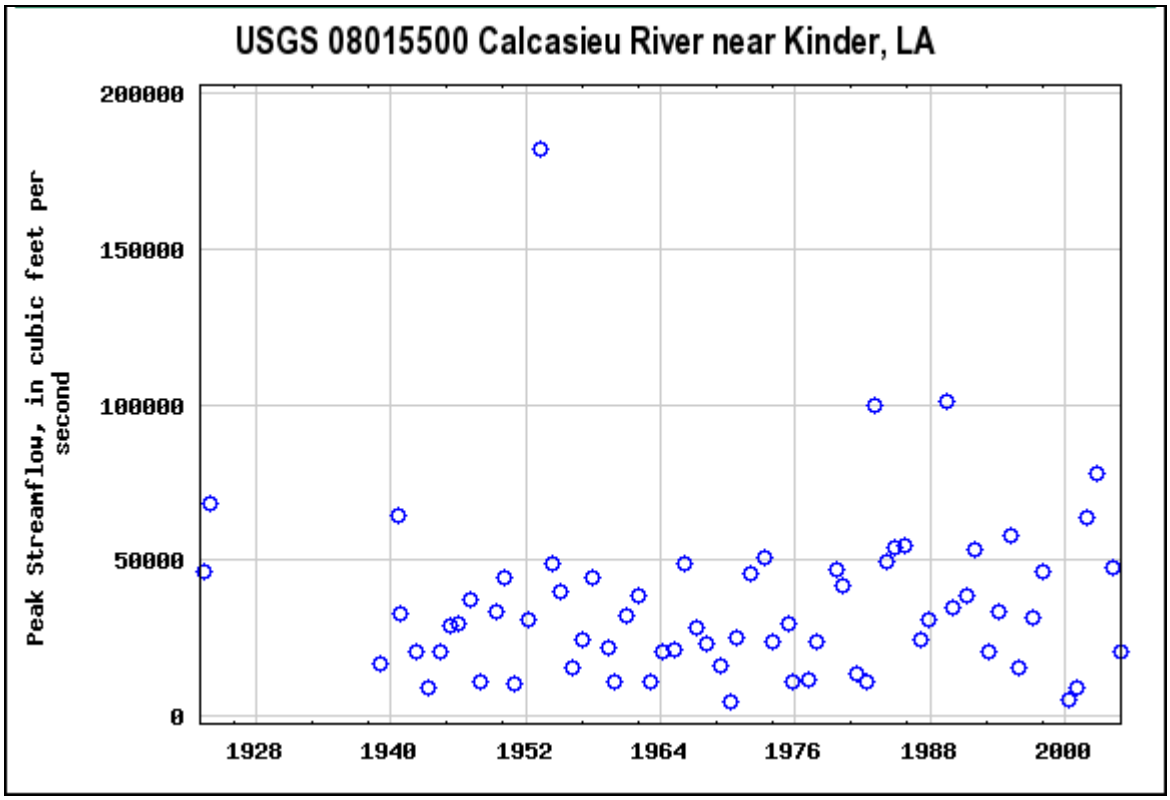

Figure II-4. Maximum measured flows since the USGS streamflow gage was installed near Kinder, Louisiana (Source: USGS).

*Estuarine Classifi*cation

Morphological development of an estuary is dependent on the ever-changing balance between the intensity of the freshwater inflow, wave forcing, and tidal influences. Dalrymple *et al.* (1992) characterized the following two types of estuarine systems:

1. *Wave-dominated* – In these estuaries the wave energy tends to be significant at the entrance and sediment eroded from the coast is transported alongshore forming a spit or barrier beach. Formation of the spit constricts the size of the tidal entrance to the estuary. Eventually, the inlet cross-section represents a balance between eroding sediment from the barrier and tidal currents through the entrance. Within the main basin of the estuary, the currents diminish rapidly. Towards the head of the estuary, fluvial processes tend to dominate; therefore, the central portion of the estuary represents the lowest total energy and likely is characterized by extensive tidal flats and/or salt marshes. Figure II-5 shows a schematic of the characteristics of a wave-dominated estuary.
2. *Tide-dominated* - As a result of relatively large tidal currents at the estuary entrance, the mouth of the estuary typically contains sandbanks oriented in the direction of flow. Since no well-defined barrier beach system develops, tidal energy propagates more freely into the upper parts of the estuary. However, bottom friction within the constricted energy will cause a gradual decrease in tidal energy from the region of the entrance to the head of the estuary. Similar to wave-dominated estuaries the river flow becomes dominant in the upper reaches of the estuary, but this transition from tidal to river energy dominance tends to be more gradual for tide-dominated estuaries.

Based on the morphological structure of the Lake Calcasieu system, the natural estuary can be clearly classified as wave-dominated. The strong tidal currents through the main entrance channel combined with the rapid attenuation of tide range across the barrier beach and chenier plain demonstrate a rapid reduction in tidal energy between the Gulf and Lake Calcasieu. Moreover, the long narrow entrance channel prevents wave energy from entering the estuary from the Gulf. Tidal currents within the main basin of the Lake are negligible and wave energy is limited by the shallow nature of the main basin and the limited fetch. Therefore, the overall estuarine characteristics follow the conceptual model shown in Figure II-5.

Anthropogenic changes to the estuarine have made site-specific changes to the morphology of the system. For example, channelization of the flow by dredging of the CSC has allowed tidal energy (relatively strong currents) to propagate further into the estuary. For this portion of the system, where the CSC is characterized by a narrow deep channel separated from the main basin of Lake Calcasieu by dredge spoil islands, the system is more characteristic of a tide-dominated estuary. Development of the dikes adjacent to the channel has limited overland tidal flow; therefore, salt marsh development has been inhibited and/or prohibited. Many of these dikes prevented salt water intrusion into the freshwater and brackish marsh systems that pre-dated the CSC navigation improvements. However, the deepwater channel prevents the energy reduction in the middle portion that is characteristic of a natural wave-dominated estuary. Instead, the relatively high tidal currents exacerbate sediment transport of fine-grained material located within the main portion of the CSC.

Changes in the hydrologic and salinity regime have occurred since navigation improvements were initiated. As shown in Figure II-6, a general shift from brackish to saline habitat occurred between 1949 and 1997 along the portion of the CSC that runs through Lake Calcasieu. This link between salinity intrusion into the upper parts of the estuary and surrounding marsh systems provides clear evidence that the navigation improvements associated with the CSC have allowed the tidal excursion to propagate further landward than the previous natural estuarine system. This alteration in tidal excursion supports the observations of increased tidal velocities through the CSC, with the associated higher sediment transport potential of a more tide-dominated estuary.

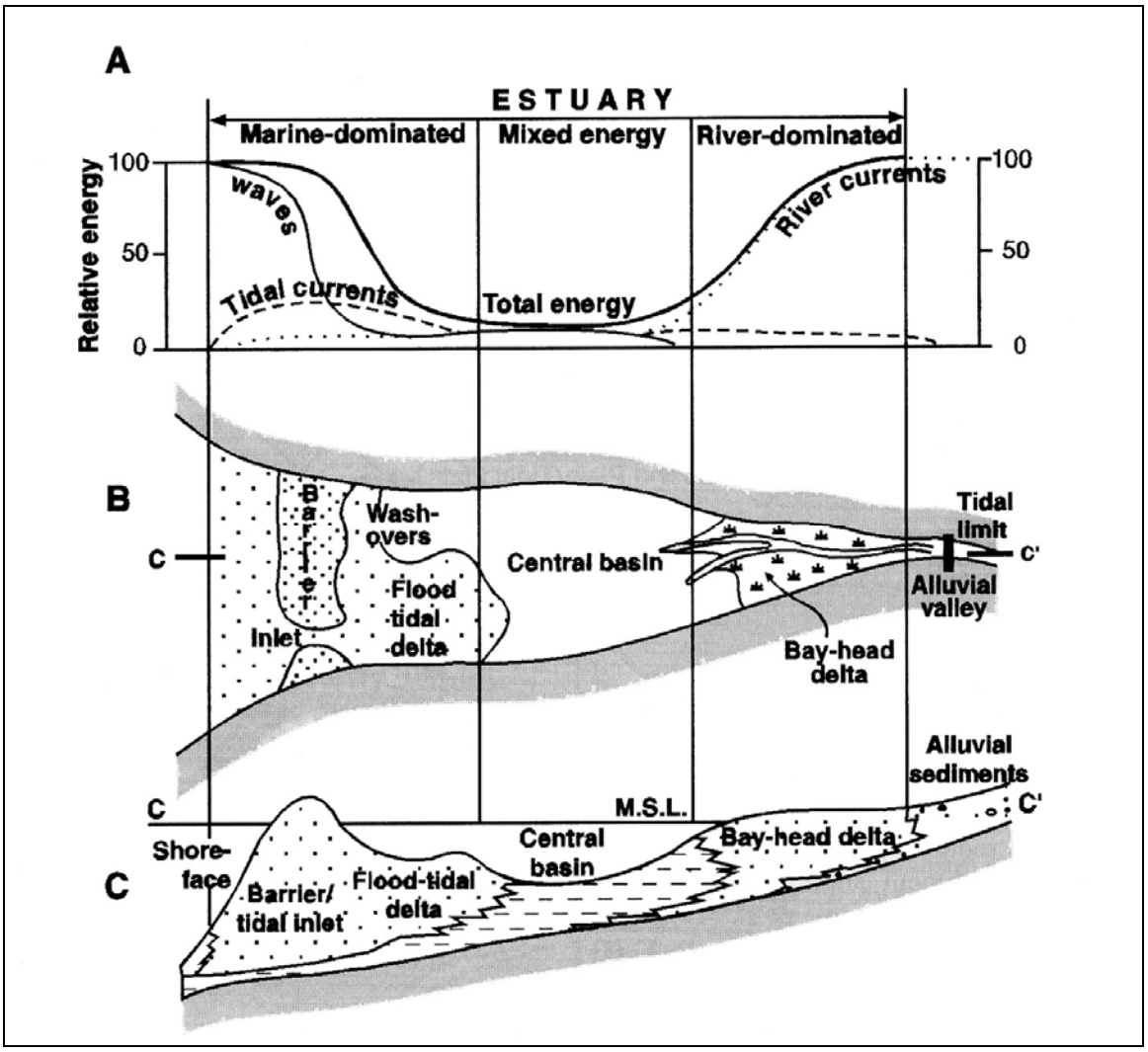

Figure II-5. Distribution of (A) relative energy, (B) morphological components, and (C) sedimentary facies in a longitudinal section with an idealized wave-dominated (microtidal) estuary (Source: Dalrymple *et al*., 1992).

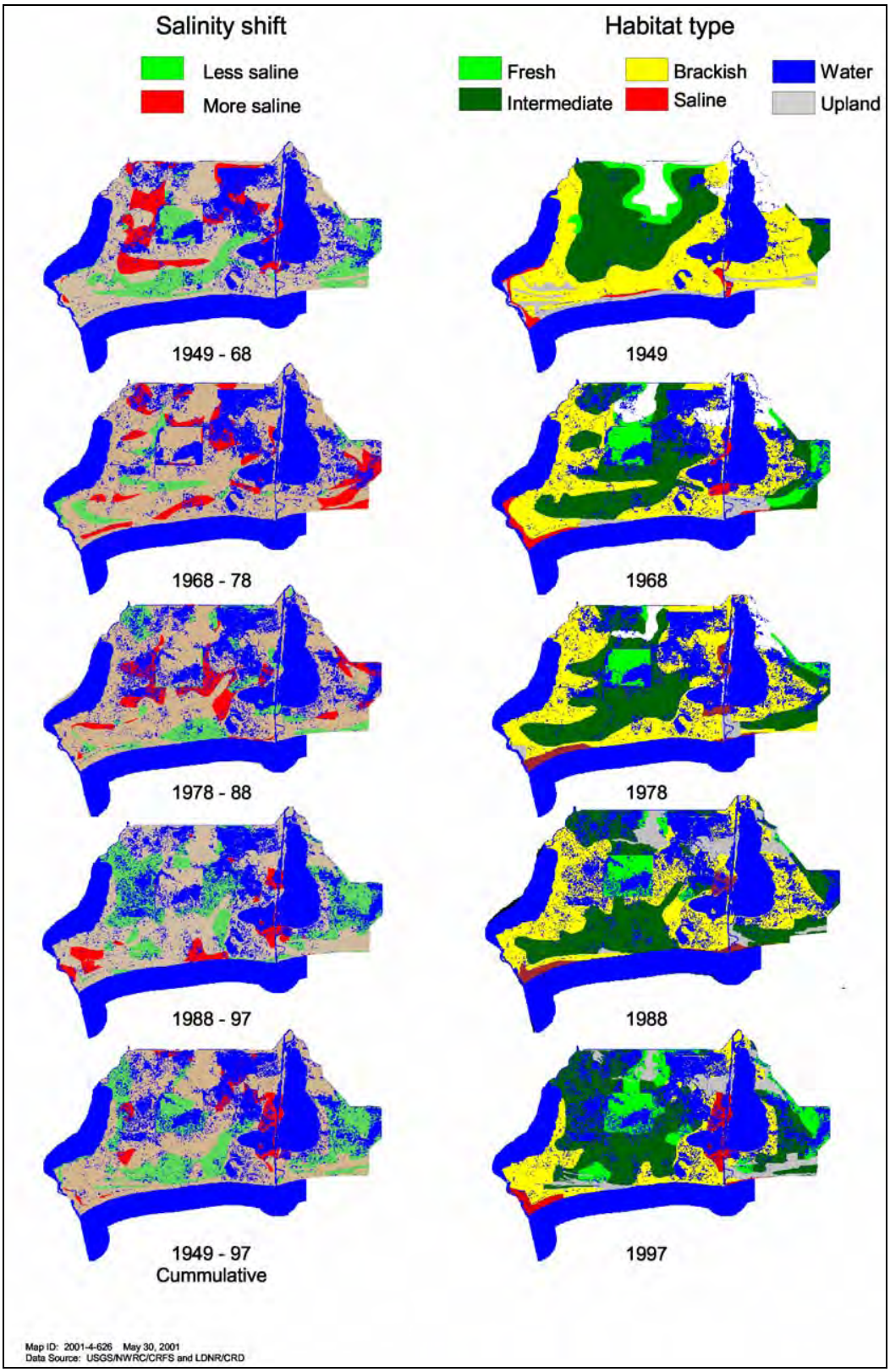

Figure II-6. Wetland and salinity shifts in the Calcasieu-Sabine Basin based on historical vegetative surveys between 1949 and 1997 (Source: Louisiana DNR, 2002).

III. DATA COLLECTION AND ANALYSIS

Accurate numerical modeling of system hydrodynamics is dependent upon measured conditions within the estuary for two important reasons:

- To provide 'real' observations of hydrodynamic behavior to calibrate and verify the model results
- To define accurately the system geometry and boundary conditions for the numerical model

To support hydrodynamic modeling efforts in Lake Calcasieu, tidal water elevation variations were measured at eight locations within the system. Cross-channel current measurements (ADCP) were surveyed through a tidal cycle along the entrance channel in Cameron, LA. Meteorological measurements were taken for a two-month period to aid in the development of the hydrodynamic model.

The system geometry was defined using historical bathymetry, dredging surveys, collected bathymetry and aerial photographs. The bathymetric information was utilized to develop the computational grid of the system geometry for the hydrodynamic modeling effort. Tidal elevation measurements within the system were used for both forcing conditions and to evaluate tidal attenuation through the estuarine system. Data collected by other sources (USACE and NOAA) was also collected to supplement the data collection program.

III.1 WATER ELEVATION MEASUREMENTS

Changes in water surface elevation were measured using internal recording tide gages. These tide gages were installed on fixed platforms (pier pilings and abutments) to record changes in water pressure over time. Variations in the water surface can be due to tides, wind set-up, or other low frequency oscillations of the sea surface. The tide gages were installed in 8 locations within the Lake Calcasieu estuary system as shown in Figures III-1 and III-2. The gages were deployed in late November 2006 and recovered mid-December 2006. Data records span at least 29 days to yield an adequate time period for resolving the primary tidal constituents and to isolate the periods of heavy precipitation that occurred during the deployment. NOAA tidal gauges Station 8768094 and Station 8767816 are also shown in Figures III-1 and III-2.

The tide gages used for the study consisted Brancker XR-420 instruments. Data collections parameters were set for 10-minute intervals, with each 10-minute observation resulting from a 16-second burst of measurements that are averaged for each observation. Each of these instruments use strain gage transducers to sense variations in pressure, with resolution of 0.001% full scale and a pressure accuracy of 0.01% full scale. Each gage was calibrated prior to installation to assure accuracy.

Once the data were downloaded from each instrument, the water pressure readings were corrected for variations in atmospheric pressure. Hourly atmospheric readings were obtained from the NOAA meteorological station in Cameron, LA (Calcasieu Pass, Station #8768094), interpolated to 10-minute intervals, and subtracted from the pressure readings, resulting in water pressure above the instrument. Further, a (constant) water density value of 1025 kg/m^3 was applied to the readings to convert from pressure units (psi) to head units (for example, meters of water above the tide gage). All of the tide gages were surveyed into local benchmarks to provide vertical rectification of the water level; these survey values were used to

adjust the water surface to a known vertical datum. The result from each gage is a time series representing the variations in water surface elevation relative to Mean Low Gulf (MLG). Figures III-3 and III-4 present the water levels at each gage location.

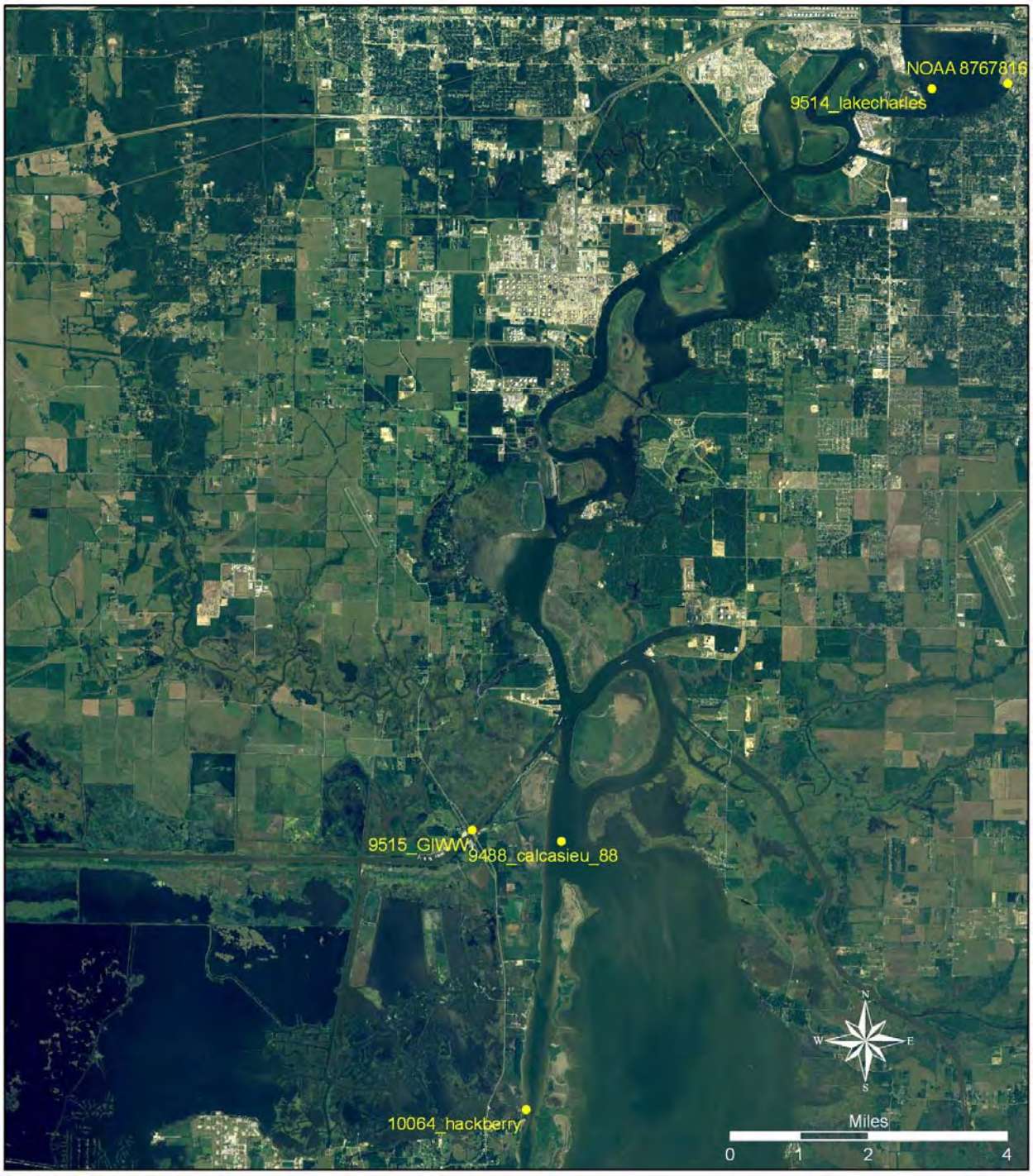

Figure III-1. Tide gage locations in the northern portion of Lake Calcasieu. Yellow points are tide gage locations.

Figure III-2. Tide gage and ADCP transect locations in the southern portion of Lake Calcasieu. Yellow points are tide gage locations and red is the ADCP transect location.

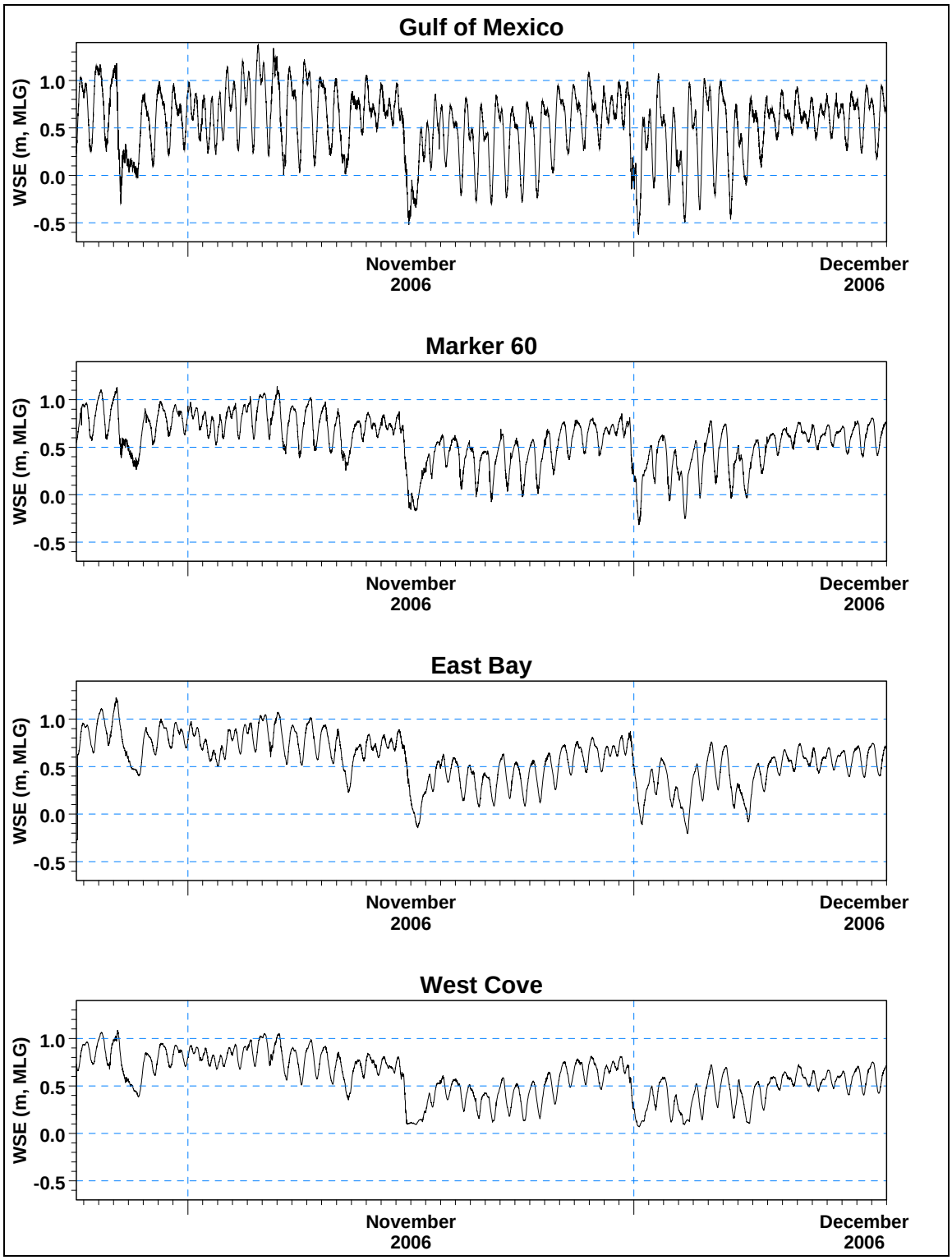

Figure III-3. Tidal elevation observations for Gulf of Mexico (10066), Marker 60 (9507), East Bay (9487), and West Cove (9506).

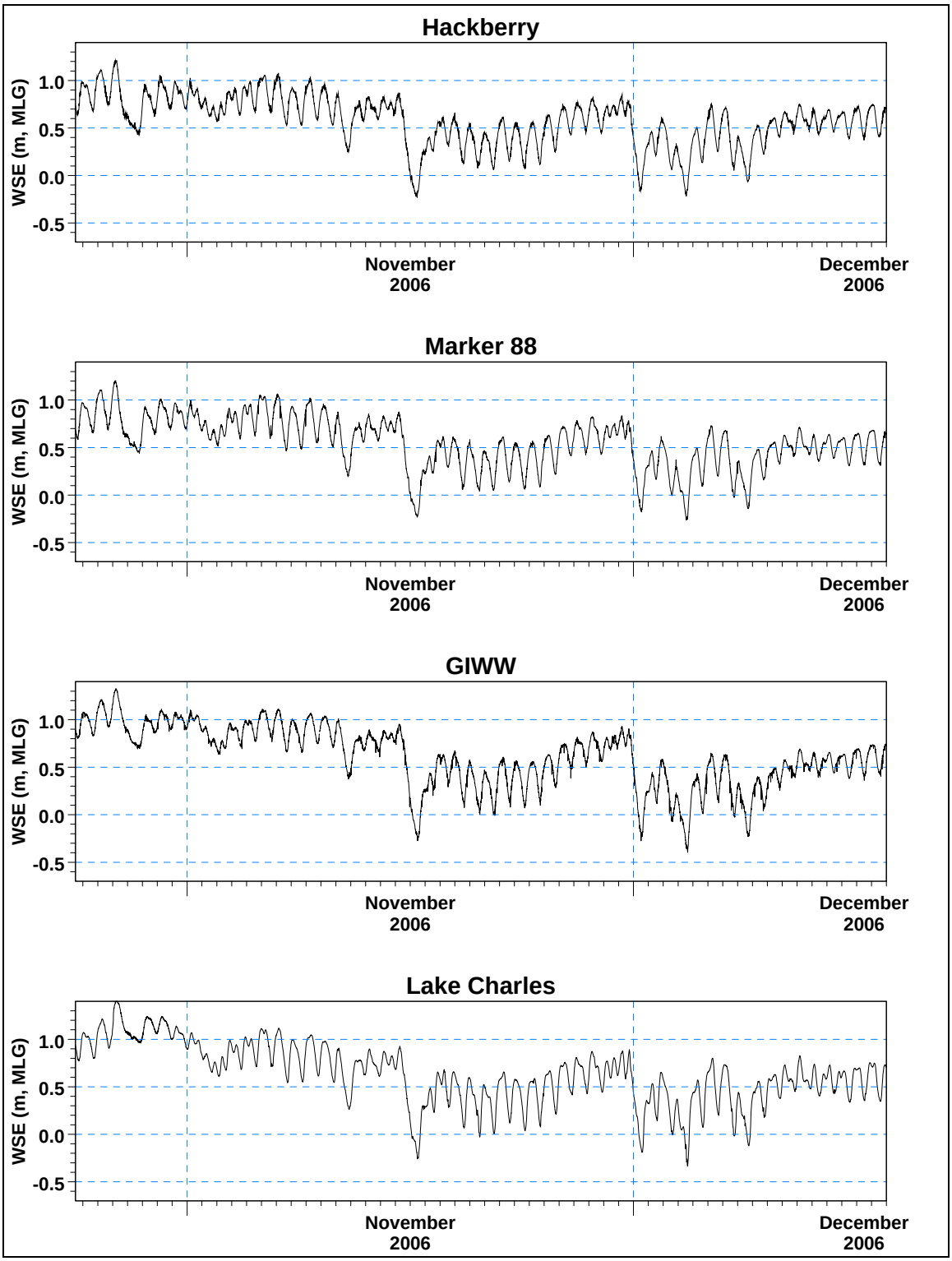

Figure III-4. Tidal elevation observations for Hackberry (10064), Marker 88 (9488), GIWW (9515), and Lake Charles (9514).

Analyses of the tide and bathymetric data provided insight into the hydrodynamic characteristics of the system. Harmonic analysis of the tidal time series produced tidal amplitude and phase of the major tidal constituents, and provided assessments of hydrodynamic 'efficiency' of each system in terms of tidal attenuation. This analysis also yielded an assessment of the relative influence of non-tidal, or residual, processes (such as wind forcing) on the hydrodynamic characteristics of each system.

Figures III-3 and III-4 shows the tidal elevation for the period October 24 through December 18, 2006 at eight locations around Lake Calcasieu: Offshore in the Gulf of Mexico (Gage 10066), Marker 60 (Gage 9507), East Bay (Gage 9487), West Cove (Gage 9506), Hackberry (Gage 10064), Marker 88 (Gage 9488), GIWW (Gage 9515), and Lake Charles (9514). The curves have a predominant diurnal (once-a-day), variation, with the Gulf of Mexico record exhibiting a slight semi-diurnal (twice-a-day) component. The water level records at all of the gage locations show the significant impact which meteorological events have upon water levels. Four events can be clearly seen within the tide records (October 27, November 15, December 1, and December 4). The gage records also exhibit a strong modulation of the lunar and solar tides, resulting in the familiar spring-neap fortnightly cycle. The spring (maximum) tide range was approximately 1.3 meters, and occurred on November 5, 2006. The neap (or minimum) tide range was 0.45 meters, occurring November 28, 2006.

To better quantify the changes to the tide from the inlet to inside the system, the standard tide datums were computed from a subset of the 54-dayrecord. A subset of the entire record was used due to the influence of metrological events on the water levels within the Calcasieu basin. The subset was selected to minimize the influence of non-tidal forces on the tidal datums. The computed datums are presented in Table III-1. For most NOAA tide stations, these datums are computed using 19 years of tide data, the definition of a tidal epoch. For this study, a significantly shorter time span of data was available; however, these datums still provide a useful comparison of tidal dynamics within the system. The Mean Higher High Water (MHHW) and Mean Lower Low Water (MLLW) levels represent the mean of the daily highest and lowest water levels. The Mean High Water (MHW) and Mean Low Water (MLW) levels represent the mean of all the high and low tides of a record, respectively. The Mean Tide Level (MTL) is simply the mean of MHW and MLW.

Harmonic analyses were performed on the time series from each gage location. Harmonic analysis is a mathematical procedure that fits sinusoidal functions of known frequency to the measured signal. The amplitudes and phase of 23 known tidal constituents result from this procedure. Table III-2 presents the amplitudes of the eight largest tidal constituents. The S_1, or the familiar once-a-day solar diurnal, tide is the strongest contributor to the signal with an amplitude of 0.224 meters in the Gulf of Mexico. The range of the K_1 tide is twice the amplitude, or 0.448 meters. Other diurnal tides, O_1, Q_1 and M_1, possess significant contributions to the tidal amplitudes throughout the Lake Calcasieu system. Semi-diurnal tides strongly contribute to the observed tide; the M_2, or the familiar twice-a-day lunar semi-diurnal tide, is the strongest semi-diurnal contributor to the signal with an amplitude of 0.166 meters. S_2 (12.00 hour period) and N_2 (12.66-hour period) tides both have significant contributions. The Msf is a fortnightly tide which increases throughout the system.

Table III-1. Tide datums computed from 12-day records collected in Lake Calcasieu in Dec 2006. Datum elevations are given relative to MLG in meters.							
Location	Tide Datum (meters)						
	Max Tide	MHHW	MHW	MTL	MLW	MLLW	Min Tide
Offshore	1.022	0.902	0.803	0.574	0.346	0.112	-0.465
Marker 60	0.459	0.399	0.374	0.215	0.057	-0.012	-0.427
East Bay	0.430	0.335	0.303	0.172	0.042	-0.030	-0.253
West Cove	0.376	0.303	0.281	0.156	0.030	-0.013	-0.220
Hackberry	0.612	0.515	0.511	0.351	0.189	0.141	-0.155
Marker 88	0.473	0.361	0.356	0.187	0.019	-0.031	-0.372
GIWW	0.315	0.166	0.143	0.023	-0.096	-0.219	-0.518
Lake Charles	0.797	0.652	0.641	0.418	0.194	0.228	-0.037

Table III-2. Tidal Constituents, Lake Calcasieu, Cameron, LA, Oct-Dec 2006.								
	AMPLITUDE (meters)							
	K1	O1	M2	S2	N2	Msf	Q1	M1
Period (hours)	23.93	25.82	12.42	12.00	12.66	354.61	26.87	24.83
Offshore	0.224	0.208	0.166	0.078	0.052	0.053	0.047	0.018
Marker 60	0.125	0.115	0.055	0.039	0.022	0.076	0.028	0.010
East Bay	0.109	0.095	0.045	0.016	0.014	0.090	0.019	0.009
West Cove	0.095	0.079	0.034	0.009	0.011	0.070	0.019	0.004
Hackberry	0.108	0.094	0.042	0.011	0.011	0.092	0.021	0.005
Marker 88	0.117	0.100	0.050	0.013	0.012	0.092	0.023	0.005
GIWW	0.098	0.091	0.044	0.009	0.010	0.133	0.017	0.006
Lake Charles	0.116	0.107	0.068	0.020	0.013	0.136	0.015	0.005

The observed astronomical tide is therefore the sum of several individual tidal constituents, with a particular amplitude and frequency. For demonstration purposes a graphical example of how these constituents add together is shown in Figure III-5.

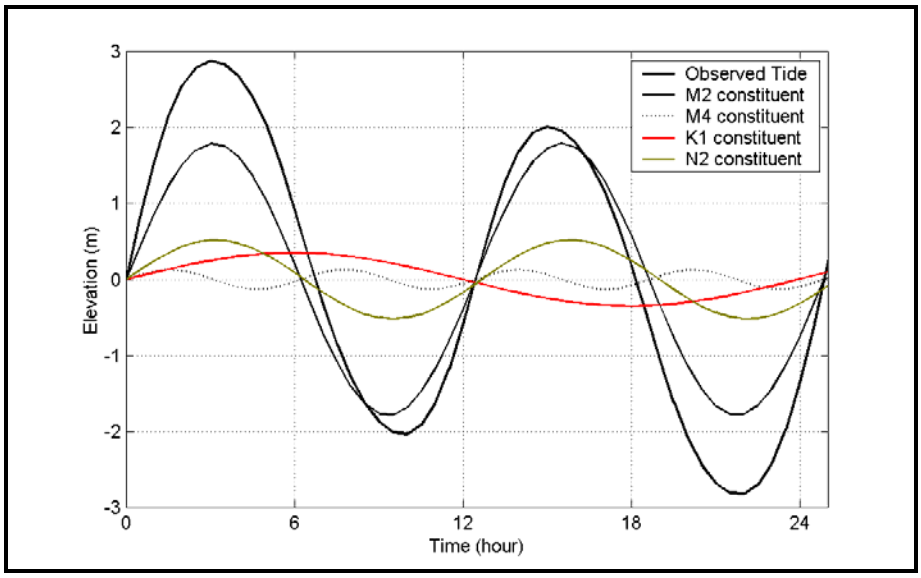

Figure III-5. Example of an observed astronomical tide as the sum of its primary constituents.

Table III-2 also shows how the constituents vary as the tide propagates into the upper reaches. Note the reduction in amplitudes from the Gulf of Mexico through the inlet to Marker 60, and the further reduction at the upper portions Calcasieu basin. The amplitude reduction is greatest in the upper reaches of Lake Calcasieu and along the edges on the east and west side. The decrease in the amplitude of the constituents is evidence of frictional damping.

Table III-3 presents the phase delay of the M_2 tide at all tide gage locations compared to the offshore gage in the Gulf of Mexico. Phase delay is another indication of tidal damping, and results with a later high tide at inland locations. The greater the frictional effects and distance, the longer the delay between locations.

Table III-3. M_2 Tidal Attenuation, Centerville Lake Calcasieu, Oct-Dec 2006 (Delay in hours relative to the Gulf of Mexico).

Location	Delay (hours)
Offshore	--
Marker 60	0.54
East Bay	3.34
West Cove	2.43
Hackberry	3.68
Marker 88	4.10
GIWW	4.95
Lake Charles	5.26

In addition to the tidal analysis, the data were further evaluated to determine the importance of tidal versus non-tidal processes to changes in water surface elevation. These other processes include wind forcing (set-up or set-down) within the system, as well as sub-tidal

oscillations of the sea surface. Variations in water surface elevation can also be affected by freshwater discharge into the system, if these volumes are relatively large. Which is true for a number of the storm events during the instrument deployment. This analysis calculated the energy (or variance) of the original water elevation time series, and compared these energy values to that of the purely tidal signal (re-created by summing the contributions from the 23 known harmonic constituents). Subtracting the tidal signal from the original elevation time series resulted with the non-tidal, or residual, portion of the water elevation changes. The energy of this non-tidal signal is compared to the tidal signal, and yields a quantitative measure of how important these non-tidal physical processes can be to hydrodynamic circulation within the estuary. The results of this analysis Lake Calcasieu region are posted in Table III-4.

Table III-4. Percentages of Tidal versus Non-Tidal Energy, Lake Calcasieu, Oct to Dec 2006.

	Total Variance ($ft^2 \cdot sec$)	Tidal (%)	Non-tidal (%)
Offshore	1.261	57.8	42.2
Marker 60	0.716	30.7	69.3
East Bay	0.699	24.9	75.1
West Cove	0.567	21.1	78.9
Hackberry	0.719	23.7	76.3
Marker 88	0.764	25.4	74.6
GIWW	1.074	19.1	80.9
Lake Charles	1.065	25.1	74.9

Table III-4 shows that the percentage of tidal energy was largest in the offshore signal in Gulf of Mexico; as should be expected given the tidal attenuation through the system. In general, the energy of the signal decreases with distance from the offshore gage, with the lowest energy found in upper regions of the estuarine systems. Due to the complex hydrodynamics that characterize the upper portion of the estuary, there is not a consistent reduction in tidal energy with increased distance from the inlet. Specifically, tidal fluctuation measurements illustrating the lowest percentage of tidal energy were in the vicinity of the CSC and GIWW confluence. At this location, water elevations are influenced by all three major hydrodynamic inputs to the system: tidal flow from the Gulf through the CSC, tidal flow from Lake Sabine through the GIWW, and freshwater inflow from the Calcasieu River. The analysis also shows that tides are responsible for approximately 25% of the water level changes. Meteorological effects in this data set were significant contributors to the total observed water level changes. The relative increase in non-tidal energy within this system is likely due to the decrease in tidal energy as a result of frictional forces and the relatively shallows waters of the upper system being more susceptible to wind forcing, rather than actual growth of residual forces. The damping can be seen in Figure III-6.

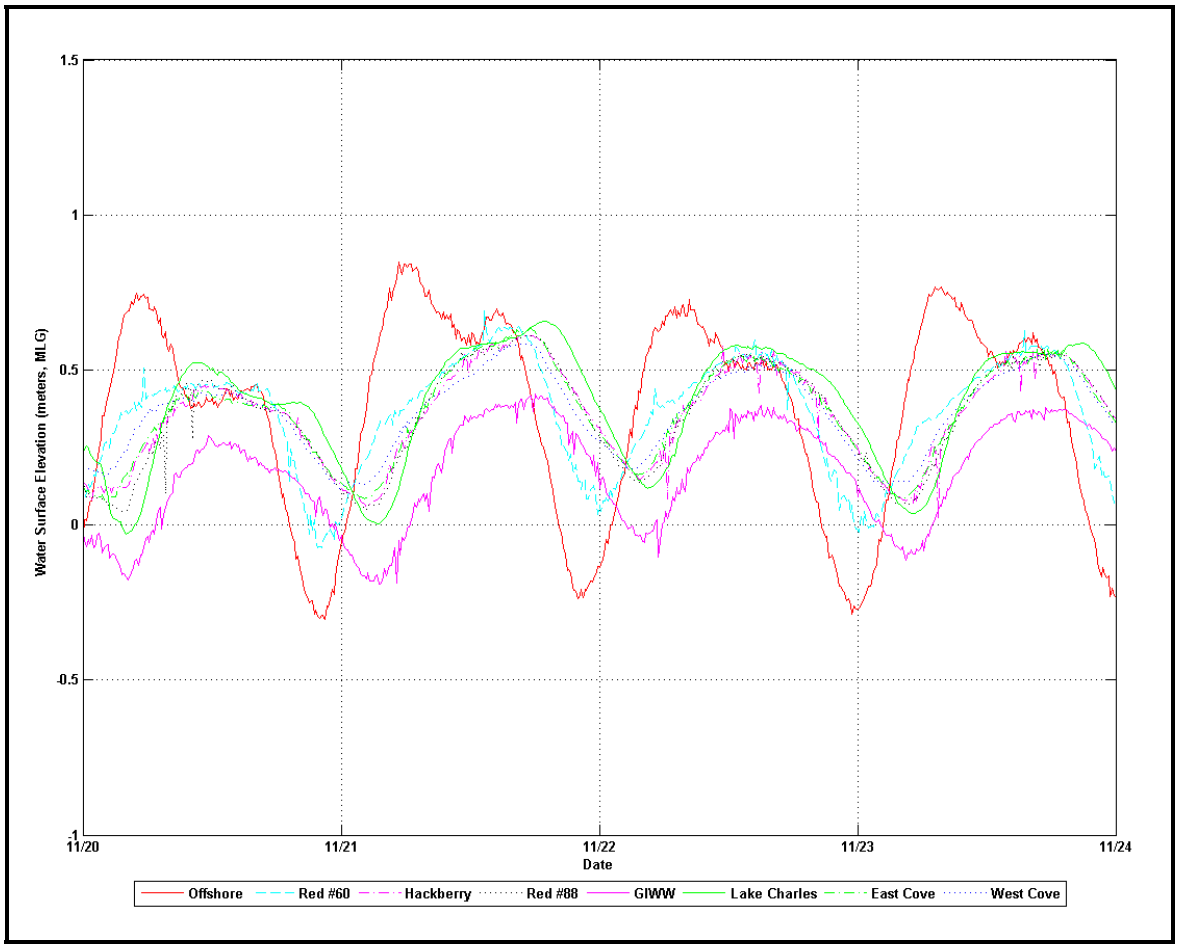

Figure III-6. Water elevation variations for a 4-day period in the Lake Calcasieu. Notice the reduced amplitude as well as the delay in times of high- and low- tide relative to Gulf of Mexico due to frictional damping through the estuary.

III.2 CURRENT MEASUREMENTS

The measurements were collected using an Acoustic Doppler Current Profiler (ADCP) mounted aboard a small survey vessel. The boat repeatedly navigated a pre-defined transect line across the main channel, approximately every 30 minutes, with the ADCP continuously collecting current profiles. This pattern was repeated for an approximate 12.5-hour duration to ensure measurements over the entire tidal cycle. The results of the data collection effort are high-resolution observations of the spatial and temporal variations in tidal current patterns throughout the survey area.

Measurements were obtained with a BroadBand 1200 kHz Acoustic Doppler Current Profiler (ADCP) manufactured by RD Instruments (RDI) of San Diego, CA. The ADCP is factory calibrated and does not require *in situ* calibration during deployment. The ADCP was mounted to a specially constructed mast, which was rigidly attached to the rail of the survey vessel. The ADCP was oriented to look downward into the water column, with the sensors located approximately 0.4 meters below the water surface. The mounting technique assured no flow disturbance due to vessel wake.

The ADCP emits individual acoustic pulses from four angled transducers (at 20° from the vertical) in the instrument. The instrument then listens to the backscattered echoes from discrete depth layers in the water column. The difference in time between the emitted pulses and the returned echoes, reflected from ambient sound scatters (plankton, debris, sediment, etc.), is the time delay. BroadBand ADCPs measure the change in travel times from successive pulses. As particles move further away from the transducers sound takes longer to travel back and forth. The change in travel time, or propagation delay, corresponds to a change in distance between the transducer and the sound scatter, due to a Doppler shift. The propagation delay, the time lag between emitted pulses, and the speed of sound in water are used to compute the velocity of the particle relative to the transducer. By combining the velocity components for at least three of the four directional beams, the current velocities are transformed using the unit's internal compass readings to an orthogonal earth coordinate system in terms of east, north, and vertical components of current velocity.

Vertical structure of the currents is obtained using a technique called 'range-gating'. Received echoes are divided into successive segments (gates) based on discrete time intervals of pulse emissions. The velocity measurements for each gate are averaged over a specified depth range to produce a single velocity at the specified depth interval ('bin'). A velocity profile is composed of measurements in successive vertical bins.

The collection of accurate current data with an ADCP requires the removal of the speed of the transducer (mounted to the vessel) from the estimates of current velocity. 'Bottom tracking' is the strongest echo return from the emission of an additional, longer pulse to simultaneously measure the velocity of the transducer relative to the bottom. Bottom tracking allows the ADCP to record absolute versus relative velocities beneath the transducer. In addition, the accuracy of the current measurements can be compromised by random errors (or noise) inherent to this technique. Improvements in the accuracy of the measurement for each bin are achieved by averaging several velocity measurements together in time. These averaged results are termed 'ensembles'; the more pings used in the average, the lower the standard deviation of the random error.

For this study, the standard deviation (or accuracy) of current estimates (resulting from an ensemble average of 10 individual pulses) was approximately 0.1 m/sec. Each ensemble took approximately 5-6 seconds to collect. Averaging parameters resulted in a horizontal resolution of approximately 5-10 meters along the transect line. For example, the ADCP transect was approximately 380 meters across, resulting in approximately 40 to 70 independent velocity profiles per transect. The vertical resolution was set to 0.5 m, or one velocity observation per every 50 centimeters of water depth. The first measurement bin was centered 1.2 meters from the surface, allowing for the transducer draft as well as an appropriate blanking distance between the transducer and the first measurement.

Current measurements were collected by the ADCP as the vessel navigated repeatedly a pre-defined transect line across in main channel in Cameron, LA (Figure III-2). The line-cycles were repeated every half-hour throughout the survey. The first cycle was begun at 11:32 hours (Central Daylight Time, CDT) and the final cycle was completed at 00:06 hours (CDT), for a survey duration of approximately 12.5 hours on October 25, 2006.

The transect line was designed to measure as accurately as possible the volume flux through the entrance channel between the Gulf of Mexico and Lake Calcasieu during a complete tidal cycle. The transect line ran across the channel from east-to-west direction and was then repeated west-to-east approximately every 30-minutes. The current measurements

observed during the ebb and flood tides across ADCP transect can be seen in Figures III-7 through III-11. The color variations in the plots indicate the magnitude of the current in each of the measurement bins.

In the area around the ADCP transect the channel is wide and approximately 15 meters deep. The eastern bank slopes gradually towards the main channel, while the western bank is more steep. The maximum currents (flood and ebb) are centered within the channel, with velocities decreasing along the edges due to frictional losses. Tidal currents within the channel reached maximum speeds over 2 m/sec on the flood tide. During slack-water periods, currents were vertically coherent, Figure III-8. Flow rates throughout the entire survey are shown in Figure III-12.

Figure III-11 represents the channel velocities after the passage of an LNG tanker heading northbound on a flood tide. The plot illustrates the significant disruption to the regular flow patterns as a result of the ships passage. Figure III-10 shows the last transect measured prior to the passage of the tanker and shows a cohesive concentrated flow centered at midpoint of the cross-section towards the surface, while the next transect shows a split flow and uneven distribution of flow throughout the cross-section.

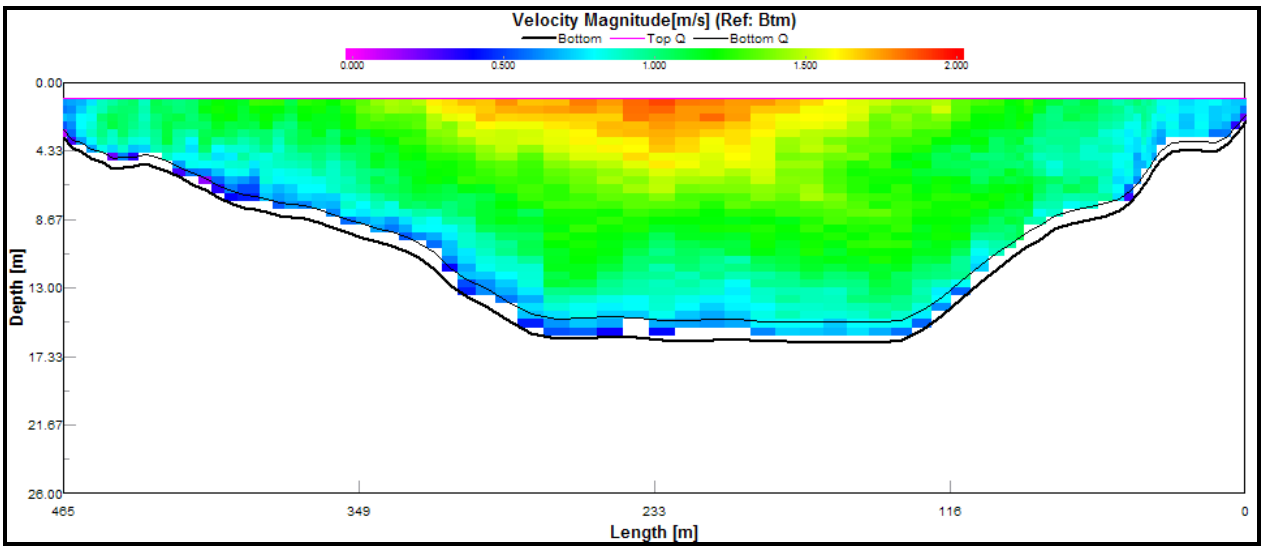

Figure III-7. Color contour plot of velocity magnitude across the main channel measured at 12:35 EDT on October 25, 2006 during the ebb tide. Colors variations indicate the magnitude of flow moving in each measurement bin.

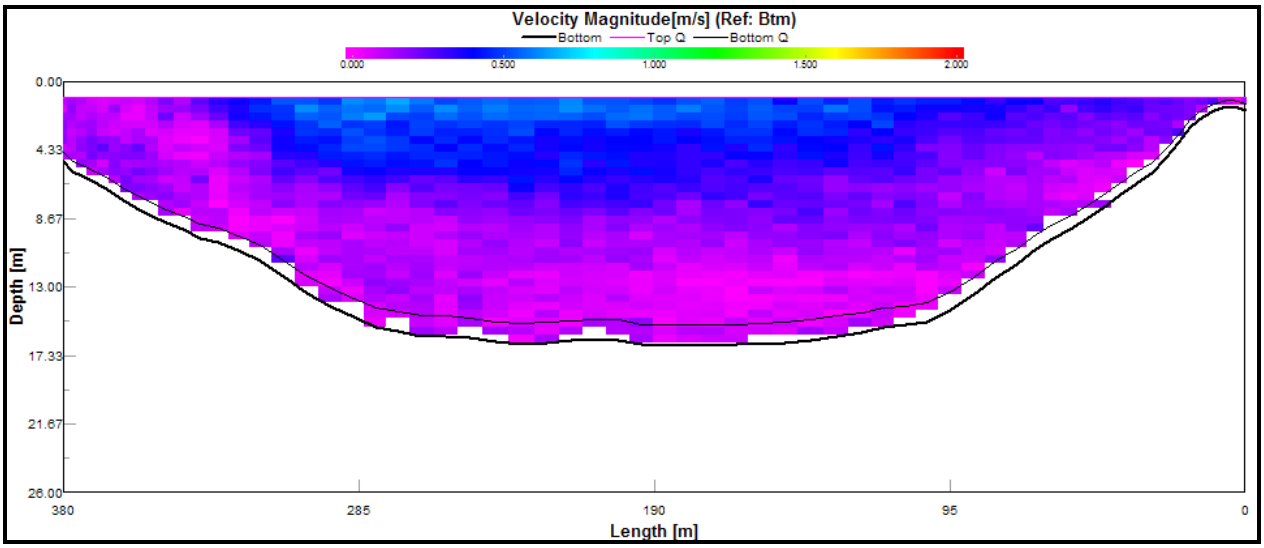

Figure III-8. Color contour plot of velocity magnitude across the main channel measured at 14:59 EDT on October 25, 2006 during the transition from ebb tide to flood tide. Colors variations indicate the magnitude of flow moving in each measurement bin.

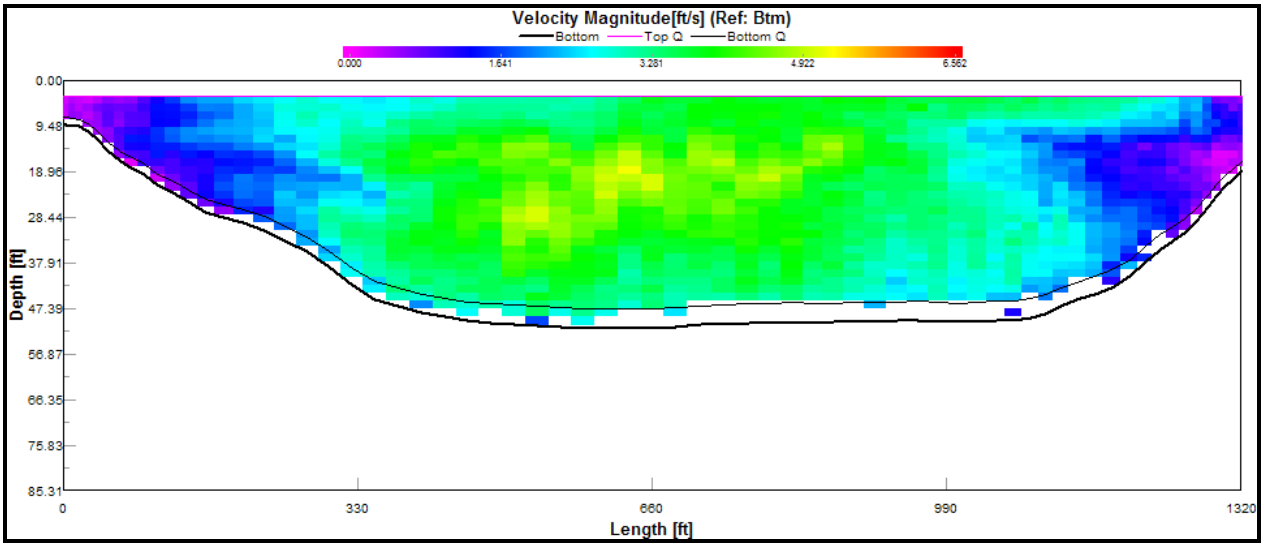

Figure III-9. Color contour plot of velocity magnitude across the main channel measured at 19:55 EDT on October 25, 2006 at the peak measured flood tide. Colors variations indicate the magnitude of flow moving in each measurement bin.

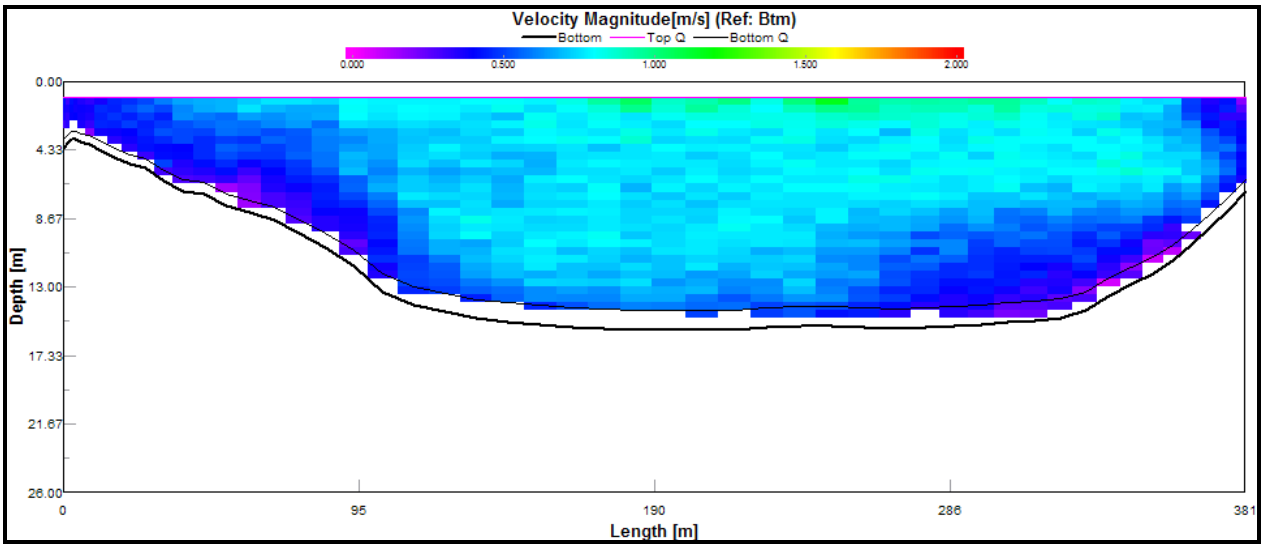

Figure III-10. Color contour plot of velocity magnitude across the main channel measured at 17:56 EDT on October 25, 2006. Transect measured prior to the passage of LNG tanker. Colors variations indicate the magnitude of flow moving in each measurement bin.

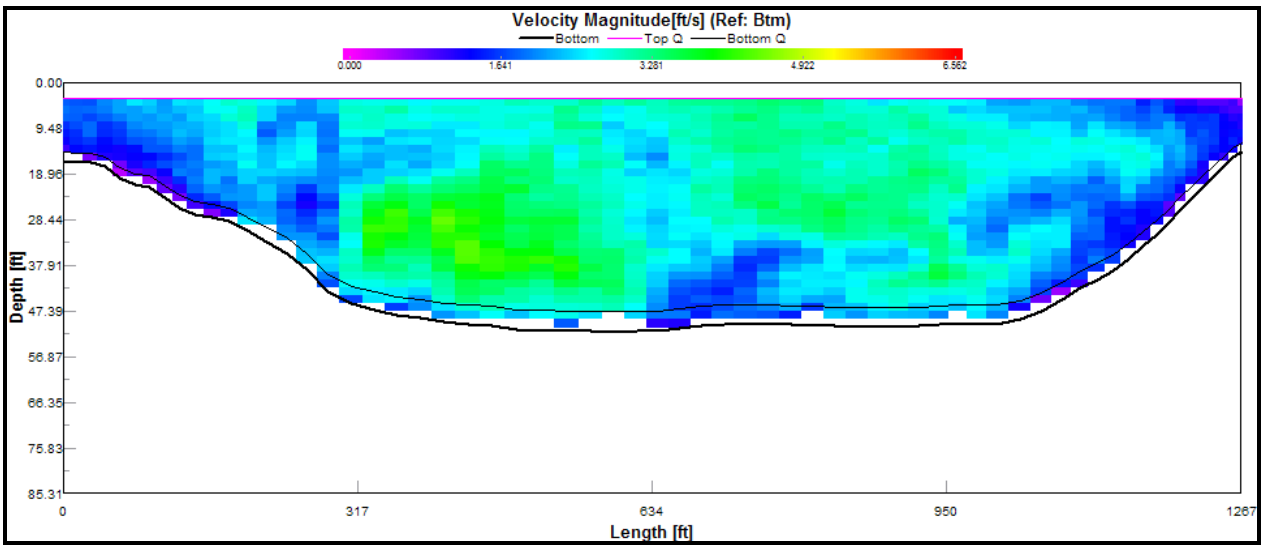

Figure III-11. Color contour plot of velocity magnitude across the main channel measured at 18:26 EDT on October 25, 2006 immediately after the passage of LNG tanker heading northbound on the flood tide. Colors variations indicate the magnitude of flow moving in each measurement bin.

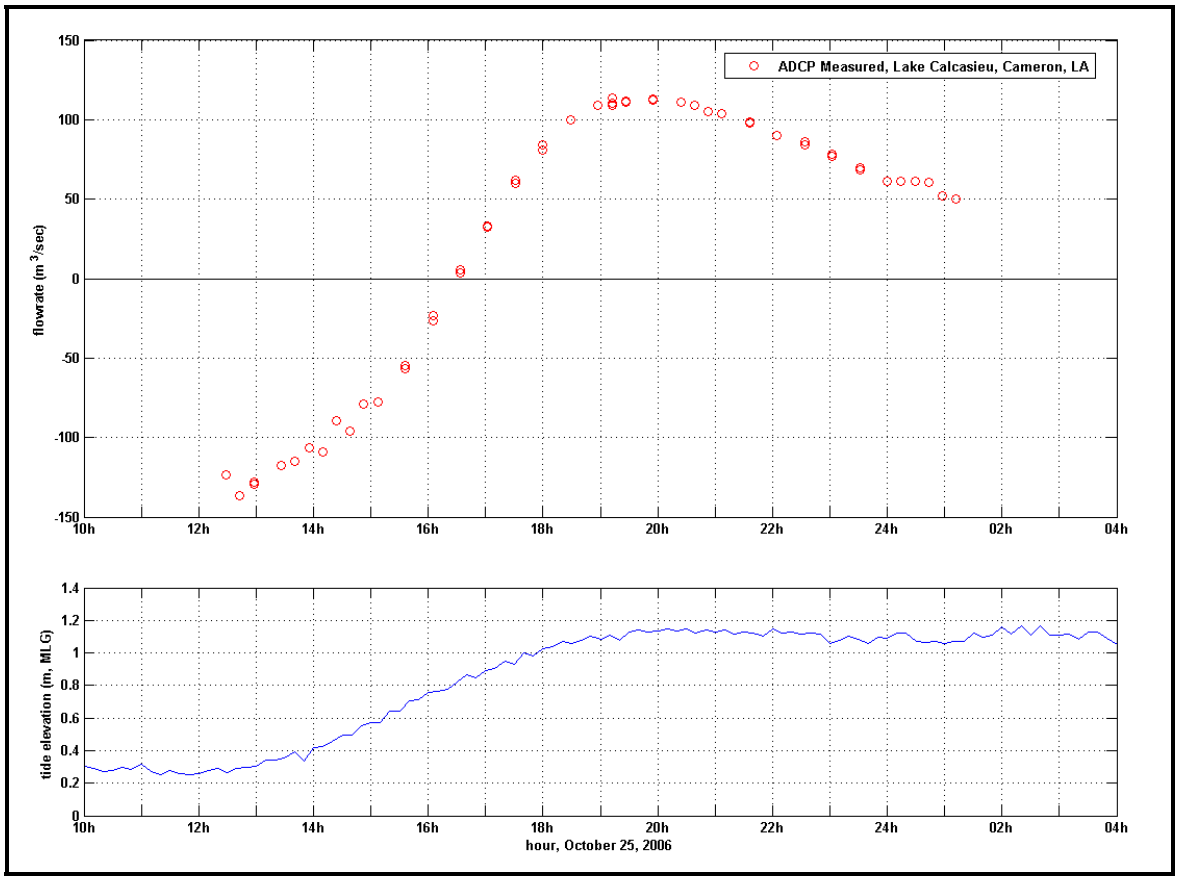

Figure III-12. Measured flow rates for the ADCP transect in the inlet of Lake Calcasieu, Cameron, LA. Positive flow indicated flooding tide, while negative flow indicates ebbing tide. Bottom plot represents the tidal elevation observations for Gulf of Mexico (Gage 10066).

III.3 WIND SPEED AND DIRECTION MEASUREMENTS

Wind speed and direction data were collected at a single location near the entrance to the Lake Calcasieu shipping channel by Ocean Data Technologies, Inc. Data collection spanned October 24 to December 20, 2006.

An R.M. Young model 05106-5A wind monitor was used to obtain these data. This propellar-vane-type unit produces an AC sine wave signal of frequency proportional to the rate of rotation. Wind direction output is a variable analog voltage proportional to vane azimuth. These output signals were input to a Campbell model CR-510 data logger. The CR-510 unit powered the wind sensor (via rechargeable battery and 10W photovoltaic cell), transformed the raw wind signals into calibrated values, and recorded these data to internal memory.

The CR-510 was programmed to record time, wind speed, wind direction, standard deviation of wind direction, maximum gust, minimum wind speed, and internal temperature. Data values were recorded every 10 minutes, with each value resulting from an average of readings obtained every 5 seconds. Accuracy of the wind speed data was of order 0.3 meters/second, with a minimum threshold value of 1.1 meters/second required to initiate rotor motion.

The wind sensor was mounted atop a mast near the entrance to the Lake Calcasieu shipping channel, immediately adjacent to a NOAA wind station. The sensor elevation was approximately 6.4 meters (21 feet) above a concrete pier, which in turn was approximately 1.6 meters (5.2 feet) above the water elevation (at the time of installation, October 24, 2006 at 1410 hours CDT). The installed height of the wind sensor was therefore 8 meters (26.2 feet) above water elevation.

The sensor was installed on October 24, 2006 at 1430 hours (Central Daylight Time) and recorded data successfully until December 20, 2006 0700 hours (Central Standard Time). A complete (100%) data record was recovered.

Time series graphs for the program are presented as Figure III-13. Wind speeds were depicted in the top plot; wind direction as the middle plot, followed by internal temperature as the bottom plot. The internal temperature data reflect temperatures sensed within the (airtight) enclosure, and can be affected by both atmospheric conditions as well as direct sunlight exposure. The diurnal variability represents day-night temperature changes. These data were included as a check against water temperature readings.

Several events were observed when speeds exceeded 10 meters/second. Five (5) events exceeded this threshold, and all such events featured winds from either the northwest, north or northeast directions. Wind events from the south or southeast were found milder than those from the northern quadrants. Wind speeds exceeding 10 m/s were uncommon, occurring only about 2.5% of the time overall. Speeds exceeded 7.5 m/s about 14% of the time, and exceeded 5 m/s about 37% of the time. About two-thirds of the time, wind speeds were less than 5 m/s (see Table III-5).

The strongest wind event occurred on November 15 with speeds of 15.2 m/s from the northwest. Winds during this event were initially from the southeast, about 5 meters/second, but swung clockwise rapidly to the northwest as speeds increased. Peak speeds were measured about 17:20 in the afternoon; wind gusts during this event were also the strongest on record, 20.8 m/s. Winds persisted from the northwest direction for about two days before abating. This wind event appeared to be accompanied by gradual atmospheric warming as shown by internal temperature data.

Another strong northwest wind event occurred November 30. (Average) wind speeds peaked at 12.9 m/s from the northwest (maximum gusts were 16.6 m/s), increasing through the afternoon and abating by early the next morning, December 1. This event was similar to the previous event: winds were mild from the southeast prior to a rapid increase while swinging to the northwest. Winds decreased subsequently as directions shifted toward the northeast. Other notable northerly wind events occurred on October 27 (peak speed 12.7 m/s) and November 11 (peak speed 11.9 m/s).

A strong southeast wind event was observed from November 27 to November 28. Peak speeds during this event were 9.5 m/s, but sustained winds of 8 m/s (on average) were measured through this 24-hour time period. Winds were steady from the southeast (132°). Peak gusts during this time were 11.7 m/s. These strong southeast events would have a different effect on circulation response than events from the northwest.

Figure III-14 presents detailed directional distribution (rose plot) and scatterplot of speeds during the program. A majority of winds were from the southeast, nearly 18% of the time, with 9% blowing from the east-southeast and 9% blowing from the south. Winds from the west were

rare. The scatterplot illustrates the strongest winds were from the northwest, although northwest winds were observed less frequently than those from the northeast or southeast.

Table III-6 provides a breakdown of the data set into specific directional quadrants. Winds from the northwest were least likely to occur, only 12% of the time, however these winds were also the most energetic and would likely affect circulation to a greater extent. Average wind speed from the northwest quadrant was 5.48 m/s; nearly 14% of the time speeds exceeded 10 m/s. Northeast winds were more common than from the northwest, occurring about a third of the time, with average speeds 4.8 m/s. Winds from the southeast quadrant occurred most often, nearly 43% of the time; however, of these southeast winds, only 1.9% exceeded 10 m/s. The average wind speed from the southeast was 4.52 m/s; the average wind speed from the southwest was 4.02 knots. Winds from the southern quadrants were much weaker typically than winds from the northern quadrants.

Table III-5. Wind Statistics (All speed units in meters/second, All times EDT).	
Mean wind speed vector	1.60
Mean wind direction vector	102°
Average wind speed	4.64
Maximum wind speed	15.17
Time of maximum wind speed	15-Nov-2006 17:20
Direction of maximum wind speed	321°
Maximum gust	20.80
Time of maximum gust	15-Nov-2006 16:00
Direction of maximum gust	320°
Percent Exceeding 10 m/s	2.5 %
Percent Exceeding 7.5 m/s	13.9 %
Percent Exceeding 5 m/s	37.2 %

Table III-6. Wind Statistics by Directional Quadrant *(All speed units in meters/second).*				
	NE (0°-90°)	SE (90°-180°)	SW (180°-270°)	NW (270°-360°)
% Occurrence (overall)	29.3 %	42.8 %	16.4 %	11.9 %
Average speed	4.82	4.52	4.02	5.48
Peak speed	11.93	9.98	12.71	15.17
% >10 m/s	2.1 %	0.0 %	1.9 %	13.6 %
% >7.5 m/s	17.0 %	8.4 %	7.6 %	34.4 %
% >5 m/s	42.2 %	35.9 %	26.5 %	44.4 %

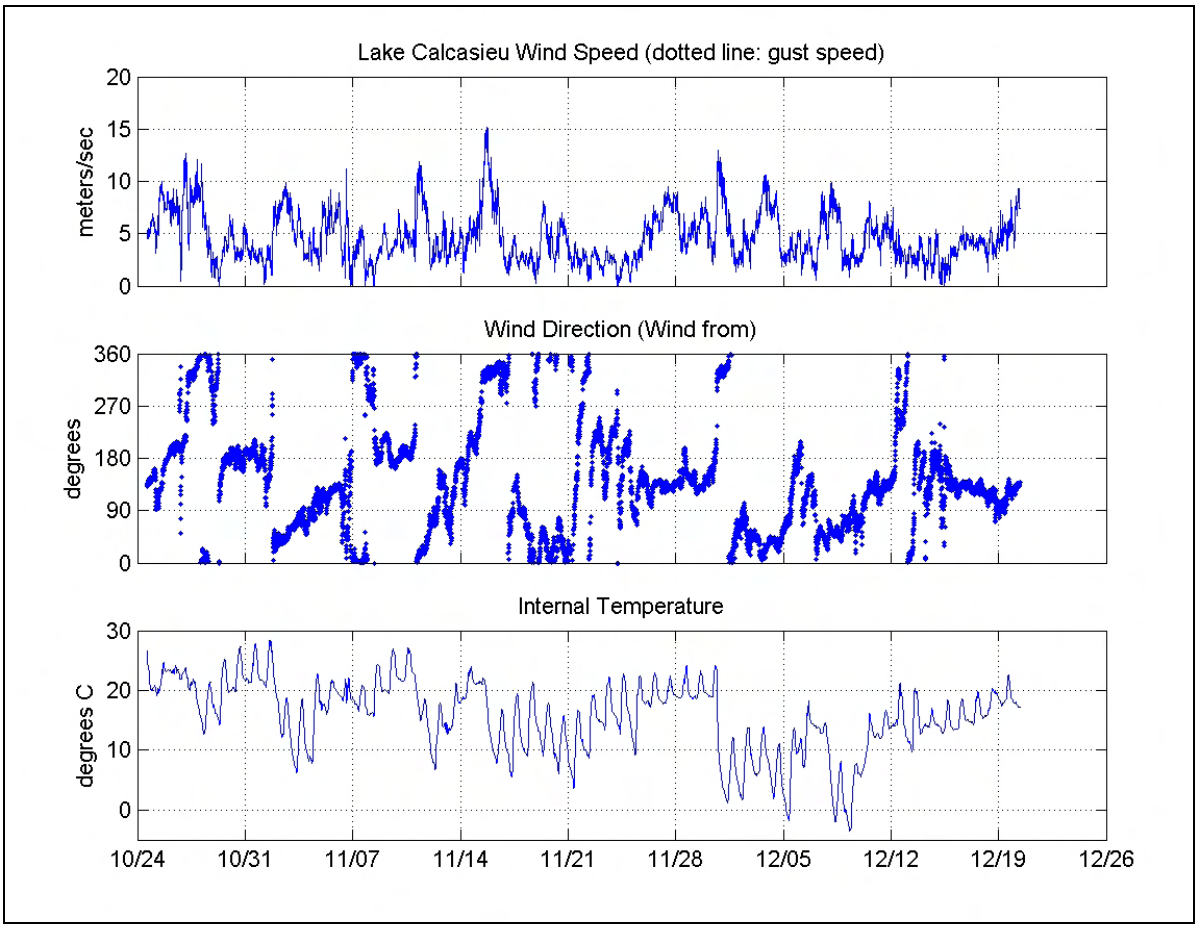

Figure III-13. Time series graphs for the wind measurement program. Wind speeds are depicted in the top plot; wind direction as the middle plot, followed by internal temperature as the bottom plot.

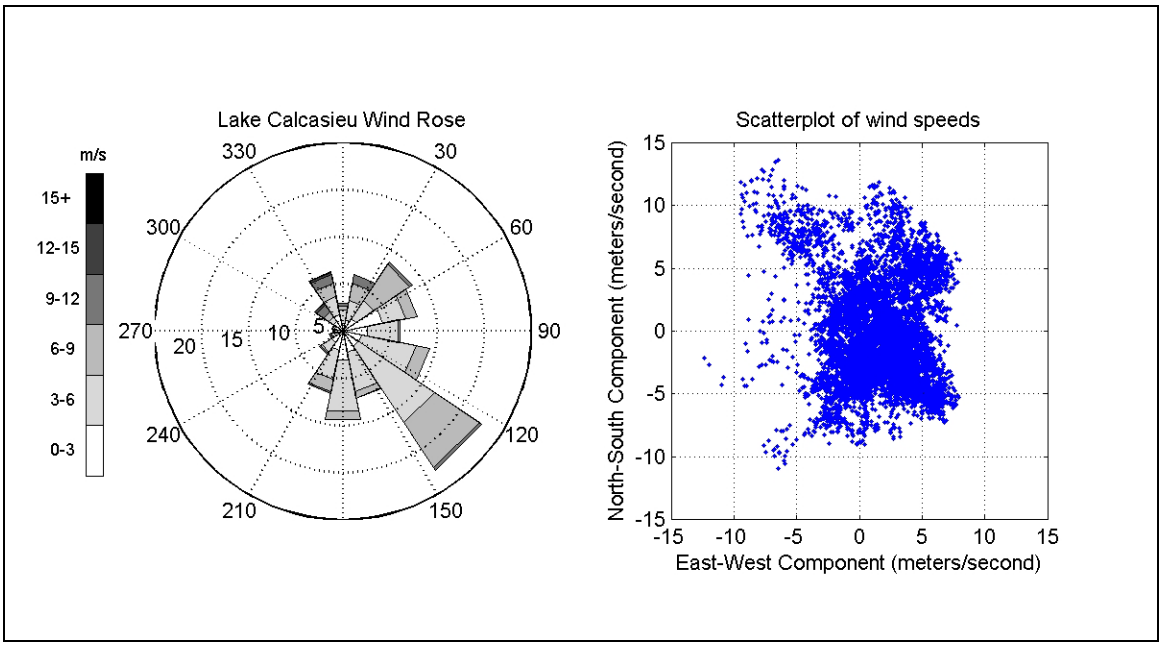

Figure III-14. Directional distribution (rose plot) and scatterplot of winds speeds during the measurement program.

III.4 BATHYMETRY

Bathymetric, or depth, survey information for Lake Calcasieu was gathered from several sources. NOAA's GEODAS hydrographic survey database served as the basis for the assembled dataset. The database provided data coverage over the entire basin, however most of the surveys within Lake Calcasieu dated from the 1930's. Therefore, this data was only used in areas outside of the navigation channels where bathymetric change would be minimal. Post dredging surveys from the USACE were used to for the main Calcasieu shipping channel and the GIWW. Gahagan & Bryant Associates, Inc. conducted a supplementary survey to provide bank-to-bank survey information along the main channel, within secondary channels, and bathymetry transitions.

The various datasets were merged to produce a single data sets consisting of water depth (Mean Low Gulf, MLG) as a function of x-y horizontal position (in Louisiana South, NAD 1983). The resulting xyz files were input to gridding software for the construction of the hydrodynamic model grid, points are shown in Figure III-15.

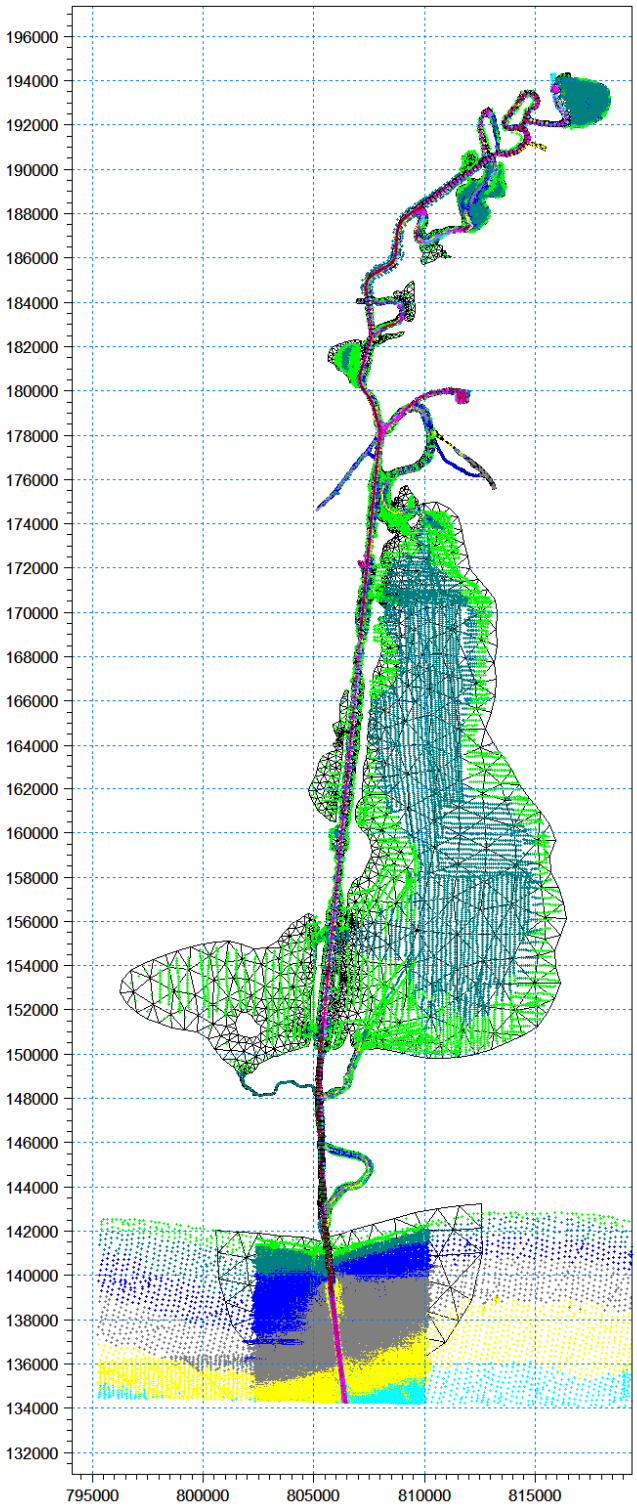

Figure III-15. Bathymetry points gathered within Lake Calcasieu. Color contours indicate depth relative to the MLG vertical datum in meters. X-Y horizontal positions along the axes are in Louisiana South State Plane Coordinates, NAD 1983, meters.

III.5 FRESH WATER INFLOW MEASUREMENTS

The fresh water river flow entering the Lake Calcasieu system from the saltwater barrier in Lake Charles, LA was measured at the USACE Calcasieu River near Salt Water Barrier measurement station. The station provided daily mean stage elevations which were converted into discharges using stage hydrographs for the recording station. A plot of the river discharges is shown in Figure III-16. The average discharge for the months of October-December was 134 m^3/s. The peak discharge on October 29 was 1,097 m^3/s. This corresponds to the eighth highest recorded stage event for the salt water barrier. The peak stage was at 6.35 ft.

No other gauging data was found for the Lake Calcasieu system. There are a number of salt water barriers positioned around the perimeter of Lake Calcasieu on the eastern and western side to prevent salt water intrusion into the surrounding marshes. The lock systems were observed to be open during the field data deployment, however there was no information available on volumes discharges or water levels stages at those locks.

III.6 WATER ELEVATION DATA

Tide gage measurements were available from NOAA at stations in Cameron and Lake Charles, LA. The station in Cameron, LA is NOAA Station 8768094, located on the eastern side of the navigation channel inside the jetties. NOAA Station 8767816 is located in Lake Charles, LA along the southeast side of the lake. Both of these gages were utilized to supplement the collected data within the hydrodynamic model. Specifically, the Cameron gage data was utilized as a visual check on damping of the offshore tide signal by the jetties extending into the Gulf and the Lake Charles gage was used to verify the Lake Charles tide gage deployed as part of this project was accurate. Since the NOAA tide gages do not report water surface elevations (WSE) to the same vertical datum as the project, this data was not utilized to quantitatively assess estuarine hydrodynamics. However, the eight (8) tide gages deployed during the project provided sufficient information to quantitatively determine tidal attenuation throughout the Lake Calcasieu estuarine system.

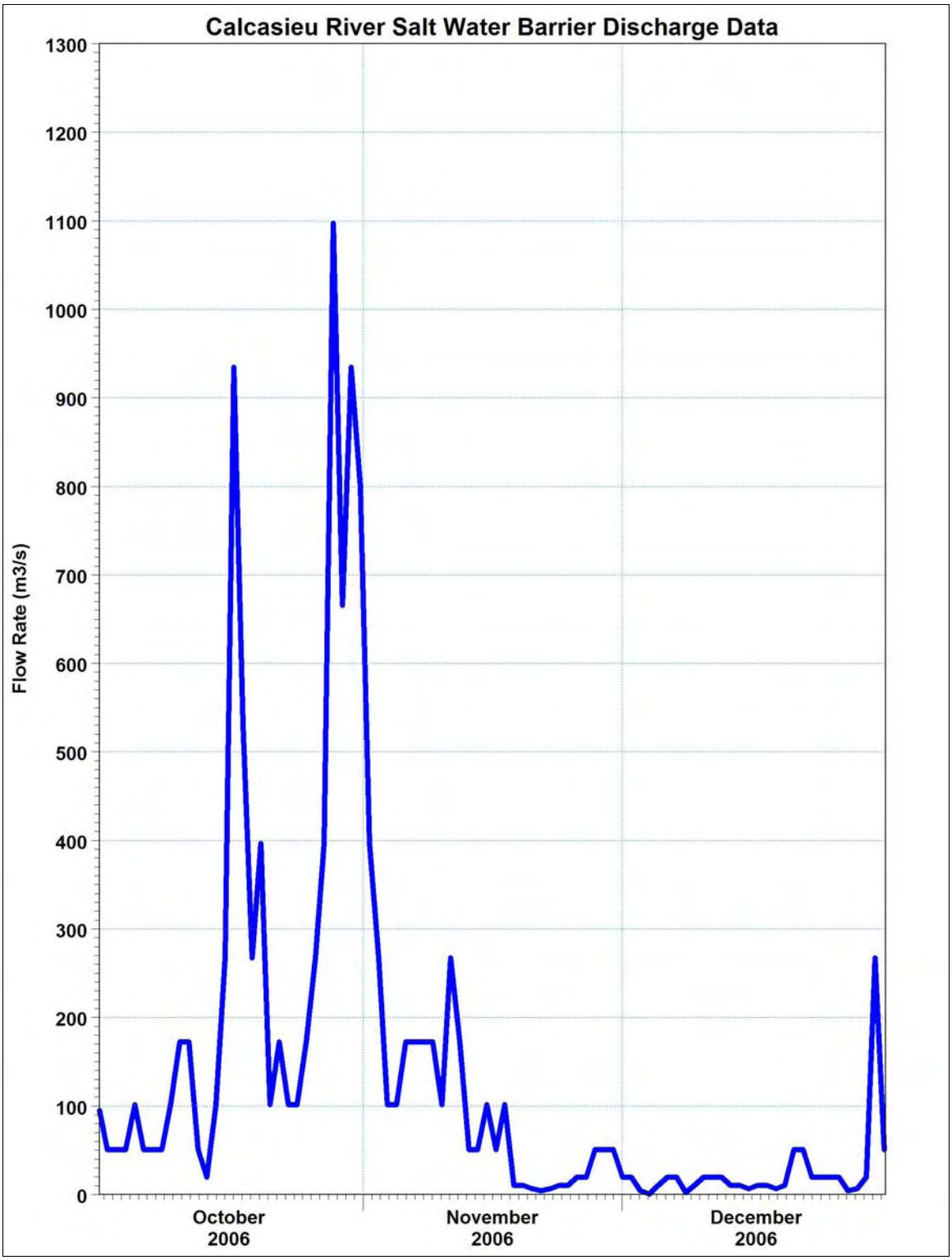

Figure III-16. Daily mean discharge from salt water barrier in Lake Charles. Recorded at Lake Charles Calcasieu River Salt Water Barrier measurement station.

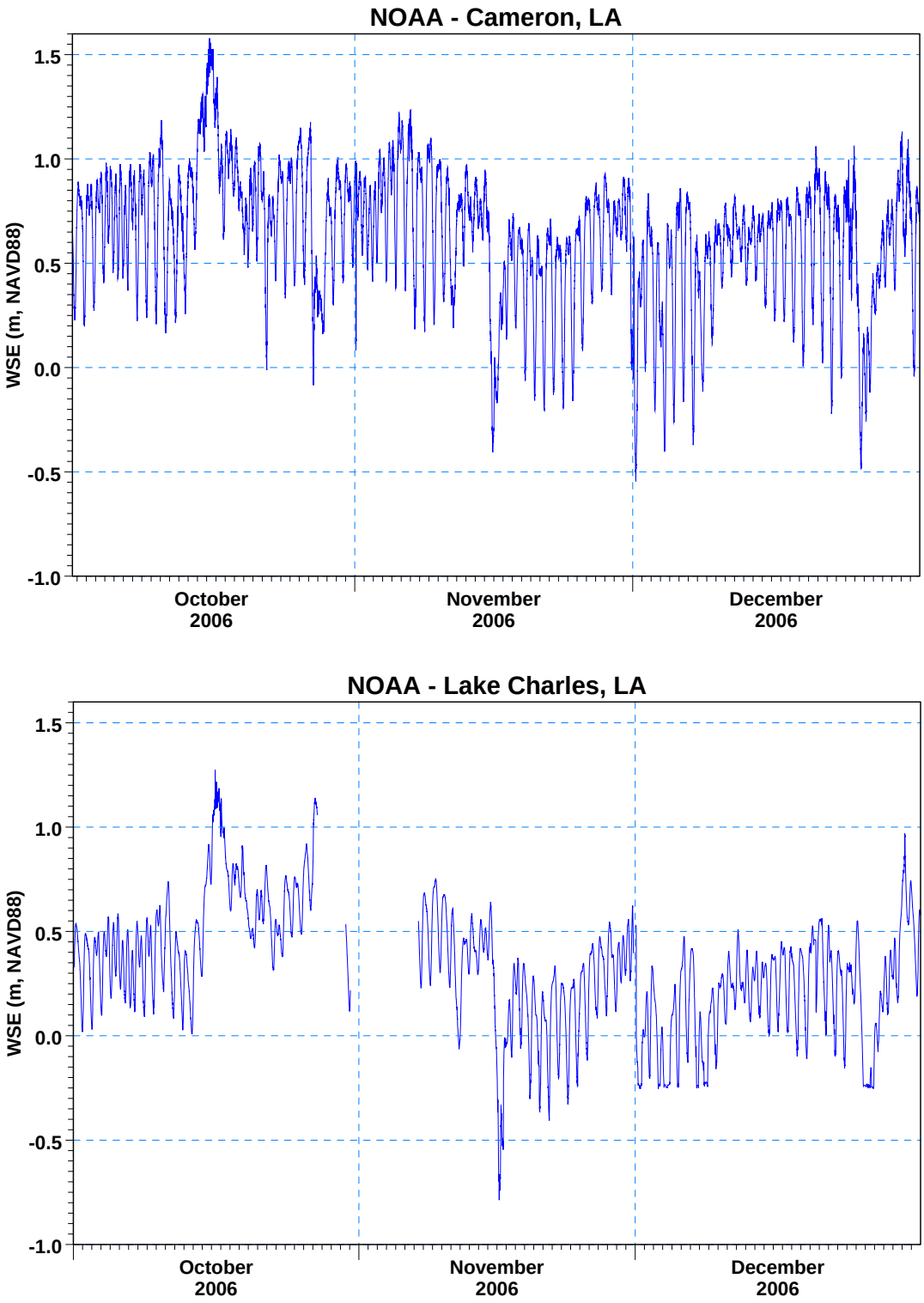

Figure III-17. Tidal elevation observations for NOAA Stations Cameron (8768094) and Lake Charles (8767816).

IV. HYDRODYNAMIC MODELING

A hydrodynamic study was performed to understand the dynamics of the Lake Calcasieu system. The dynamics are influenced by a number of features: extensive bayous/marshes to the east and west of main system, the Calcasieu River entering to the north of Lake Charles, the Gulf Intracoastal Waterway (GIWW) connecting the Calcasieu basin to the Sabine Basin to the west, the navigation channel connecting the Gulf of Mexico to Lake Calcasieu in Cameron, and metrological forces acting upon the system. Therefore, the development of a numerical model capable of accurately simulating hydrodynamic circulation within the Lake Calcasieu system requires a significant level of detail to accurately represent the natural system and the forces acting upon it.

A site map showing the study area is shown in Figure IV-1. The southern end of the system consists of inlet from the Gulf of Mexico into Lake Calcasieu. The inlet is stabilized on the east and west side by rubble mound jetties extending approximately 6,000 feet into the Gulf of Mexico. The navigation channel extends from the jetties north past Cameron, LA into Lake Calcasieu. Lake Calcasieu is divided to the West Cove and the main basin of Lake Calcasieu to the east. The navigation channel is bordered by numerous dredge disposal islands and marshes along its length towards the intersection with the GIWW. The GIWW intersects the Calcasieu Ship Channel (CSC) near the northern terminus of the lake. The GIWW to the west connects Sabine Lake to Lake Calcasieu. To the east, the water flow in GIWW is inhibited by a navigation lock. Extending northward the CSC extends to Lake Charles. The Calcasieu River empties into Lake Charles through a saltwater barrier just north of the main body of Lake Charles.

The main portion of Lake Calcasieu and West Cove are shallow embayments, with a mean water depth of only 1.5m and 1.3m, respectively. Salt marsh areas are contained on the margins of both basins. In addition, large expanses of brackish and freshwater marsh systems are contained by the dike system surrounding Lake Calcasieu.

Circulation in Lake Calcasieu system was simulated using the MIKE-21 HDFM model developed by the Danish Hydraulics Institute (DHI, 2007). It is a two-dimensional, depth-averaged finite volume model, capable of simulating transient hydrodynamics on a flexible mesh. The modelling system is designed in an integrated modular framework with a variety of add-on modules capable for the simulation of flows, waves, sediments and ecology in rivers, lakes, estuaries, bays, coastal areas and seas. The model is widely accepted and tested by profession engineers and scientist for analyses of estuaries and/or rivers around the world. The software is currently utilized by and for USACE (New York District, New England District, and San Francisco District), US Geological Survey, Bureau of Reclamation, and the US Federal Emergency Management Agency (FEMA). FEMA has officially approved MIKE 21 for use in national flood insurance program studies (NFIS) for applications in both coastal and riverine environments.

To calibrate the model, field measurements of water elevations, currents, meteorological conditions, freshwater inflow, and bathymetry were required; (see Chapter III for details of the data collection program). Tide data were acquired within the Gulf of Mexico, and also at seven additional stations located within the Lake Calcasieu system (Figures III-1 and III-2). All temperature-depth recorders (TDRs or tide gages) were installed for a 55-day period to measure tidal variations through one spring-neap tidal cycle and to capture time periods where metrological effect were minimal compared to tidal forces. In this manner, attenuation of the

tidal signal as it propagates through the various sub-sections of the system was evaluated accurately. Also, two NOAA tide gage records were available for comparison with the tide gage data from the project deployments (Figures III-1 and III-2). This additional water elevation information was used to assist in validation of the modeling effort.

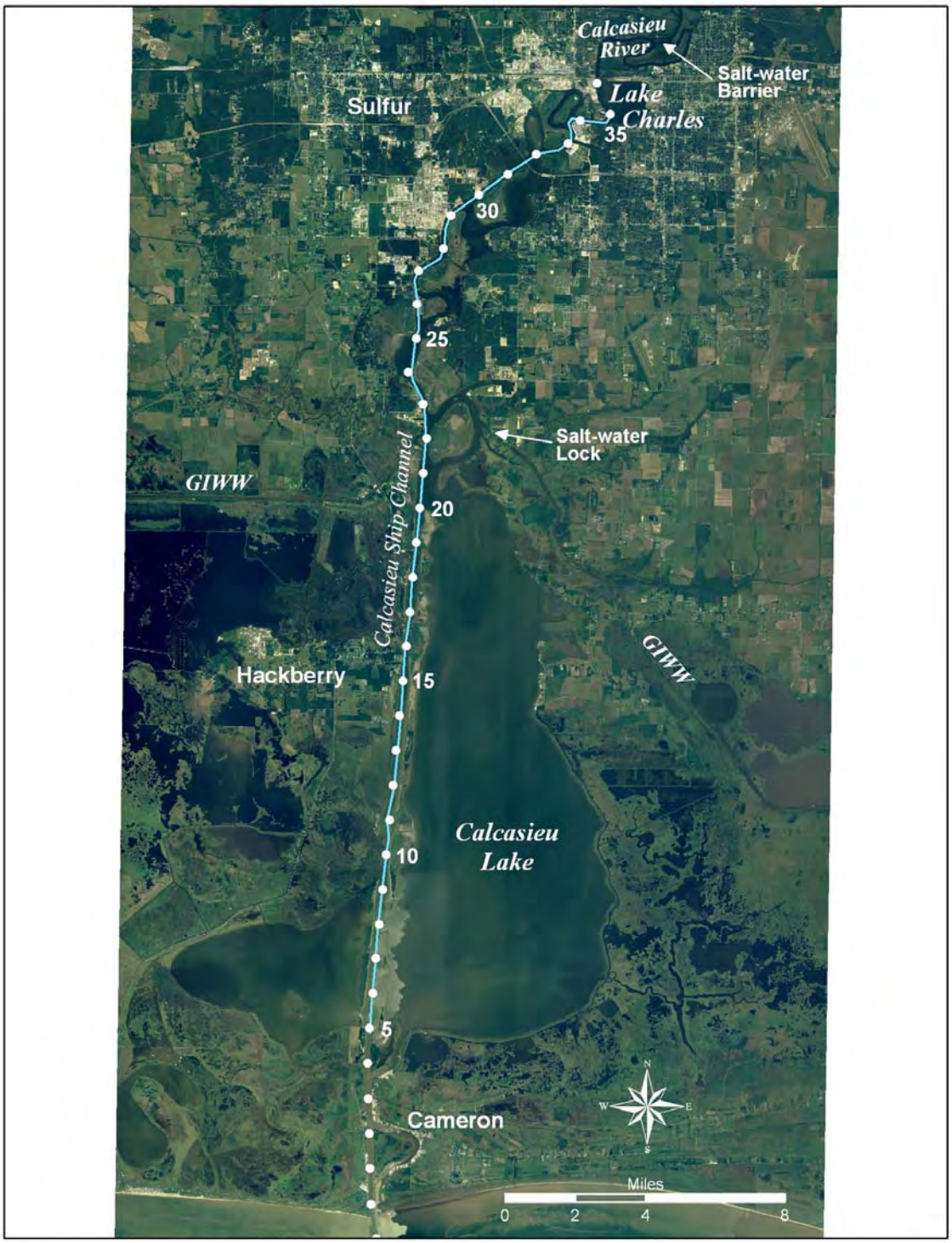

Figure IV-1. A site map showing the study area around Lake Calcasieu.

IV.1 MODEL THEORY

The flexible mesh version of the MIKE 21 model was used in the hydrodynamic simulations performed in this study. This is a code that utilizes an unstructured computational mesh, with linear triangular and quadrilateral elements. Unstructured meshes are well-suited to modeling coastal areas with complex shoreline and bathymetric contours, and also allow for greater density of computational elements to be applied in areas of interest in the model domain.

MIKE 21 HDFM is a finite volume model designed for simulating two-dimensional depth-averaged hydrodynamic systems. The dependent variables include velocity, water depth, temperature, salinity, and density. The model solves the depth-averaged Navier Stokes equations. Reynolds assumptions are incorporated as an eddy viscosity effect to represent turbulent energy losses. The eddy viscosity can be applied using several different turbulence models that are included in the model code, and can be described separately for vertical and horizontal mixing. Other terms in the governing equations permit friction losses (approximated either by a Chezy or Manning formulation), Coriolis effects, surface ice, tidal potential, and surface wind stresses. All the coefficients associated with these terms may vary from element to element.

Spatial discretization of the governing equations is based on a cell-centered finite volume method. Time integration is based on one of two methods that can be selected by the modeler; a first order explicit Euler or a second order Runge Kutta formulation.

IV.2 MODEL SETUP

There are four main steps required to implement hydrodynamic model:

- Grid generation
- Boundary condition specification
- Calibration
- Verification

The extent of the finite element mesh was generated using digital aerial photographs and shoreline data provided by Gahagan & Bryant, Inc. (GBA). The digital orthophotographs were part of a data set developed for the Port of Lake Charles in 1999 and 2005. Shorelines from the digital orthophotography were digitized to provide landward limits of the two-dimensional model grid. A time-varying water surface elevation boundary conditions (measured tide) were specified along the open boundaries of the system based on the tide gauge data collected in Gulf of Mexico and the GIWW to the west of the CSC. At the saltwater barrier in Lake Charles, a time-varying discharge boundary condition was specified. The meteorological data from the observation station was specified across the mesh. Once the mesh and boundary conditions were set, the model was calibrated to ensure accurate predictions of tidal circulation. Various friction and eddy viscosity coefficients were adjusted, through several model calibration simulations for the system, to obtain agreement between measured and modeled tides. The calibrated model provides the requisite information for future detailed examination of circulation and sediment transport analysis.

IV.2.1 Grid Generation

The finite element mesh generation process for the model was completed through the use of the MIKE Zero software package. The digital shoreline and bathymetry data were imported into MIKE Zero, and a finite element grid was generated to represent the Calcasieu system. All

regions in the system were represented by two-dimensional (depth-averaged) elements. The finite element grid for the system provided the detail necessary to evaluate accurately the variation in hydrodynamic properties within the estuary. Fine resolution was required to simulate the numerous channel constrictions (e.g., navigation channel) that significantly impact the system hydrodynamics. The completed grid is made up of triangular two-dimensional elements and is shown in Figures IV-2 to IV-5. Reference water depths at each node of the model were interpreted from bathymetry data obtained in the recent field surveys, dredging surveys, and the NOS data archive. The final interpolated grid bathymetry is shown in Figure IV-6. The model computed water elevation and velocity at each node in the model domain.

Grid resolution is governed by two factors: 1) expected flow patterns, and 2) the bathymetric variability in each region. Smaller cross channel node spacing in constrictions and transition channels was designed to provide a more detailed analysis in these regions of rapidly varying velocities and bathymetry. Widely spaced nodes were utilized in areas where velocity gradients were likely to be less acute; for example, on open water sections of Lake Calcasieu and West Cove. Appropriate implementation of wider node spacing and larger elements reduced computer run time with no sacrifice of accuracy.

IV.2.2 Boundary Condition Specification

Four types of boundary conditions were employed for the MIKE21 model: 1) "slip" boundaries, 2) tidal elevation boundaries, 3) flow boundary conditions, and 4) meteorological forces. All of the elements with land borders have "slip" boundary conditions, where the direction of flow was constrained shore-parallel. The model generated all internal boundary conditions from the governing conservation equations.

The model was forced at the open boundaries using water elevations measurements obtained in Gulf of Mexico and the GIWW, wind blowing across the surface of the water body, and flow volumes specified at the saltwater barrier (described in Chapter III). This measured time series consists of all physical processes affecting variations of water level: tides, winds, and other non-tidal oscillations of the sea surface. The rise and fall of the tide in Gulf of Mexico is the primary driving force for estuarine circulation. Dynamic (time-varying) model simulations specified a new water surface elevation at the offshore and GIWW boundaries along with a discharge at saltwater barrier every 60 seconds. The model specifies the water elevations at the boundaries and the flow rate into the system, and uses these values to calculate water elevations at every nodal point within the system, adjusting each value according to solutions of the model equations. For example, changing water levels in the Gulf of Mexico produce variations in surface slopes within the system; these slopes drive water either into the system (if water is higher offshore) or out of the system (if water levels fall in the lake). In addition to the tidal and flow boundary conditions, wind conditions were specified across the mesh. The wide expanses of open shallow water in the lake are influenced by the shear stress of the wind across the water setting up or down the water surface which influence the circulation pathways within the system.

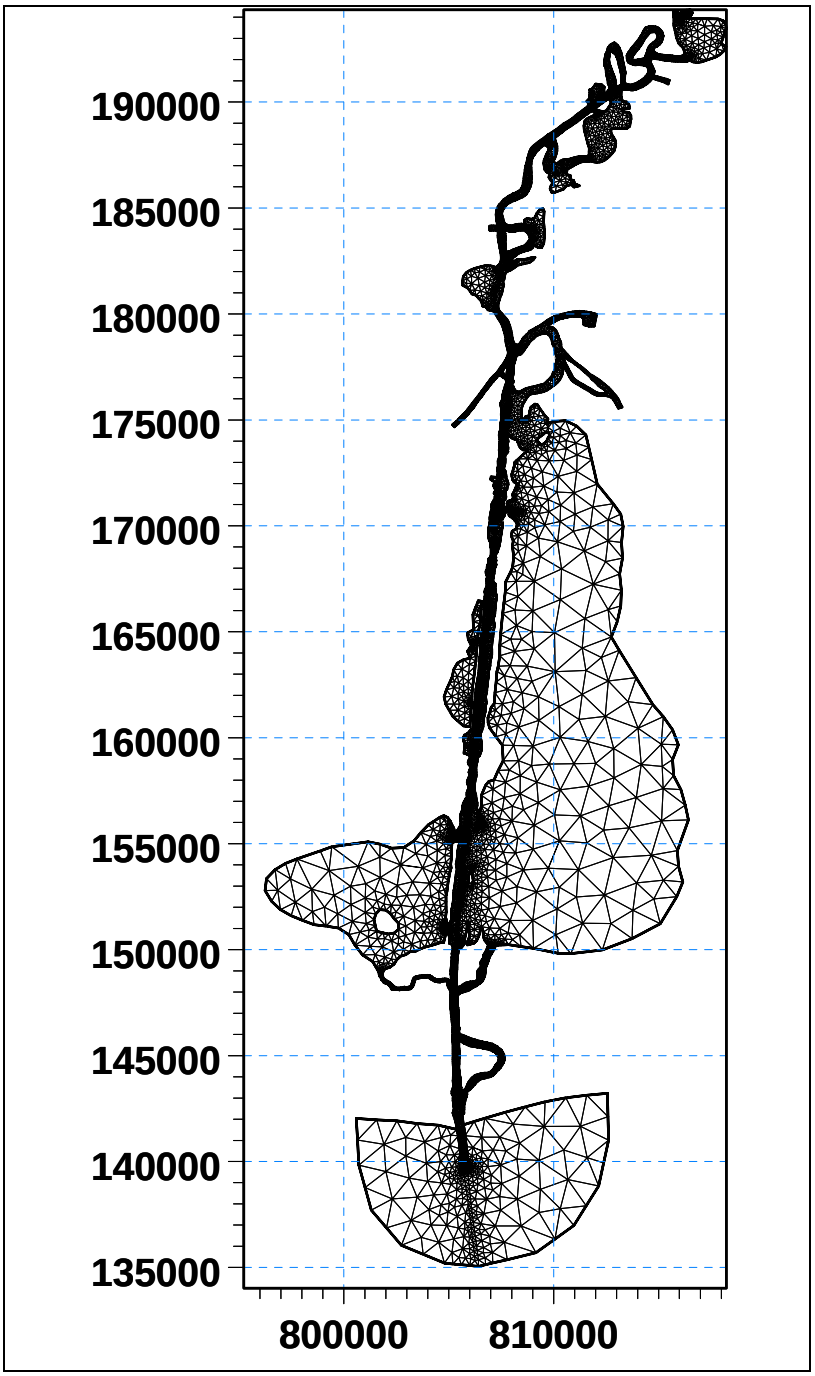

Figure IV-2. The model finite element mesh developed for Lake Calcasieu system. X-Y horizontal positions along the axes are in Louisiana South State Plane Coordinates, NAD 1983. (meters)

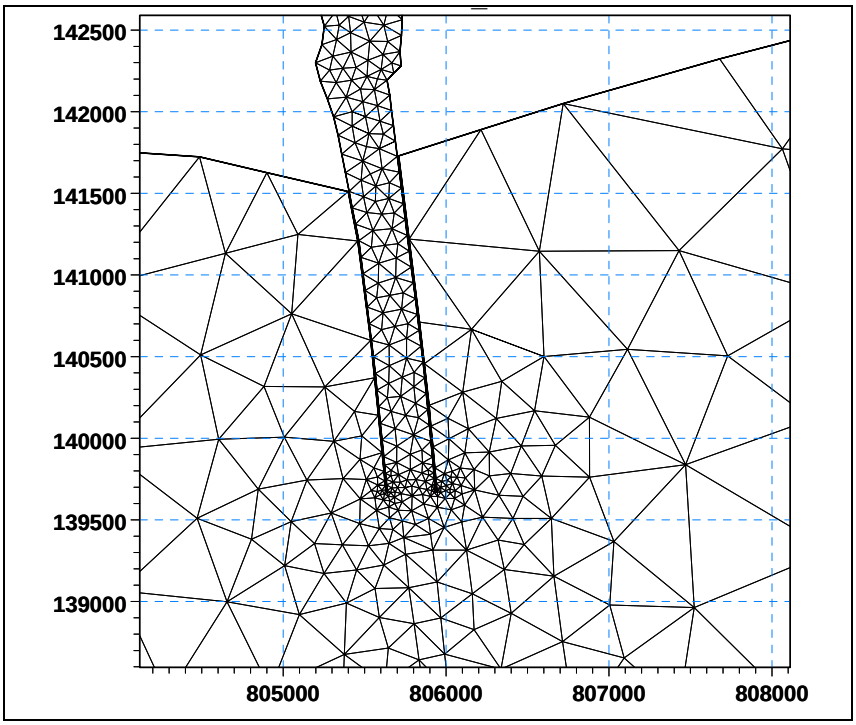

Figure IV-3. Details of the finite element mesh along the jettied entrance channel to Lake Calcasieu, Cameron, LA. X-Y horizontal positions along the axes are in Louisiana South State Plane Coordinates, NAD 1983. (meters)

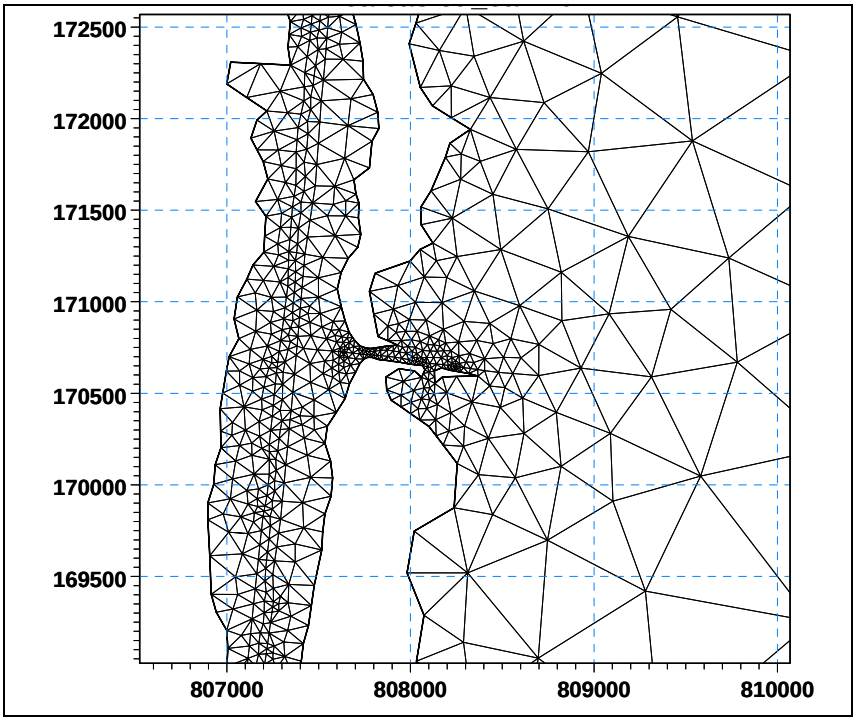

Figure IV-4. Details of the finite element mesh around Texaco Pass, Hackberry, LA. X-Y horizontal positions along the axes are in Louisiana South State Plane Coordinates, NAD 1983. (meters)

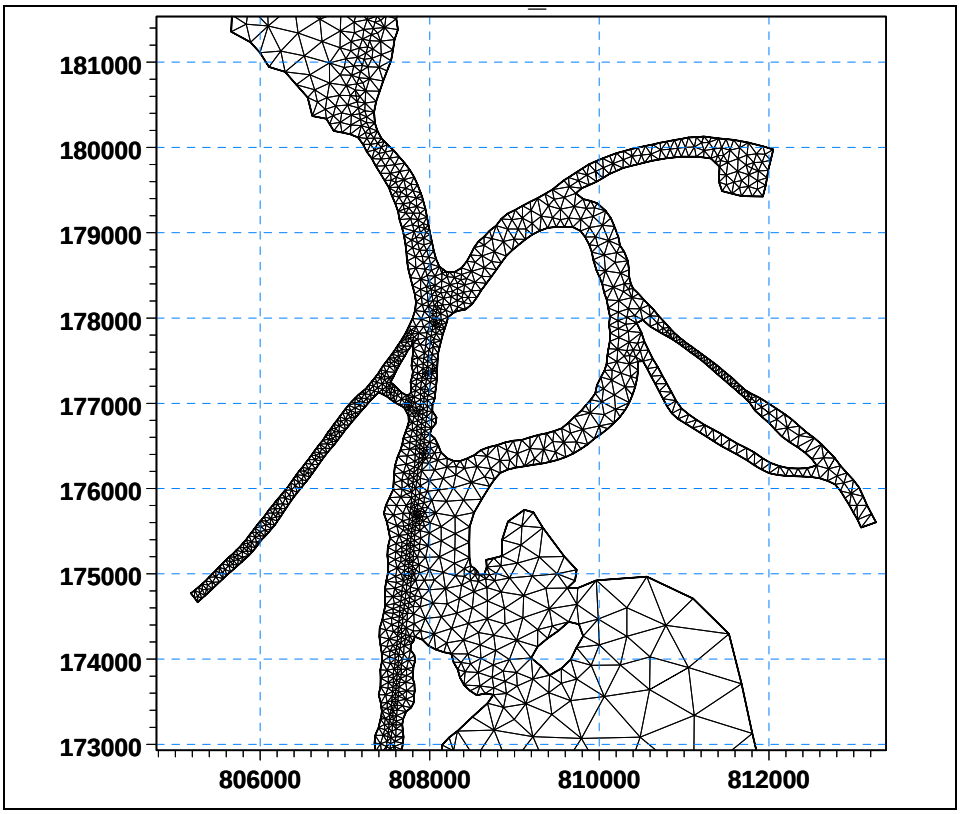

Figure IV-5. Details of the finite element mesh at the junction of GIWW and Devils' Elbow. X-Y horizontal positions along the axes are in Louisiana South State Plane Coordinates, NAD 1983. (meters)

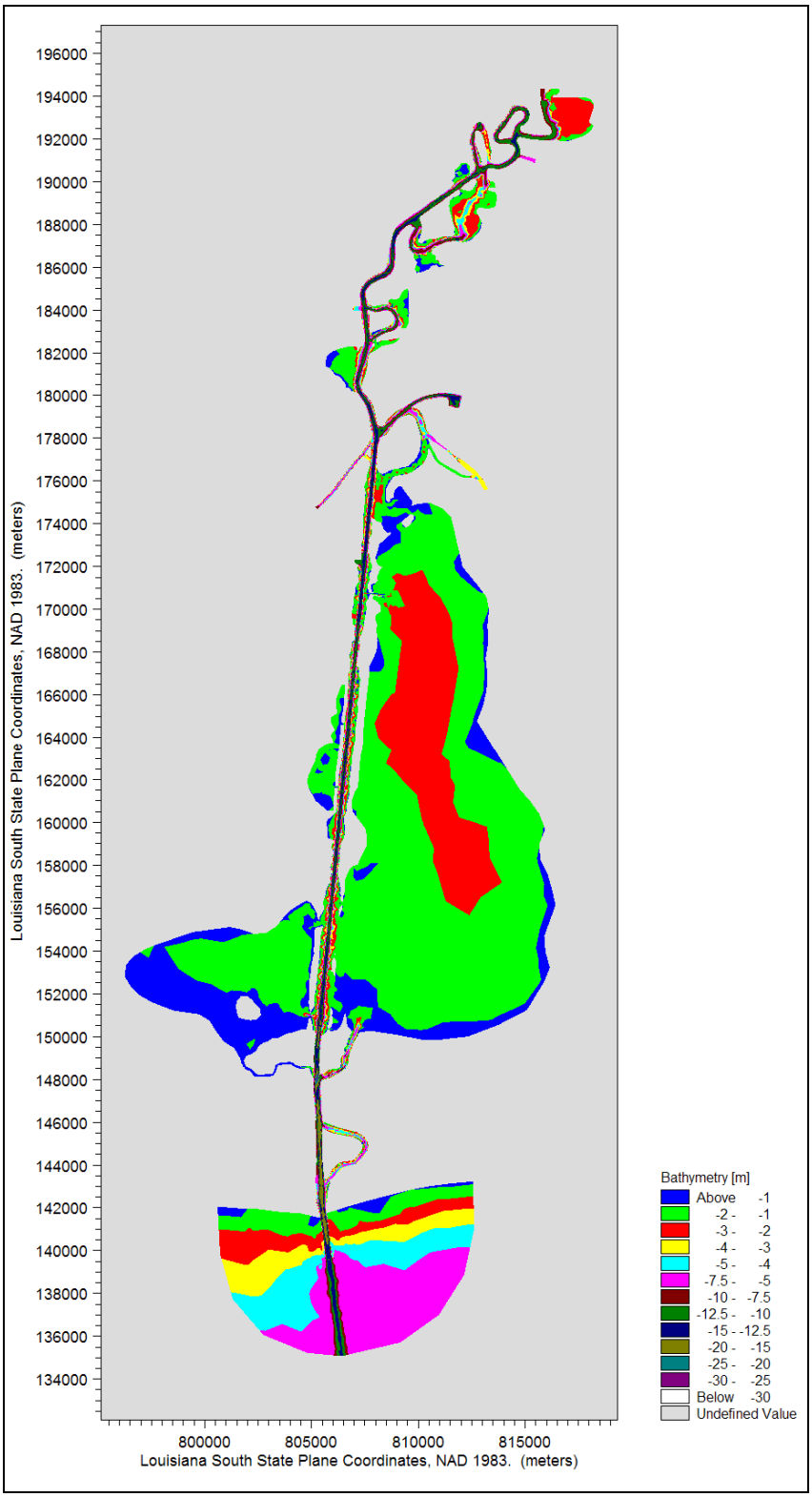

Figure IV-6. Bathymetric data interpolated to the finite element mesh of hydrodynamic model. Depth contours are in meters referenced to MLG. X-Y horizontal positions along the axes are in Louisiana South State Plane Coordinates, NAD 1983. (meters)

IV.3 CALIBRATION

After developing the finite element grid and specifying boundary conditions, the model was calibrated. Calibration ensured the model predicts accurately what was observed during the field measurement program. Numerous model simulations were required to calibrate the model, with each run varying specific parameters such as friction coefficients, turbulent exchange coefficients, fresh water inflow, and subtle modifications to the system bathymetry to achieve a best fit to the data.

Calibration of the hydrodynamic model required a close match between the modeled and measured tides at each of the gage locations where tides were measured. Initially, the model was calibrated by the visual agreement between modeled and measured tides. To refine the calibration procedure, water elevations were output from the model at the same locations in the estuary where tide gauges were installed, and the data were processed to calculate standard error as well harmonic constituents (of both measured and modeled data) over the 7.5 day calibration period. The amplitude and phase of six primary tidal constituents (K_1, M_2, S_2, N_2, O_1, and M_1) were compared and the corresponding errors for each were calculated. The intent of the calibration procedure is to minimize the error in amplitude and phase of the individual constituents. In general, minimization of the K_1 amplitude and phase becomes the highest priority, since this is the dominant constituent based on amplitude and overall energy. Emphasis is also placed on the M_2 and O_1 constituents, as the M_2 constituent represents the largest semi-diurnal lunar component and O_1 representing the second largest diurnal lunar constituent within the system. S_2 represents the principal solar semidiurnal constituent. N_2 represents the larger lunar elliptic semidiurnal constituent. M_1 represents the smaller lunar elliptic diurnal constituent.

The calibration was performed for an approximate eight-day period, beginning 1200 hours EDT November 17, 2006 and ending 1200 EDT November 25, 2006. This time period included a 12-hour model spin-up period, and a 7.5 day period used for calibration. This representative time period was selected because influence of the large weather system traversing the region had subsided and it included tidal conditions where the wind-induced portion of the signals (i.e. the residual) was minimal, hence more typical of tidal circulation within the system. The selected time period also spanned the new moon which represents the spring (bi-monthly maximum) tide ranges. Throughout the selected 7.5 day period, the tide ranged approximately a meter offshore to less than a half-meter at the other gauging stations. The ability to model a range of flow conditions is a primary advantage of a numerical tidal circulation model. Modeled tides were evaluated for time (phase) lag and height damping of dominant tidal constituents. The calibrated model was used to analyze existing detailed flow patterns and compute residence times.

IV.3.1 Friction Coefficients

Friction inhibits flow along the bottom of estuary channels or other flow regions where water depths can become shallow and velocities relatively high. Friction is a measure of the channel roughness, and can cause both significant amplitude attenuation and phase delay of the tidal signal. Friction was approximated in MIKE21 HDFM as a Manning coefficient. First, Manning's friction coefficient values of 40 $m^{1/3}/s$ were specified for all elements. These values correspond to typical Manning's coefficients determined experimentally in smooth earth-lined channels with no weeds (low friction) to winding channels with pools and shoals with higher friction (e.g. Henderson, 1966). Final calibrated friction coefficients (show in Figure IV-7) were largest for shallow and marshy areas, where values were set between 20 and 30 $m^{1/3}/s$. Small changes in these values did not change the accuracy of the calibration. The Chezy formulation

for friction coefficients also was considered; however, initial evaluation indicated similar model results as the Manning formulation. Therefore, final calibration was performed with the use of Manning coefficients.

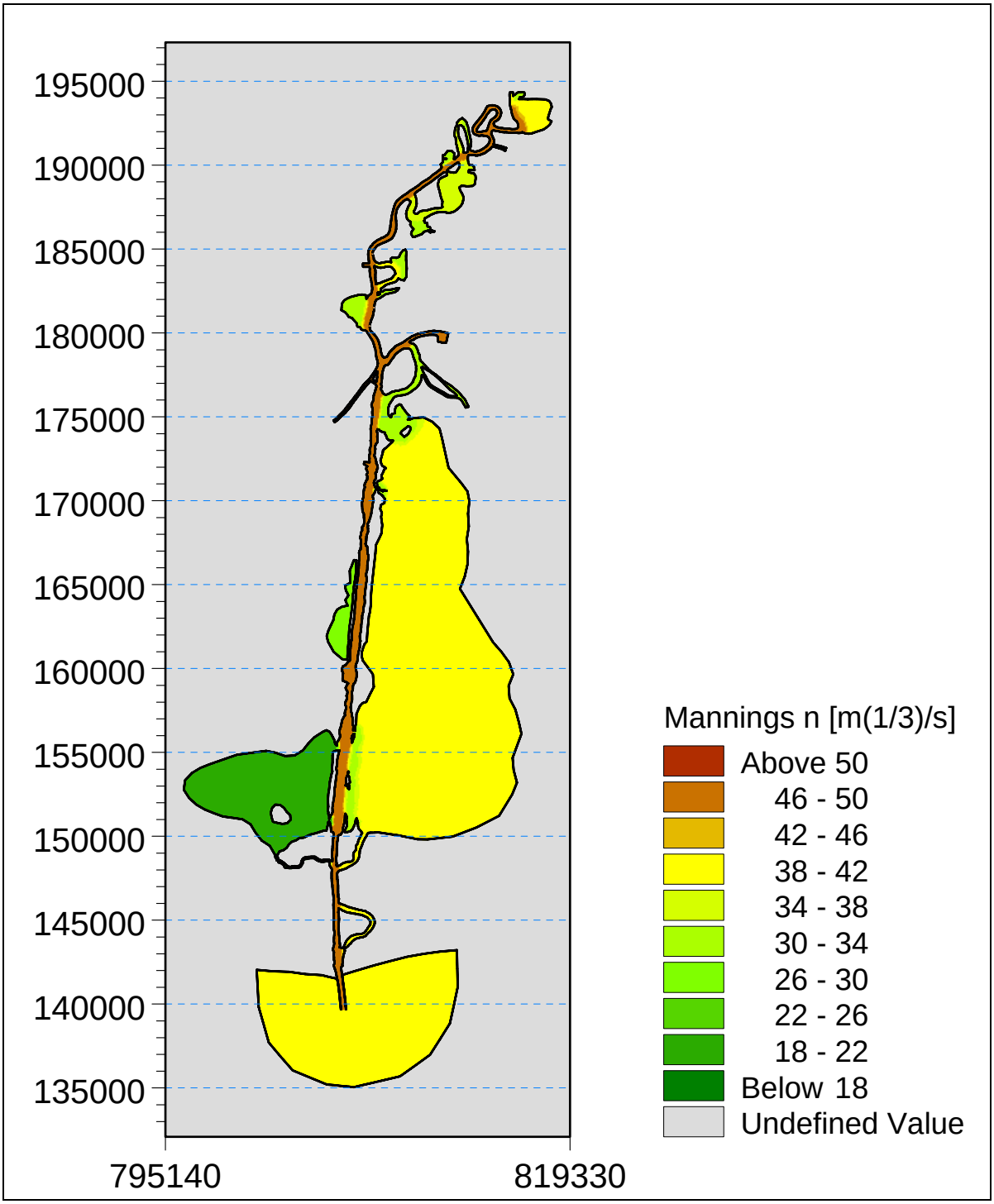

Figure IV-7. Final calibrated Manning's friction coefficients. X-Y horizontal positions along the axes are in Louisiana South State Plane Coordinates, NAD 1983 (meters). The Manning number used in MIKE21 is the reciprocal value of the Manning number typically used.

IV.3.2 Eddy Viscosity Coefficients and Density

Eddy viscosity coefficients approximate energy losses due to internal friction between fluid particles. The significance of energy losses increases where flow is swift, such as inlets and constrictions, where turbulent flow can dominate. The Smagorinsky formulation was selected to represent the eddy viscosity within the model. The model was relatively insensitive to variations in eddy viscosity. Therefore, recommended values between 0.25 and 1.0 were utilized within the modeling domain.

The density formulations within the MIKE21 HDFM hydrodynamic model contain coefficients to account for salinity and temperature. For the Lake Calcasieu model, the barotropic density formulation was selected. It assumes both temperature and salinity to be constant during the simulation. Since continuous measurements of salinity and temperature throughout the modeling domain were not available, other formulations that vary these parameters within the transport equations over time and space could not be implemented accurately.

IV.3.3 Comparison of Modeled Tides and Measured Tide Data

Several calibration model runs were performed to determine how changes to various parameters (e.g. friction and eddy viscosity coefficients) affected the model results. These trial runs achieved good agreement between the model simulations and the field data. Comparison plots of modeled versus measured water levels at the eight gauge locations is presented in Figures IV-8 through IV-17. The largest variations were in West Cove and Lake Charles due to non-tidal forces. West Cove is interconnected to the fringing marshes and Mud Lake by small boat navigation channels and marsh channels (Shell Canal, West Lake Canal, Black Ridge Canal), which are not accounted for in the model. The variation in tidal amplitudes likely results from absence of marsh detail within the model domain. The marshes will absorb the incoming tide and then release water more slowly on the outgoing tide. The absence of the marshes within the model domain reduces storage volume within West Cove, resulting in the slight over-prediction of high and low tide elevations. Figure IV-11 shows that the variations are minor, less than 0.1 meters, and therefore are not considered significant locally within model or system wide. The NOAA Lake Charles gauge shows minor variations, which are likely attributable to the bathymetry information that was available within Lake Charles which dated back to the 1930's. Comparison of the model predictions at the NOAA station and Lake Charles gage (9514) shows that model is accurately predicting the responses within the lake and variations seen are a localized to that gage.

Measured tidal constituent amplitudes and time lags (ϕ_{lag}) for the calibration time period are shown in Table IV-1 and IV-2. The constituent values for the calibration time period differ from those in Tables III-2 because constituents were computed for only 7.5 days, rather than the entire 54-day period represented in Tables III-2. Errors associated with tidal constituent height were on the order of hundredths of meter, which was less than the accuracy of the tide gage gauges ($\pm$0.04 m). Time lag errors were generally less than the time increment resolved by the measured tide data (1/6 hours or 10 minutes), indicating good agreement between the model and data.

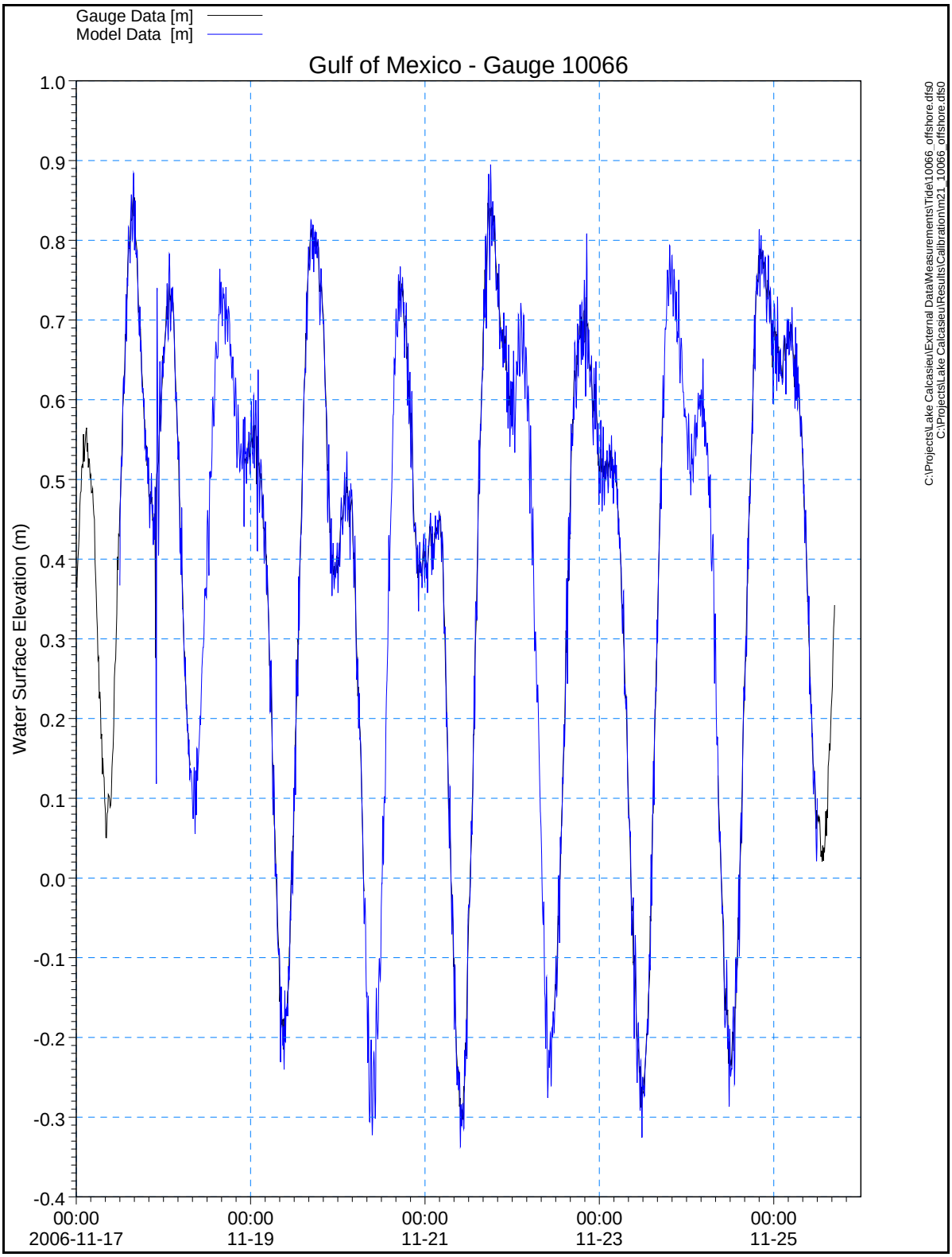

Figure IV-8. Comparison of water surface variations simulated by the model (solid blue line) to those measured within the system (solid black line) for the calibration time period, for the offshore gauging station.

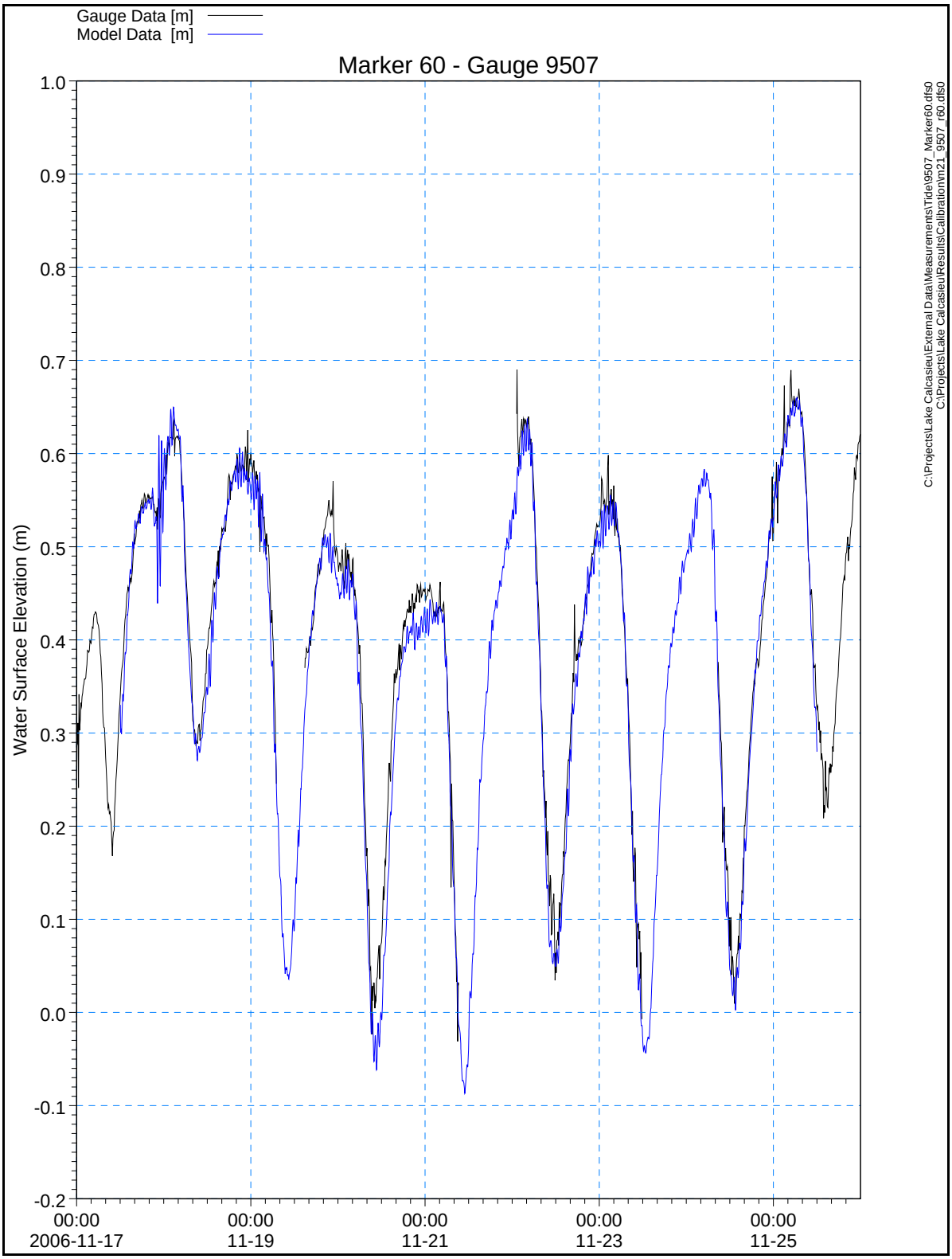

Figure IV-9. Comparison of water surface variations simulated by the model (solid blue line) to those measured within the system (solid black line) for the verification time period at the Marker 60 gauging station (9507).

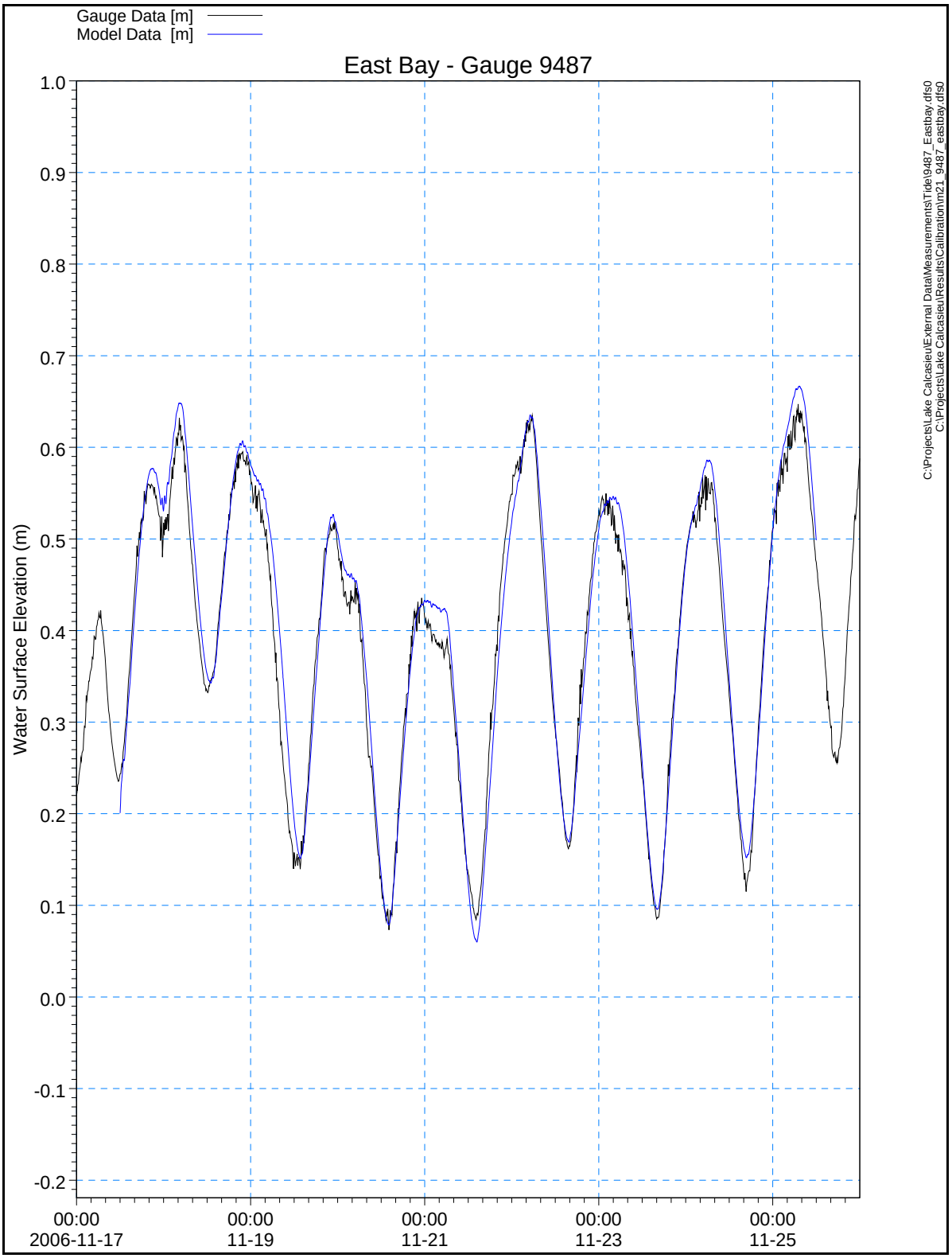

Figure IV-10. Comparison of water surface variations simulated by the model (solid blue line) to those measured within the system (solid black line) for the verification time period at the Sweetheart East Bay gauging station (9487).

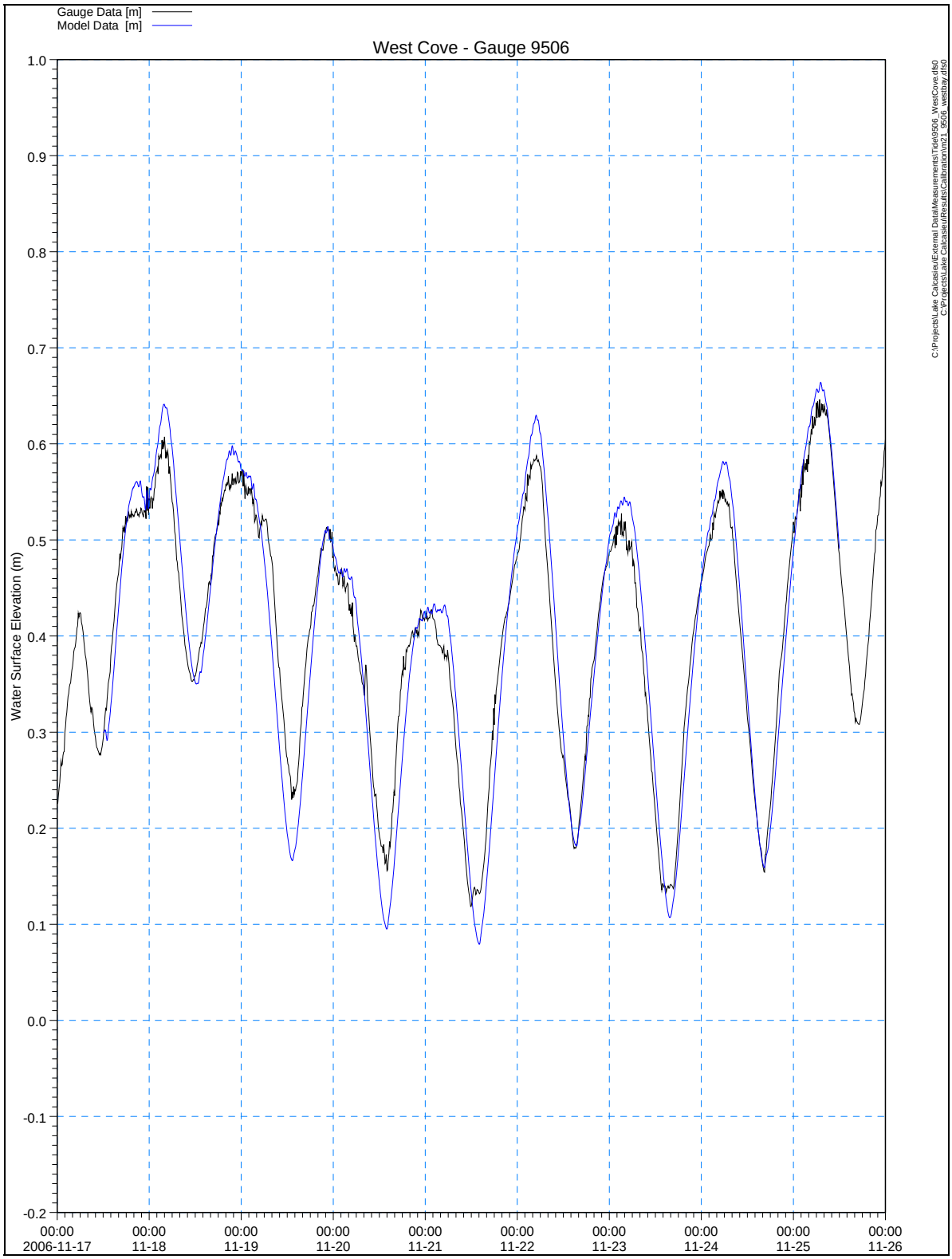

Figure IV-11. Comparison of water surface variations simulated by the model (solid blue line) to those measured within the system (solid black line) for the verification time period at the West Cove gauging station (9506).

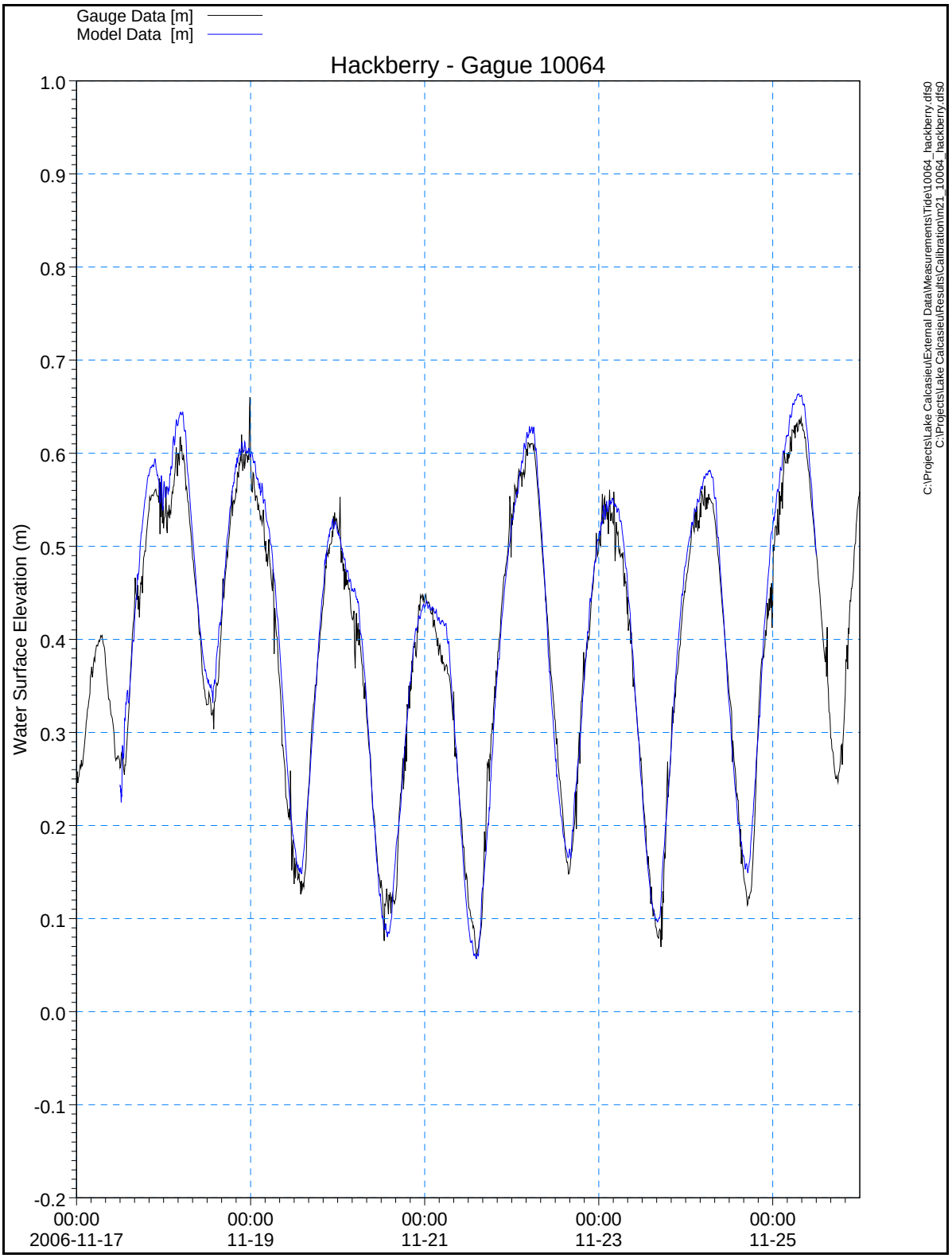

Figure IV-12. Comparison of water surface variations simulated by the model (solid blue line) to those measured within the system (solid black line) for the verification time period at the Hackberry gauging station (10064).

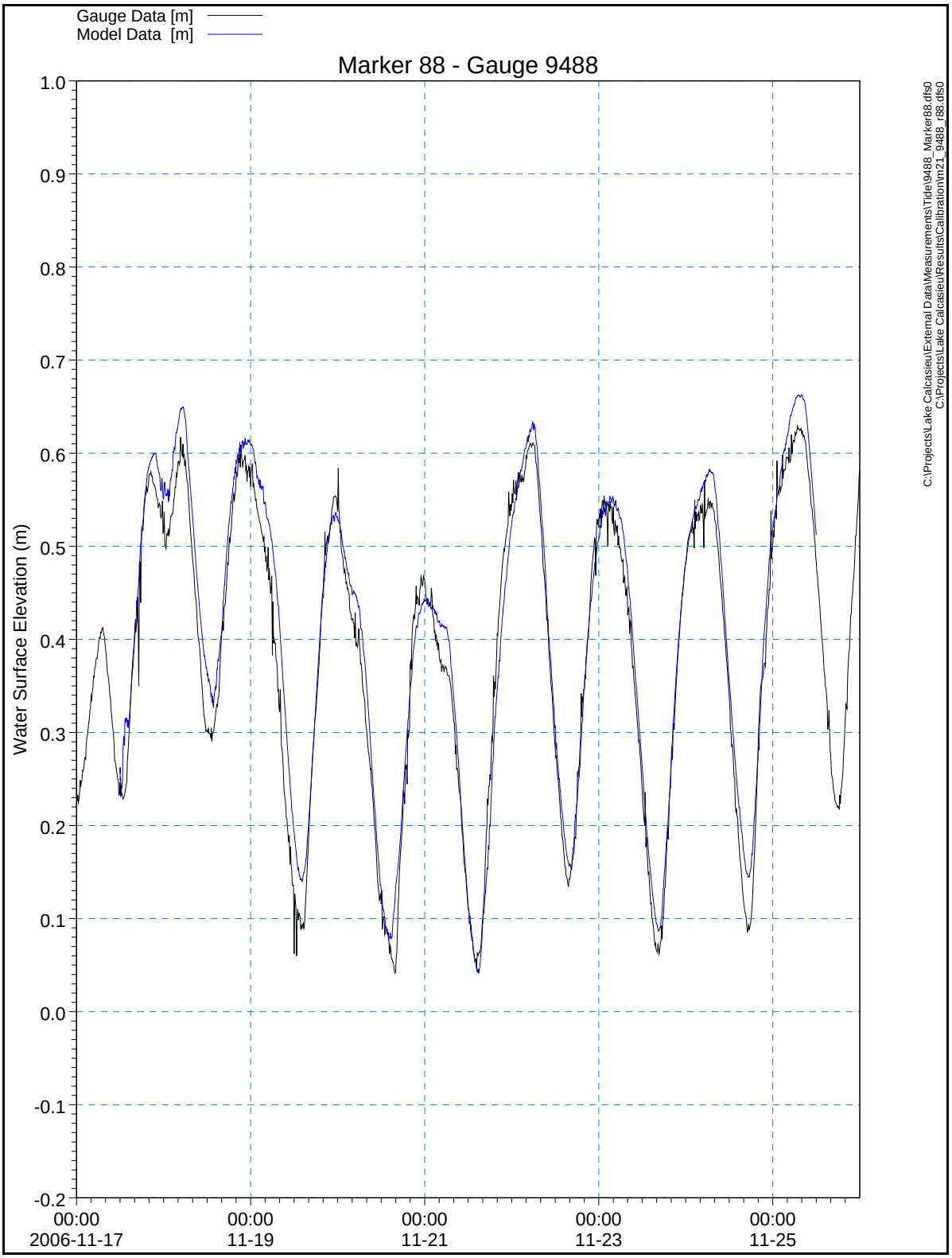

Figure IV-13. Comparison of water surface variations simulated by the model (solid blue line) to those measured within the system (solid black line) for the verification time period for the Marker 88 gauging station (9488).

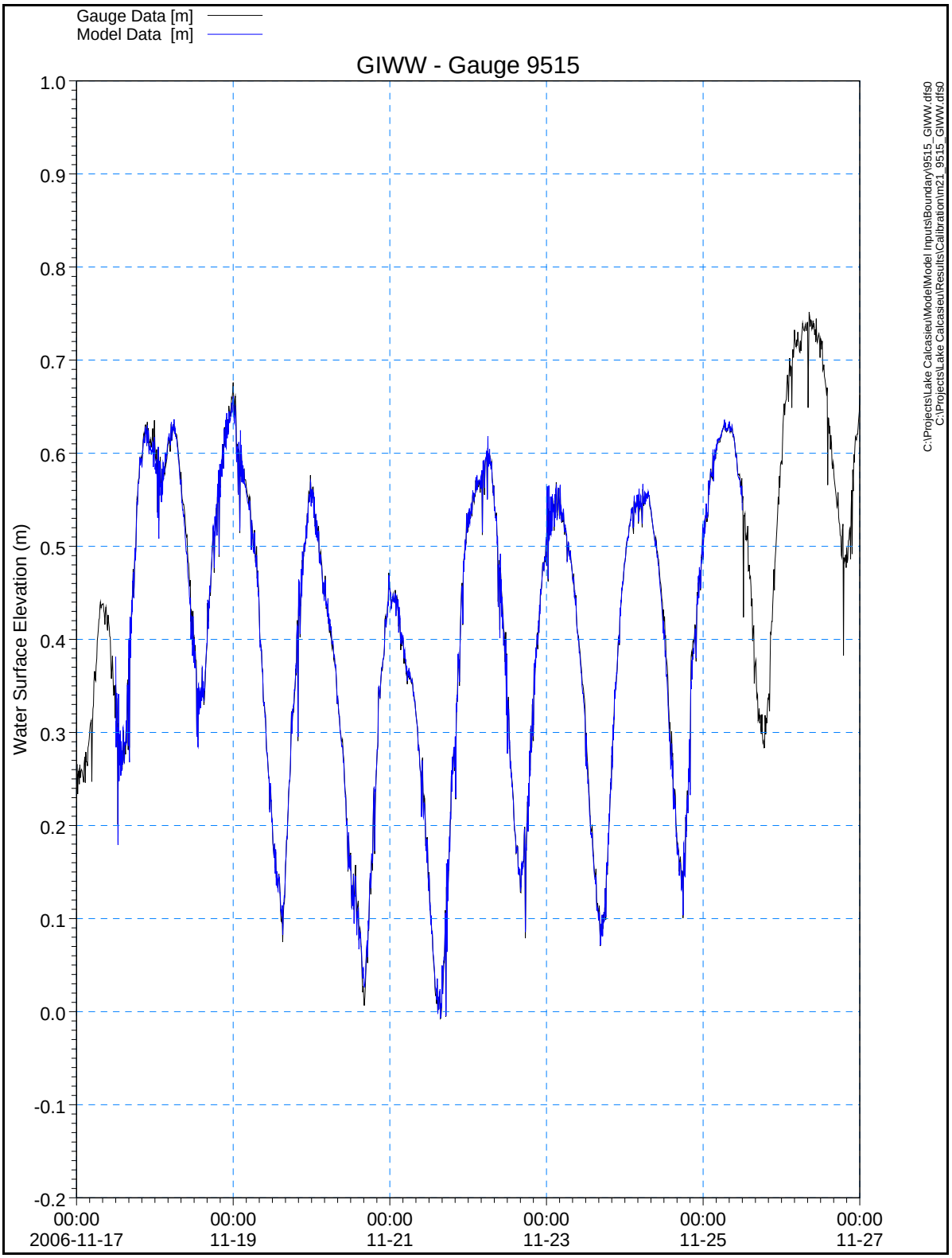

Figure IV-14. Comparison of water surface variations simulated by the model (solid blue line) to those measured within the system (solid black line) for the verification time period at the GIWW gauging station (9515).

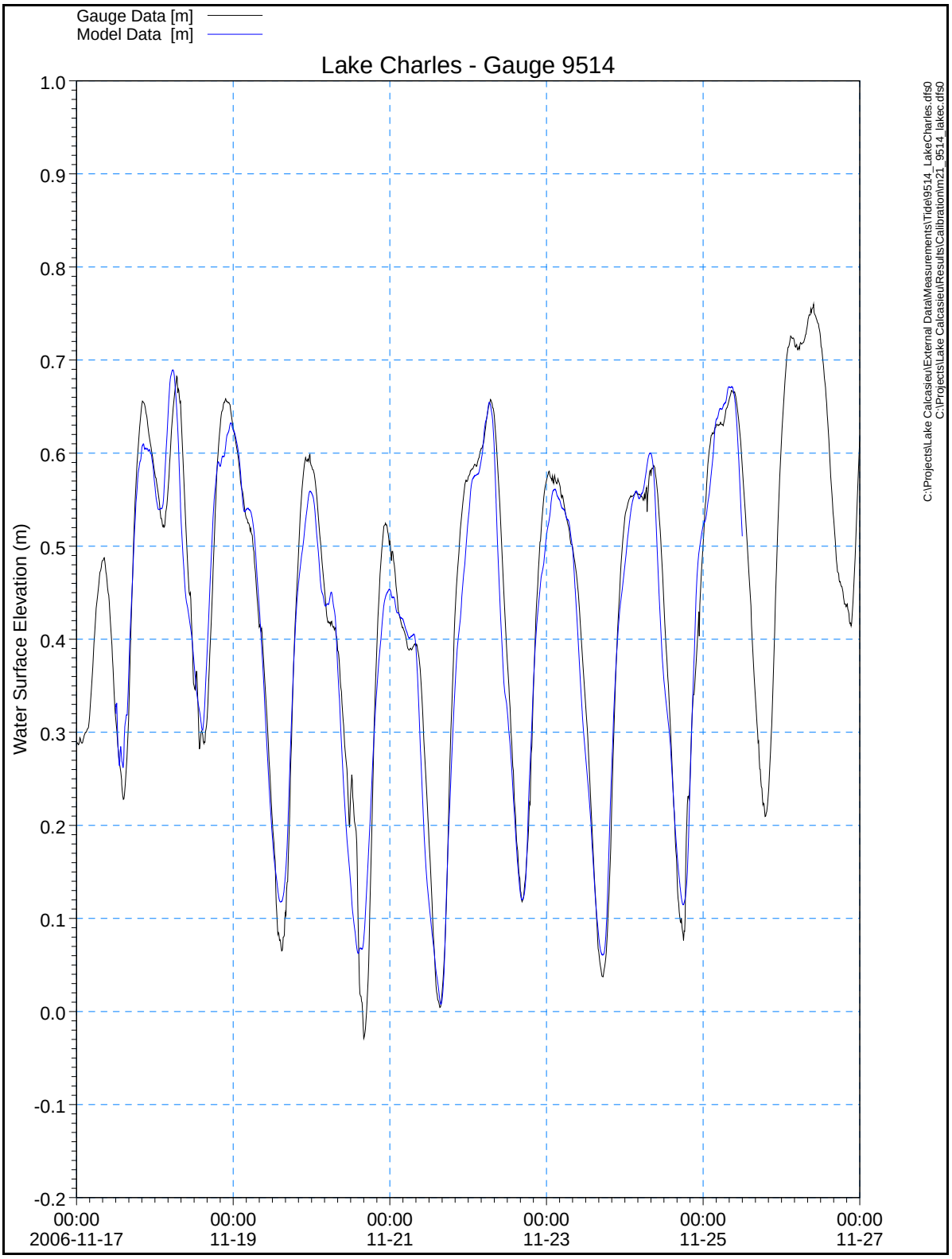

Figure IV-15. Comparison of water surface variations simulated by the model (solid blue line) to those measured within the system (solid black line) for the verification time period at the Lake Charles gauging station (9514).

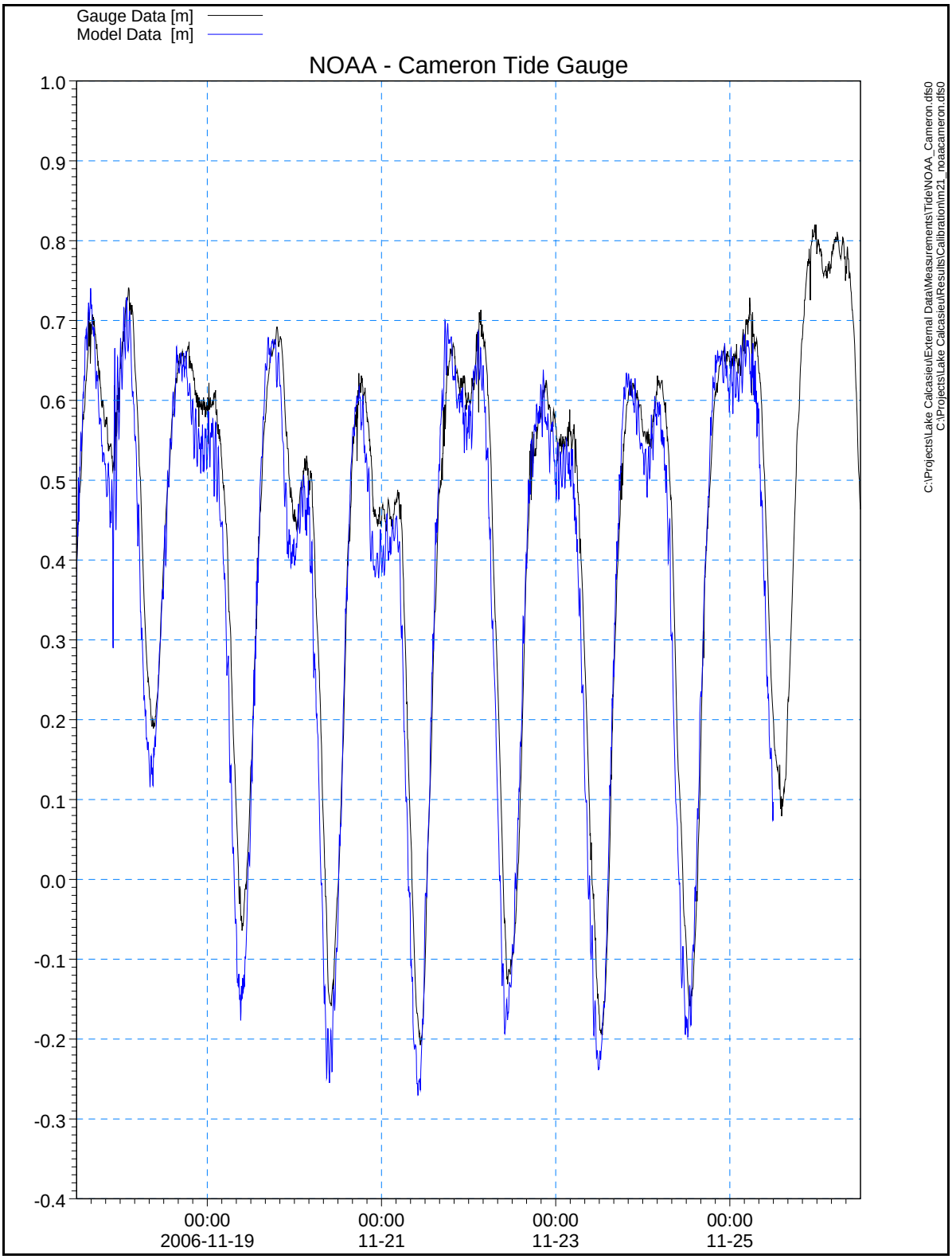

Figure IV-16. Comparison of water surface variations simulated by the model (solid blue line) to those measured within the system (solid black line) for the verification time period at the NOAA's Cameron gauging station (NOAA 8768094).

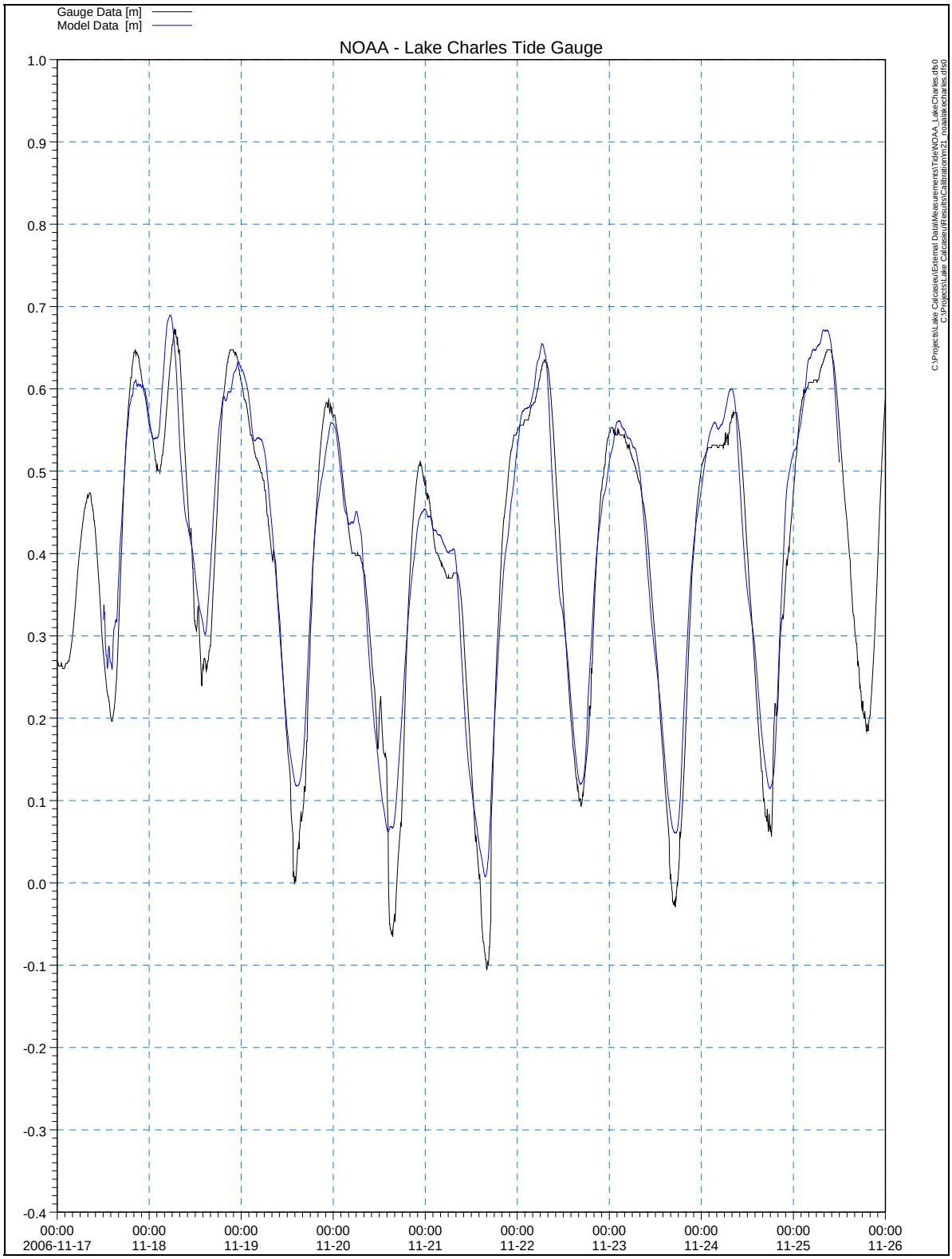

Figure IV-17. Comparison of water surface variations simulated by the model (solid blue line) to those measured within the system (solid black line) for the verification time period at the NOAA's Lake Charles gauging station (NOAA 8767816).

Table IV-1. Comparison of tidal constituent amplitudes calibrated MIKE21 model versus measured tidal data for the period November 17 to November 25, 2006.

Model Verification Run						
Location	Constituent Amplitude (m)					
	K_1	M_2	S_2	N_2	O_1	M_1
Offshore	0.162	0.238	0.056	0.070	0.204	0.242
Marker 60	0.068	0.113	0.032	0.057	0.118	0.206
East Bay	0.019	0.079	0.004	0.042	0.056	0.185
West Cove	0.015	0.068	0.002	0.036	0.055	0.178
Hackberry	0.027	0.081	0.005	0.044	0.056	0.170
Marker 88	0.036	0.080	0.005	0.043	0.049	0.162
GIWW	0.062	0.080	0.019	0.048	0.039	0.123
Lake Charles	0.049	0.089	0.007	0.045	0.055	0.152
Measured Tidal Data						
Location	Constituent Amplitude (m)					
	K_1	M_2	S_2	N_2	O_1	M_1
Offshore	0.164	0.236	0.056	0.068	0.205	0.238
Marker 60	0.082	0.095	0.034	0.055	0.140	0.212
East Bay	0.007	0.081	0.010	0.038	0.066	0.179
West Cove	0.017	0.087	0.012	0.049	0.082	0.203
Hackberry	0.025	0.075	0.011	0.039	0.076	0.172
Marker 88	0.031	0.093	0.012	0.050	0.071	0.169
GIWW	0.064	0.076	0.020	0.045	0.044	0.114
Lake Charles	0.054	0.097	0.027	0.042	0.084	0.145
Error						
Location	Constituent Amplitude (m)					
	K_1	M_2	S_2	N_2	O_1	M_1
Offshore	-0.001	0.002	0.000	0.002	-0.001	0.003
Marker 60	-0.014	0.018	-0.002	0.002	-0.023	-0.006
East Bay	0.012	-0.002	-0.006	0.004	-0.010	0.006
West Cove	-0.002	-0.019	-0.010	-0.013	-0.028	-0.024
Hackberry	0.002	0.006	-0.007	0.005	-0.020	-0.002
Marker 88	0.005	-0.013	-0.007	-0.006	-0.022	-0.007
GIWW	-0.002	0.004	-0.001	0.003	-0.005	0.009
Lake Charles	-0.005	-0.008	-0.020	0.003	-0.029	0.007

Table IV-2. Comparison of tidal constituent phase calibrated MIKE21 model versus measured tidal data for the period November 17 to November 25, 2006.						
Model Verification Run						
Location	Phase (degrees)					
	ΦS_1	ΦM_2	ΦS_2	ΦN_2	ΦO_1	ΦM_1
Offshore	-95.5	59.2	-129.4	-117.0	-82.8	90.7
Marker 60	-47.0	90.9	-96.7	-88.3	-34.8	139.2
East Bay	-13.9	174.0	-17.1	-0.2	-2.6	171.8
West Cove	-14.3	168.8	-21.8	-5.9	-3.0	171.4
Hackberry	-16.7	169.0	-21.9	-5.7	-5.1	169.2
Marker 88	-13.5	-177.2	-13.8	2.8	-2.0	172.3
GIWW	-11.4	-172.1	-3.2	13.5	0.5	174.6
Lake Charles	-11.4	-178.4	-9.5	7.2	0.1	174.4
Measured Tidal Data						
Location	Phase (degrees)					
	ΦS_1	ΦM_2	ΦS_2	ΦN_2	ΦO_1	ΦM_1
Offshore	-96.0	58.3	-130.3	-117.9	-83.3	90.3
Marker 60	-45.6	83.3	-101.9	-98.0	-33.6	140.5
East Bay	-18.1	177.2	-14.1	4.4	-6.6	167.7
West Cove	-20.5	160.3	-30.0	-14.8	-9.6	165.0
Hackberry	-15.5	177.0	-13.8	3.0	-4.0	170.3
Marker 88	-16.8	-178.1	-9.8	8.5	-5.0	169.1
GIWW	-10.8	-170.5	-1.7	15.1	1.3	175.3
Lake Charles	-8.9	-166.4	1.5	19.6	2.8	177.0
Error						
Location	Phase (minutes)					
	ΦS_1	ΦM_2	ΦS_2	ΦN_2	ΦO_1	ΦM_1
Offshore	1.9	1.9	1.8	2.0	1.9	1.9
Marker 60	-5.7	15.7	10.4	20.6	-5.2	-5.3
East Bay	16.7	-6.7	-6.0	-9.8	17.1	17.0
West Cove	25.0	17.6	16.4	18.6	28.4	26.5
Hackberry	-4.5	-16.5	-16.2	-18.4	-5.1	-4.6
Marker 88	13.2	1.9	-7.9	-12.0	13.0	13.2
GIWW	-2.7	-3.3	-3.1	-3.4	-3.3	-2.9
Lake Charles	-10.0	-24.8	-22.0	-26.1	-11.5	-10.6

IV.4 ADCP VERIFICATION OF THE LAKE CALCASIEU SYSTEM

An additional model verification check was possible by using collected ADCP velocity data to verify the performance of the model in representing the system dynamics. Computed flow rates from the model were compared to flow rates determined using the measured velocity data. The ADCP data survey efforts are described in Section III.2. For the model ADCP verification, the Calcasieu model was run for the period covered during the ADCP survey on October 25, 2006.

The verification model period was performed for an approximate eight-day period, beginning 1500 hours EDT October 24, 2006 and ending 1500 EDT November 1, 2006. This

time period included a 12-hour model spin-up period, and a tide cycle period used to compare to the ADCP data. Model flow rates were computed in MIKE21 HDFM at measurement line (channel cross-section) that correspond to the actual ADCP transect followed in the survey across the inlet into the Lake Calcasieu system, see Figure IV-18.

Data comparisons at the ADCP transect show excellent agreement with the model predictions, with R^2 correlation coefficient between data and model results range being 0.96. A comparison of the measured and modeled volume flow rates at the survey transect are shown in Figure IV-19. The plot in the figure shows the flow comparison. Each ADCP point (black circles shown on the plots) is a summation of flow measured along the ADCP transect at a discrete moment in time. The 'bumps' and 'skips' of the flow rate curve (more evident in the model output) can be attributed mostly to the peculiar nature of the forcing tide in this region, but also to the effects of winds (i.e., atmospheric effects) on the water surface, changes in runoff from the bayou/marshes draining into the system, and friction across the seabed periodically retarding or accelerating the flow through the inlets. If water surface elevations changed smoothly as a sinusoid, the volume flow rate would also appear as a smooth curve. However, since the rate at which water surface elevations change does not vary smoothly, the flow rate curve is expected to show short-period fluctuations.

Figure IV-18. ADCP transect location in the southern portion of Lake Calcasieu, the red line indicates the ADCP transect location.

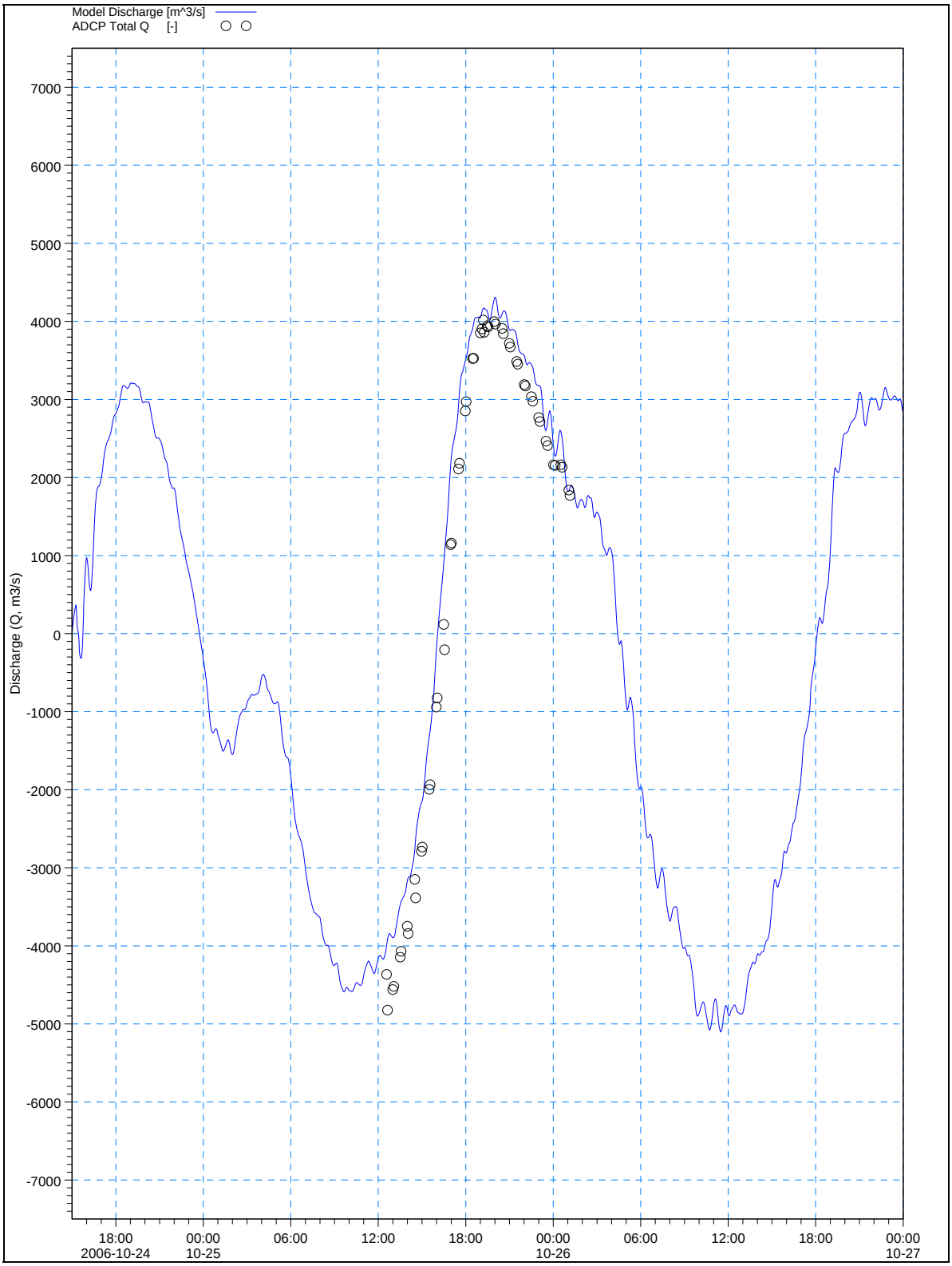

Figure IV-19. Comparison of measured volume flow rates versus modeled flow rates (top plot) across the entrance to channel to Lake Calcasieu, over a 12.5 hours on October 25, 2006 (R^2 = 0.96). Flood flows into the inlet are positive (+), and ebb flows out of the inlet are negative (-).

IV.5 MODEL CIRCULATION CHARACTERISTICS

The final calibrated and validated model serves as a useful tool for investigating the circulation characteristics of the Lake Calcasieu system. Using model inputs of bathymetry and tide data, current velocities and flow rates can be determined at any point in the model domain. This is a very useful feature of a hydrodynamic model, where a limited amount of collected data can be expanded to determine the physical attributes of the system in areas where no physical data record exists.

Examining the flows in and out the main channel, the overall system exhibits ebb dominance. This is not unexpected do to the amount of fresh water draining into the system, as well as the microtidal forcing within the Gulf of Mexico. The fresh water continually entering the system requires less water to enter from the Gulf of Mexico on a flood cycle, than is required to exit on an ebb cycle. Flow velocities are the strongest along the main channel between river miles 1 to 5. This is due to the constrained nature of the channel between the tip of the jetties and the southern end of the lake. Depth-averaged velocities in the inlet generally peak around 1.2-1.4 m/s for ebbing tides, and 1.0-1.2 m/s for flooding tides. A close-up of the model output is presented in Figure IV-20, which shows contours of flow velocity, along with velocity vectors which indicate the direction and magnitude of flow, for a single model time-step, at the portion of the tide where maximum ebb velocities occur at the inlet.

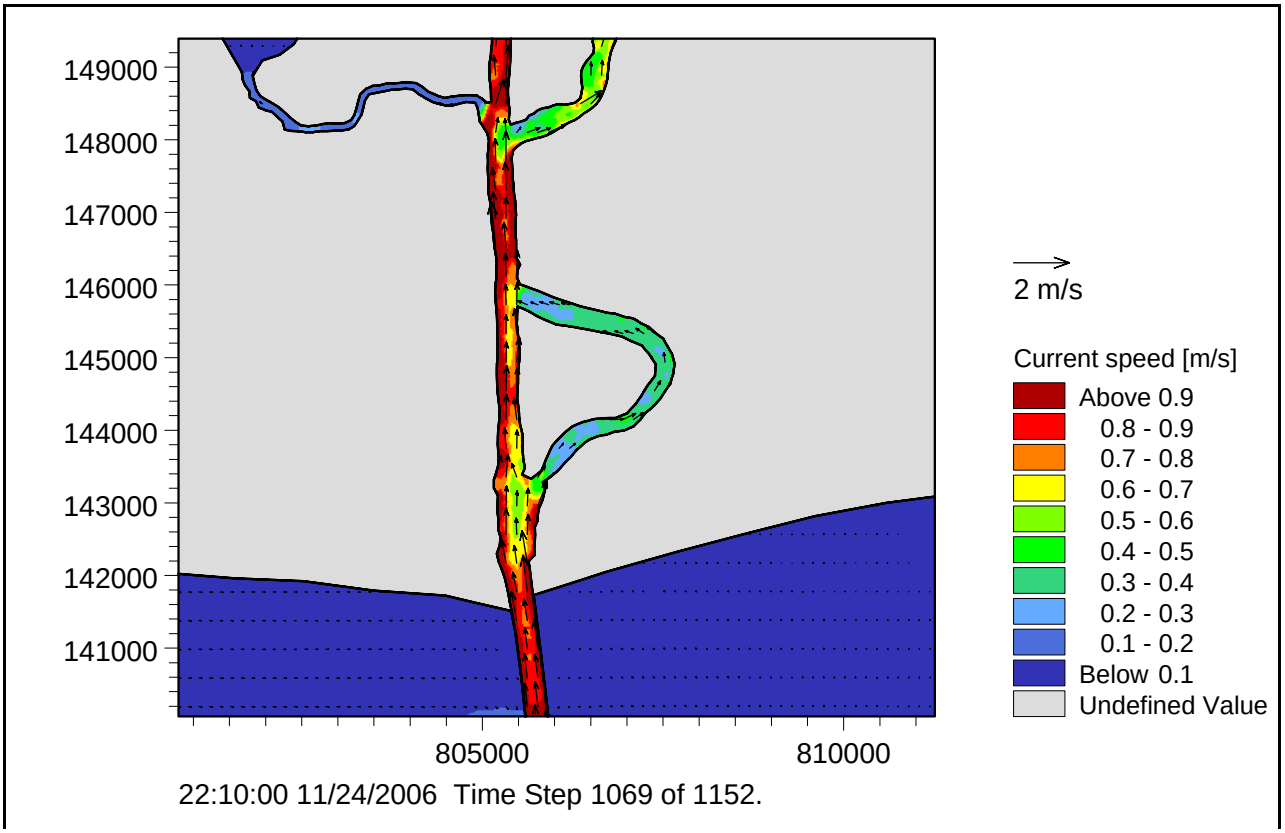

Figure IV-20. Example of hydrodynamic model output in channel between the Gulf of Mexico and Lake Calcasieu for a single time step where maximum flood velocities occur for this tide cycle. Color contours indicate flow velocity, and vectors indicate the direction and magnitude of flow.

Between river miles 5 and 21 the flow is divided between the main channel and the main body of Lake Calcasieu. A portion of the ebbing flow bypasses the main channel just south of the Devils Elbow and flows into the lake. The secondary flow route through the main body of the lake creates relatively high velocity ebb currents returning flow to the CSC in the area not constrained by disposal islands. Velocities are the greatest along the constrained sections of the main channel and at the flow constrictions at the north and south end of the lake, Figure IV-21. The depth-averaged flow velocities are often below the threshold for suspending sediment in this region, with peaks at maximum flood and ebb flows that likely suspend sediment for short periods of time. Velocities and the related shear stress causing sediment suspension is described in Section V.

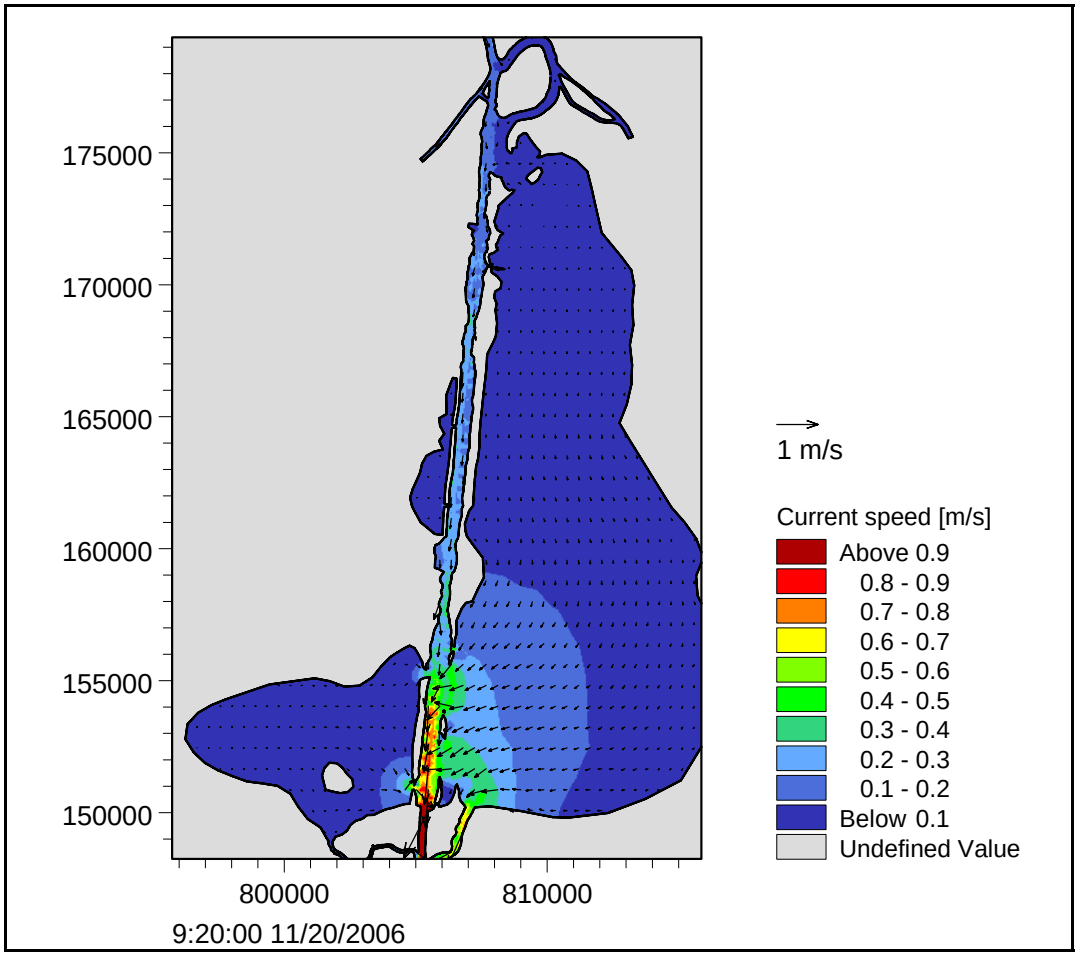

Figure IV-21. Example of hydrodynamic model output in channel along Lake Calcasieu for a single time step where maximum ebb velocities occur for this tide cycle. Color contours indicate flow velocity, and vectors indicate the direction and magnitude of flow.

At the north end of the lake the flow is generally constrained to the GIWW which extends west to Sabine and the navigation channel to Lake Charles. The circulation patterns around the Devils elbow are very quiescent, with flow velocities remaining below 0.1 m/s for all phases of the tide. Due to the configuration of this channel, the relatively low velocities indicate likely settling of suspended material. This hypothesis is supported by the significant volume of historic dredging in this area.

The channel is constrained north of river mile 23 until it reaches Lake Charles at mile 35. Flow magnitudes are generally between 0.1 and 0.3 m/s along the main channel and lower in the fringing bays and marshes. Velocities decrease further towards the head of the system, as shown in Figure IV-22.

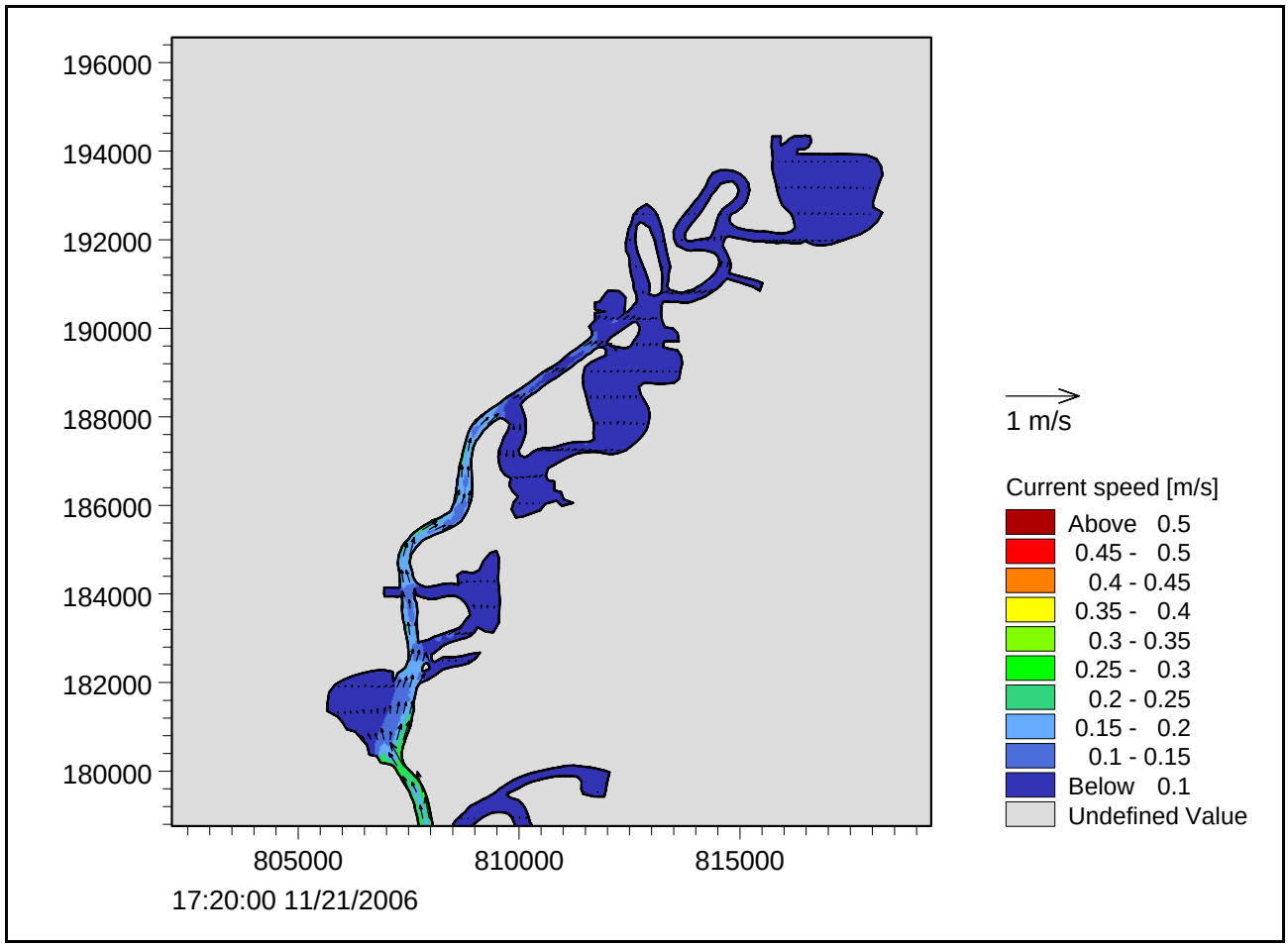

Figure IV-22. Example of hydrodynamic model output along Calcasieu Ship Channel for a single time step where maximum flood velocities occur for this tide cycle. Color contours indicate flow velocity, and vectors indicate the direction and magnitude of flow.

V. SEDIMENT TRANSPORT MODELING

The purpose of the sediment transport modeling for Lake Calcasieu was to determine trends in mud transport and, to the extent possible, quantify the flow regime and how this affects sediment sources and sinks. The results of the modeling analysis provide information required to support and verify plan formulation and alternative analysis regarding sediment placement and management within the system to minimize dredging and placement impacts to the channel and ecosystem resources. In addition, the model results will be utilized to support the preparation of the Dredged Material Management Plan (DMMP) and Environmental Impact Statement for the project.

The numerical tools selected to simulate fine-grained sediment transport within the Lake Calcasieu estuarine system was the Mud Transport (MT) and Advection-Dispersion (AD) models that are available as modules in the DHI MIKE 21 hydrodynamic modeling suite. These modeling tools allow specification of spatially varying mud layers, as well as specification of background and boundary suspended sediment characteristics. A complete description of the modeling approach is described below.

The accuracy of model predictions is directly dependent on the quality of the input data. For the Lake Calcasieu system, sediment data required to parameterize the model was derived from a variety of sources including available U.S. Army Corps of Engineers reports, regional studies of observed suspended sediment concentrations and mud characteristics, and other task reports regarding the Lake Calcasieu DMMP effort. With the exception of the critical shear stress flume study performed by Texas A&M University (Ravens, 2007), information used to parameterize the model was not directly collected for the purpose of sediment transport modeling in the Lake Calcasieu system. However, environmental work associated with previous dredging efforts, as well as numerous scientific studies of the Lake Calcasieu and nearby Lake Sabine estuary systems, provided a significant amount of data regarding the distribution of sediments.

V.1 SEDIMENT CHARACTERISTICS AND DOMINANT PROCESSES

In 1968 the CSC was substantially widened to 400 ft and dredged to its current depth of 40 ft. In addition, the USACE completed construction of the Calcasieu River Saltwater Barrier on the Calcasieu River north of the city of Lake Charles at this same time. This barrier prohibited the flow of the saltwater into the upper reaches of the Calcasieu River to protect agricultural water supplies. The structure consists of a lock and a flood control barrier with adjustable gates. In its current configuration, the Calcasieu Ship Channel (CSC) is comprised of three main sections:

- 42-foot deep and 800-foot wide approach channel from the Gulf of Mexico to the seaward end of the jetties.
- 40-foot deep and 400-foot wide ship channel extending from the jetties to channel mile marker 34.1
- 35-foot deep and 250-foot wide ship channel from channel mile marker 34.1 to 36.

Figure V-1 shows the CSC mile marker locations for reference. As shown, the beginning of the CSC is at the landward end of the jetties protecting the entrance. Sediment from Ship Channel mile marker 5 to 36 have historically been dredged with a cutterhead suction dredge and placed in upland confined or semi-confined disposal sites (GBA, 2007). In addition, some

materials have been beneficially used in Black Lake, Brown Lake, and the Sabine National Wildlife Refuge.

Figure V-2 summarizes the dredging performed along the CSC from 1994 to 2005. The data used to create this figure is shown in Table 1 and was developed by GBA (2007). For this 11-year period, the total dredging performed per mile, between Mile 5 and Mile 25.6 varied from 22,500 CY (Mile 5-5.7) to 3,078,100 CY (Mile 15.2 to 16.1). Only 3 reaches had less than 1,000,000 CY dredged over the 11-year span (Mile 5-5.7, Mile 9.5-10.4 and Mile 24.6-25.6). The average dredged quantity between Mile 5 and Mile 25.6 was 1,918,500 CY per mile or 174,400 CY/mile/year. Twenty (20) of the 22 sections were dredged at least 4 times over the 11 years. Mile 21.8-22.7 was dredged 7 times in 11 years. Dredging volumes and frequency are markedly reduced from Mile 26 northwards. Between Mile 26 and Mile 36, the average total volume dredged was 135,600 CY per mile over a 10-year period; however, this information is not included in Table V-1 because it is beyond the study limits of the analysis. As reported in the Calcasieu River and Pass Shoaling Study (GBA, 2007), the evaluation of dredge volumes prior to 1994 indicated differing quantities of dredged material between mile markers 5 and 36; therefore, the most recent 11 years of relatively consistent dredging were utilized for this evaluation.

A majority of the sediment in the CSC is comprised of fine silt and clay. From Mile 9 north to Mile 36, the sediments are typically 90% silt and clay with a small amount of fine sand. The organic content is higher in these sections, sometimes approaching 10% especially north of the GIWW (GEC, 2007). The southern portion of the CSC contains a higher sand content: 20% sand at Mile 9, 41% sand at Mile 7, and 78% sand at Mile 6. The larger proportion of coarse-grained sediments in this region is likely due to (a) sediments derived from the barrier beach system and nearshore waters in the Gulf of Mexico and (b) higher ambient tidal currents in this region that prevents settling of fine-grained material.

The confined channel south of mile marker 5 creates a tidal “jet” that causes water flowing into Lake Calcasieu during the flood cycle to transport sand in a northerly direction. As the tidal flow becomes less confined in the southern portion of the lake, velocities decrease and the entrained sand settles out. Based on the dredging volumes shown in Table V-1, this portion of the channel requires maintenance dredging volumes of ~150,000 CY per mile per year. A majority of this sediment consists of material north of mile marker 7, consisting of sediments that are more than 50% silt and clay. This trend indicates that sandy material derived from seaward portions of the estuary, as well as the adjacent beaches and nearshore waters, are not a dominant factor in the long-term maintenance dredging requirements of the CSC. This is further supported by the absence of a well-defined flood tidal shoal at the intersection of the CSC with the southern limit of the lake.

A plot of the maximum velocities observed under normal tidal conditions (Figure V-3) helps illustrate the general flow regime governing sediment transport processes within the CSC. The strong gradient in velocity between Mile 5 and Mile 9 shows the relatively rapid transition between currents that can readily suspend sand-sized materials (peak currents in excess of ~0.9 meters/second to more quiescent tidal flow conditions, where *in situ* sediments are dominated by silt and clay material. A second area of observed sediment accretion is the confluence of the Gulf Intracoastal Waterway (GIWW) and the main channel, immediately north of Mile 22. The dredging record from 1994 to 2005 shows approximately 200,000 CY more material removed between Miles 20 and Mile 22 as compared to neighboring portions of the CSC. The confluence of the Calcasieu River and the GIWW (to both the east and west), the lower CSC, and an opening to the main portion of Lake Calcasieu make the region between

Miles 20 and 23 dynamic relative to the introduction and settling of upland-derived sediments. Specifically, the Calcasieu River and the GIWW are potential sources of significant freshwater inflow during upland flood events. Due to the relatively large watershed of the Lake Calcasieu estuarine system, where maximum observed flows in the Calcasieu River were 180,000 cubic feet per second, a substantial amount of terrestrial sediments are introduced to the system during significant upland flooding events. In addition, the bordering salt/brackish marsh systems along the GIWW and the tidal flow from Lake Sabine to the west also provide an influx of suspended sediments during periods of high freshwater inflow. It is unclear whether the high rate of shoaling in this region is due to the complex current patterns associated with the convergence of several tidal channels, or potentially due to changes in other parameters (e.g. salinity) that might make deposition more favorable.

Figure V-1. Lake Calcasieu Ship Channel location map. Mile markers are labeled every 5 miles.

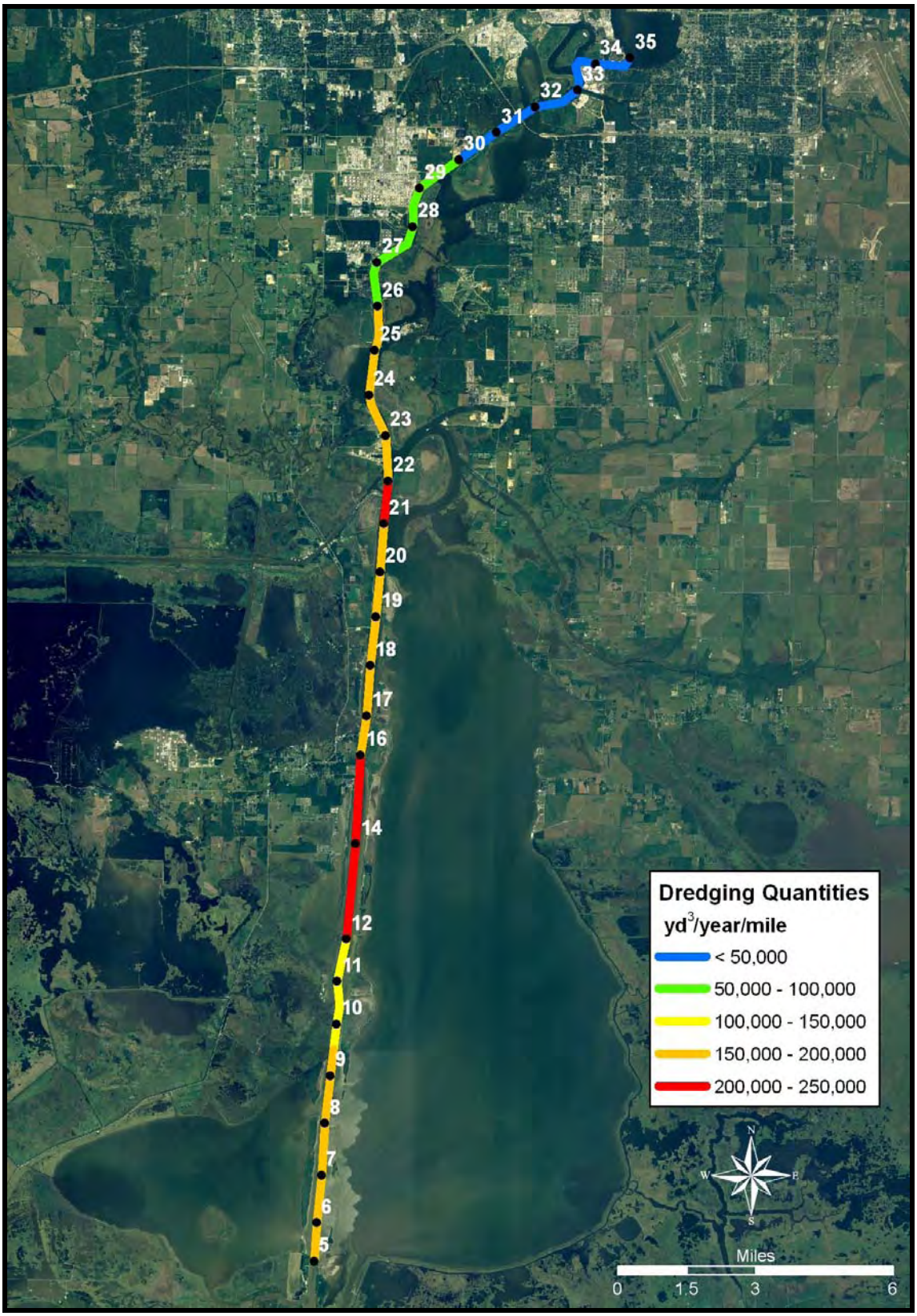

Figure V-2. Average dredging quantities (CY/year/mile) along the Calcasieu Ship Channel for the period of 1994 to 2005.

Table V-1. Dredging Quantities (in cubic yards) on the Calcasieu Ship Channel by Mile (1994-2005).

Contract #	Contract Date	Contract Complete	Dredged Dimensions	Devil's Elbow	Clooney Isl. Loop	Turning Basin	Nav Gap – Mile 8.5	Mile 5-5.7	Mile 5.7-6.6	Mile 6.6-7.6	Mile 7.6-8.5	Mile 8.5-9.5	Mile 9.5-10.4	Mile 10.4-11.4	Mile 11.4-12.3	Mile 12.3-13.3	Subtotal
05-C-0045	12-Jul-05	8-Mar-06	400**'X-42.0	1,056,407													1,056,407
04-C-0048	12-Aug-04	23-Feb-05	400**'X-42.0										109,057	360,000	750,000	700,000	1,919,057
04-C-0041	30-Jun-04	29-Sep-04	400**'X-42.0						36,366	94,312	289,570	76,407	119,826		-	-	616,481
03-C-0058	11-Sep-03	25-Jan-04	400'X-42.0	1,081,670													1,081,670
03-C-0044	19-Jun-03	29-Nov-03	400**'X-42.0														0
01-C-0038	4-Apr-01	20-Jan-02	400'X-42.0				32,629	15,003	133,581	321,391	706,743	266,417	199,853	304,044	316,993	314,378	2,611,032
00-C-0092	13-Sep-00	14-Aug-01	400'X-42.0	1,063,161	207832												1,270,993
99-C-0050	16-Jul-99	12-Nov-99	400'X-42.0						265,759	336,549	826,221	539,385	560,608	796,694	563,684	528,611	4,417,511
98-C-0065	18-Aug-98	8-Jul-99	400'X-42.0	999,220													999,220
96-C-0039	10-Apr-96	26-Oct-96	400'X-42.0	954,781				7,521	117,439	328,241	610,432	422,557			550,125	370,956	3,362,052
94-C-0099	12-Sep-94	30-May-95	400'X-42.0	1,395,780	347,925	326,765											2,070,470
			SUMMATION BY MILE	6,551,019	555,757	326,765	32,629	22,524	553,145	1,080,493	2,432,966	1,304,766	989,344	1,460,738	2,180,802	1,913,945	19,404,893

Contract #	Contract Date	Contract Complete	Dredged Dimensions	Mile 13.3-14.2	Mile 14.2-15.2	Mile 15.2-16.1	Mile 16.1-17.1	Mile 17.1-18.0	Mile 18.0-18.9	Mile 18.9-19.90	Mile 19.90-20.8	Mile 20.8-21.8	Mile 21.8-22.7	Mile 22.7-23.7	Mile 23.7-24.6	Mile 24.6-25.6	Subtotal
05-C-0045	12-Jul-05	8-Mar-06	400**'X-42.0					342,000	287,000	384,000	145,000	145,000	760,000	421,000		119,000	2,603,000
04-C-0048	12-Aug-04	23-Feb-05	400**'X-42.0	723,000	663,000	788,000	750,000									109,225	3,033,225
04-C-0041	30-Jun-04	29-Sep-04	400**'X-42.0	-	-	-	-										0
03-C-0058	11-Sep-03	25-Jan-04	400'X-42.0										308,577	440,072	420,560		1,169,209
03-C-0044	19-Jun-03	29-Nov-03	400**'X-42.0	52,000	439,000	501,000	437,000	347,000	236,000	234,000	334,000	438,000	100,000				3,118,000
01-C-0038	4-Apr-01	20-Jan-02	400'X-42.0	250,465	-	-	-										250,465
00-C-0092	13-Sep-00	14-Aug-01	400'X-42.0		430,164	662,016	513,258	281,406	182,679	182,679	469,934	421,877	421,877	500,000	357,733	357,733	4,781,356
99-C-0050	16-Jul-99	12-Nov-99	400'X-42.0	569,731													569,731
98-C-0065	18-Aug-98	8-Jul-99	400'X-42.0		505,665	606,400	444,500	456,700	302,400	426,900	502,650	578,900	663,800	512,200	455,785	163,300	5,619,200
96-C-0039	10-Apr-96	26-Oct-96	400'X-42.0	547,604	564,739	520,722	578,232	606,790	495,592	460,245	542,776	645,644	242,343				5,204,687
94-C-0099	12-Sep-94	30-May-95	400'X-42.0										233,295	486,705	355,585	157,740	1,233,325
			SUMMATION BY MILE	2,142,800	2,602,568	3,078,138	2,722,990	2,033,896	1,503,671	1,687,824	1,994,360	2,229,421	2,729,892	2,359,977	1,589,663	906,998	27,582,198

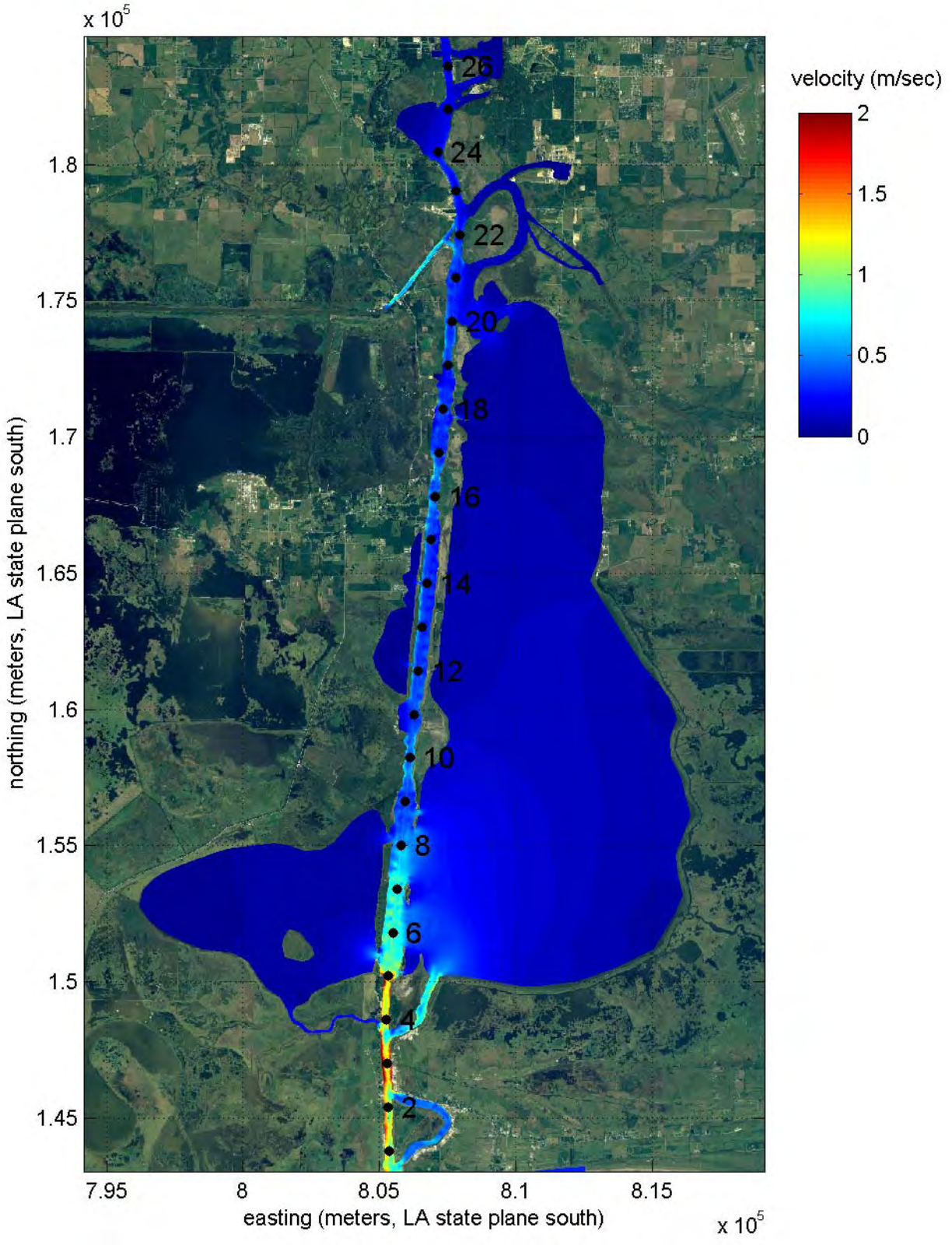

Figure V-3. Maximum velocities observed during average tidal conditions. These hydrodynamic results are from the calibration run. Channel miles also provided as black dots.

In wave-dominated estuaries like Lake Calcasieu the wave energy tends to be significant at the entrance and sediment eroded from the coast is transported alongshore forming a spit or barrier beach. Formation of the spit constricts the size of the tidal entrance to the estuary. Eventually, the inlet cross-section represents a balance between eroding sediment from the barrier and tidal currents through the entrance. Within the main basin of the estuary, the currents diminish rapidly. Towards the head of the estuary, fluvial processes tend to dominate; therefore, the central portion of the estuary represents the lowest total energy and likely is characterized by extensive tidal flats and/or salt marshes. The gradual change in sediment composition (sand-dominated sediment at the south, fine-grained sediments in the middle and fine sediments with a high organic content in the far northern reaches) reflects the transition across the Lake Calcasieu estuarine system from a fluvial-dominated region in the north to a more wave-dominated system through the main basin, southern portion of the CSC, and the inlet.

Figure V-4 shows locations of sediment cores taken within the CSC from Mile 6 north to Mile 23.5. Each sediment sample was analyzed to determine the percent of sand silt and clay present. The results are plotted by mile marker in Figure V-5 below. The southern reach of the sampling, from Mile 6 to Mile 9 shows a high percent of sand present in the samples. The sample from Mile 6 contains almost 80% sand which decreases to about 20% sand in the sample from Mile 9. This large sand fraction is carried into this section of the CSC through the inlet from the Gulf of Mexico. Sand caught in suspension is carried through the inlet by the tidal flow during the flooding tide. As the tidal flow exits the narrow inlet (Mile 5) some flow is dispersed to the southern portion of the lake. This gradual widening of the tidal flow results in lower velocities. In turn, the slower tidal flow allows the suspended sand to settle out and be deposited on the channel bottom. Figure V-5 shows that the sand carried into the CSC in this manner does not travel much farther north than Mile 9. From that point northwards, the silt and clay content increases while the sand content remains small.

For a majority of the central portion of the CSC (Mile 11 to 20.5) there is a mix of 30-40% silt, 40-60% clay and 15% or less sand. This change in sediment composition reflects the transition from the tidally-dominated area near the inlet to the wave-dominated estuary which comprises a majority of Lake Calcasieu. The tidal currents are not strong enough to carry significant quantities of the heavier sand into this central region of the channel. The finer silts and clays make up a majority of the sediments in this area.

From Mile 21.5 to 23.5 there is a third regime of sediment composition. The samples from this area see the clay content increasing to greater than 60%. The silt content is approximately 30% with sand accounting for roughly 5% of the sample. This region of the CSC marks another transition within the system from the estuarine environment to the south into a more fluvial region dominated by the freshwater flows of the Calcasieu River. This area also contains significant anthropogenic changes to the system, most notably the Gulf Intracoastal Waterway (GIWW).

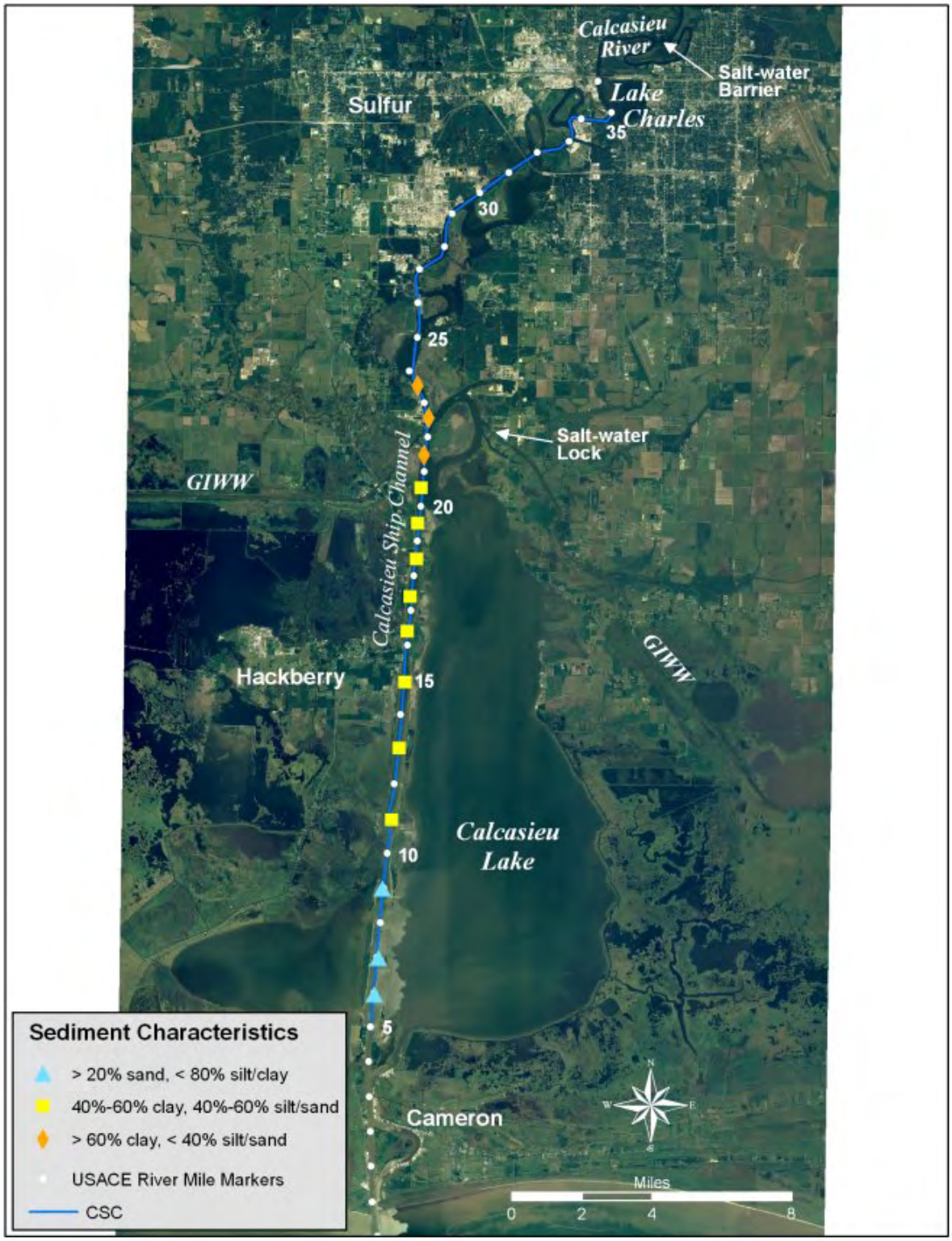

Figure V-4. Sediment sampling locations within the CSC from Mile 6 to 23.5.

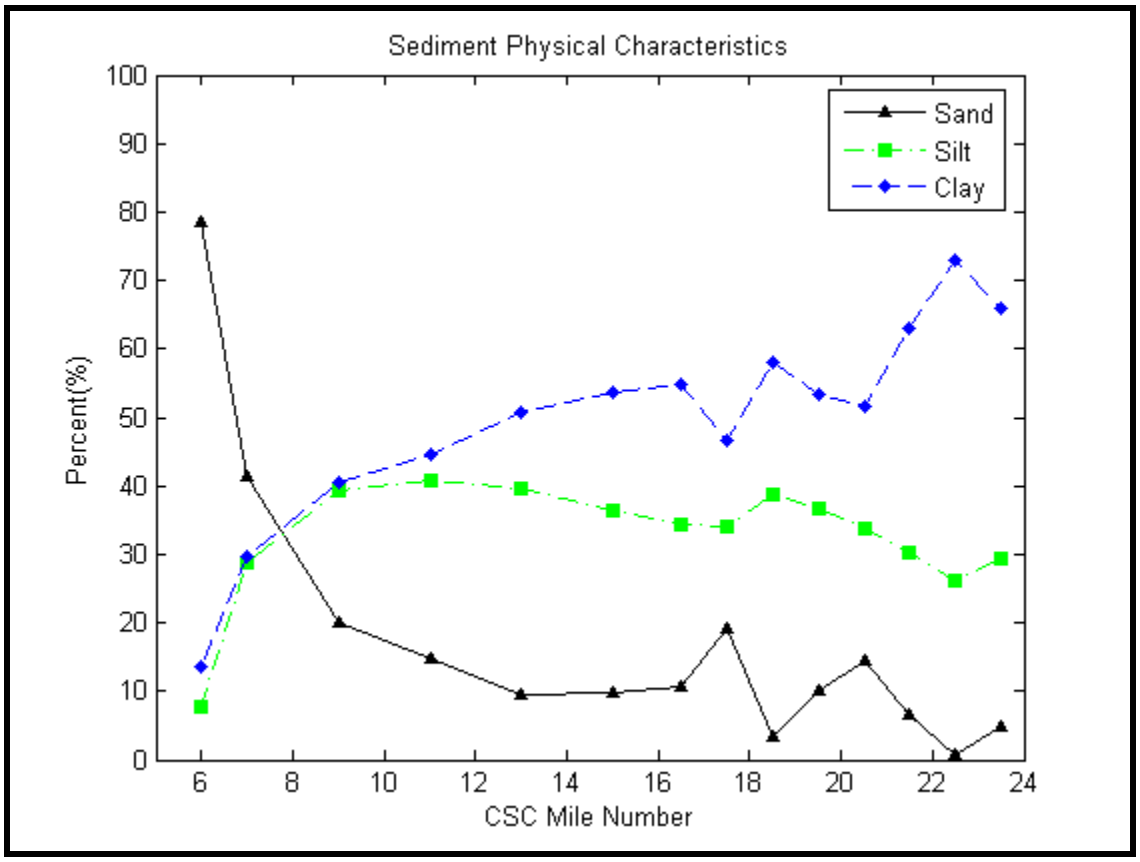

Figure V-5. Sediment physical characteristics within the CSC from Mile 5.5 to 23.5.

V.2 MODEL DESCRIPTION

Sediment transport analyses of the Lake Calcasieu system was performed using the Mud Transport (MT) and Advection-Dispersion (AD) models that are available as modules in the DHI MIKE 21 hydrodynamic modeling suite. The MT and AD modules is designed to run concurrently with the hydrodynamic model, and allows changing bathymetry computed by MT computations to modify the hydrodynamic solution, time step by time step.

MIKE 21 MT models two-dimensional fine-grained simulates processes such as flocculation, hindered settling, wave-current interaction, slope sliding, and consolidation. The model is coded to include up to 12 separate bottom sediment layers, and up to eight separate sediment fractions in the water column. Figure V-6 shows how different layers can be included in the model, and the different processes that can be included in a simulation. In this example from the MT module manual (DHI, 2007), three layers are specified; one of weak fluid mud where hindered settling of the sediment flocs occurs; a middle layer of fluid mud which is undergoing the process of consolidation of the sediment flocs; and a third bed layer that is not fully consolidated.

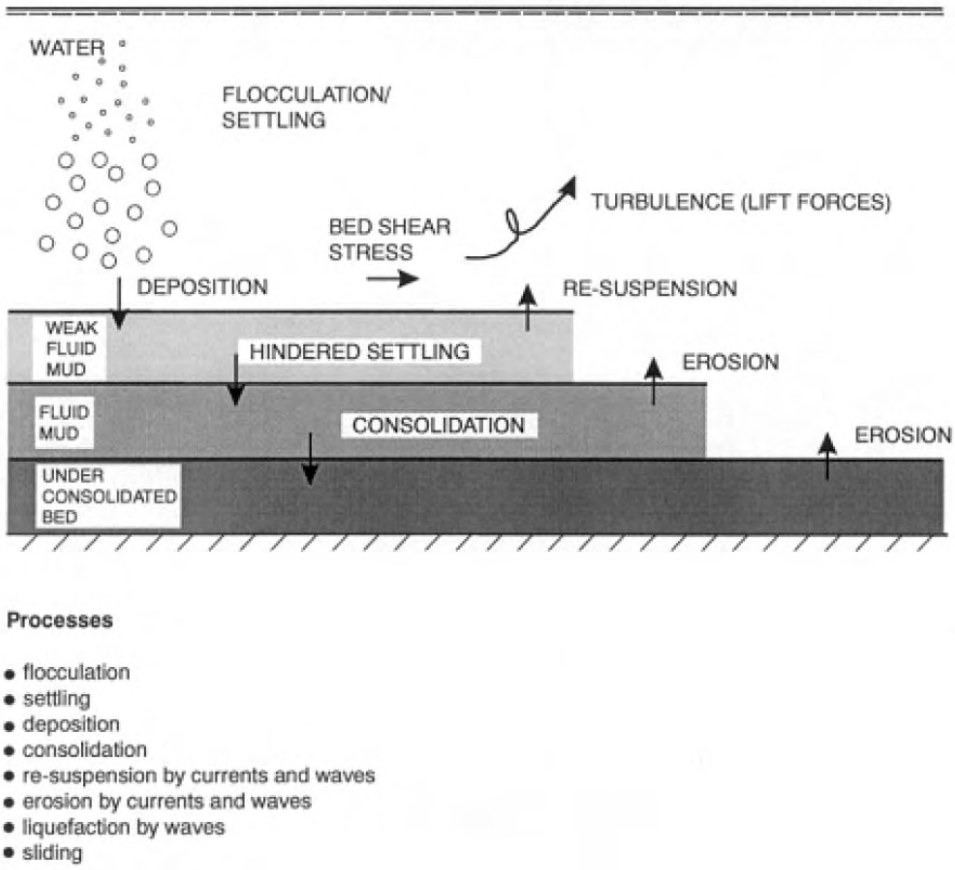

Figure V-6. A schematic diagram (DHI, 2007) showing how sediment layers and transport processes are included in the MT module of the MIKE 21 modeling suite.

The bottom sediment layers are individually characterized by parameters including critical shear velocity for incipient erosion, layer density, and thickness. Separately, sediment fractions in the water column are used to track the movement of different sized material through the model domain, and are characterized by sediment fall velocity and critical shear stress of deposition (the value of shear stress below which deposition will occur for each sediment fraction). Additional inputs to the MT module include bed roughness, initial suspended concentrations of each sediment fraction, and boundary conditions.

Each of the input parameters required by the MT module can be specified as being constant throughout the model domain, or as spatially varying. By varying parameters spatially, different bottom sediment characteristics can be set in the model in different areas of the grid.

The MIKE 21 AD module simulates the advection and dispersion of the different sediment fractions specified for the water column calculations in the MT module, and is therefore the core code for computing sediment transport. Similar to the main HD module, the AD module is a two-dimensional, depth-averaged finite volume model. The formulation of the model is a third-order, Lax-Wendroff-like discretization scheme.

MT/AD module outputs include total suspended solids (TSS) and concentrations of each separate water column sediment fraction, computed shear stress, total bed change from the start of the simulation. Each output variable is provided at each model element for every time

step of the simulation. Using the data MIKE Zero data manager provided as part of the modeling suite, post-processing of the output data can be performed to determine maximum and average shear stresses during the course of the simulation period, and across the entire model domain.

V.3 MODEL INPUT PARAMETERS

Sediment transport was modeled during the same simulation period used for the hydrodynamic model calibration. The model was run to simulate normal tidal currents during the eight-day period between noon of November 17, 2006 through noon of November 25, 2006. This period was used in the initial development of the transport model because it represents a period when tidal dynamics contributed the greater part of the boundary forcing to the system, as apposed to meteorological forcing from winds, barometric pressure gradients, and rainfall within the watershed area of the Lake. The model time step was set at 60 seconds, the same as the original hydrodynamic analysis.

Bottom sediment characteristics utilized in the mud transport model were specified based on available data from Lake Calcasieu. When necessary, data gaps where filled using data from similar systems, like Sabine Lake and Pass. For the Lake Calcasieu model, two sediment layers where specified, a top layer 0.3 meters (1.0 feet) thick of soft mud and a bottom layer of hard mud. The thickness of the bottom layer was made to be great enough so that this layer would not be completely eroded through during the simulation.

The critical shear stress for the start of erosion was specified as 0.5 Pa for the top soft layer throughout the model domain. For the harder second layer, critical shear stress was varied spatially, in order to differentiate between sediments in the CSC (above mile 9) and the sandier sediments south of mile 9 (Figure V-7). The critical shear stress for the various segments of the channel were based on the *in situ* flume tests performed at two sites along the CSC (Ravens, 2007). The density of the two layers was specified as 630 kg/m^3, based on Ravens (2007).

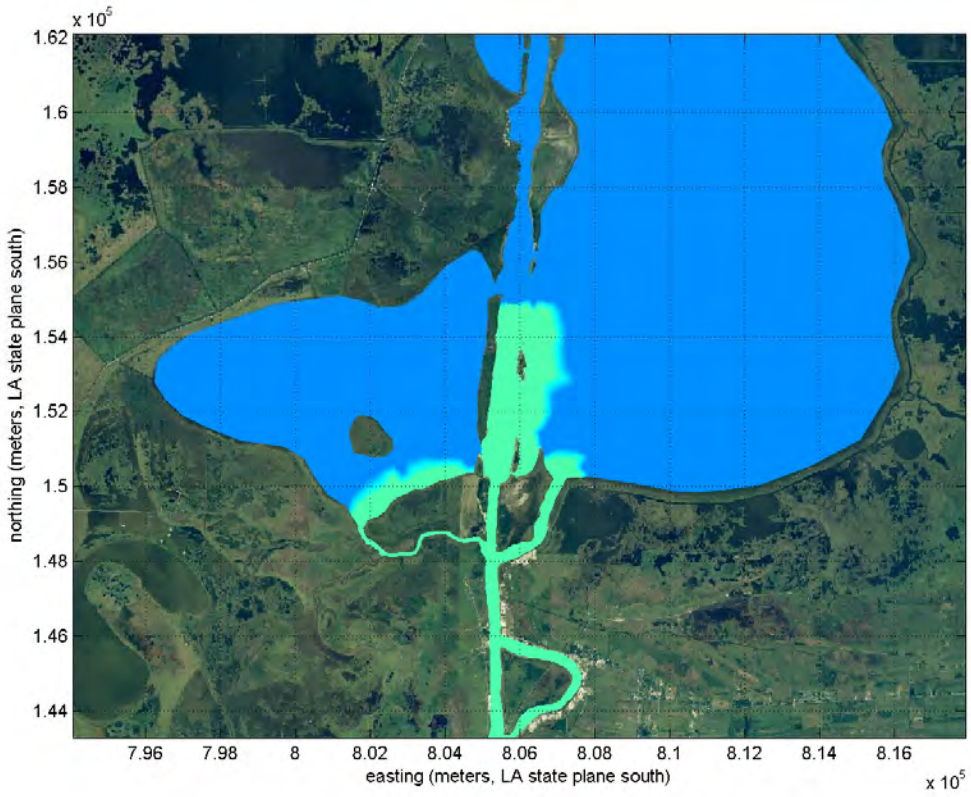

Figure V-7. Map showing distribution of specified critical shear stress for second sediment layer. Light blue (main body of the Lake) indicates areas specified as 0.5 Pa, and the pale green (below mile 9 of the CSC) indicates area specified as 0.9 Pa.

The value of bed roughness (k) used as an input to the model was based upon results from an evaluation of bank erosion in the Sabine-Neches Waterway (Maynord, 2005). From this analysis, the bottom friction coefficient (C_f) was determined to be 0.005 for ambient conditions. The relationship between C_f and k is expressed as

$$C_f = 2\left\{2.5\left[\ln\left(\frac{30h}{k}\right) - 1\right]\right\}^{-2},$$

where h is the water depth.

In addition to the parameters specified for the bed layers, a sediment grain size distribution was specified for the water column calculation. Using grain size distributions determined in the previous analysis of Lake Calcasieu sediments (USACE, 2004), four separate sediment fractions were specified for the water column, as listed in Table V-2. These fractions included one non-cohesive sand fraction, and three cohesive fractions of progressively smaller size. The model requires that the fall velocity of each component be specified. Fall velocities were computed using sediment grain sizes from the USACE analysis using the relationship

$$V_f = \frac{gd^2\left(\frac{\rho_s}{\rho_w} - 1\right)}{18\nu},$$

where g is the gravitational constant, d is the sediment grain diameter, ρ_s and ρ_w are the densities of the sediment grains and water, respectively, and ν is the kinematic viscosity of water.

The distribution of each fraction in the modeled bed layers was specified based again on the USACE analysis of cores, and is listed in Table V-2.

Table V-2. Sediment fractions characteristics used for the Lake Calcasieu cohesive transport model.

Fraction	grain size (mm)	fall velocity (mm/sec)	Distribution in bed layers	type
1	0.1	7.71	5 %	non-cohesive
2	0.03	6.94×10^{-1}	10 %	cohesive
3	0.007	3.78×10^{-2}	20 %	cohesive
4	0.0015	1.73×10^{-3}	65 %	cohesive

Boundary and initial total suspended sediment (TSS) concentrations in the model were specified based on data presented in Yu-Chun (2005) and by the EPA (2002). Initial TSS concentrations in the Lake were specified as 0.003 kg/m^3. The Gulf boundary was specified as 0.003 kg/m^3. At the GIWW and salt barrier, TSS concentrations were specified as 0.050 kg/m^3 and 0.100 kg/m^3, respectively.

Other parameters set for the Calcasieu model were the inclusion of morphological calculations in the simulation, the selection of the faster, low order time integration and spatial discretization schemes.

V.4 MODEL RESULTS

Several outputs can be selected from the simulation of mud transport in Lake Calcasieu. The key outputs for this analysis are bed change during the course of the simulation, total suspended solids (TSS), and computed shear stress. The output data were processed using utilities provided with the MIKE Zero simulation manager software, as well as using Matlab utilities provided by DHI.

V.4.1 Shear Stress

Figures V-8 and V-9 below show the average shear stress under normal tidal conditions, as modeled during the 8 day calibration period. Even under average conditions, areas of relatively high shear stress (greater than 0.3 Pa) can be observed. Sections to note include Mile 19.5 (173,400 m northing), Mile 15.5-17 (167,000m - 169,400m northing) and Mile 9.5-10.5 (157,400 - 159,000). Each of these sections are similar in that they are areas where the CSC become more narrow. The same amount of flow which had been carried by the wider sections of the channel, are now forced through a smaller cross-sectional area. This constriction forces the flow to speed up and so the shear stress increases due to the increased velocity.

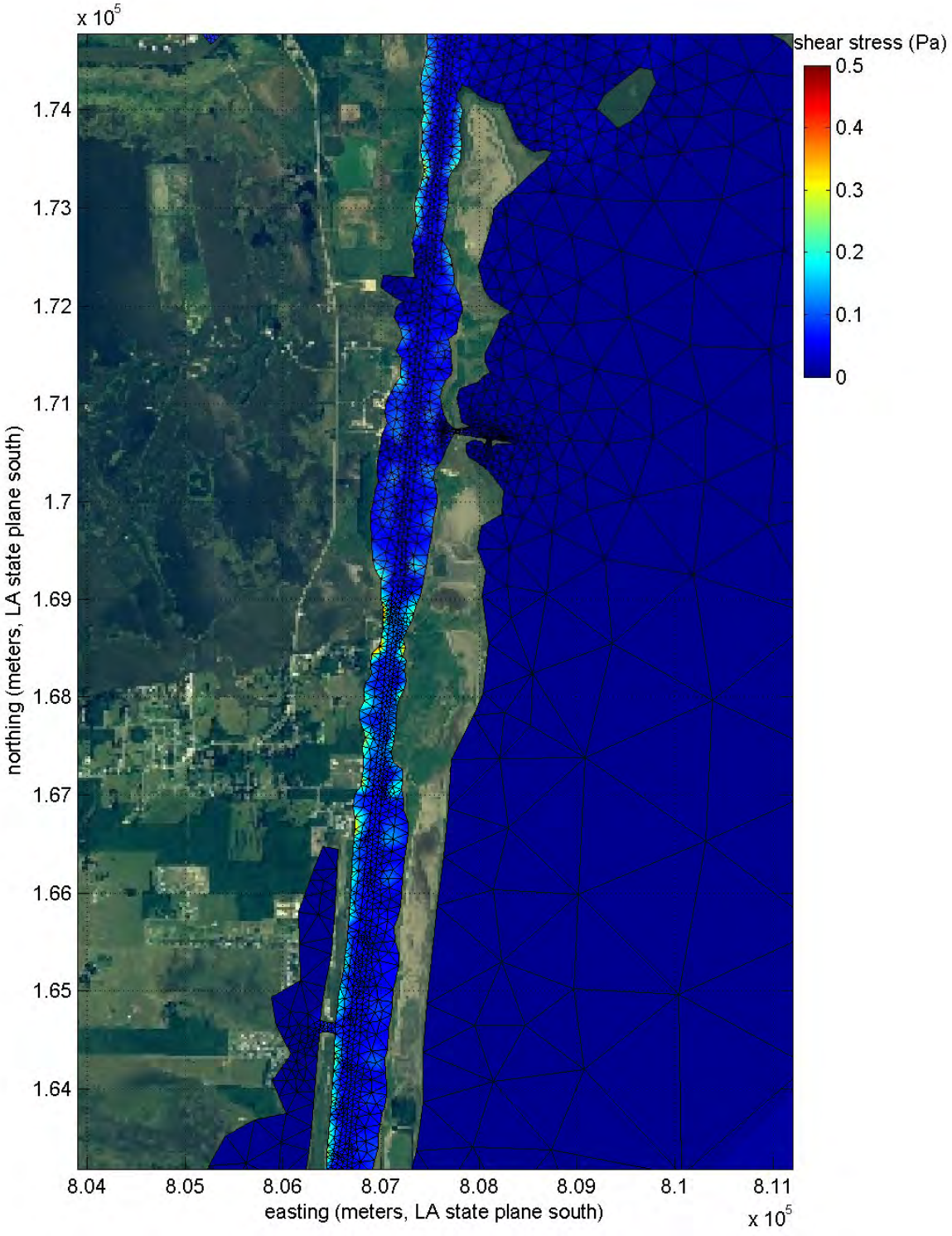

Figure V-8. Average shear stress in the upper navigation channel computed during 8 day calibration period.

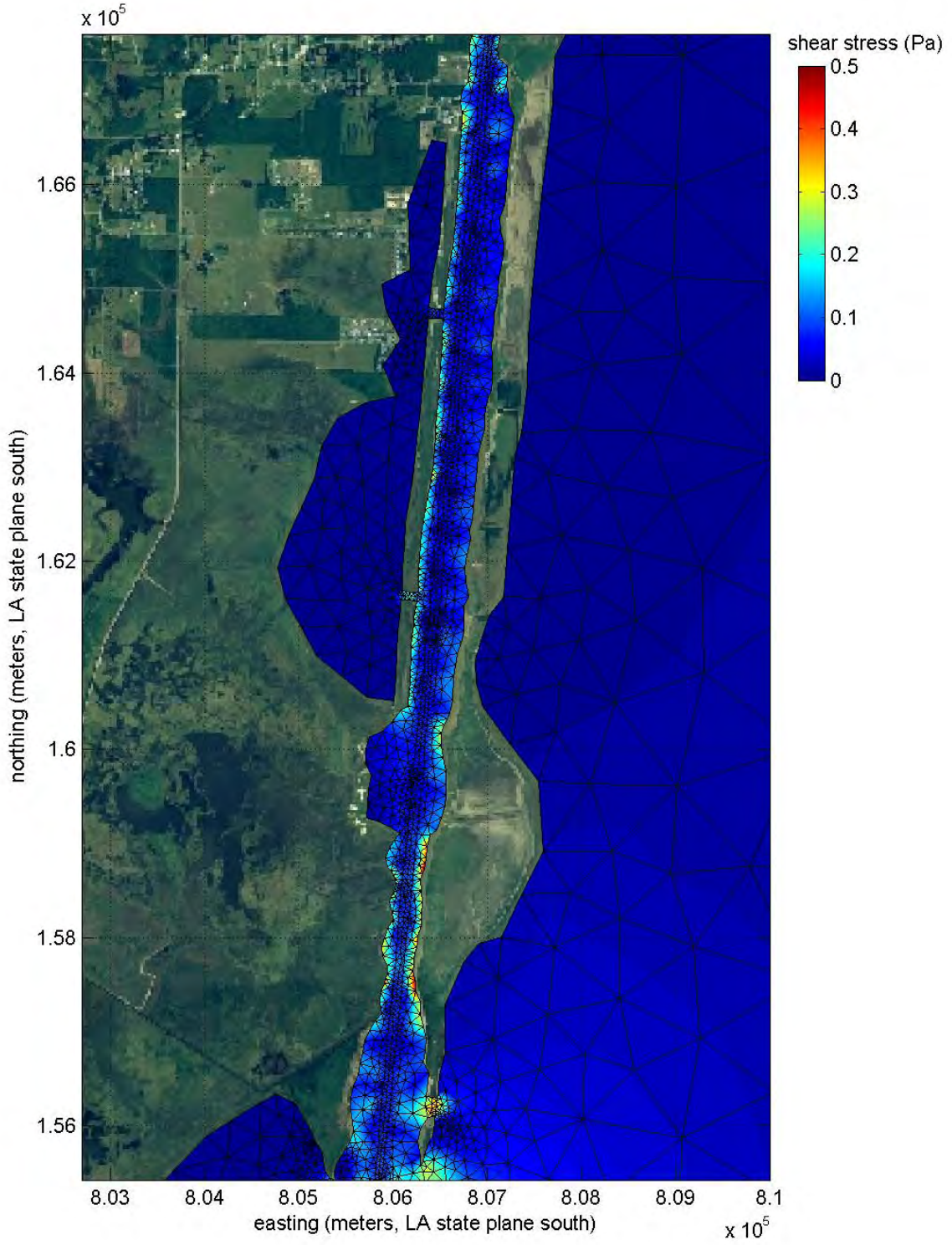

Figure V-9. Average shear stress in the lower navigation channel computed during 8 day calibration period.

Figures V-10 and V-11 show the maximum shear stress observed during the 8 day calibration period. Again, these results represent standard tidal conditions within the CSC. The

areas discussed above show very large (greater than 0.7 Pa) shear stresses on both sides of the channel. In addition to these areas where the channel is constricted, from approximately Mile 15 to Mile 11 (166,200m - 159,800m northing) there are high maximum shear stresses along the western bank of the CSC. The maximum velocities in this section of the CSC are on the order of 0.5 m/s. A large majority of this flow is carried in the navigation channel itself. In this stretch of the CSC, the channel is very near to the western bank which results in these high velocities impacting on the channel margin and toe of the bank itself.

By comparison, the reach from Mile 17.5-19 (170,200m - 172,600m northing) shows the channel banks almost the same distance apart as the lower reaches mentioned above. An important difference is that the channel itself is centered in between the two banks, rather than up against the west bank as it is in the lower reaches. The result is that the maximum shear stresses are lower in this section (0.5 Pa) and the these maxima are seen only in relatively small discontinuous areas, as opposed to the continuous relatively large shear stresses seen along the western bank in the lower sections of the CSC. A final difference to note is that these lower maximum shear stresses along Mile 17.5-19 are also observed along the channel margin and not across the relatively wide shallow flat adjacent to the channel bank. With the navigation channel centered between the banks, and the existence of sufficient shallow areas along the channel margins, the tidal flow is less restricted allowing dissipation of tidal energy without substantial bottom shear stresses that could initiate sediment movement.

V.4.2 Total Suspended Sediments

TSS output from the model shows the concentration, in the water column, of all the separate sediment fractions combined. Though the MT module does track the concentration of each fraction separately, TSS was used in the analysis of model results because it is a standard water quality parameter.

Results are presented for the entire Lake model in Figure V-12 and V-13 for average and maximum TSS computed during a four-tidal cycle (49.7 hour) period at the end of the total eight-day simulation period. The average and maximum values were determined for each element separately. The average values in Figure V-12 show that the largest average TSS (1.95 kg/m^3) is located near CSC mile 10.5.

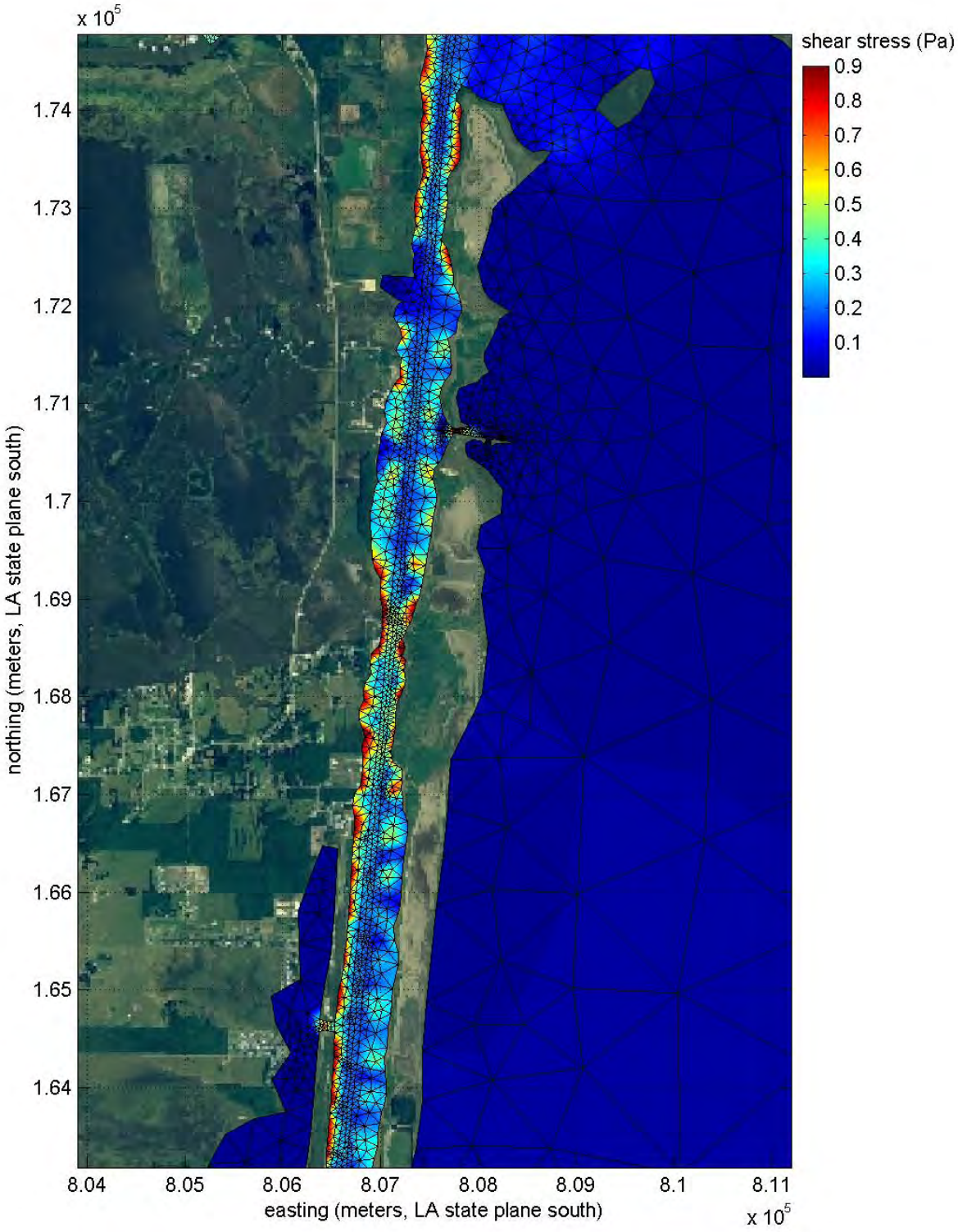

Figure V-10. Maximum shear stress in the upper navigation channel computed during 8 day calibration period.

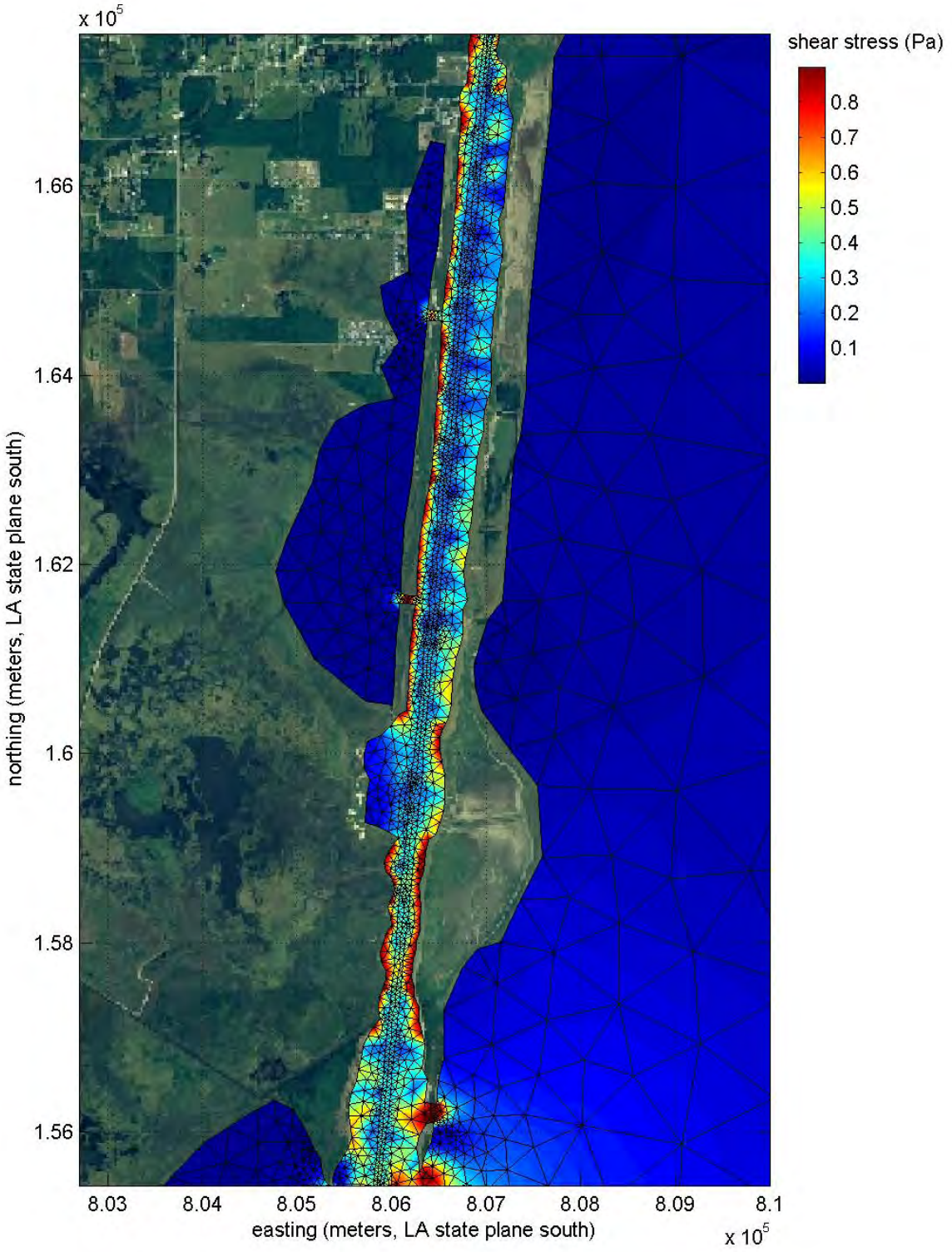

Figure V-11. Maximum shear stress in the lower navigation channel computed during 8 day calibration period.

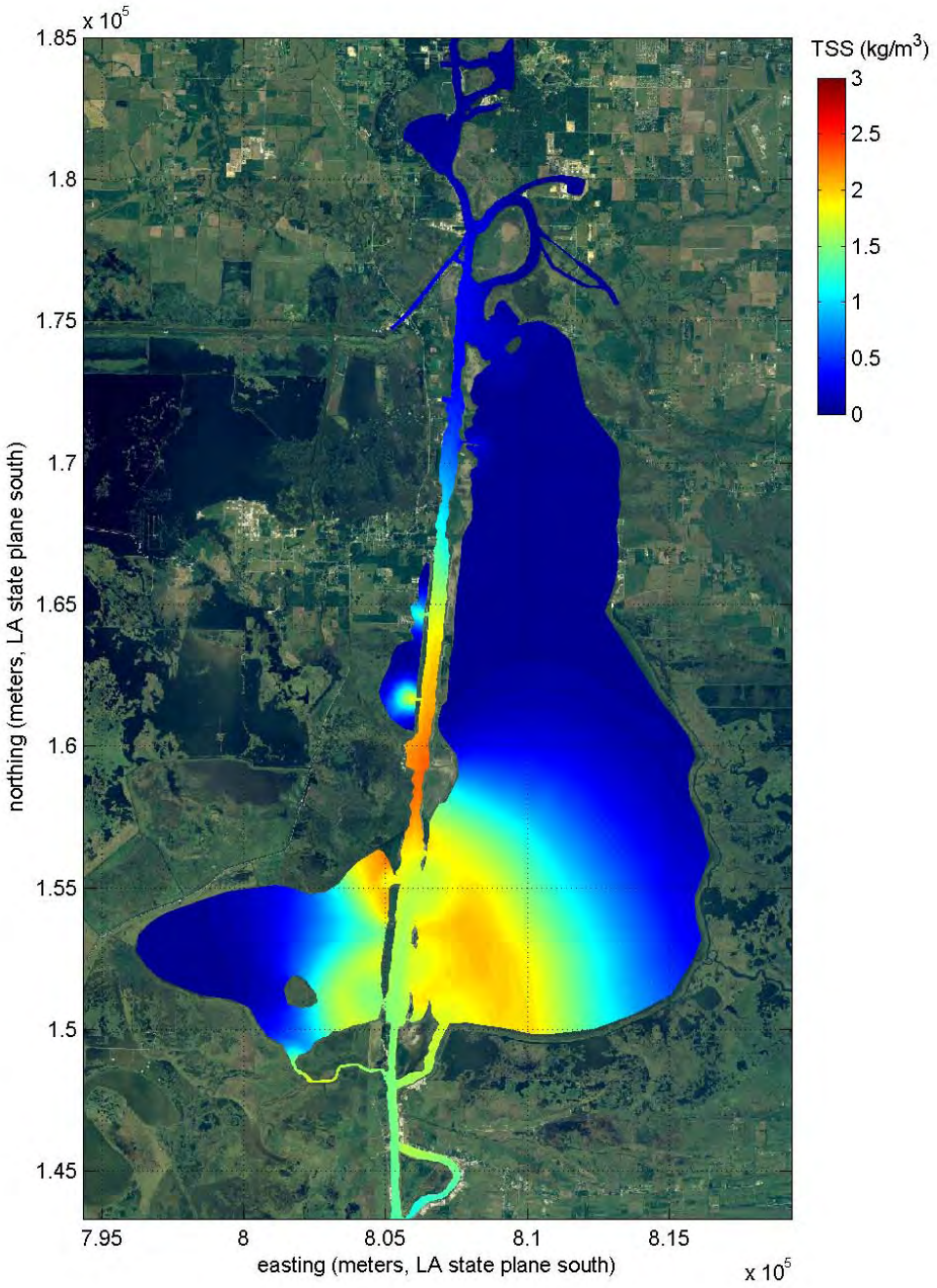

Figure V-12. Average total suspended solids (TSS) computed for each model element over four tide cycles.

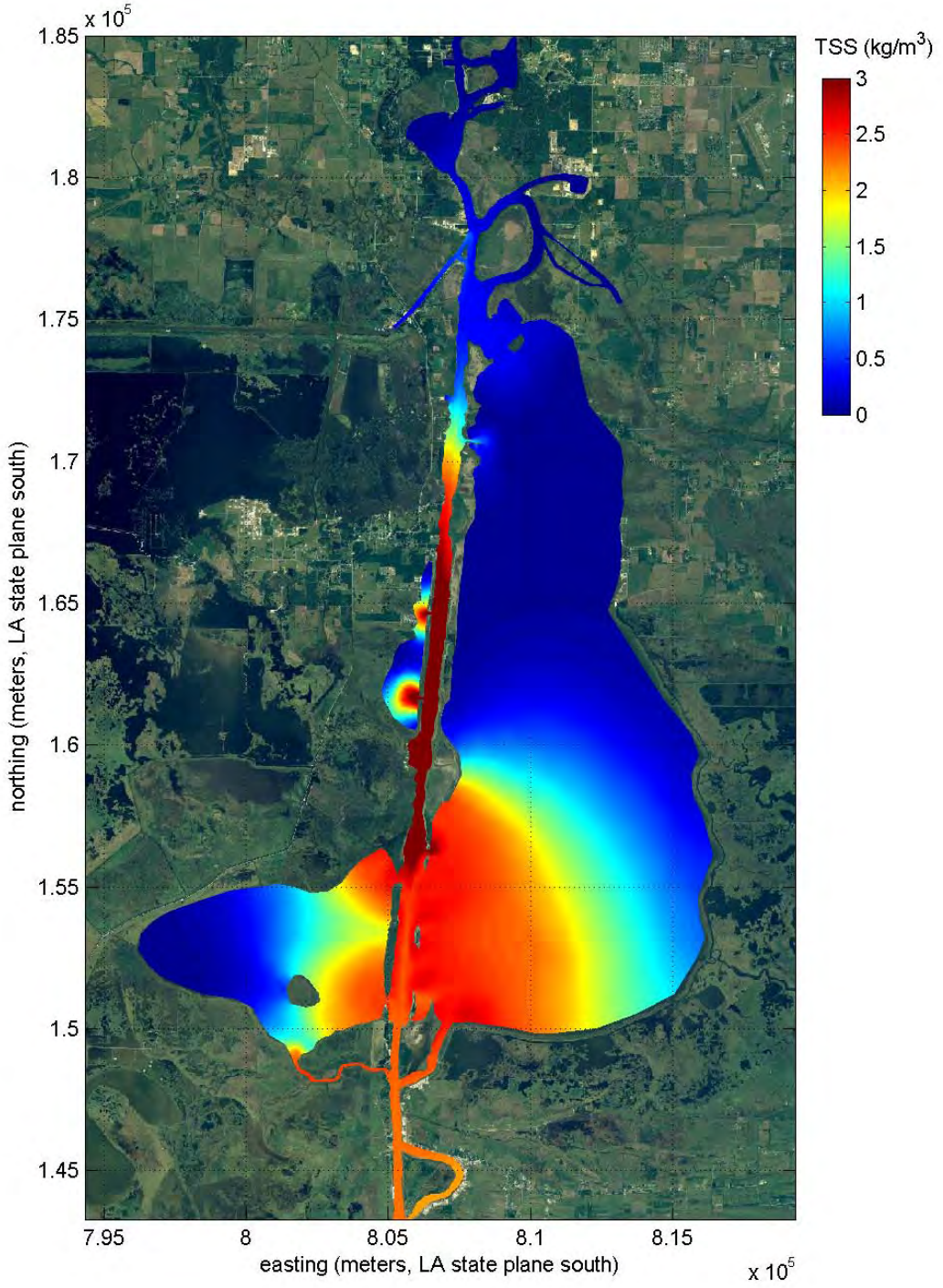

Figure V-13. Maximum total suspended solids (TSS) computed for each model element over four tide cycles.

The maximum TSS results presented in Figure V-13 show a similar trend, with the highest concentrations computed between CSC miles 9 and 15. The concentrations along this reach are generally greater than 3.00 kg/m3.

Figures V-14 through V-17 show how the computed TSS varies along the length of the CSC, between the maximum excursions of the flood and ebb portions of the tide. Excursion is simply the movement of water during the cycle of the tide. An example of this can be made by following a parcel of water that is at CSC mile 10 at slack low water (i.e., the beginning of the flood tide cycle). During the flood tide, the parcel will move northward along the CSC, until high slack water at the beginning of the next ebb phase of the tide. The farthest distance traveled by this parcel of water during the full course of the flood tide would be described as its excursion. This similarly occurs during the ebb tidal phase.

Figure V-14 and V-15 show the distribution of TSS at a single model timestep, which corresponds to the maximum excursion of a flood tide. The two figures overlap, where Figure V-14 shows results for CSC miles 13.5 through 20 and Figure V-15 shows results for miles 9 through 16. The largest values of TSS occur between CSC miles 14 and 17.

Similar to the flood excursion, Figures V-16 and V-17 show the distribution of TSS at the maximum excursion of an ebb tide. The maximum values of TSS occur between CSC miles 10 and 12.

In making a comparison of dredged volumes (Figure V-2) and the maximum excursion of TSS through the tide cycle, there does seem to be some correlation between the area where the greatest dredging volumes are taken (Figure V-2) and the excursion of the northern limit of the high TSS area. The northern limit of the high TSS area moves between CSC miles 12 and 17, the reach which roughly corresponds to the area with the greatest dredging requirement (i.e., between miles 12 and 16). Based on this observation, it appears that this gradient in TSS (the change in TSS over a distance) strongly influences the amount of material that is deposited in the CSC.

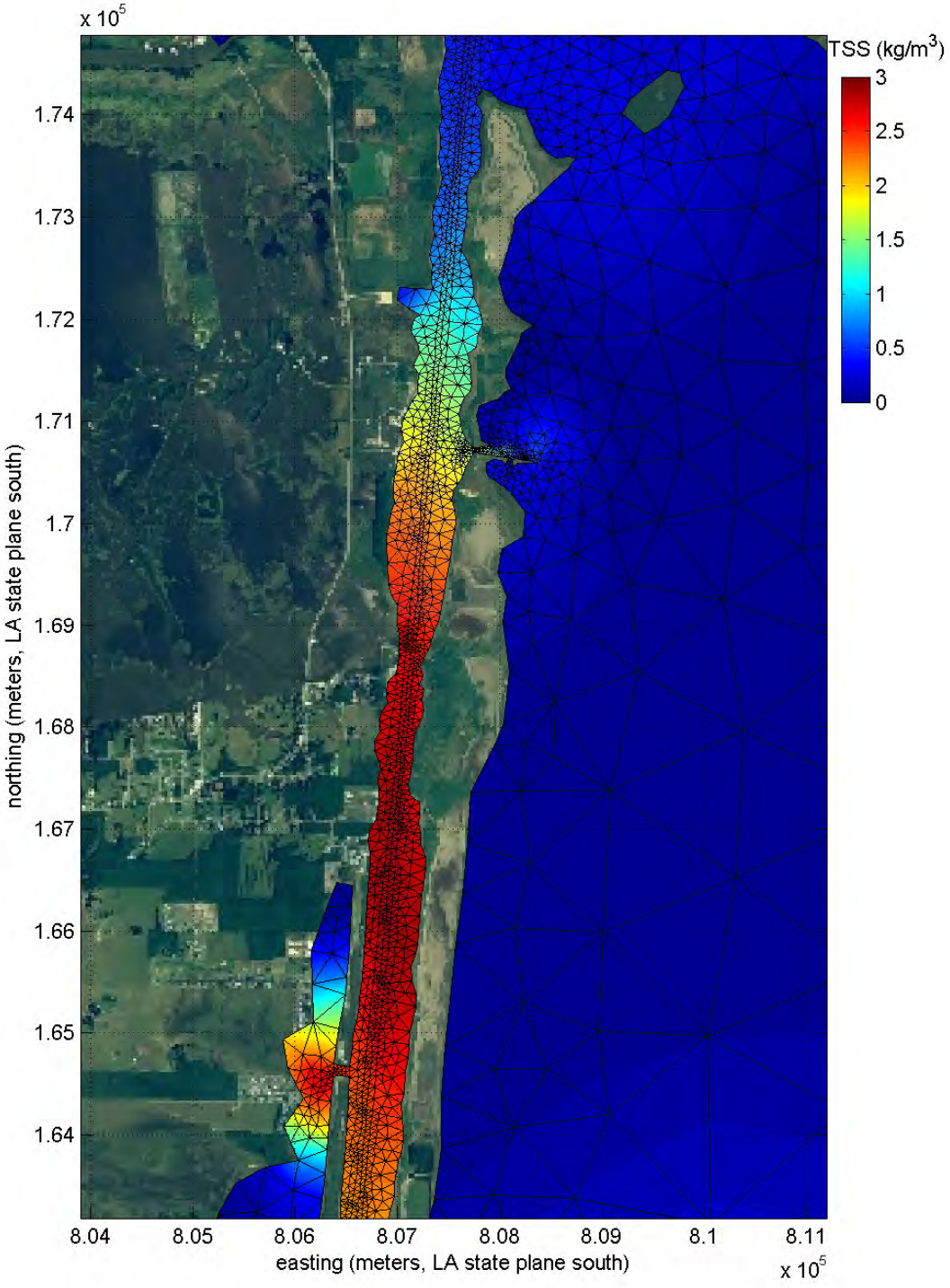

Figure V-14. Total suspended solids (TSS) in the upper CSC (miles 13.5 to 20) computed for a single model time step, representative of maximum flood tide excursion.

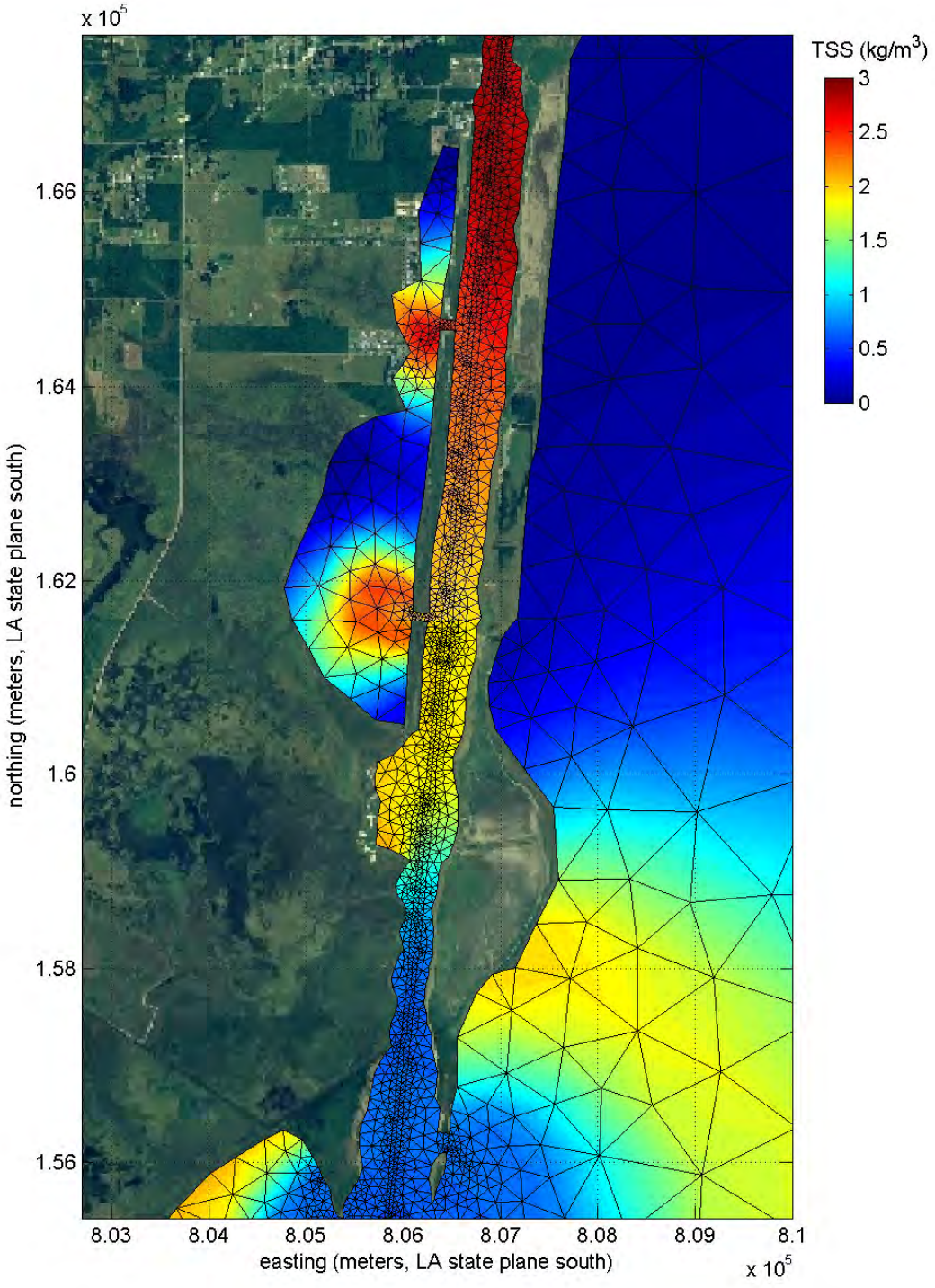

Figure V-15. Total suspended solids (TSS) in the lower CSC (miles 9 to 16) computed for a single model time step, representative of maximum flood tide excursion.

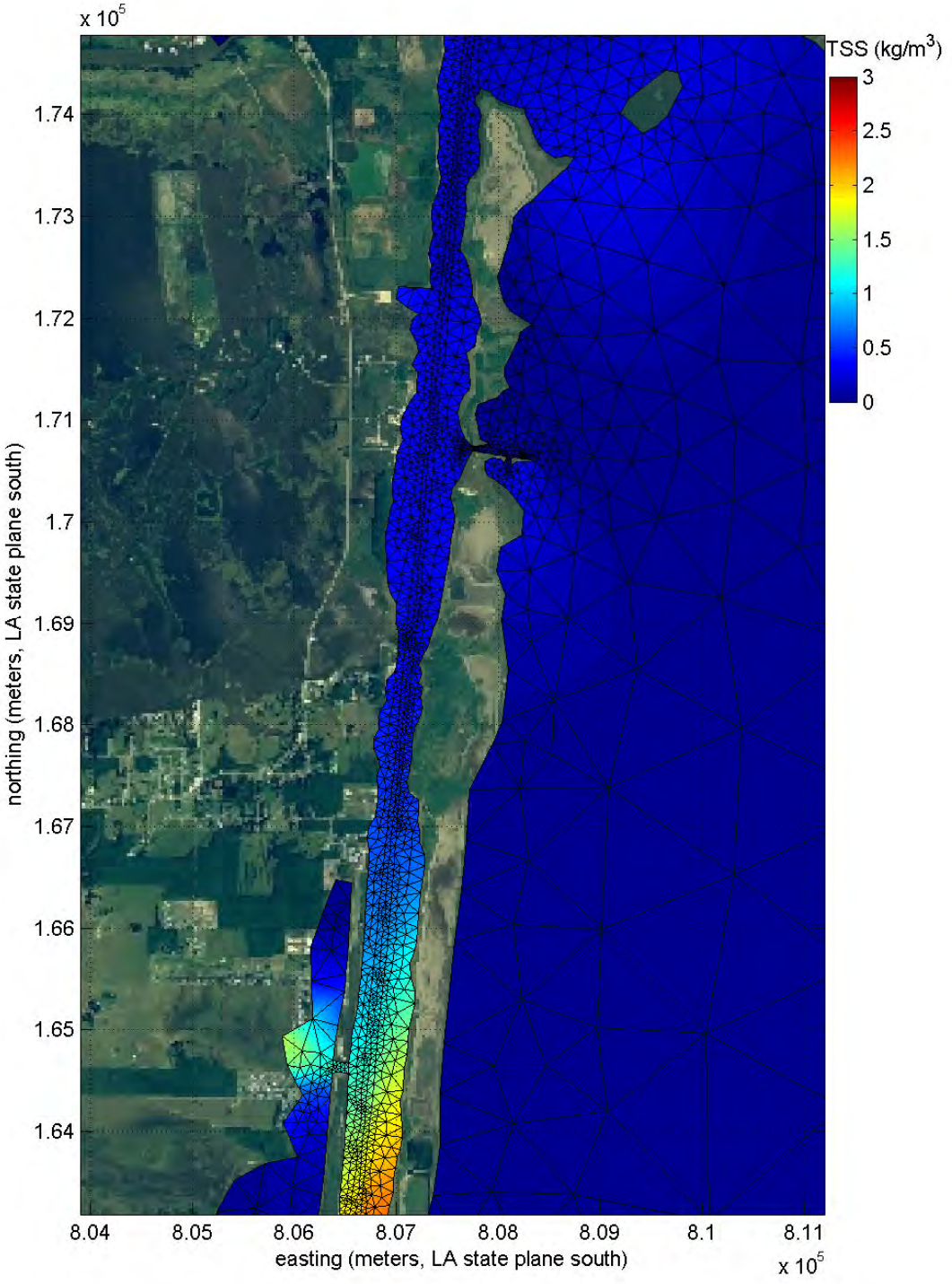

Figure V-16. Total suspended solids (TSS) in the upper CSC (miles 13.5 to 20) computed for a single model time step, representative of maximum ebb tide excursion.

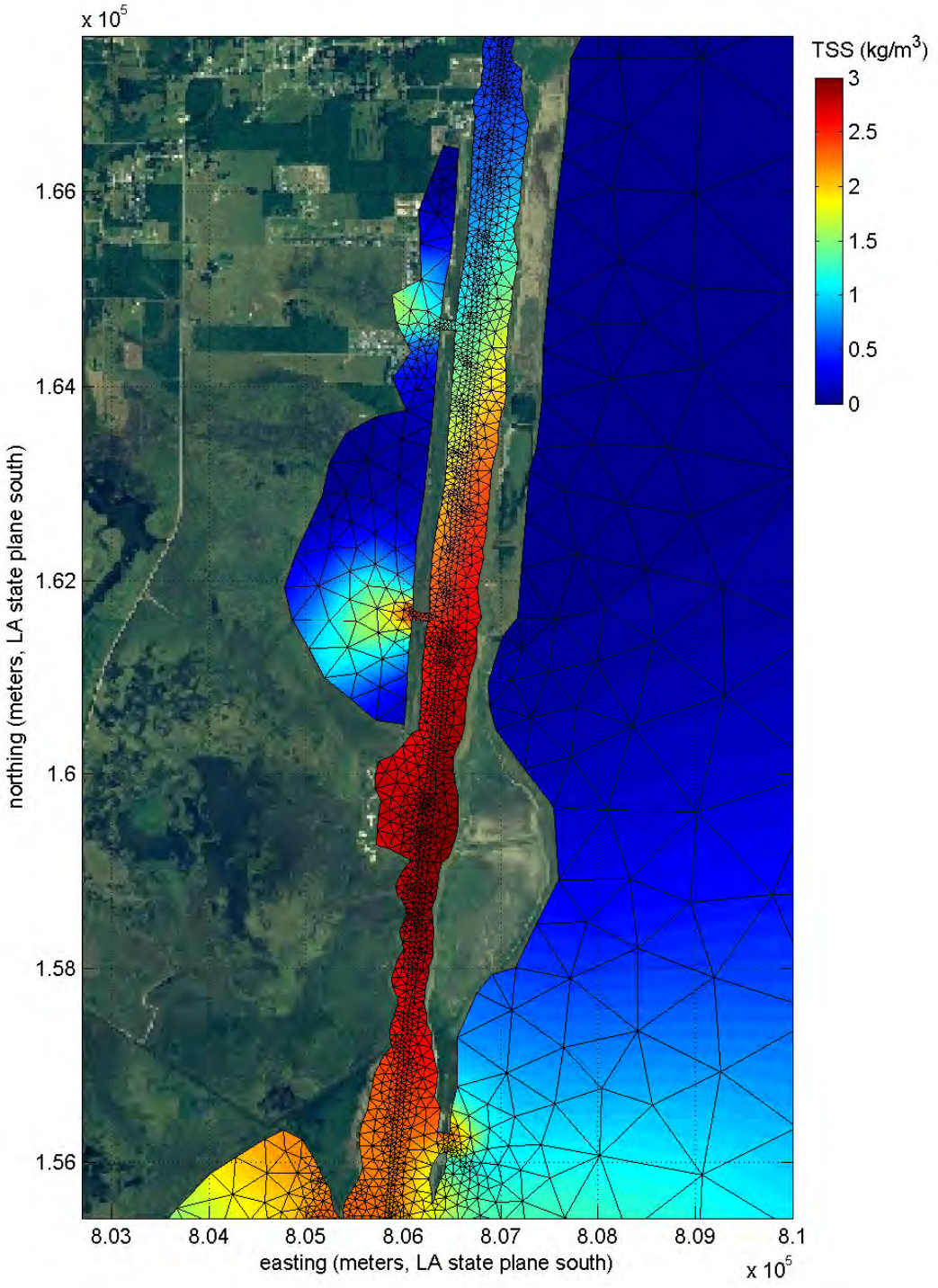

Figure V-17. Total suspended solids (TSS) in the lower CSC (miles 9 to 16) computed for a single model time step, representative of maximum ebb tide excursion.

V.4.3 Bed Change

Bed change output from the model shows the overall difference in bathymetry created by the modeled erosion and accretion of all the separate sediment fractions. Since this type of model results is directly dependent on the duration of the modeled time period, it is more instructive to focus on trends, rather than actual quantities of material eroded or accreted over the domain. As developed, the sediment transport model quantifies bed change trends within the confined portion of the CSC (Mile Markers 9 to 20) to the level needed for alternatives analyses associated with future ship channel improvements and/or expansion of Confined Disposal Facilities (CDFs).

Without detailed bathymetric change measurements over a relatively short time period, it is not possible to accurately calibrate a numerical model of sediment transport and bed change. However, a comparison of modeled bed change to historic dredging volumes can provide confidence that the model is accurately depicting sediment transport pathways and erosion/accretion trends within the model domain. The overall modeled bed change as computed during a four-tidal cycle (49.7 hour) period at the end of the total eight-day simulation period is shown in Figure V-18. As noted above, the results are provided in a semi-quantitative manner, since actual bed change is dependent on the duration of the model run. Results illustrate areas of both erosion and deposition, where the relative magnitude of these changes is represented by color shading as shown on the figure. Comparison of the model results to Figure V-2 indicates that the model is accurately predicting accretion trends within the primary area of interest for this analysis, i.e. the confined portion of the CSC between Mile Markers 9 and 20. For this stretch of the CSC, recent historic dredging records indicate that the region requiring the most maintenance dredging is between Mile Markers 12 and 16 (Figure V-2). This region correlates to the area that shows a steep temporal gradient in TSS (Figures V-14 and V-17) as well as an area characterized as “higher deposition” by the modeled bed change. Similar to the dredging records, the modeled bed change also indicates relatively lower deposition rates toward both the southern and northern limits of this confined CSC section. This ability of the mud model to predict bed change characteristics similar to observed bed change provides confidence that the model can be utilized to assess existing trends in sediment transport, as well as potential future trends associated with navigation channel improvements and/or modification of the CDFs.

Although the primary area of interest for the modeling effort is the confined portion of the CSC described above, it is important to recognize that the Lake Calcasieu estuarine system is complex and sediment transport patterns are dominated by different forcing mechanisms within each unique part of the overall system. Based on the morphological structure of the Lake Calcasieu system, the estuary can be clearly classified as wave-dominated. The strong tidal currents through the main entrance channel combined with the rapid attenuation of tide range across the barrier beach and chenier plain demonstrate a rapid reduction in tidal energy between the Gulf and Lake Calcasieu. Moreover, the long narrow entrance channel prevents wave energy from entering the estuary from the Gulf. This narrow channel characterized by relatively high tidal velocities is capable of transporting sand-sized material from the barrier beach system and nearshore areas into the estuary. As shown in Figure V-4, the material south of Mile Marker 9 is at least 20% sand and this increases to near 80% at Mile Marker 6. Since the fine-grained sediment transport model selected for this study has limited capabilities for simulating movement of coarse-grained sediments (e.g. bed load transport), the poor correlation between dredged volumes and modeled bed change in the lower portion of the CSC (Mile Markers 5 to 9) was expected.

Bottom sediment variability also is indicative of the change in morphology between the confined portion of the CSC (from Mile Marker 9 to 20) and the remaining portion of the CSC to the north. According to the data summarized in Figures V-4 and V-5, the clay fraction begins to dominate the bottom sediments north of Mile Marker 20. This region represents the confluence of both the west and east sections of the GIWW, the confined portion of the CSC, the northern reaches of Lake Calcasieu, and the Calcasieu River. Due to the complex morphology, as well as the numerous potential sources of sediment influx, it was not possible to accurately simulate deposition within this region. The more riverine morphology of this area suggests that episodic freshwater inflow events likely are a major source of sediments requiring maintenance dredging in this region. As developed, the existing mud transport model was developed for average tidal and freshwater inflow conditions, with boundary TSS levels based upon regional average conditions. However, the model can be utilized in the future to simulate deposition processes in this region by developing data sets that would include TSS measurements within all major tributaries into the system during significant freshwater inflow events.

Regardless of the model limitations within the southern and northern reaches of the system, the model can be utilized to adequately simulate the erosion and deposition of bottom sediments within the confined portion of the CSC. As shown in Figures V-19 and V-20, most of the western channel margins and a significant portion of the eastern margins of the channel experience net erosion. For areas where the entire channel width is relatively narrow, current velocities and the associated bottom shear stress along the flanks of the channel increase, leading to higher erosion rates at these locations. Profiles 1 and 5 shown in Figure V-21 illustrate these characteristics. For other portions of the CSC, the navigation channel runs close to the west bank, causing larger tidal velocities in the shallows along the west side of the CSC and the associated erosion (see Profiles 3 and 4 on Figure V-21 as examples). Profile 2 illustrates the conditions where relatively large shallow flats exist along both the east and west channel margins. For this case, the main navigation channel and the channel margins experience accretion (Figure V-19). According to the model, the entire length of the CSC in this region is highly depositional, which correlates well to the continual need for maintenance dredging of this area.

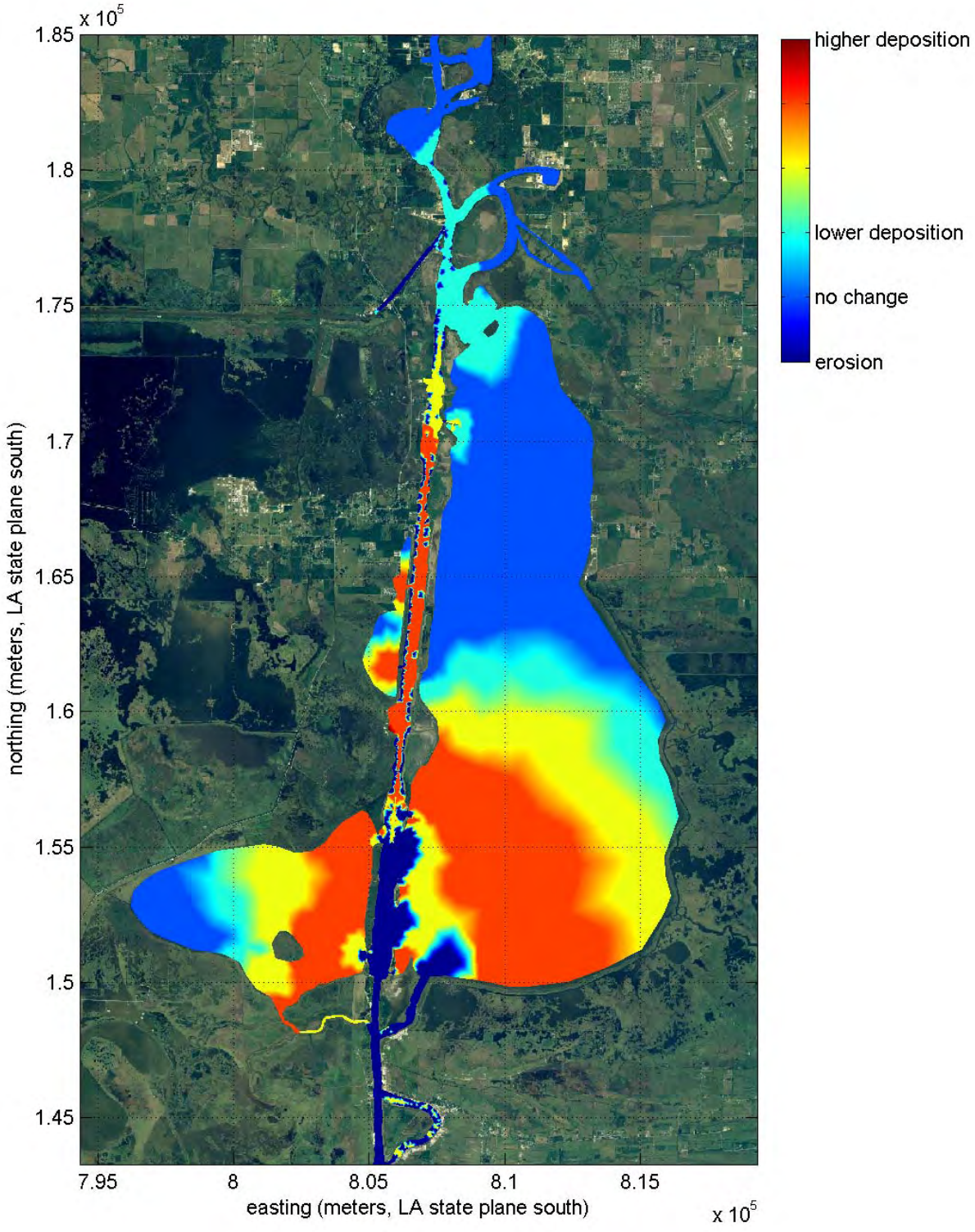

Figure V-18. Bed change potential computed from mud transport model results, showing areas of erosional and depositional potential.

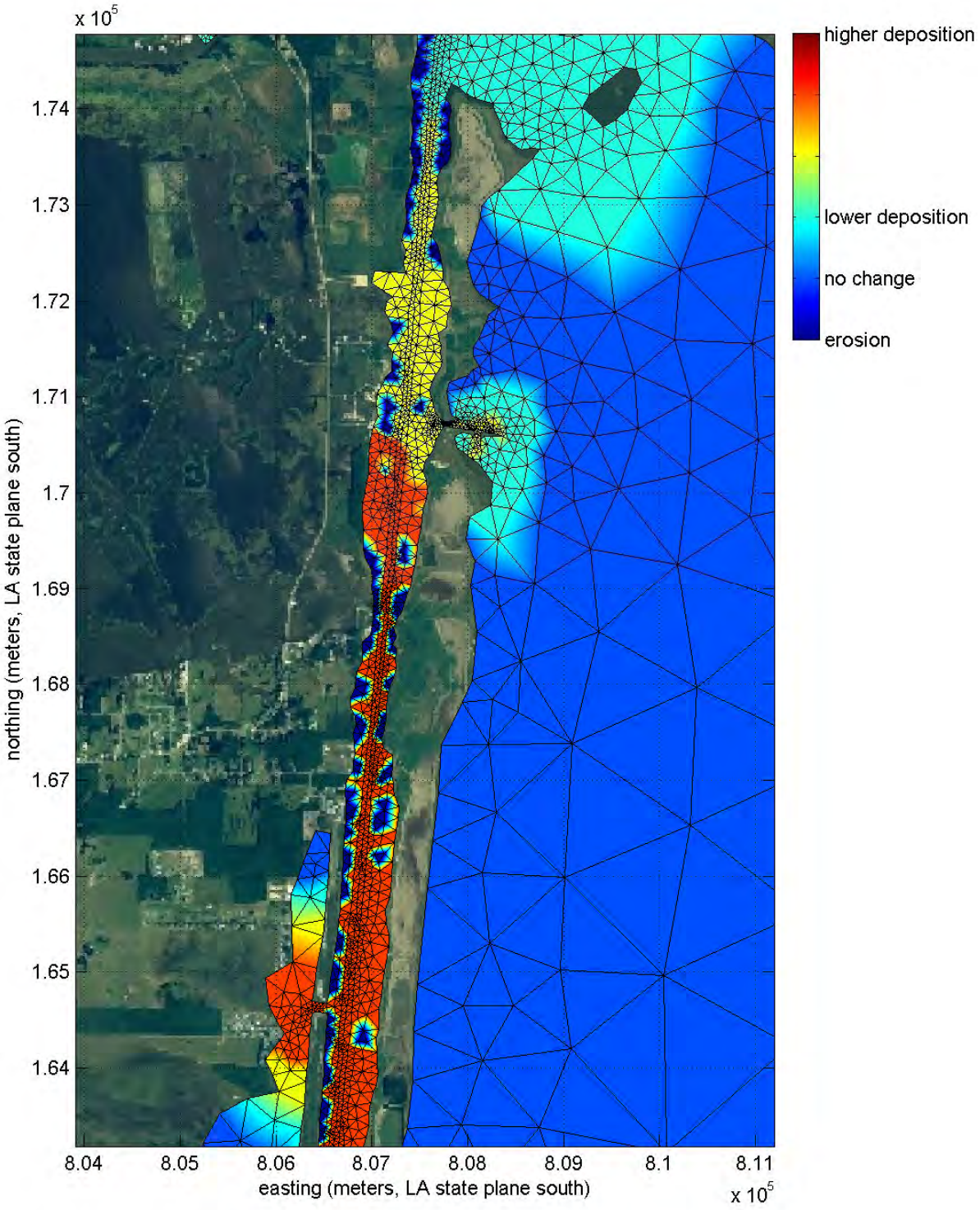

Figure V-19. Bed change potential in the upper portion of navigation channel computed from mud transport model results, showing areas of erosional and depositional potential.

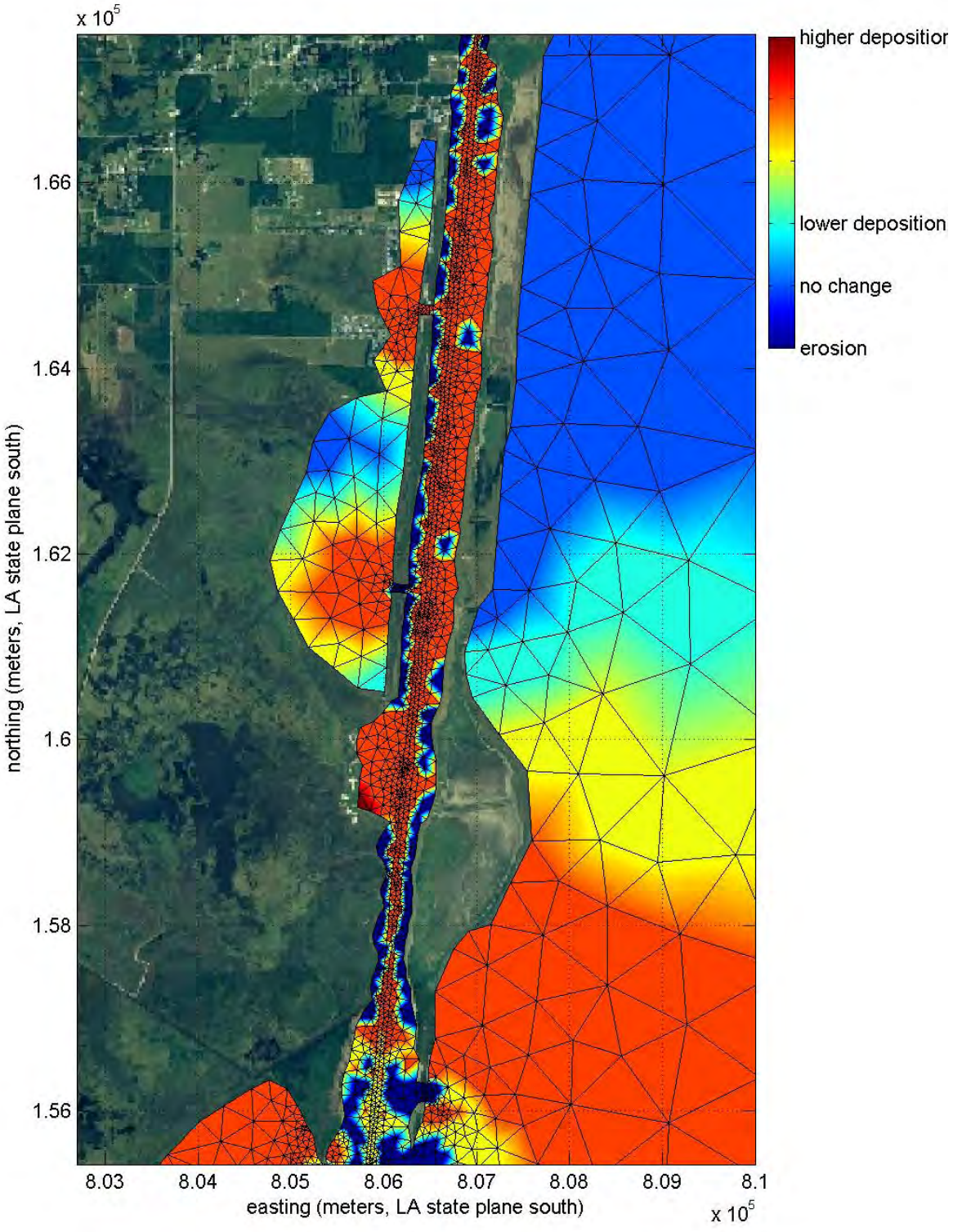

Figure V-20. Bed change potential in the lower portion of navigation channel computed from mud transport model results, showing areas of erosional and depositional potential.

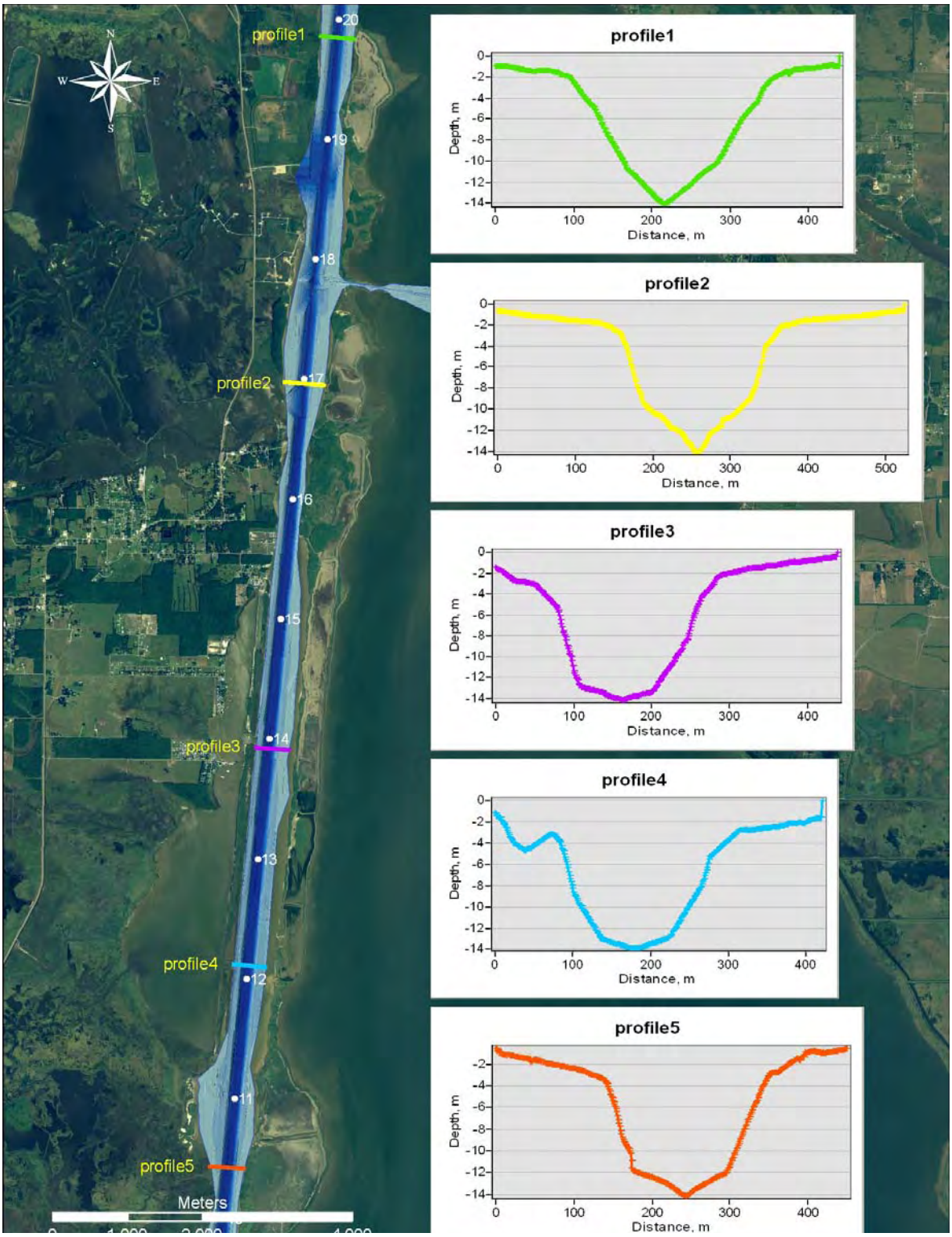

Figure V-21. Surveyed cross-sections at selected locations with the confined portion of the CSC.

VI. INFLUENCE OF VESSEL PASSAGE ON SEDIMENT SUSPENSION

The passage of a deep-draft vessel moving in a narrow waterway can have a significant hydrodynamic impact. Specifically, the draw-down and associated return flow velocities are a first order concern when discussing the suspension of sediments along the channel margins. In an effort to quantify this effect, the current work included a field deployment within the Lake Calcasieu shipping channel. Details on the field deployment and results are presented below.

VI.1 DATA COLLECTION

The Calcasieu shipping channel joins the Gulf of Mexico with the industrial facilities bordering Lake Calcasieu, Louisiana. Tankers, freighters, and other large vessels traverse this waterway daily, and during passage create hydrodynamic responses within the channel which affect local sediment transport. Observations of vessel passage events in the Calcasieu shipping channel were made from December 19, 2006 to January 9, 2007.

Data acquisition systems were installed at two (2) locations in the Calcasieu shipping channel (Figure VI-1). The channel runs in the north-south direction: north is the inbound direction, south the outbound direction. One system was installed at channel Marker 85, north of Hackberry, Louisiana. The second system was installed against channel Marker 69, approximately 8 nautical miles south of Marker 85. These channel markers were located on the western side of the shipping channel in relatively shallow water. Data were acquired using a Nortek Acoustic Wave and Current profiler (AWAC).

The Nortel AWAC measures surface elevation, water velocity, pressure, as well as echo amplitude. Echo amplitude provides a relative indication of the loudness of the received acoustic echoes reflected back from the water column and is an indicator of the relative volume of sound scatterers (such as suspended sediment) present in the ensonified water volume.

The AWACs were fixed to the channel marker pilings along the edge of the shipping channel. A specially-designed bracket offset the AWAC about 1 meter (horizontally) from the piling and assured an upward orientation. The AWACs were installed nominally 3.4 meters below the water surface (Figure VI-2). The water depth at each site was approximately 4 meters, meaning the AWACs were located about 60 cm (2 feet) above the channel bed. The 1-meter offset distance also mitigated flow disturbance due to the proximity of the piling.

The AWACs were programmed to burst sample every 20 minutes. This burst sample consisted of 2048 samples (at 2 Hz) for water velocity, and 4096 samples (at 4 Hz) of surface track. Burst samples began 2 minutes into each 20-minute window, continuing for 1024 seconds (17 minutes 4 seconds), followed by a sleep period of 56 seconds. The first 120 seconds of the 20-minute sample window were used to average current profiles and mean pressure.

Approximately 5 valid bins were measured during each 20-minute velocity profile ensemble. Average velocity profiles had a vertical resolution of 0.5 meters, with the first profile measurement centered 0.9 meters above the instrument and the final profile bin centered approximately 2.9 meters above the sensor. These bins were fixed, independent of water level at the time of measurement.

Figure VI-1. Location of the two Nortek Acoustic Wave and Current profiler (AWAC) deployment locations.

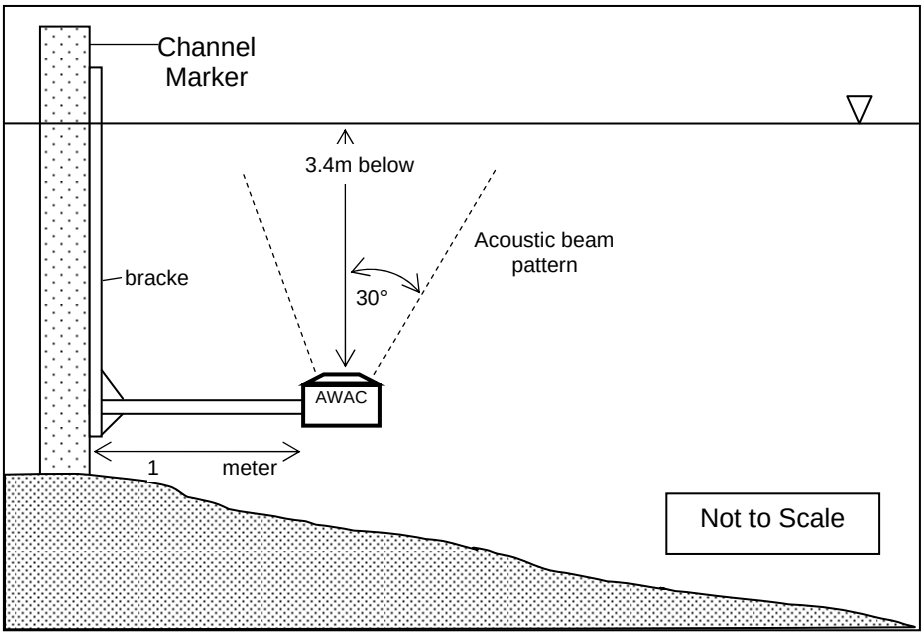

Figure VI-2. Schematic of AWAC mounting relative to channel marker piling. AWAC was mounted approximately 3.4 meters below the surface, and offset 1 meter from the piling.

In contrast to the averaged data, the high-frequency burst velocity and echo amplitude samples were obtained over a single bin, or depth interval, above the instrument. The precise location of this bin varied from burst to burst due to changes in tide (elevation), relying on the preceding pressure average to locate the bin as optimally as possible. The bin length was fixed at 0.96 meters; the center of the bin was generally 2 meters below the sea surface. Therefore the resulting velocity and echo amplitude for each burst should be considered representative of average conditions between 1.5 meters to 2.5 meters below the mean sea surface (generally mid-depth).

VI.2 CURRENT OBSERVATIONS

Current profiles were obtained every 20 minutes, each measurement resulting from a 2-minute average. This averaging interval was sufficient to assure short-term events, such as the passing of lighter water craft or fishing vessels, would have no effect on the profiles. The passage of larger vessels, if occurring during the 2-minute averaging window, would affect the measurements. The averages were screened to edit wild points other spurious data. About 2.6% of the data required editing (40 samples of 1530).

Figure VI-3 presents currents observed at the northern location, Marker 85. The results represent a vertical average of the profile (i.e. all valid samples in the profile averaged together). Cross-channel (or east-west) velocities are represented in the upper graph, along-channel (or north-south) velocities in the middle, followed by surface elevation (pressure) time series. Cross-channel flows were expectedly weak. Nearly all the flow was in the along-channel direction. Flood currents are positively-valued; ebb currents are negative values.

Peak flood currents at Marker 85 were approximately 0.5 meters/second (or 1 knot). Peak ebb currents were -0.9 meters/second, or about 1.8 knots. Also evident was a low-frequency trend to the velocity time series, particularly a subtidal ebb beginning about December 28 through the end of the deployment in mid-January. This low-frequency ebb may have been

runoff of excess surface water from the surrounding watershed. Note that flow at this location was southward (i.e. always negative) from about January 5 to January 9, suggesting runoff was greater than the upstream tidal forcing. Water levels were higher than normal (above the mean) during this time.

Current and elevation variability were at diurnal time scales for much of the time, however semi-diurnal reversals were also observed, particularly when tides were small (for example, from December 26 to about December 29).

Figure VI-4 represents observations at Marker 69, located about 8 miles downstream. The format of the graphs is consistent with Figure VI-3: cross-channel velocity (upper plot), along-channel velocity (middle), and surface elevation (lower plot). Currents and water elevation at this location were similar to those obtained upstream; however, a few subtle distinctions should be noted. Peak flood currents were similarly 0.5 meters/second, however the peak ebb flows were weaker than those to the north, 0.6 meters/second (1.2 knots, versus 1.8 knots at Marker 85). Peak-to-peak tidal currents were also weaker in the south than the north, especially from December 30 to about January 4. These differences may be due to the relative narrowness of the channel at the two locations, as well as potential storage effects of Lake Calcasieu, which is located between the two measurement stations.

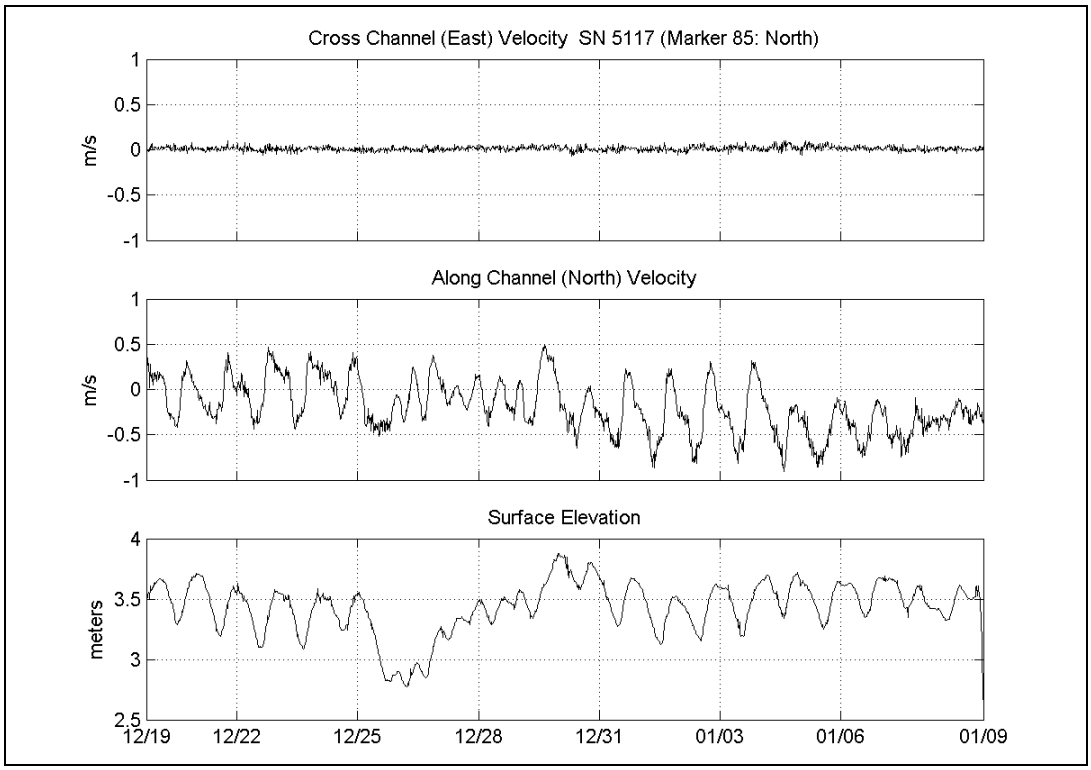

Figure VI-3. Averaged velocity and surface elevation time series at channel Marker 85.

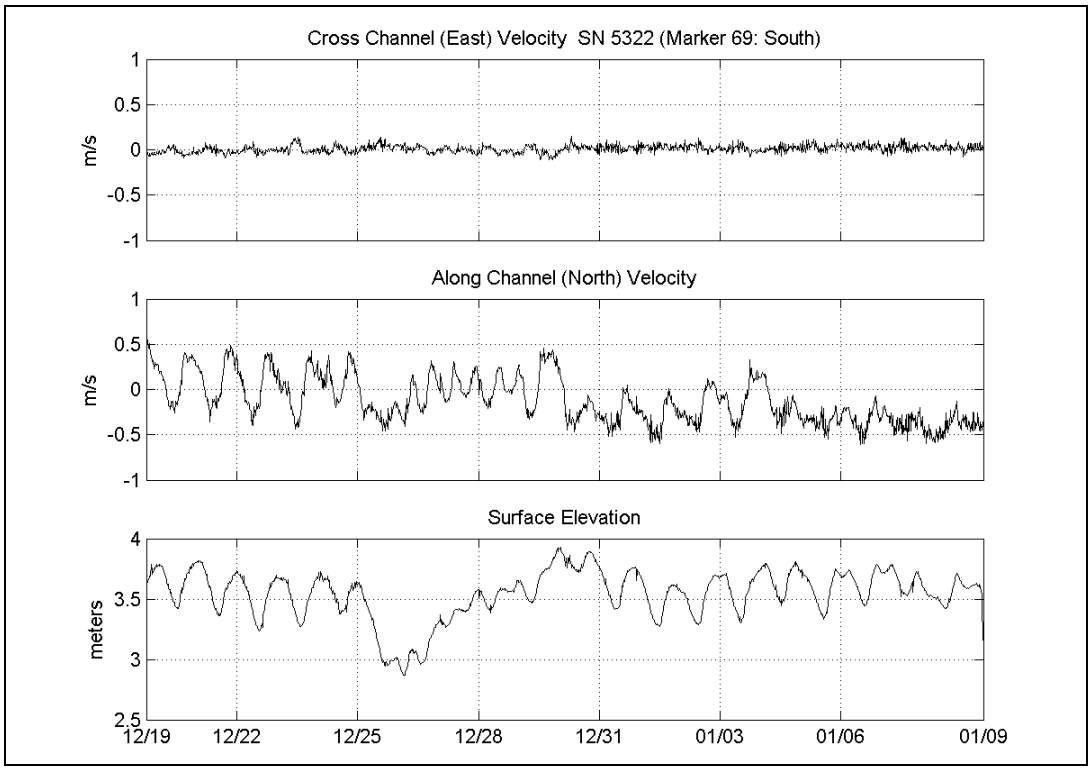

Figure VI-4. Averaged velocity and surface elevation time series at channel Marker 69.

VI.3 HYDRODYNAMIC RESPONSE TO VESSEL PASSAGE

The AWACs were programmed to burst sample every 20 minutes, i.e. record data rapidly for a finite time period. Surface elevation, pressure, velocity, and echo amplitude data were recorded during each 1024-second burst. Surface elevation (AST) was sampled at 4 Hz; all other parameters were recorded at 2 Hz. These data provide high-resolution observations of the effects of vessel passage.

A total of 1530 bursts were recorded, a majority of the bursts showed no significant events or unusual signals. The passage of large vessels possessed clear characteristics however: a significant drawdown of the surface elevation, as much as 1 meter, as well as a corresponding flow surge at the channel edge, as much as 2 meters/second (4 knots) at the peak. In addition, echo amplitude counts increased significantly at times, indicating higher levels of sound scatterers (such as suspended sediment) were present. Time scales of these events were of order 1-2 minutes. These characteristics were used to develop a screening procedure to identify vessel passage events.

Visual observations noted during the system installation, during the passage of a large tanker, indicated the maximum drawdown occurred just prior to the vessel passing the channel marker. This is the only indication of the precise timing of peak drawdown and velocity surge at the channel marker relative to vessel position in the channel.

It should be noted that surface waves generated by the vessel wake were found to be a lower order effect. There was no evidence in the data of consistent surface waves generated during (large) vessel passages. The slow rate of passage (6-8 kts) limits wake, unlike fast

ferries or other higher-speed watercraft. Surface waves were therefore neglected from subsequent analysis.

Initial filtering of the data yielded 161 unique events. This initial list of potential events at both sites was further refined to remove bursts that may have passed the initial screen but were obviously not associated with vessel passages. This screening was manual, and somewhat subjective, based on quality of the burst data as well as consistency with more obvious (intuitive) vessel passage events. For example, it was found that when a small vessel tied up near the channel marker, the acoustic surface track data would be extremely noisy (reflections from the boat hull), increasing signal variance and limiting the effectiveness of the low-pass filter processing. Further, other events were discarded if the vessel passage occurred at the beginning or end of a burst, indicating an incomplete record of the event. These manual screen procedures reduced the number of events to 137.

Further refinement was performed to pair events between locations so direct comparison of the hydrodynamic response for a specific vessel might be possible. Events at channel Marker 85 (to the north) site were matched to events at Marker 69 (south) using arrival time windows and common attributes such as the magnitude of the water elevation drawdown and the direction of the resulting velocity surge. Events included in previous screens but not included in the final matched list were discarded because there appeared to be no single obvious match or multiple possible matches. A total of 84 events (42 events per location) were found to match with reasonable confidence. This list of paired events (or bursts) is presented as Table VI-1.

The most useful indictor was the precise time of each event, which allowed estimates of the possible arrival window at the next (upstream or downstream) location. Vessel speed was calculated simply as the distance between locations divided by the travel time, specifically the difference of arrival times at each location. The arrival time at each location was determined as the time of peak drawdown or, similarly, the time of peak velocity surge. The time of peak surge and peak drawdown were effectively in phase, occurring within +/- 10 seconds of one another for most events. The typical vessel speed was order 6-8 knots. Vessel direction was estimated using the time of arrival at each location, and denoted as inbound (northerly) or outbound (southerly).

For each event listed in Table VI-1, an accompanying figure is presented in Appendix 1. These figures present observations throughout the complete burst; the upper plots represent channel Marker 85 (north) and the lower figure represents channel Marker 69 (south). For each location, the surface elevation (drawdown) is plotted, followed by the cross-channel (east-west) velocity surge, the along-channel (north-south) velocity surge, and finally echo amplitude time series (average of all three beams).

Statistics of these events were calculated and presented in Table VI-2. The first column of Table VI-2 (event number) corresponds to the event number of Table VI-1 for consistency. The remaining columns of VI-2 represent the peak drawdown, peak surge speed, and surge direction at each location. These parameters were relative to ambient conditions at the time. Peak drawdown refers to the reduction of surface elevation during the event, and was calculated as the mean surface elevation (from the 2-minute average value prior to the burst) minus the maximum surface depression during the event. This correctly accounts for variability of surface elevation over the 3-week deployment (refer back to Figures VI-3 and VI-4) and allows for direct comparison between events at different times. The same relative values were calculated for velocity surge, determining the peak values during the event and then subtracting

ambient flow conditions to account for differences in channel outflow and tides from burst to burst. Surge direction considered both along- and cross-channel components, and hence may or may not be strictly in the up- or down-stream direction.

Table VI-1. Matching Vessel Passage Events.

	Channel Marker 69 (South) AWAC #5322			**Channel Marker 85 (North) AWAC #5117**		
Event Number	Burst Number	Date	Start Time	Burst Number	Date	Start Time
1	100	20-Dec-2006	19:02:01	97	20-Dec-2006	18:02:01
2	139	21-Dec-2006	08:02:01	136	21-Dec-2006	07:02:01
3	174	21-Dec-2006	19:42:01	177	21-Dec-2006	20:42:01
4	192	22-Dec-2006	01:42:01	188	22-Dec-2006	00:22:01
5	197	22-Dec-2006	03:22:01	194	22-Dec-2006	02:22:01
6	246	22-Dec-2006	19:42:01	242	22-Dec-2006	18:22:01
7	252	22-Dec-2006	21:42:01	249	22-Dec-2006	20:42:01
8	258	22-Dec-2006	23:42:01	254	22-Dec-2006	22:22:01
9	260	23-Dec-2006	00:22:01	263	23-Dec-2006	01:22:01
10	276	23-Dec-2006	05:42:01	280	23-Dec-2006	07:02:01
11	277	23-Dec-2006	06:02:01	281	23-Dec-2006	07:22:01
12	334	24-Dec-2006	01:02:01	330	23-Dec-2006	23:42:01
13	405	25-Dec-2006	00:42:01	401	24-Dec-2006	23:22:01
14	496	26-Dec-2006	07:02:01	493	26-Dec-2006	06:02:01
15	550	27-Dec-2006	01:02:01	554	27-Dec-2006	02:22:01
16	551	27-Dec-2006	01:22:01	555	27-Dec-2006	02:42:01
17	620	28-Dec-2006	00:22:01	623	28-Dec-2006	01:22:01
18	640	28-Dec-2006	07:02:01	637	28-Dec-2006	06:02:01
19	715	29-Dec-2006	08:02:01	712	29-Dec-2006	07:02:01
20	800	30-Dec-2006	12:22:01	797	30-Dec-2006	11:22:01
21	803	30-Dec-2006	13:22:01	800	30-Dec-2006	12:22:01
22	846	31-Dec-2006	03:42:01	843	31-Dec-2006	02:42:01
23	873	31-Dec-2006	12:42:01	877	31-Dec-2006	14:02:01
24	874	31-Dec-2006	13:02:01	879	31-Dec-2006	14:42:01
25	927	01-Jan-2007	06:42:01	931	01-Jan-2007	08:02:01
26	957	01-Jan-2007	16:42:01	953	01-Jan-2007	15:22:01
27	993	02-Jan-2007	04:42:01	990	02-Jan-2007	03:42:01
28	1061	03-Jan-2007	03:22:01	1065	03-Jan-2007	04:42:01
29	1062	03-Jan-2007	03:42:01	1066	03-Jan-2007	05:02:01
30	1086	03-Jan-2007	11:42:01	1083	03-Jan-2007	10:42:01
31	1088	03-Jan-2007	12:22:01	1085	03-Jan-2007	11:22:01
32	1130	04-Jan-2007	02:22:01	1126	04-Jan-2007	01:02:01
33	1162	04-Jan-2007	13:02:01	1165	04-Jan-2007	14:02:01
34	1197	05-Jan-2007	00:42:01	1194	04-Jan-2007	23:42:01
35	1235	05-Jan-2007	13:22:01	1232	05-Jan-2007	12:22:01
36	1318	06-Jan-2007	17:02:01	1314	06-Jan-2007	15:42:01
37	1393	07-Jan-2007	18:02:01	1399	07-Jan-2007	20:02:01
38	1394	07-Jan-2007	18:22:01	1401	07-Jan-2007	20:42:01
39	1406	07-Jan-2007	22:22:01	1410	07-Jan-2007	23:42:01
40	1460	08-Jan-2007	16:22:01	1463	08-Jan-2007	17:22:01
41	1511	09-Jan-2007	09:22:01	1508	09-Jan-2007	08:22:01
42	1515	09-Jan-2007	10:42:01	1512	09-Jan-2007	09:42:01

Table VI-2. Vessel Passage Event Statistics.						
	Channel Marker 85 (North) AWAC #5117			**Channel Marker 69 (South) AWAC #5322**		
Event Number	Drawdown (meters)	Surge Speed (m/s)	Surge Direction (degrees)	Drawdown (meters)	Surge Speed (m/s)	Surge Direction (degrees)
1	0.43	0.70	29	0.81	1.04	38
2	0.55	0.93	8	0.87	1.01	355
3	0.37	0.65	173	0.58	0.56	270
4	0.64	1.00	21	1.04	1.33	19
5	0.49	0.92	16	0.94	1.20	28
6	0.49	0.85	27	0.81	1.15	37
7	0.41	0.71	331	0.76	0.65	16
8	0.56	0.68	20	0.92	1.06	18
9	0.49	0.70	167	0.76	0.97	163
10	0.73	1.49	165	1.29	1.85	142
11	0.65	1.38	167	1.45	2.03	139
12	0.85	1.27	38	1.10	1.30	33
13	0.54	1.29	32	0.89	1.41	30
14	0.49	0.77	19	0.79	0.87	4
15	0.85	1.31	151	1.23	1.72	144
16	0.87	1.64	150	1.20	1.87	146
17	0.56	0.88	167	0.89	1.24	143
18	0.61	0.44	237	0.86	0.91	4
19	0.48	0.24	184	0.80	0.79	6
20	0.71	0.28	168	0.77	0.32	155
21	0.44	0.22	225	0.66	0.89	349
22	0.86	1.21	22	1.05	0.35	196
23	0.59	1.12	153	1.07	1.57	143
24	0.52	1.17	167	0.82	1.26	148
25	0.78	1.20	119	0.92	0.79	130
26	0.47	0.93	9	0.96	1.22	17
27	0.94	1.36	23	1.10	1.11	10
28	1.00	1.70	134	1.57	2.00	138
29	0.73	1.04	155	1.24	1.95	140
30	0.71	0.27	166	0.97	0.21	172
31	0.65	0.20	177	0.96	0.92	244
32	0.53	1.17	19	0.87	1.25	33
33	0.31	0.42	154	0.75	0.86	156
34	0.48	1.06	9	1.14	1.56	24
35	0.61	0.43	199	0.60	0.98	162
36	0.43	0.81	253	0.65	1.03	358
37	0.51	1.07	152	1.05	1.68	137
38	0.42	1.10	163	0.87	1.42	144
39	0.83	1.39	136	1.66	2.31	129
40	0.47	0.69	162	1.04	1.20	142
41	0.70	0.94	11	1.00	0.36	161
42	0.86	1.40	32	1.04	1.24	351

The goal of the screening procedure was to match these events to specific vessel passages, in so doing match the hydrodynamic response to vessel size and speed. Copies of vessel traffic log were obtained and allowed identification of specific vessels during most events.

The vessel traffic log lists vessel name, drafts (both inbound and outbound), length, beam, and dead weight tonnage, as well as dates/times of transit past various markers. The traffic log was incomplete, however 36 events (of 42) were able to be matched to specific vessels with reasonable confidence.

Table VI-3 presents the list of vessels matched to the events of Tables VI-1 and VI-2. Table VI-3 includes also vessel speed and direction. There totaled 25 outbound passages and 17 inbound passages. Of the 36 identified vessel events, nine (9) vessels were observed during both inbound and outbound transits.

Figure VI-5 presents a graphical representation of data in Table VI-2 and Table VI-3, comparing specific characteristics for all identified events.

- The top plot shows the relative drawdown at both locations. Drawdown at Marker 69 (south) was consistently greater than drawdown at Marker 85. On average, drawdown at Marker 85 was about 60% of the drawdown at Marker 69. These differences are assumed related to the specific channel geometry at the two locations. The mean drawdown at Marker 85 (for all events) was 0.61 meters; the mean drawdown at Marker 69 was 0.97 meters. The maximum drawdown observed was 1.66 meters (event 39).
- The second plot (from the top) presents the peak velocity surge magnitude (or speed) for each event. Note the strong correlation to drawdown amplitude; surge velocities were typically greater at Marker 69 than at Marker 85. Peak velocity surge was 2.31 meters/second (4.5 knots, or 7.6 feet/second). Again, this peak surge was measured about mid-depth of the water column. Conversely, recall that the averaged ebb currents were typically weaker at Marker 69 (Figure VI-4) than those measured at Marker 85 (Figure VI-3); this fact was attributed to channel geometry also, specifically that channel width at Marker 85 was narrower and more constricted and therefore may have resulted in modest flow acceleration.
- The middle plot represents the vessel displacement for each event. Vessel displacement was calculated simply as the length*beam*draft, an approximate indicator of vessel displacement. This indicator was preferred over vessel DWT values since vessel draft differed between inbound and outbound transits (DWT neglected draft changes between inbound and outbound transits). Drawdown and surge magnitudes appeared loosely correlated to vessel size, as would be expected; however, the correlation was not perfect. Some factors influencing this correlation could be (actual) vessel speed, hull shape and drag form, distance from the channel marker during passage, or other (unknown/unmeasured) factors complicating the relationship.
- The fourth plot (from the top) represents the along-channel surge velocity component. In most cases, the along-channel components were approximately equivalent between sites (unlike speeds), suggesting that the cross-channel components of surge velocity were greater at Marker 69 than at Marker 85. Differences in channel geometry (such as channel width) may be a possible cause. In addition, southerly surges, which occur during inbound passages, appeared greater than northerly surges. Inbound (southerly) surges were of order 1.5 meters/second in contrast to outbound surges of order 1 meter/second. Recall that this surge value was corrected for mean channel flow. Potential cause for this behavior may be vessel draft: deeper draft, hence greater surge, during inbound passages when vessels were fully loaded, and shallower draft on the outbound after offloading.
- The bottom plot shows average (estimated) vessel speeds for each event. Vessel direction, either northerly (inbound) or southerly (outbound) was opposite to the along-

channel surge velocity. A northward-traveling (inbound) vessel generates a southward velocity surge along the channel edge; an outbound vessel generates a northerly surge.

Table VI-3. Vessel Specifications per Event.

Event	Vessel Name	Vessel Direction	Vessel Speed (knots)	Length (feet)	Beam (feet)	Draft (feet)	DWT (tons)
1	*(no match)*	outbound	-7.2				
2	*(no match)*	outbound	-8.0				
3	Freighter Dunlin Arrow	inbound	8.3	601	95	27	38760
4	*(no match)*	outbound	-7.4				
5	*(no match)*	outbound	-6.9				
6	Crude Ship Guardian	outbound	-6.4	798	137	28	96920
7	Freighter Dunlin Arrow	outbound	-7.7	601	95	28	38760
8	Tanker Maritime Tuntiga	outbound	-7.0	591	106	30	44508
9	Tanker NCC Riyad	inbound	8.1	601	106	30	37221
10	Crude Ship SPT Sapphire	inbound	5.9	810	138	37	96173
11	Crude Ship Cape Baker	inbound	5.8	899	164	35	164274
12	Tanker STS Tiete	outbound	-6.8	799	139	29	109773
13	Crude Ship Cape Baker	outbound	-6.6	899	164	31	164274
14	Tanker Panama Sol	outbound	-7.5	407	66	26	12756
15	Crude Ship Overseas Elaine	inbound	6.0	800	138	39	94813
16	Tanker Sea Pride 1	inbound	6.0	802	139	39	89999
17	Freighter Golden Gem	inbound	7.5	740	106	39	64619
18	*(no match)*	outbound	-7.5				
19	Tanker Seabulk Magnachem	outbound	-7.3	630	95	32	39344
20	Crude Ship Minerva Concert	outbound	-7.8	790	138	27	105817
21	Crude Ship Lochness	outbound	-7.6	811	136	29	90607
22	*(no match)*	outbound	-7.7				
23	Tanker Sea Lady	inbound	5.5	784	138	26	105611
24	Crude Ship Patriot	inbound	5.1	798	137	39	96920
25	Tanker Stena Consul	inbound	7.0	599	106	26	47171
26	Crude Ship Patriot	outbound	-6.5	798	137	28	96920
27	Tanker Sea Lady	outbound	-8.0	784	138	25	105611
28	Crude Ship Overseas Cathy	inbound	6.5	821	144	36	111928
29	Tanker Cape Bari	inbound	6.1	899	157	31	159186
30	Crude Constitution	outbound	-7.8	799	138	28	104624
31	Tanker Stena Consul	outbound	-8.0	599	106	33	47171
32	Freighter Ventico B	outbound	-5.8	737	106	40	61345
33	Freighter Topflite	inbound	7.6	623	106	19	52544
34	Tanker Cape Bari	outbound	-7.5	899	157	30	159186
35	Crude Ship Overseas Cathy	outbound	-8.1	821	144	28	111928
36	LNG Edo	outbound	-6.8	936	143	34	93619
37	Crude Ship Desh Prem	inbound	4.4	800	138	39	114600
38	Crude Ship Heidmar Sabine	inbound	3.6	785	122	37	78655
39	LNG Seri Anggun	inbound	6.1	928	142	37	67800
40	Tanker New River	inbound	7.0	660	90	22	39482
41	Crude Ship Desh Prem	outbound	-8.0	800	138	29	114600
42	LNG Seri Anggun	outbound	-7.1	928	142	34	67800

The data show clear differences between wake-related motions at the two measurement locations, particularly in the magnitude of the elevation drawdown and corresponding velocity surge. These differences can likely be attributed to differences in site-specific geometry such as channel width, (possibly) shoreline curvature or bottom topography. It would be instructive to investigate more completely the local channel geometries, or perhaps other factors, at these two particular locations to identify possible causes why velocities at Marker 69 were greater than those observed at Marker 85. A starting point for this evaluation might be to obtain recent high-resolution bathymetric survey data (if available).

Peak velocities did not appear to result from wave forms generated by the bow, secondary or tertiary wakes following vessel passage. Further, inspection of burst data during events when there was no vessel-related velocity surges showed ambient wind-driven wave energy was negligible (expected for a confined channel).

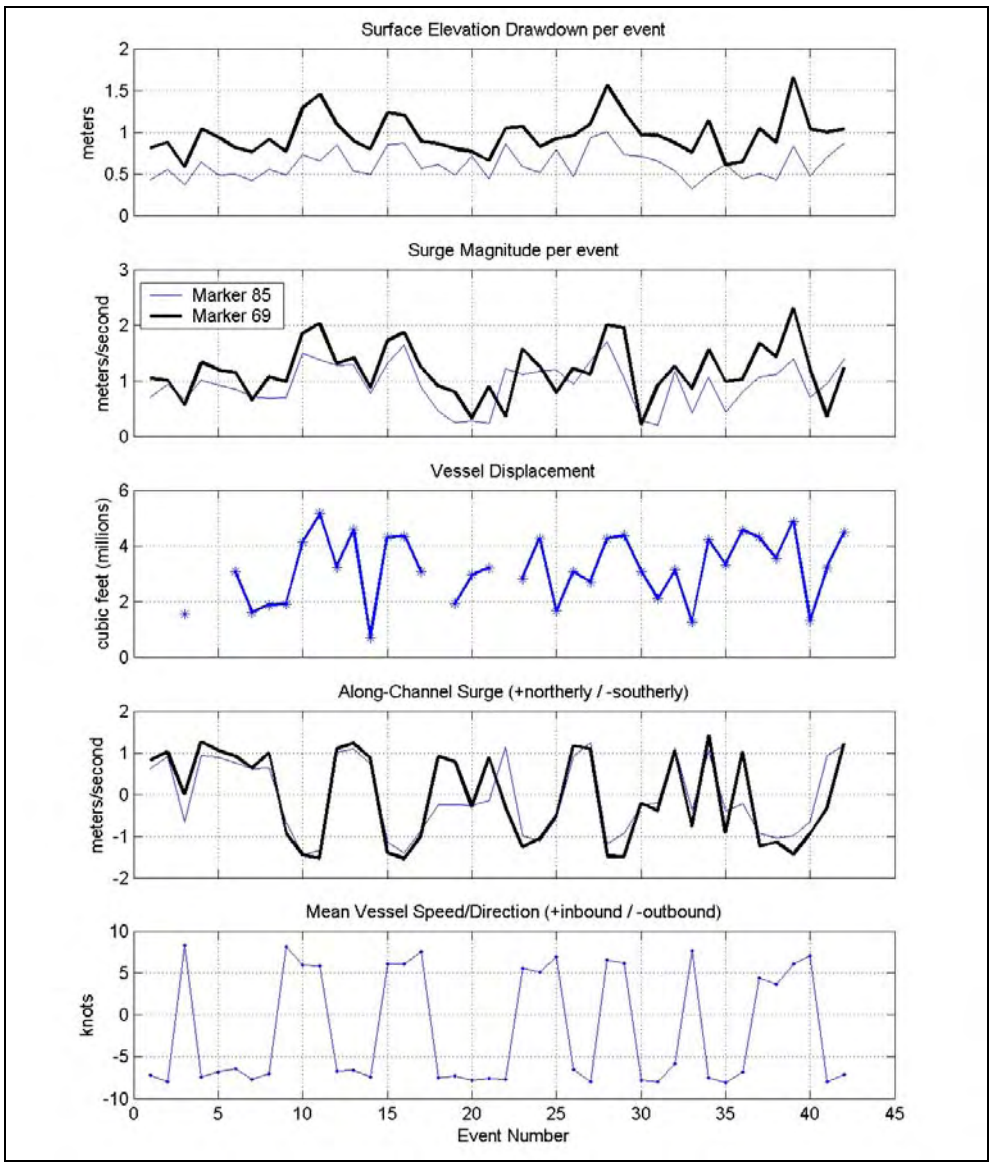

Figure VI-5. Events statistics at channel Marker 85 (north) and channel Marker 69 (south). Marker 85 event values are shown in the light line; Marker 69 values shown as the heavy line.

Figures VI-6 and VI-7 show plots of vessel size versus drawdown and maximum surge velocity, respectively, where vessel size is estimated as vessel length x beam x draft. While there is a general trend that drawdown and velocities increase with increasing vessel size, there is significant scatter within the data. This suggests that other variables such as vessel speed, draft, and hull characteristics may also play important roles in defining the hydrodynamic response during vessel passage. In addition, surge velocities were generally larger at Channel Marker 69 (south) than at Channel Marker 85 (north), likely due to the more constrained morphology of the channel system at the southerly location.

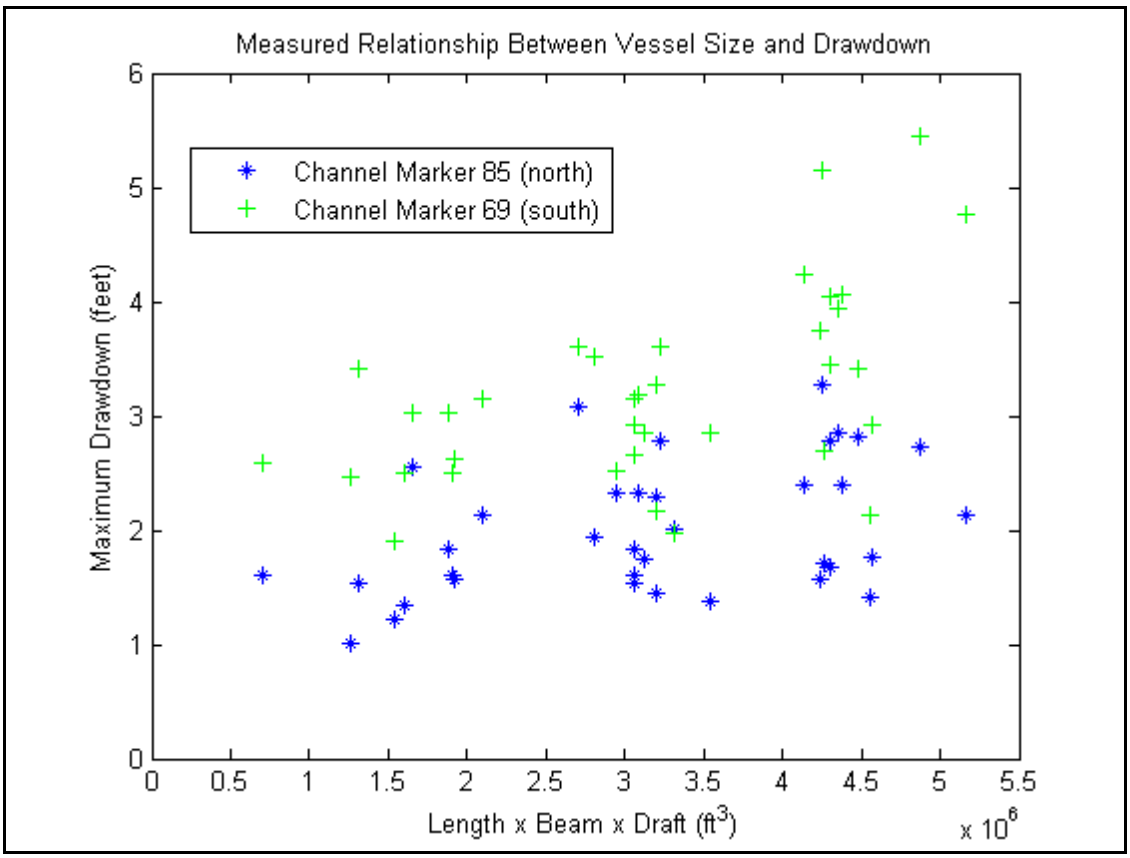

Figure VI-6. Maximum measured drawdown versus vessel size (length x beam x draft).

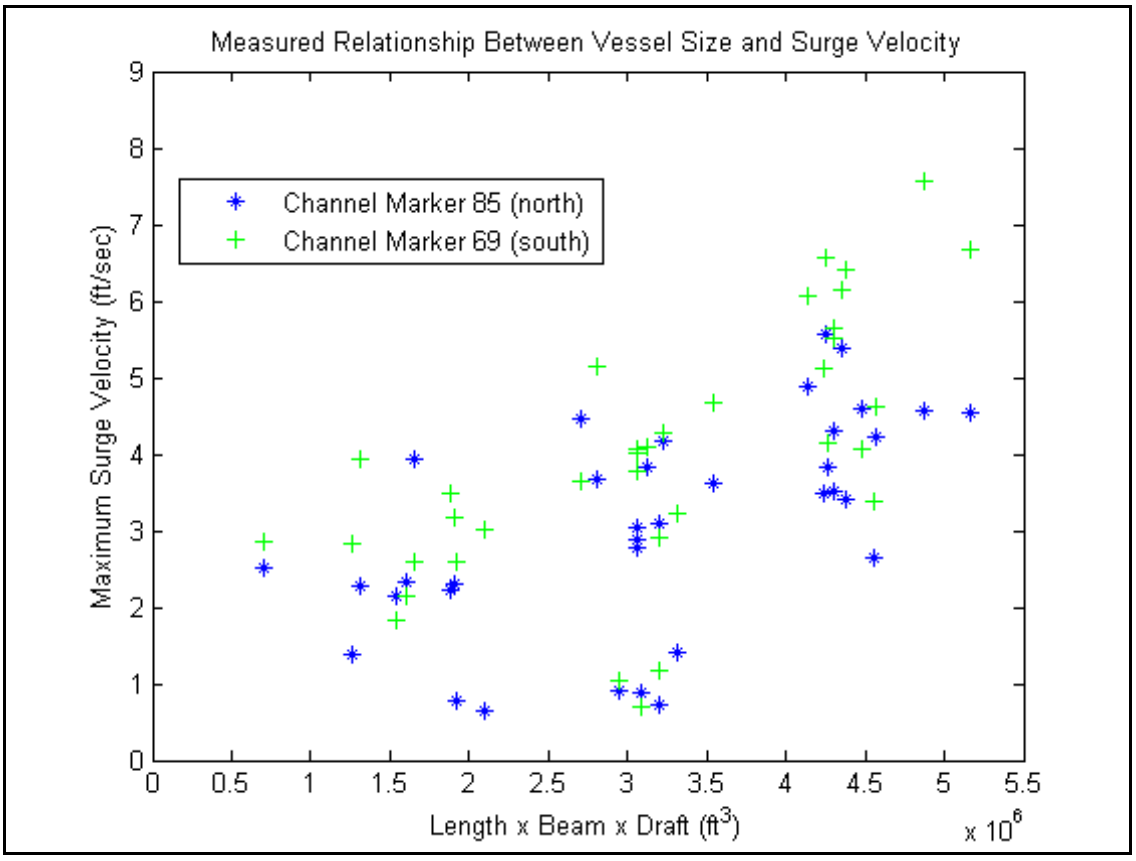

Figure VI-7. Maximum measured velocity versus vessel size (length x beam x draft).

VI.4 SEDIMENT SUSPENSION

The echo amplitude data show that the surge events (at times) caused increases in the volume of acoustic scatterers, which can be reasonably interpreted as increases in suspended sediment. Since the potential for sediment transport increases relative to water velocity magnitude, the data presented in this report suggests events triggering sediment suspension in the Calcasieu shipping channel were correlated primarily to direct water displacements during vessel passages.

Sediment suspension during vessel passage is in keeping with observations made during field work described in Ravens, 2007. This work set out to make field measurements of sediment erodibility in Lake Calcasieu correlating flow rates at the bed and measured turbidity. It was noted in the report that their testing was made difficult due to the passage of ships which resulted in sediment suspension and increased levels of background turbidity.

To quantify the impact of vessel passage on sediment suspension, the peak velocities from each event were used to calculate shear stress at the channel banks. The shear stress (τ) is calculated as

$$\tau = \tfrac{1}{2} C_f \rho V^2$$

where C_f is a friction coefficient, ρ is the water density and V is the maximum surge velocity. Maynord (2005) suggests a C_f value of 0.01 for calculating bed shear stress during a

drawdown/return flow event such as the ones measured in this work. This value is higher than what is typically used for open channel flow calculations so that the effects of the rapid acceleration and developing boundary layer are approximated.

Both Ravens (2007) and Maynord (2005) determined that a shear stress of 0.5 Pa is the appropriate critical shear stress for the initiation of sediment suspension, based upon bottom sediment characteristics. Ravens (2007) was concerned directly with Lake Calcasieu while Maynord (2005) was working in the nearby Sabine/Neches Waterway in Texas. The similarity in critical shear stress estimates in both investigations offer some confidence of the value used here. A plot of shear stress from the measured events is shown below in Figure VI-8

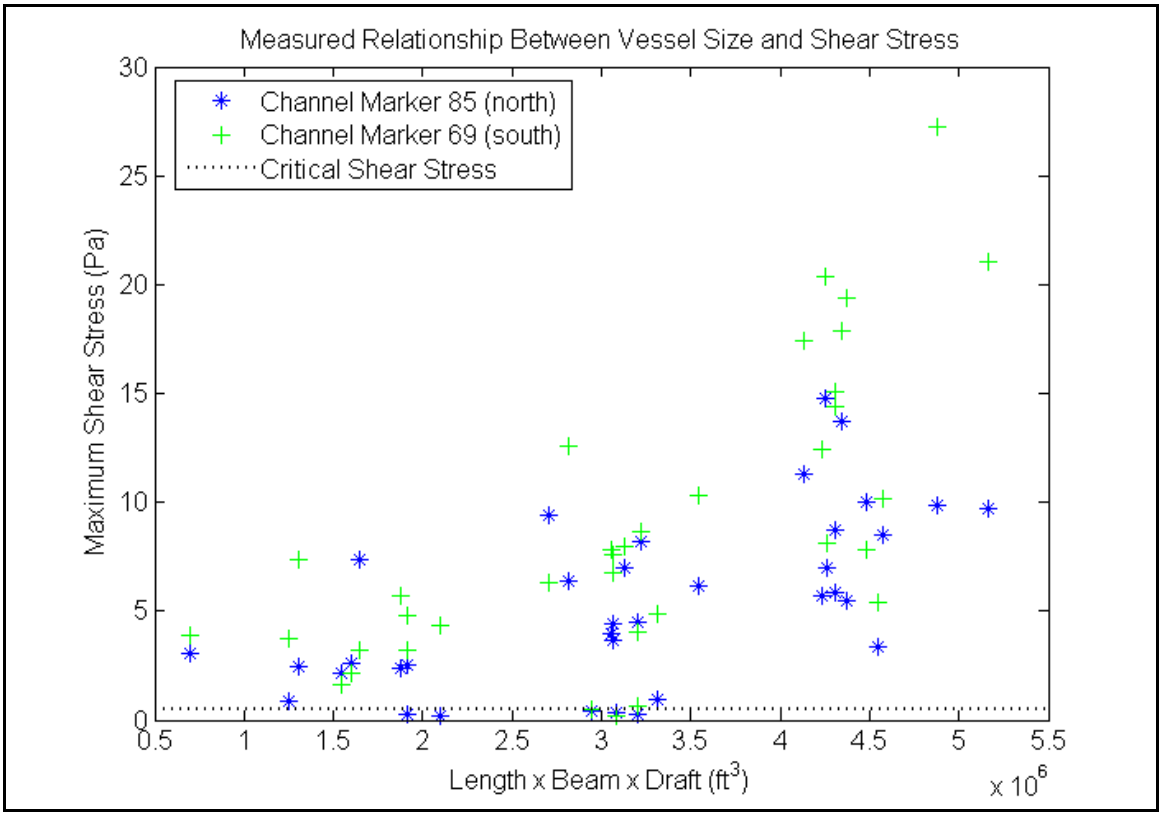

Figure VI-8. Maximum calculated shear stress versus vessel size (length x beam x draft).

The critical shear stress value of 0.5 Pa is plotted at the bottom of the figure as a dotted line. It can be seen that a majority of the data falls above this threshold, with most events registering between 2-10 Pa. In total, 92% of measured events exceeded the shear stress required to initiate sediment movement.

From these calculations, together with the anecdotal information from the field deployment relating to this work and also described in Ravens (2007), it can be seen that vessel traffic in the Calcasieu Ship Channel is a major cause of sediment re-suspension.

VII. EVALUATION OF PROPOSED DMMP ALTERNATIVES

During the development of the Dredged Material Management Plan (DMMP) a number of modifications to the existing Calcasieu system were proposed that would stabilize eroding shorelines along the Calcasieu Ship Channel (CSC) and enlarge existing dredge disposal areas along the CSC. The modifications were grouped together into a single alternative to be examined within the hydrodynamic and sediment transport models to determine changes that would occur to the tidal flow regime and the associated affects on sediment transport. A brief description of each modification is below, detailed descriptions and drawings of the proposed modifications to the system are presented within the DMMP.

Modifications included in Alternative 1:

- Rock dike along the eastern side of the Calcasieu Ship Channel from approximate river mile 11 to 16. The toe of the proposed rock dike is seaward of the existing shoreline.

- Stone rock dike along Dredge Disposal Site H which is located from approximately river mile 8.5 to 9.5. The dike is on western side of the Calcasieu Ship Channel.

- Expansion of the backside of Dredge Disposal Site 17 into Lake Calcasieu and rock dike along western side of the Calcasieu Ship Channel from approximately river mile 18.5 to 20.

- Expansion of Dredge Disposal Sites D and E into Lake Calcasieu from approximately river mile 11.5 to 16.

VII.1 MODEL SETUP

The finite element mesh generated for the existing conditions hydraulic and sediment transport models was modified to include proposed modifications. Preliminary engineering drawings for modifications, provided by Gahagan & Bryant, Inc. (GBA), were converted into line files and imported into MIKE Zero to generate the modified finite element mesh. A few sections of the existing grid were refined to provide a smooth transition of elements around the modified sections of the Calcasieu system. Otherwise, the grid specifications for the system were identical to those used in the existing conditions mesh. The final finite element grid for Alternative 1 is shown in Figures VII-1 to VII-3. Figure VII-4 shows the interpolated grid bathymetry on the modified mesh.

The boundary conditions for the hydraulic model were specified using the files developed for the calibration runs of the existing conditions model (Chapter IV). The boundary conditions represent an approximate eight-day period, beginning 1200 hours EDT November 17, 2006 and ending 1200 EDT November 25, 2006. This time period included a 12-hour model spin-up period, and a 7.5 day period used for calibration. The calibration period was selected for the alternatives runs due to the limited influence of aberrant weather systems traversing the region during much of the instrumented period. Wind-induced effects upon the tidal circulation were minimal; hence, this time period was more typical of tidal circulation within the system. Therefore, the period selected for modeling represented the most appropriate conditions for evaluation of impacts associated with the construction of the proposed alterative.

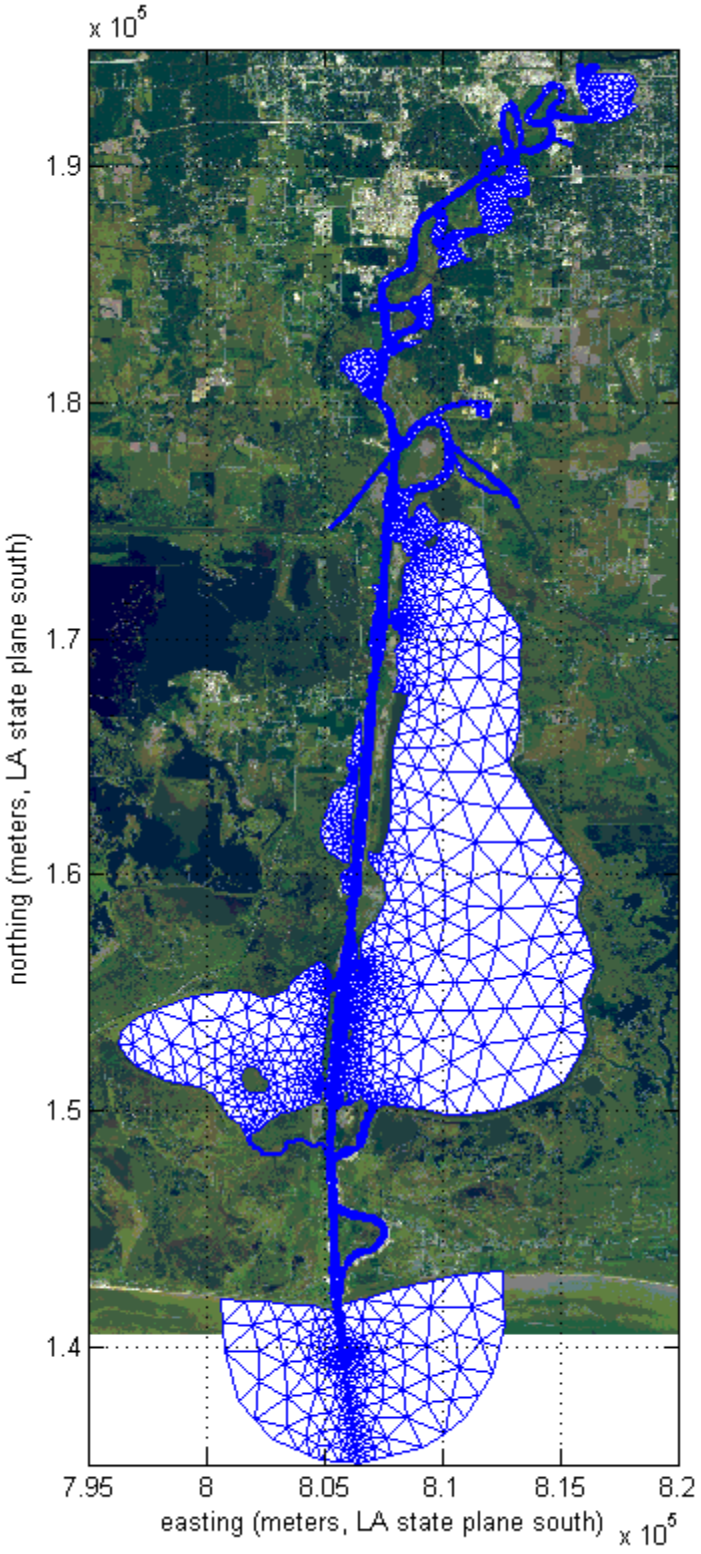

Figure VII-1. The model finite element mesh developed for Alternative 1. X-Y horizontal positions along the axes are in Louisiana South State Plane Coordinates, NAD 1983 (meters).

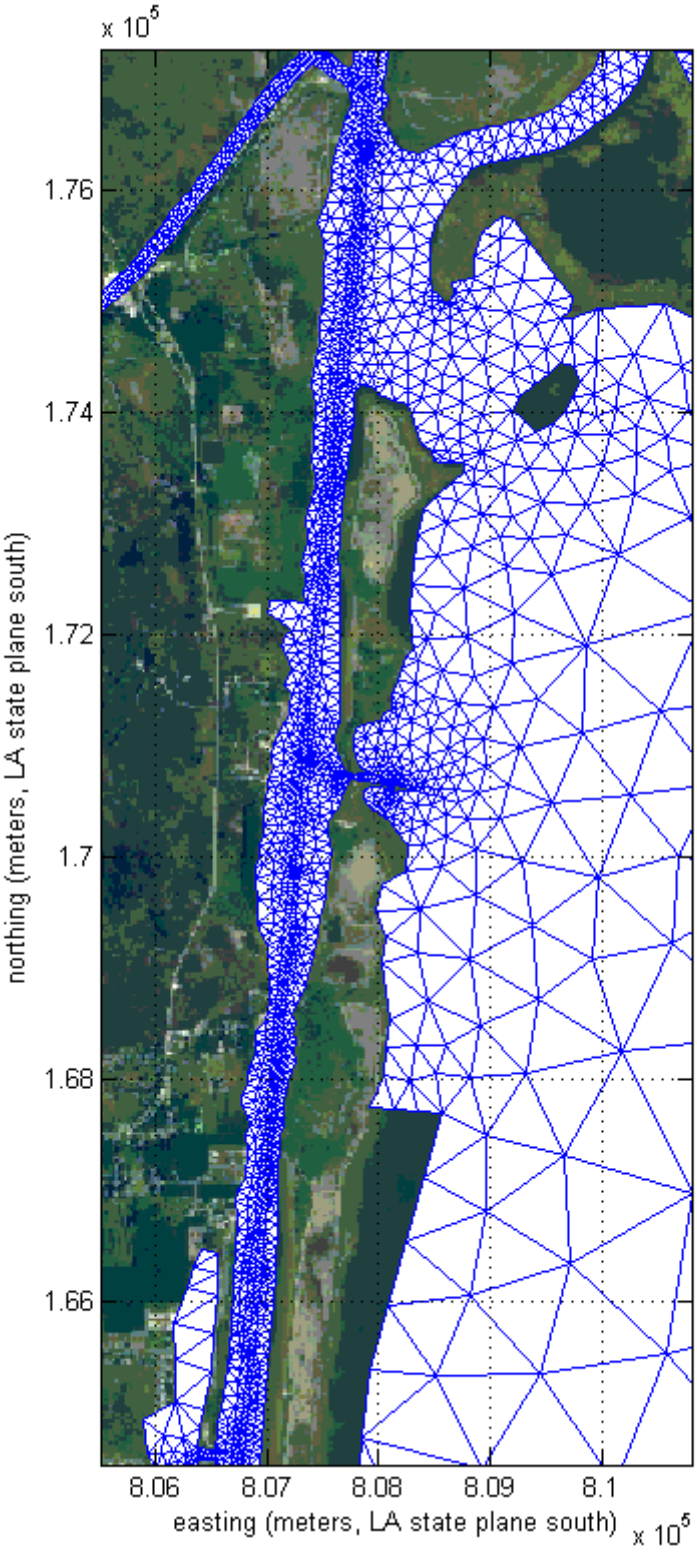

Figure VII-2. The model finite element mesh developed for Alternative 1. X-Y horizontal positions along the axes are in Louisiana South State Plane Coordinates, NAD 1983 (meters).

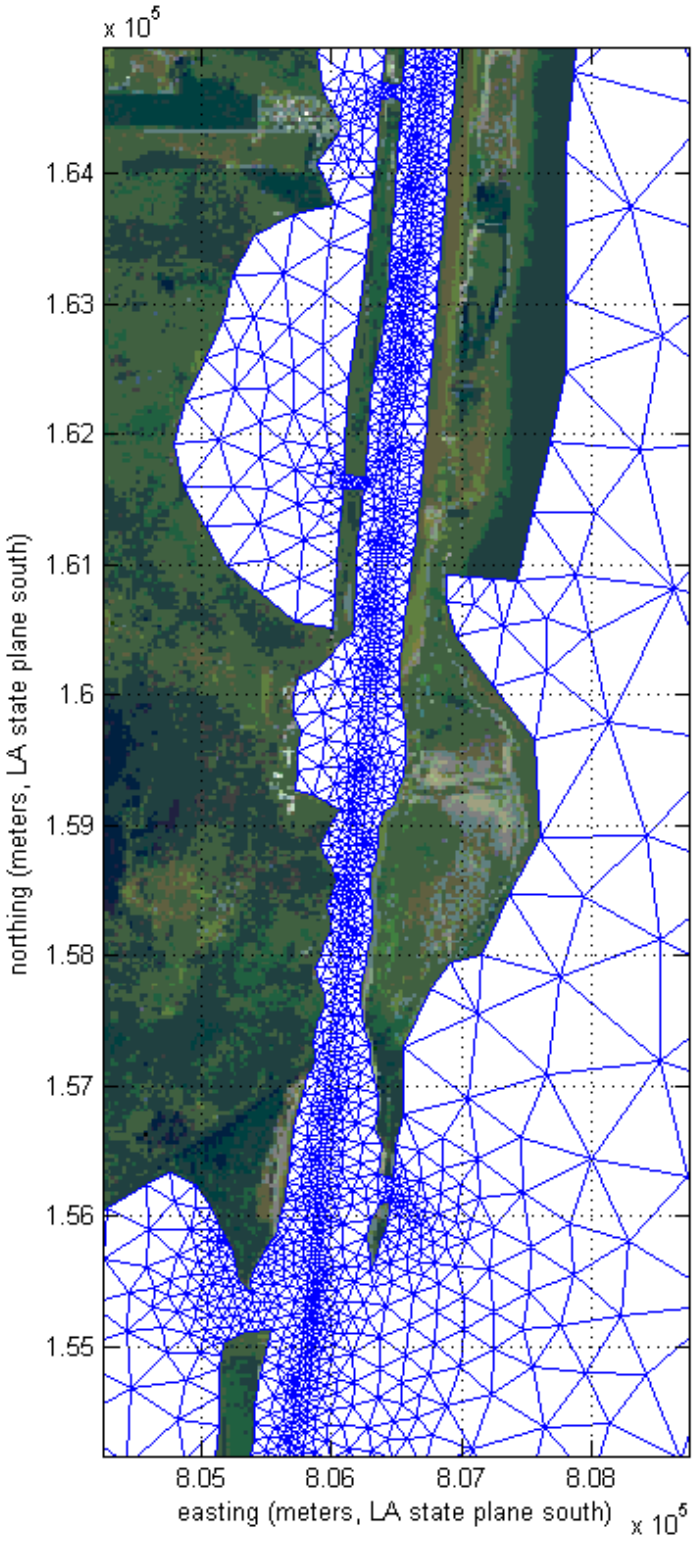

Figure VII-3. The model finite element mesh developed for Alternative 1. X-Y horizontal positions along the axes are in Louisiana South State Plane Coordinates, NAD 1983 (meters).

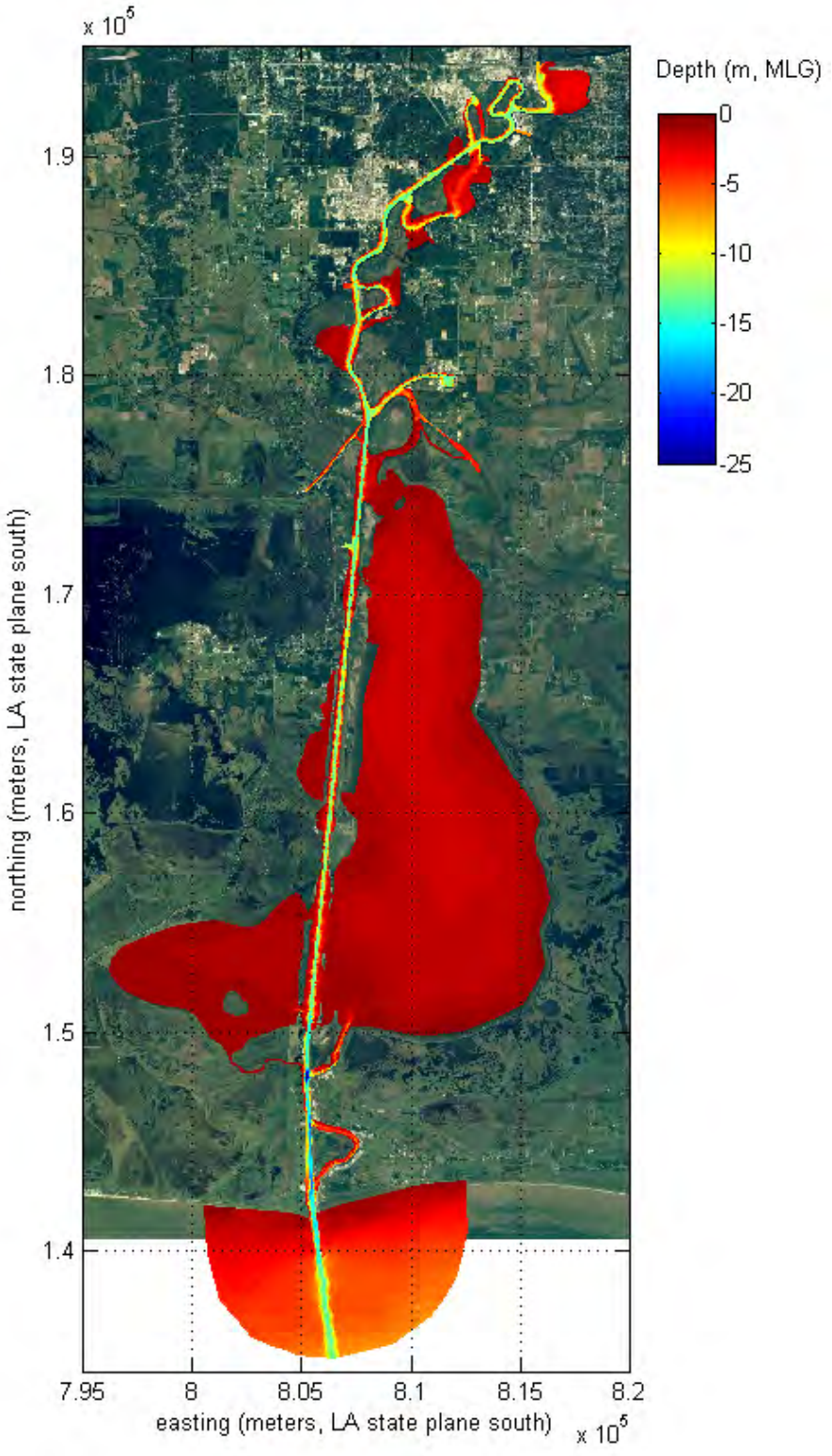

Figure VII-4. Bathymetric data interpolated to the finite element mesh of hydrodynamic model. Depth contours are in meters referenced to MLG. X-Y horizontal positions along the axes are in Louisiana South State Plane Coordinates, NAD 1983 (meters).

Friction coefficients, eddy viscosity coefficients, the density formulations, forcing conditions, and formulations were all carried forward from the calibrated and verified hydrodynamic model in Chapter IV for the development of the Alternatives model. The same is true for the sediment transport model, all of the coefficients, parameters, and formulations were specified using the information developed in Chapter V. The purpose of the hydraulic and sediment transport modeling for Alternative 1 was to determine changes and trends that occur in Lake Calcasieu as a result of the proposed modifications. Therefore, no modifications were made to the model parameters.

VII.2 HYDRODYNAMIC MODEL RESULTS

Examining the water surface elevation records at several locations around the Calcasieu system from the calibration run and the alternatives run reveals the addition of stone revetments and enlargement of the disposals sites along the CSC and eastern side of Lake Calcasieu has no apparent effect upon the propagation of tide through the system. The proposed modifications are contained along margins of the CSC on the shallow channel banks, and these modifications have a negligible effect upon the navigation channel which conveys a majority of the flow within the system. Figure VII-5 shows the gage records from two stations along the CSC, there are no discernable differences between the tidal signals shown in the records. With the small scale of the proposed modifications relative to the main transport pathways of the system, large scale changes to the system dynamics would not be expected. This hypothesis is confirmed by the hydrodynamic modeling. However, in the vicinity of the modifications there may be changes to the localized flow.

Examining the flows in the main channel reveals no substantial changes to the flow patterns resulting from the addition of stone revetments along the CDFs. Similar flow patterns to those observed in the existing system are shown in Figures VII-6 and VII-7. Figure VII-6 shows contours of flow velocity, along with velocity vectors which indicate the direction and magnitude of flow, for a single model time-step, at the portion of the tide where maximum ebb velocities occur between river mile 10 and mile 20. The maximum flood velocities are shown in Figure VII-7. While no large scale changes to flow patterns are observed, it is important to evaluate the localized changes that occur in the vicinity of the proposed structures. A comparison of the mean current speed before and after the modifications shows an increase in velocities along the stone revetments placed on the channel margins of the CSC. Figure VII-8 shows the increased velocities along the eastern side of the channel between approximately river mile 11 to mile 16 and river mile 18 to mile 19. These stretches of channel are narrow relative to the adjacent areas, the increased velocities within the narrow channel will enhance the transport of suspended material through these stretches of channel to reaches of channel where the channel footprint widens, and current velocities decrease allowing the suspend material to settle. This is highlighted in the Figure VII-9 which shows the differences in maximum velocities.

The expansion of Dredge Disposal Sites D and E into Lake Calcasieu extends from the existing shoreline in an easterly direction out into the lake, creating abrupt changes in shoreline orientation. The effects can be seen in the significant reduction in tidal currents immediately north and south of the expansion. The shadow zones from the expansion will act as tidal ‘coves’ with a reduced tidal circulation, likely resulting in impaired water quality and/or regions of enhanced deposition of fine-grained material along the eastern side of Lake Calcasieu. It is recommended that more gradual transitions be considered to minimize the influence of Dredge Disposal Sites D and E expansion on tidal circulation.

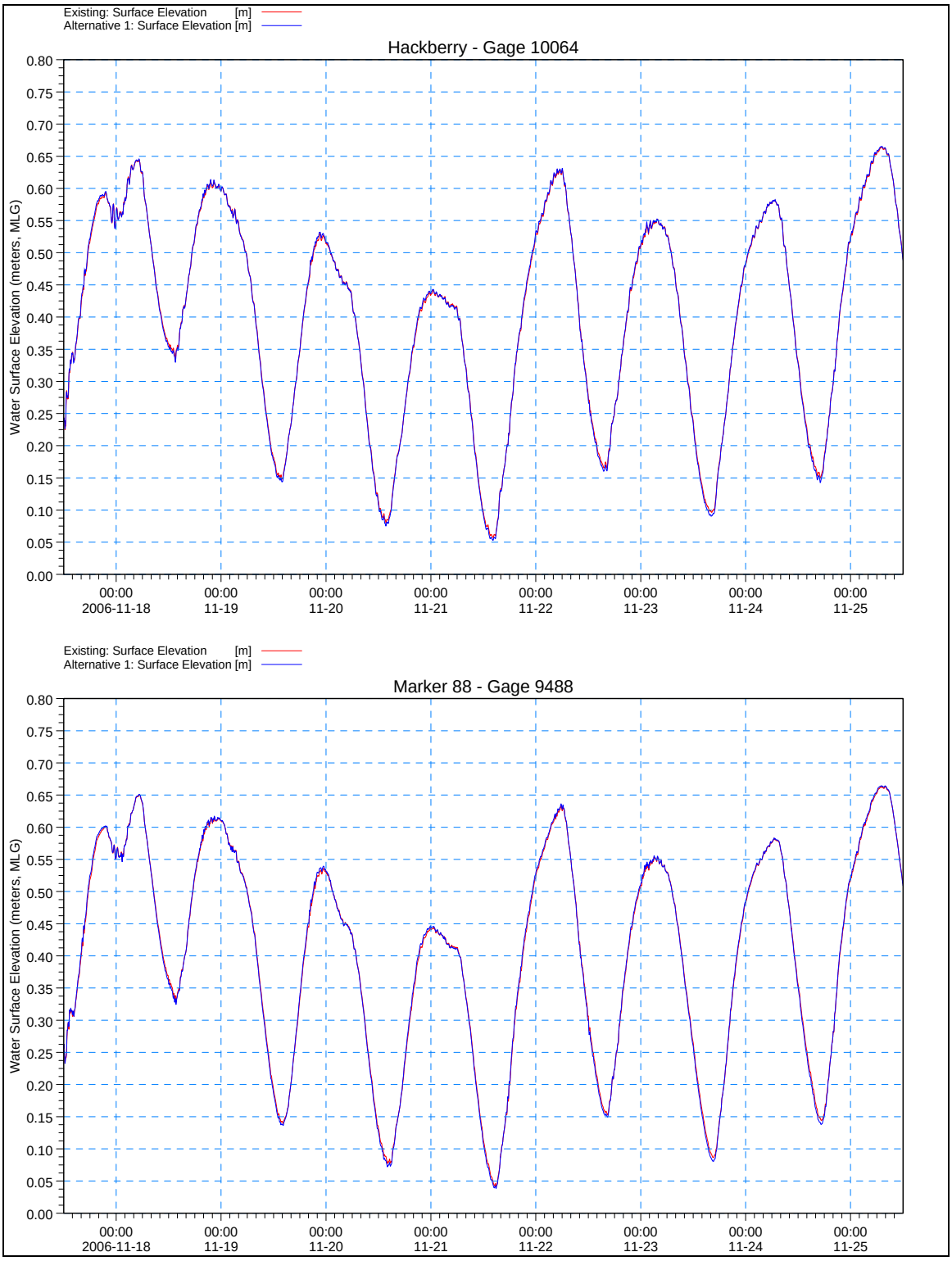

Figure VII-5. Comparison of water surface variations along the CSC between existing conditions and proposed Alternative 1. The existing conditions are represented by the dashed red line, and Alternative 1 by dashed blue line. The figures represent conditions during the calibration period, for the Hackberry and Marker 88 gauging stations.

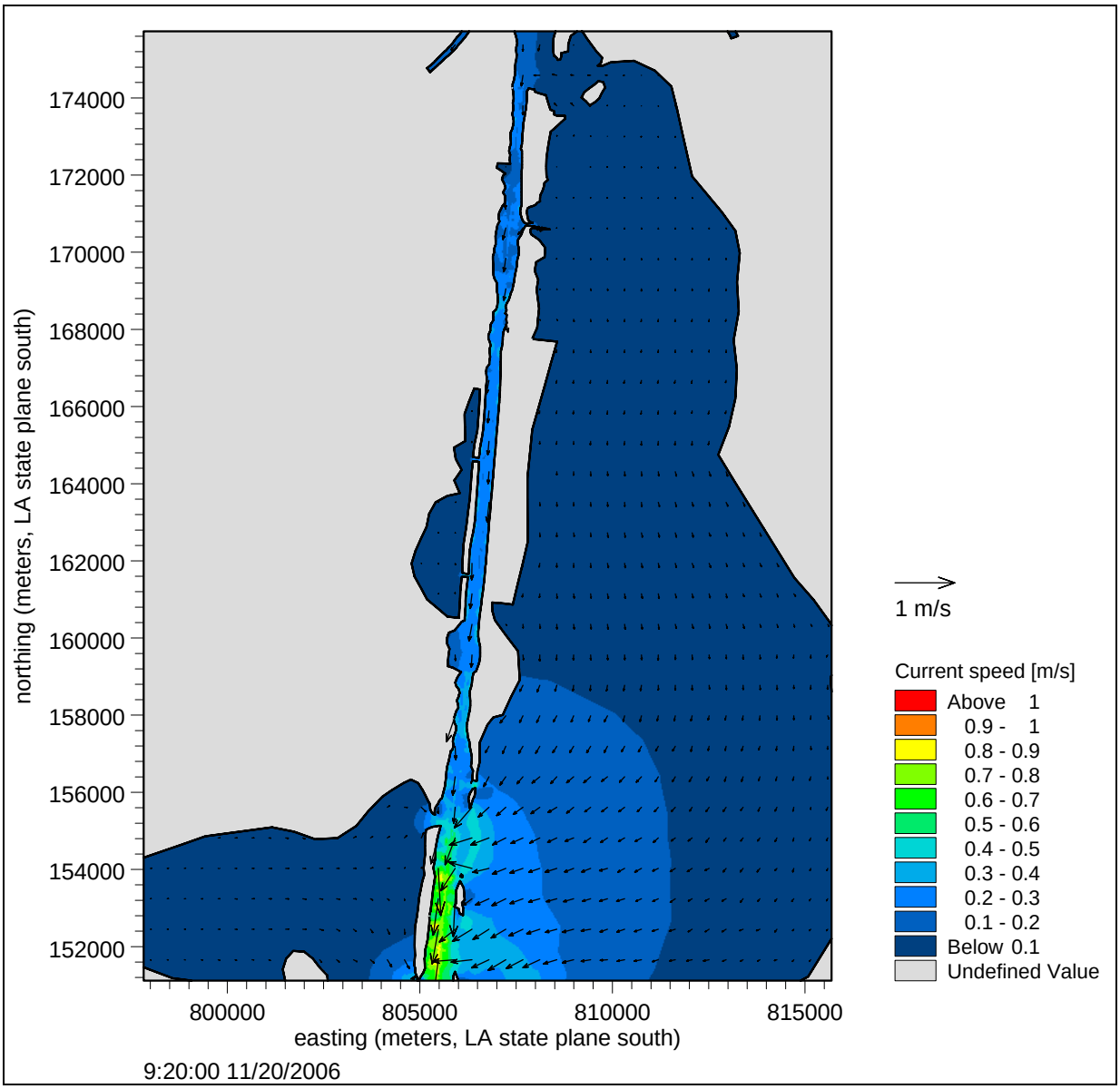

Figure VII-6. Example of hydrodynamic model output in channel along Lake Calcasieu for a single time step where maximum ebb velocities occur for this tide cycle. Color contours indicate flow velocity, and vectors indicate the direction and magnitude of flow.

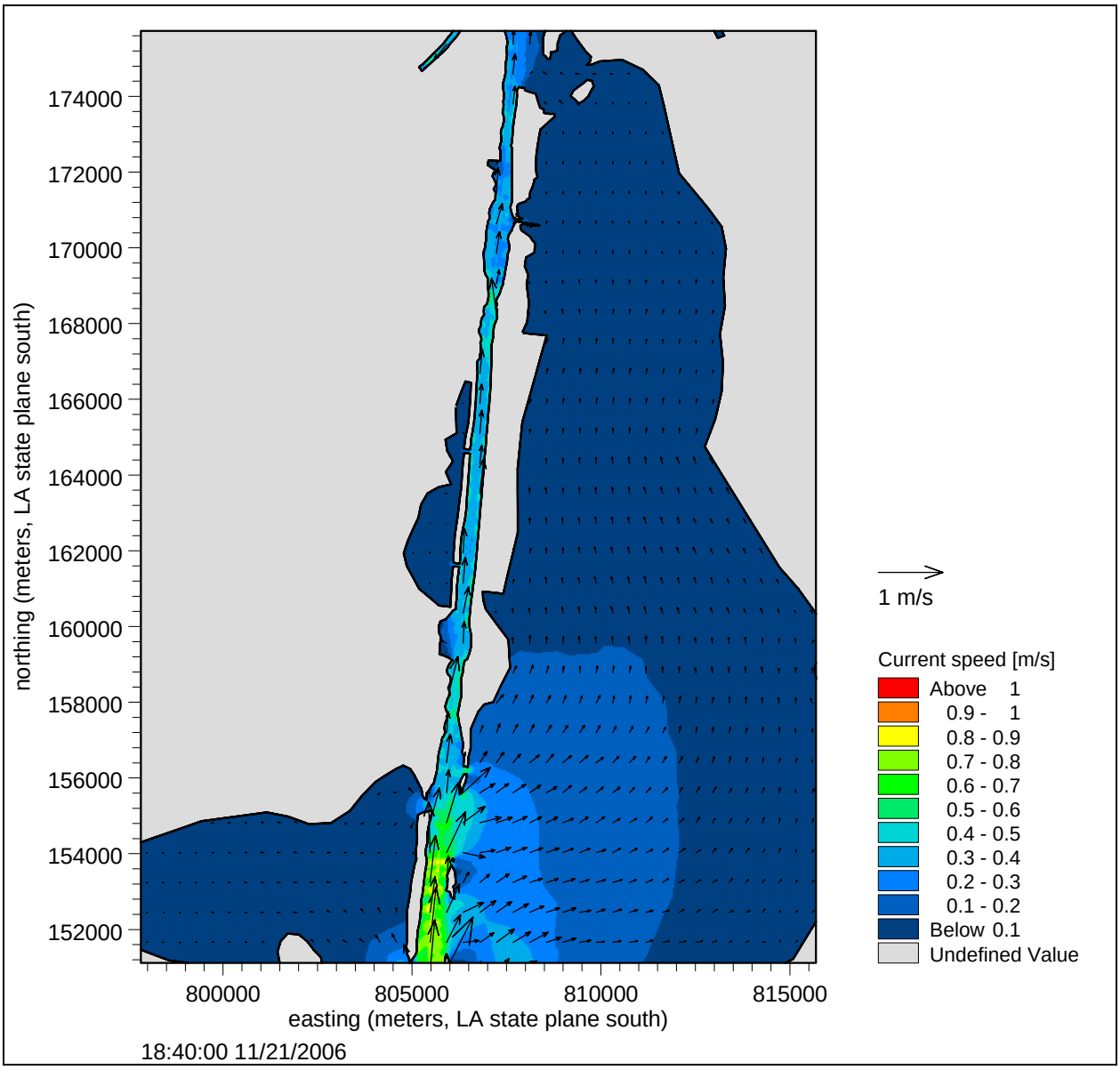

Figure VII-7. Example of hydrodynamic model output along Calcasieu Ship Channel for a single time step where maximum flood velocities occur for this tide cycle. Color contours indicate flow velocity, and vectors indicate the direction and magnitude of flow.

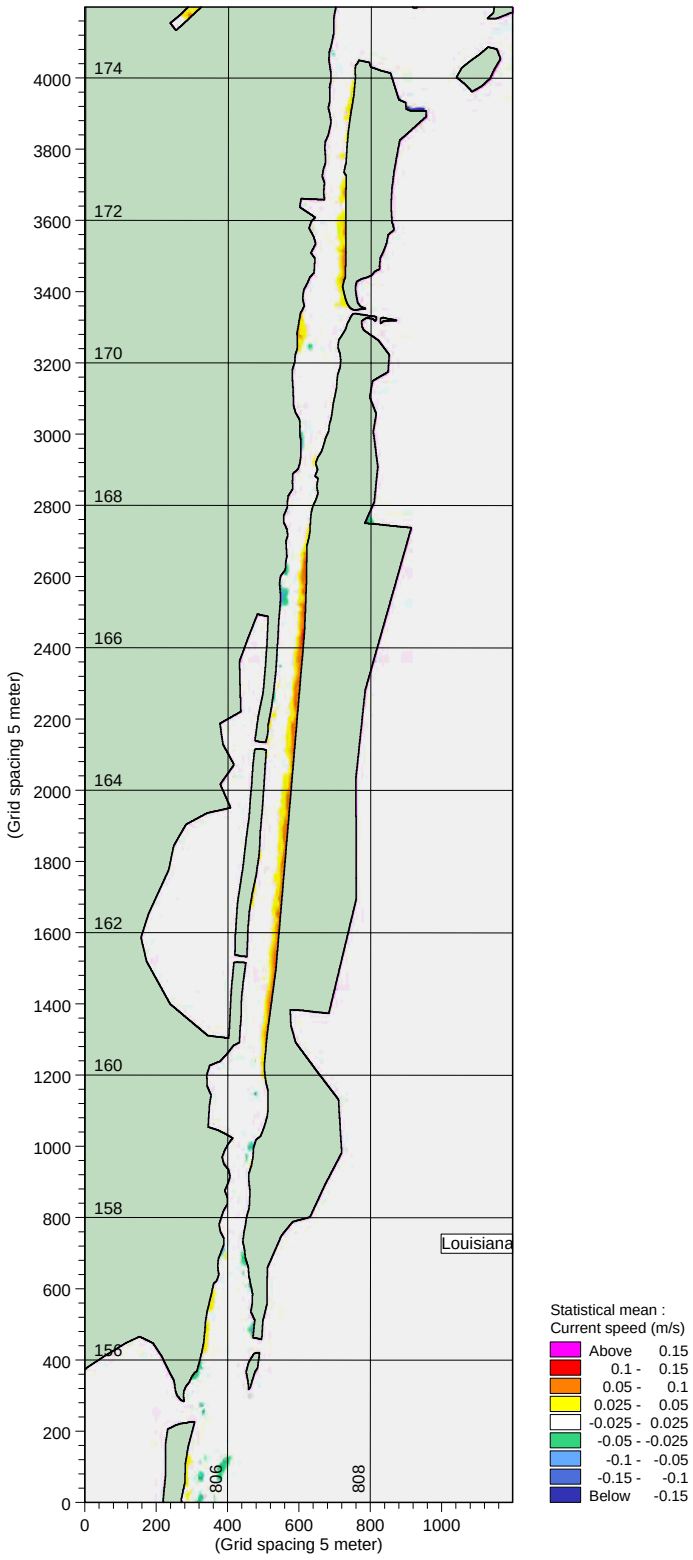

Figure VII-8. Difference in mean velocities observed during average tidal conditions between the hydrodynamic results from the Alternatives run and the calibration run. The grid is in LA state plane meters south.

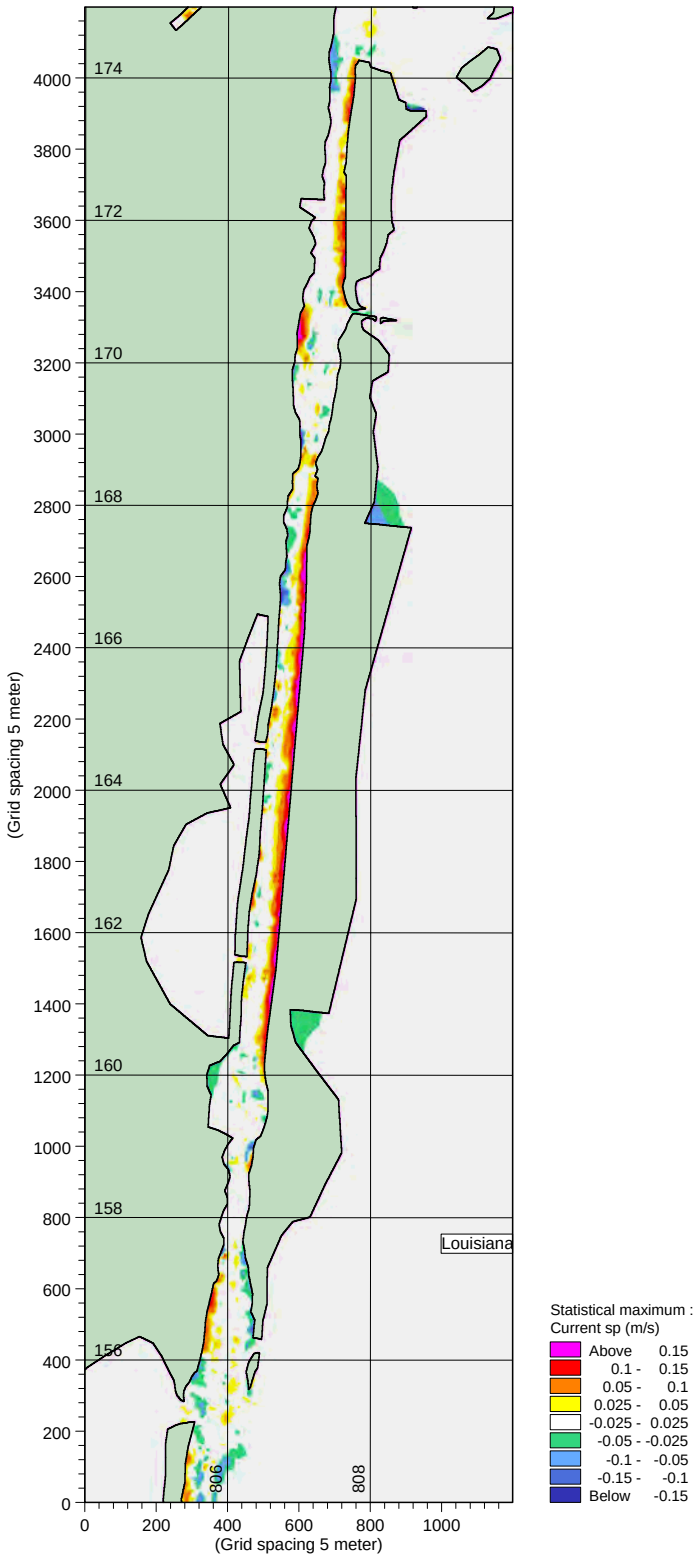

Figure VII-9. Difference in maximum velocities observed during average tidal conditions between the hydrodynamic results from the Alternatives run and the calibration run. The grid is in LA state plane meters south.

VII.3 SEDIMENT TRANSPORT MODEL RESULTS

After evaluating the impacts to the hydrodynamics as a result of the proposed modifications, it is important to evaluate how these changes affect sediment transport patterns within the system. Sections of the shipping channel already face pressures due to sediment deposition, it is important not to amplify the problem or shift the sediment deposition to another location.

The maximum shear stress under normal tidal conditions is shown below in Figure VII-10, as modeled during the 8 day calibration period. The narrowing of the channel along the proposed stone dikes increases the bed shear stress relative to the existing conditions. The largest increases in bed shear stress can be seen around on the eastern side of the navigation channel between Mile 11-16 and Mile 18-20. The foot print of the structures narrows the cross-sectional area of the channel requiring the flow to speed up in order to fit through the reduced cross-sectional area. Therefore, the shear stress increases due to the increased flow velocity.

Figures VII-11 shows difference in maximum shear stress observed during the 8-day calibration period between the Alternatives run and the calibration run. The areas along the eastern edge of the channel show the largest increase in (greater than 0.5 Pa) shear stresses. There is a slight reduction in bed shear stress along the channel between Mile 8-10, which could result in additional deposition within this portion of the CSC. The proposed revetment along disposal Site H results in negligible changes in shear stress, since it is located in wider section of channel where the addition of the structure has little influence on tidal flows.

Figure VII-10. Average shear stress in the upper navigation channel computed during 8 day calibration period.

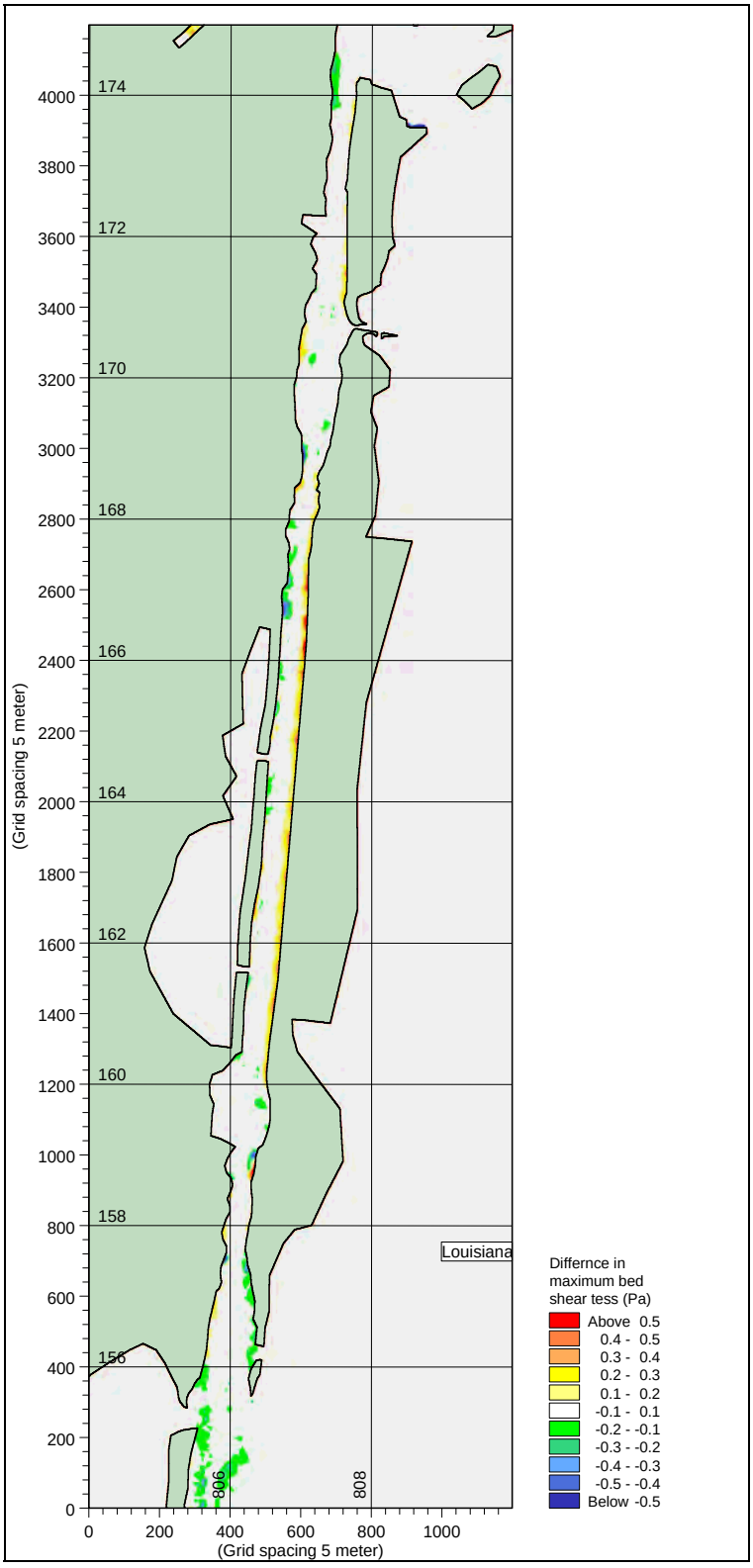

Figure VII-11. Difference in maximum bed shear stress observed during average tidal conditions between the hydrodynamic results from the Alternatives run and the calibration run. The grid is in LA state plane meters south.

Figures VII-12 through VII-13 show how the computed TSS varies along the length of the CSC, between the maximum excursions of the flood and ebb portions of the tide. Excursion is similar to that observed in the calibration run, meaning the movement of material during the cycle of the tide has not changed significantly.

The movement of sediment in the system is impacted by the addition of the expanded dredge disposal sites. However, it does not appear to drastically affect the existing sediment transport processes. The stone dikes on the margins of the channel from approximate river mile 11 to 16 and river mile 18.5 to 20 increase nearshore flow velocities and bed shears stresses; however, this influence is relatively localized, with no evidence of regional changes to sediment transport patterns. Due to the higher flow velocities along the proposed rock dikes, a reduction in sedimentation within these channel stretches can be anticipated. Portions of the CSC north and south of the alterations can expect an increase in sedimentation rates; however, model results indicate that this influence is expected to be minor.

Expansion of the CDFs into the confined portion of the CSC will potentially alter sediment transport patterns within this frequently dredged region. As proposed, the expansion of the CDFs from river mile 11 to 16 and river mile 18.5 to 20 should only cause minor impacts to sediment transport patterns and channel shoaling. As presently designed, the expansion of Dredge Disposal Sites D and E into Lake Calcasieu may create areas of increased sedimentation of fine-grained material to the north and south of the containment dikes. A more gradual change in shoreline orientation will likely eliminate potential impacts on water circulation and sedimentation at the northern and southern ends of the proposed expansion. The improvements associated with Disposal Site H are minor and are anticipated to result in negligible changes to the system hydrodynamics and sediment transport patterns.

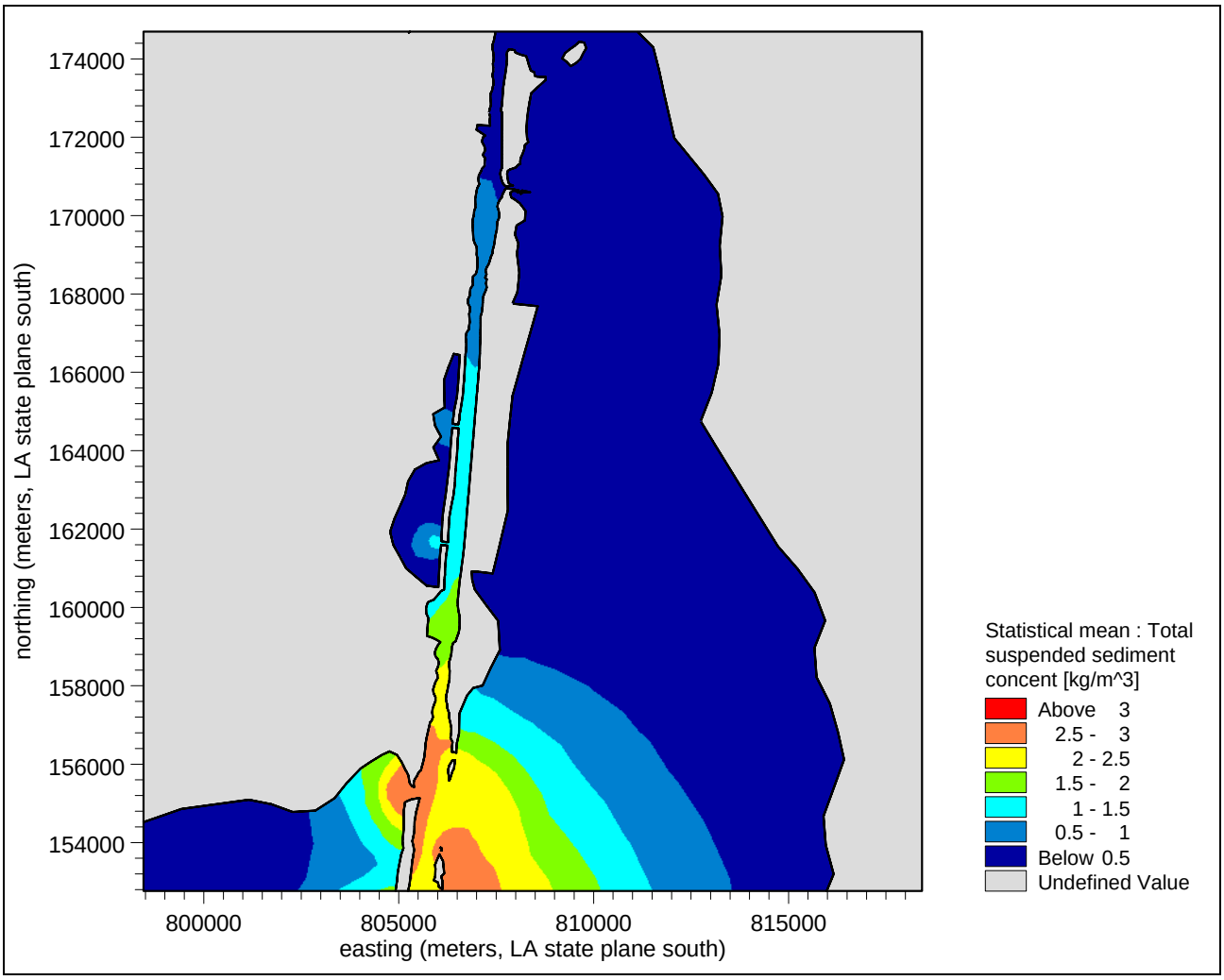

Figure VII-12. Average total suspended solids (TSS) computed at for each model element.

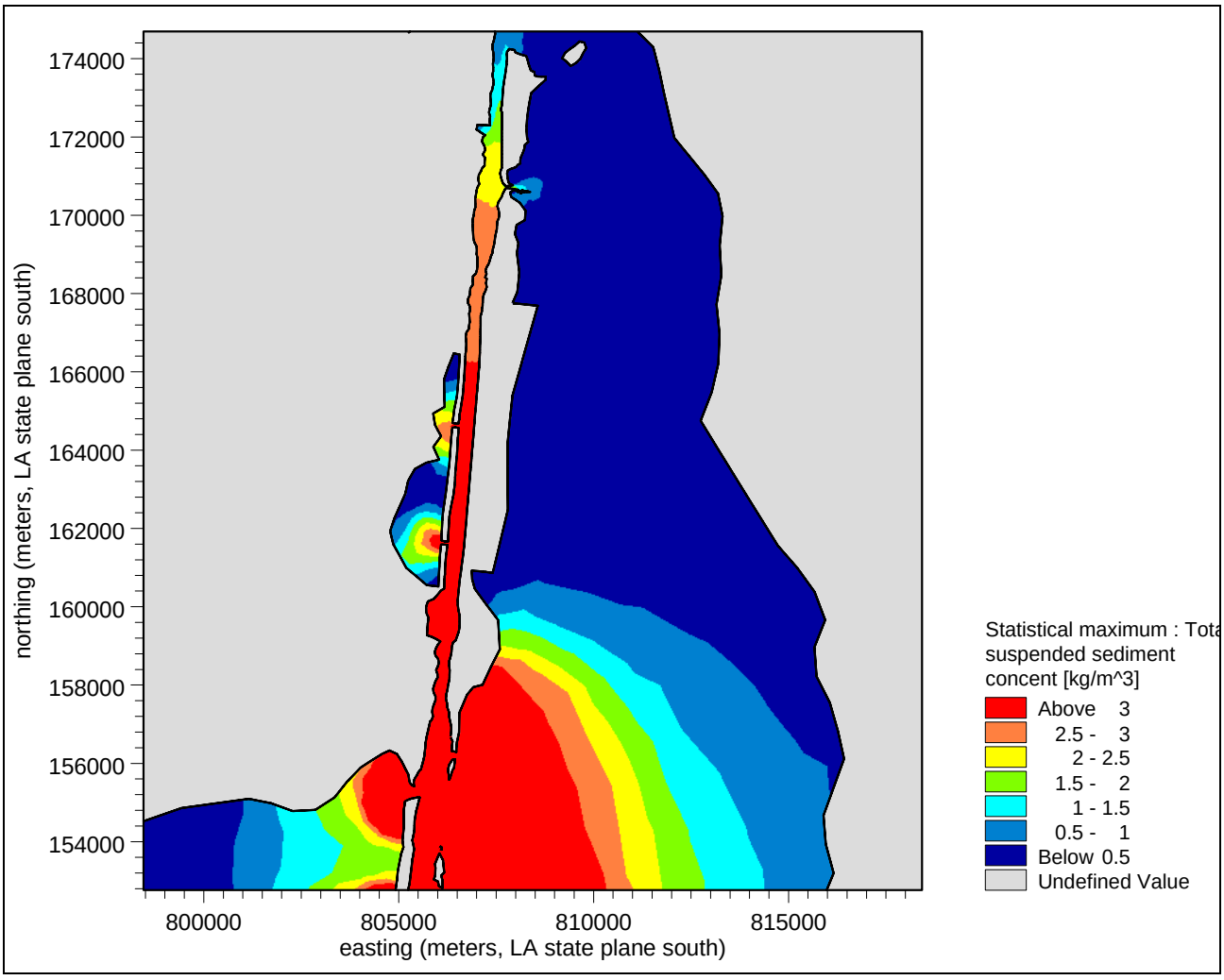

Figure VII-13. Maximum total suspended solids (TSS) computed at for each model element.

VIII. SUMMARY AND CONCLUSIONS

VIII.1 OVERVIEW

To support the development of the Calcasieu Ship Channel Dredged Material Management Plan (DMMP), a hydrodynamic and sediment transport model was developed for the Lake Calcasieu estuarine system. The objective of this modeling effort was to identify and quantify, where possible, flow regimes, sediment sources and sinks, and the sediment processes within the Calcasieu Ship Channel, Lake, and Pass. The results of the study provided information required to support and verify plan formulation and alternative analysis regarding sediment placement and management within the system to minimize dredging and placement impacts to the channel and ecosystem resources.

Prior to developing long-term solutions for dredged materials management, an understanding of the physical processes governing circulation and sediment transport were required. Due to the relatively modest tide range offshore of Calcasieu Pass (approximately 2 to 3 feet) and the shallow nature of Calcasieu Lake, wind stress on the surface of the estuary also plays an important roll in overall circulation patterns governing sediment transport. Appropriate hydrodynamic analyses of the Lake Calcasieu required a two-dimensional (vertically-averaged) modeling package that incorporated the influence of temporally varying wind fields associated with the range of conditions typical to the system. In addition, a field data collection effort was required to augment the available information including water elevation measurements and current measurements at key locations within the system. The dataset developed formed the basis for model boundary conditions, as well as calibration and validation data.

Following development of the calibrated/validated hydrodynamic model, a sediment transport model was incorporated into the two-dimensional circulation model. Since the dredged sediments are predominantly fine-grained (silts and clays), the analysis approach required evaluation of bottom sediment characteristics of the Calcasieu Ship Channel and surrounding areas. Sediment information including grain size distribution, relative shear strength of sediments, and fine-grained sediment mobilization criteria provided critical input parameters to the sediment transport model. A majority of this information was derived from existing local USACE studies (e.g. Calcasieu River and Pass Dredged Material Sedimentation Study) or regional evaluations that addressed similar estuarine morphology. The transport model incorporated these local and regional sediment characteristics, as well as results from the hydrodynamics analysis, to determine potential sediment transport pathways causing shoaling problems within the Calcasieu Ship Channel.

The primary goal of the combined hydrodynamic and sediment transport modeling effort was to identify sediment sources and sinks, as well as the associated sediment transport pathways. Once developed, the model suite can be utilized to assess the effects of alternative dredge disposal sites (e.g. larger upland disposal sites or marsh islands) on circulation and sediment transport patterns.

In addition to the influence of natural hydrodynamic processes, anthropogenic factors potentially increase maintenance dredging frequency and/or accelerate erosion of the CDFs. Due to the heavy marine traffic utilizing the Ship Channel and the confined nature of the channel between Calcasieu Pass and Lake Charles, ship wakes and/or surge can significantly influence erosion of the CDFs adjacent to the channel. Due to the significance of this potential sediment source responsible for channel shoaling, an analysis of ship-generated waves and currents was

performed. Although a substantial amount of research has been compiled regarding ship wake and surge generation, site-specific information remains the most proven technique for evaluating the influence of ship-generated waves and currents on local sediment transport processes. To assess the potential influence of ships traveling along the Calcasieu Ship Channel, a wave and current monitoring program has been performed at key locations along the shipping channel. Information derived from this monitoring effort was utilized to determine the potential magnitude of ship wakes on sediment re-suspension and transport.

The hydrodynamic and sediment transport modeling effort for Lake Calcasieu consisted of several components to support the overall goals of the project:

- *Background (Chapter II)* – a general overview of the Lake Calcasieu estuarine system.
- *Data Collection and Analysis (Chapter III)* – Presentation of data collected to calibrate and validate the modeling effort. The data sources evaluated include information from outside sources.
- *Hydrodynamic Modeling (Chapter IV)* – Description of the two-dimensional depth-averaged hydrodynamic model set-up, calibration, and validation.
- *Sediment Transport Modeling (Chapter V)* – Description of the two-dimensional depth-averaged model of fine-grained sediment transport processes including a discussion of input parameters and limitations.
- *Influence of Vessel Passage on Sediment Suspension (Chapter VI)* – An evaluation of ship wake processes and their relative contribution to sediment transport within the central portion of the Calcasieu Ship Channel.
- *Evaluation of Sediment Management Options (Chapter VII)* – A modeling analysis of selected alternatives for reducing bank erosion along portions of the CSC, as well as expansion of CDFs into the main body of Lake Calcasieu.

VIII.2 DATA COLLECTION

Accurate numerical modeling of system hydrodynamics is dependent upon measured conditions within the estuary for two important reasons:

- ♦ To provide 'real' observations of hydrodynamic behavior to calibrate and verify the model results
- ♦ To define accurately the system geometry and boundary conditions for the numerical model

To support hydrodynamic modeling efforts in Lake Calcasieu, tidal water elevation variations were measured at eight locations within the system. Cross-channel current measurements (ADCP) were surveyed through a tidal cycle along the entrance channel in Cameron, LA. Meteorological measurements were taken for a two-month period to add in the development of the hydrodynamic model.

The system geometry was defined using historical bathymetry, dredging surveys, collected bathymetry and aerial photographs. The bathymetric information was utilized to develop the computational grid of the system geometry for the hydrodynamic modeling effort. Tidal elevation measurements within the system were used for both forcing conditions and to evaluate tidal attenuation through the estuarine system. Data collected by other sources (USACE and NOAA) was also collected to supplement the data collection program.

Based on the tide data collection effort, the percentage of tidal energy was largest in the offshore signal in Gulf of Mexico; as should be expected given the tidal attenuation through the system. In general, the energy of the signal decreases with distance from the offshore gage, with the lowest energy found in upper regions of the estuarine systems. Due to the complex hydrodynamics that characterize the upper portion of the estuary, there is not a consistent reduction in tidal energy with increased distance from the inlet. Tide data analysis also showed that tides are responsible for approximately 25% of the water level changes. Meteorological effects in this data set were significant contributors to the total observed water level changes. The relative increase in non-tidal energy within this system is likely due to the decrease in tidal energy as a result of frictional forces and the relatively shallow waters of the upper system being more susceptible to wind forcing, rather than actual growth of residual forces.

Current measurements were collected by a boat-mounted ADCP. This data collection effort was performed as the vessel navigated repeatedly a pre-defined transect line across in main channel in Cameron, LA. The transect line was designed to measure as accurately as possible the volume flux through the entrance channel between the Gulf of Mexico and Lake Calcasieu during a complete tidal cycle. The transect line ran across the channel from east-to-west direction and was then repeated west-to-east approximately every 30-minutes.

Wind speed and direction data were collected at a single location near the entrance to the Lake Calcasieu shipping channel by Ocean Data Technologies, Inc. Data collection spanned October 24 to December 20, 2006. Based on the data collected, winds from the northwest were least likely to occur, only 12% of the time, however these winds were also the most energetic and would likely affect circulation to a greater extent. Average wind speed from the northwest quadrant was 5.48 m/s; nearly 14% of the time speeds exceeded 10 m/s. Winds from the southern quadrants were much weaker typically than winds from the northern quadrants.

Bathymetric, or depth, survey information for Lake Calcasieu was gathered from several sources. NOAA's GEODAS hydrographic survey database served as the basis for the assembled dataset. The database provided data coverage over the entire basin, however most of the surveys within Lake Calcasieu dated from the 1930's. Therefore, this data was only used in areas outside of the navigation channels where bathymetric change would be minimal. Post dredging surveys from the USACE were used to for the main Calcasieu shipping channel and the GIWW. Gahagan & Bryant Associates, Inc. conducted a supplementary survey to provide bank-to-bank survey information along the main channel, within secondary channels, and bathymetry transitions.

VIII.3 HYDRODYNAMIC MODELING

A hydrodynamic study was performed to understand the dynamics of the Lake Calcasieu system. The dynamics are influenced by a number of features: extensive bayous/marshes to the east and west of main system, the Calcasieu River entering to the north of Lake Charles, the Gulf Intracoastal Waterway (GIWW) connecting the Calcasieu basin to the Sabine Basin to the west, the navigation channel connecting the Gulf of Mexico to Lake Calcasieu in Cameron, and metrological forces acting upon the system. Therefore, the development of a numerical model capable of accurately simulating hydrodynamic circulation within the Lake Calcasieu system requires a significant level of detail to accurately represent the natural system and the forces acting upon it.

Circulation in Lake Calcasieu system was simulated using the MIKE-21 HDFM model developed by the Danish Hydraulics Institute (DHI, 2007). It is a two-dimensional, depth-

averaged finite volume model, capable of simulating transient hydrodynamics on a flexible mesh. The modeling system is designed in an integrated modular framework with a variety of add-on modules capable for the simulation of flows, waves, sediments and ecology in rivers, lakes, estuaries, bays, coastal areas and seas. The model is widely accepted and tested by profession engineers and scientist for analyses of estuaries and/or rivers around the world. The software is currently utilized by and for USACE (New York District, New England District, and San Francisco District), US Geological Survey, Bureau of Reclamation, and the US Federal Emergency Management Agency (FEMA).

To calibrate the model, field measurements of water elevations, currents, meteorological conditions, freshwater inflow, and bathymetry were required. Tide data were acquired within the Gulf of Mexico, and also at seven additional stations located within the Lake Calcasieu system. All tide gages were installed for a 55-day period to measure tidal variations through one spring-neap tidal cycle and to capture time periods where metrological effect were minimal compared to tidal forces. In this manner, attenuation of the tidal signal as it propagates through the various sub-sections of the system was evaluated accurately.

The final calibrated and validated model serves as a useful tool for investigating the circulation characteristics of the Lake Calcasieu system. Using model inputs of bathymetry and tide data, current velocities and flow rates can be determined at any point in the model domain. This is a very useful feature of a hydrodynamic model, where a limited amount of collected data can be expanded to determine the physical attributes of the system in areas where no physical data record exists.

Examining the flows in and out the main channel, the overall system exhibits ebb dominance. This is not unexpected do to the amount of fresh water draining into the system, as well as the microtidal forcing within the Gulf of Mexico. The fresh water continually entering the system requires less water to enter from the Gulf of Mexico on a flood cycle, than is required to exit on an ebb cycle. Flow velocities are the strongest along the main channel between river miles 1 to 5. This is due to the constrained nature of the channel between the tip of the jetties and the southern end of the lake. Depth-averaged velocities in the inlet generally peak around 1.2-1.4 m/s for ebbing tides, and 1.0-1.2 m/s for flooding tides.

Between river miles 5 and 21 the flow is divided between the main channel and the main body of Lake Calcasieu. A portion of the ebbing flow bypasses the main channel just south of the Devils Elbow and flows into the lake. The secondary flow route through the main body of the lake creates relatively high velocity ebb currents returning flow to the CSC in the area not constrained by disposal islands. Velocities are the greatest along the constrained sections of the main channel and at the flow constrictions at the north and south end of the lake. The depth-averaged flow velocities are often below the threshold for suspending sediment in this region, with peaks at maximum flood and ebb flows that likely suspend sediment for short periods of time.

At the north end of the lake the flow is generally constrained to the GIWW which extends west to Sabine and the navigation channel to Lake Charles. The circulation patterns around the Devils elbow are very quiescent, with flow velocities remaining below 0.1 m/s for all phases of the tide. Due to the configuration of this channel, the relatively low velocities indicate likely settling of suspended material. This hypothesis is supported by the significant volume of historic dredging in this area. The channel is constrained north of river mile 23 until it reaches Lake Charles at mile 35. Flow magnitudes are generally between 0.1 and 0.3 m/s along the main channel and lower in the fringing bays and marshes.

VIII.4 SEDIMENT TRANSPORT MODELING

The purpose of the sediment transport modeling for Lake Calcasieu was to determine trends in mud transport and, to the extent possible, quantify the flow regime and how this affects sediment sources and sinks. The results of the modeling analysis provide information required to support and verify plan formulation and alternative analysis regarding sediment placement and management within the system to minimize dredging and placement impacts to the channel and ecosystem resources. In addition, the model results will be utilized to support the preparation of the Dredged Material Management Plan (DMMP) and Environmental Impact Statement for the project.

The numerical tools selected to simulate fine-grained sediment transport within the Lake Calcasieu estuarine system was the Mud Transport (MT) and Advection-Dispersion (AD) models that are available as modules in the DHI MIKE 21 hydrodynamic modeling suite. These modeling tools allow specification of spatially varying mud layers, as well as specification of background and boundary suspended sediment characteristics. A complete description of the modeling approach is described below.

The accuracy of model predictions is directly dependent on the quality of the input data. For the Lake Calcasieu system, sediment data required to parameterize the model was derived from a variety of sources including available U.S. Army Corps of Engineers reports, regional studies of observed suspended sediment concentrations and mud characteristics, and other task reports regarding the Lake Calcasieu DMMP effort. With the exception of the critical shear stress flume study performed by Texas A&M University (Ravens, 2007), information used to parameterize the model was not directly collected for the purpose of sediment transport modeling in the Lake Calcasieu system. However, environmental work associated with previous dredging efforts, as well as numerous scientific studies of the Lake Calcasieu and nearby Lake Sabine estuary systems, provided a significant amount of data regarding the distribution of sediments.

A majority of the sediment in the CSC is comprised of fine silt and clay. From Mile 9 north to Mile 36, the sediments are typically 90% silt and clay with a small amount of fine sand. The organic content is higher in these sections, sometimes approaching 10% especially north of the GIWW (GEC, 2007). The southern portion of the CSC contains a higher sand content: 20% sand at Mile 9, 41% sand at Mile 7, and 78% sand at Mile 6. The larger proportion of coarse-grained sediments in this region is likely due to (a) sediments derived from the barrier beach system and nearshore waters in the Gulf of Mexico and (b) higher ambient tidal currents in this region that prevents settling of fine-grained material. Figure VIII-1 shows the CSC mile marker locations for reference.

The confined channel south of mile marker 5 creates a tidal “jet” that causes water flowing into Lake Calcasieu during the flood cycle to transport sand in a northerly direction. As the tidal flow becomes less confined in the southern portion of the lake, velocities decrease and the entrained sand settles out. Based on the historic dredging volumes, this portion of the channel requires maintenance dredging volumes of ~150,000 CY per mile per year. A majority of this sediment consists of material north of mile marker 7, consisting of sediments that are more than 50% silt and clay. This trend indicates that sandy material derived from seaward portions of the estuary, as well as the adjacent beaches and nearshore waters, are not a dominant factor in the long-term maintenance dredging requirements of the CSC. This is further supported by the absence of a well-defined flood tidal shoal at the intersection of the CSC with the southern limit of the lake.

Figure VIII-1. Lake Calcasieu Ship Channel location map. Mile markers are labeled every 5 miles.

In wave-dominated estuaries like Lake Calcasieu the wave energy tends to be significant at the entrance and sediment eroded from the coast is transported alongshore forming a spit or barrier beach. Formation of the spit constricts the size of the tidal entrance to the estuary.

Eventually, the inlet cross-section represents a balance between eroding sediment from the barrier and tidal currents through the entrance. Within the main basin of the estuary, the currents diminish rapidly. Towards the head of the estuary, fluvial processes tend to dominate; therefore, the central portion of the estuary represents the lowest total energy and likely is characterized by extensive tidal flats and/or salt marshes. The gradual change in sediment composition (sand-dominated sediment at the south, fine-grained sediments in the middle and fine sediments with a high organic content in the far northern reaches) reflects the transition across the Lake Calcasieu estuarine system from a fluvial-dominated region in the north to a more wave-dominated system through the main basin, southern portion of the CSC, and the inlet.

For a majority of the central portion of the CSC (Mile 11 to 20.5) there is a mix of 30-40% silt, 40-60% clay and 15% or less sand. This change in sediment composition reflects the transition from the tidally-dominated area near the inlet to the wave-dominated estuary which comprises a majority of Lake Calcasieu. The tidal currents are not strong enough to carry significant quantities of the heavier sand into this central region of the channel. The finer silts and clays make up a majority of the sediments in this area.

From Mile 21.5 to 23.5 there is a third regime of sediment composition. The samples from this area see the clay content increasing to greater than 60%. The silt content is approximately 30% with sand accounting for roughly 5% of the sample. This region of the CSC marks another transition within the system from the estuarine environment to the south into a more fluvial region dominated by the freshwater flows of the Calcasieu River. This area also contains significant anthropogenic changes to the system, most notably the Gulf Intracoastal Waterway (GIWW).

Although the primary area of interest for the modeling effort is the confined portion of the CSC, it is important to recognize that the Lake Calcasieu estuarine system is complex and sediment transport patterns are dominated by different forcing mechanisms within each unique part of the overall system. Based on the morphological structure of the Lake Calcasieu system, the estuary can be clearly classified as wave-dominated. The strong tidal currents through the main entrance channel combined with the rapid attenuation of tide range across the barrier beach and chenier plain demonstrate a rapid reduction in tidal energy between the Gulf and Lake Calcasieu. Moreover, the long narrow entrance channel prevents wave energy from entering the estuary from the Gulf. This narrow channel characterized by relatively high tidal velocities is capable of transporting sand-sized material from the barrier beach system and nearshore areas into the estuary. Since the fine-grained sediment transport model selected for this study has limited capabilities for simulating movement of coarse-grained sediments (e.g. bed load transport), the poor correlation between dredged volumes and modeled bed change in the lower portion of the CSC (Mile Markers 5 to 9) was expected.

Regardless of the model limitations within the southern reaches of the system, the model can be utilized to adequately simulate the erosion and deposition of bottom sediments within the confined portion of the CSC. Most of the western channel margins and a significant portion of the eastern margins of the channel experience net erosion. For areas where the entire channel width is relatively narrow, current velocities and the associated bottom shear stress along the flanks of the channel increase, leading to higher erosion rates at these locations. For other portions of the CSC, the navigation channel runs close to the west bank, causing larger tidal velocities in the shallows along the west side of the CSC and the associated erosion. According to the model, the entire length of the dredged CSC between miles 9 and 18 is highly depositional, which correlates well to the continual need for maintenance dredging of this area.

VIII.5 INFLUENCE OF VESSEL PASSAGE ON SEDIMENT SUSPENSION

The passage of a deep-draft vessel moving in a narrow waterway can have a significant hydrodynamic impact. Specifically, the draw-down and associated return flow velocities are a first order concern when discussing the suspension of sediments along the channel margins. In an effort to quantify this effect, the current work included a field deployment within the Lake Calcasieu shipping channel. Details on the field deployment and results are presented below.

The Calcasieu shipping channel joins the Gulf of Mexico with the industrial facilities bordering Lake Calcasieu, Louisiana. Tankers, freighters, and other large vessels traverse this waterway daily, and during passage create hydrodynamic responses within the channel which affect local sediment transport. Observations of vessel passage events in the Calcasieu shipping channel were made from December 19, 2006 to January 9, 2007.

Data acquisition systems were installed at two (2) locations in the Calcasieu shipping channel. The channel runs in the north-south direction: north is the inbound direction, south the outbound direction. One system was installed at channel Marker 85, north of Hackberry, Louisiana. The second system was installed against channel Marker 69, approximately 8 nautical miles south of Marker 85. These channel markers were located on the western side of the shipping channel in relatively shallow water. Data were acquired using a Nortek Acoustic Wave and Current profiler (AWAC). The AWACs were fixed to the channel marker pilings along the edge of the shipping channel. A specially-designed bracket offset the AWAC about 1 meter (horizontally) from the piling and assured an upward orientation.

The echo amplitude data from the AWACs showed that the surge events (at times) caused increases in the volume of acoustic scatterers, which can be reasonably interpreted as increases in suspended sediment. Since the potential for sediment transport increases relative to water velocity magnitude, the data presented in this report suggests events triggering sediment suspension in the Calcasieu shipping channel were correlated primarily to direct water displacements during vessel passages. Sediment suspension during vessel passage is in keeping with observations made during field work described in Ravens, 2007. This work set out to make field measurements of sediment erodibility in Lake Calcasieu correlating flow rates at the bed and measured turbidity. It was noted in the report that their testing was made difficult due to the passage of ships which resulted in sediment suspension and increased levels of background turbidity.

Both Ravens (2007) and Maynord (2005) determined that a shear stress of 0.5 Pa is the appropriate critical shear stress for the initiation of sediment suspension, based upon bottom sediment characteristics. Ravens (2007) was concerned directly with Lake Calcasieu while Maynord (2005) was working in the nearby Sabine/Neches Waterway in Texas. Using the critical shear stress value of 0.5 Pa, it was determined that 92% of measured vessel-related surge events exceeded the shear stress required to initiate sediment movement. From this analysis, together with the anecdotal information from the field deployment relating to this work and also described in Ravens (2007), it can be seen that vessel traffic in the Calcasieu Ship Channel is a major cause of sediment re-suspension.

VIII.6 EVALUATION OF SEDIMENT MANAGEMENT OPTIONS

During the development of the Dredged Material Management Plan (DMMP) a number of modifications to the existing Calcasieu system were proposed that would stabilize eroding shorelines along the Calcasieu Ship Channel (CSC) and enlarge existing dredge disposal areas along the CSC. The modifications were grouped together into a single alternative to be

examined within the hydrodynamic and sediment transport models to determine changes that would occur to the tidal flow regime and the associated affects on sediment transport. A brief description of each modification is below, detailed descriptions and drawings of the proposed modifications to the system are presented within the DMMP.

Modifications included in Alternative 1:

- Rock dike along the eastern side of the Calcasieu Ship Channel from approximate river mile 11 to 16. The toe of the proposed rock dike is seaward of the existing shoreline.

- Stone rock dike along Dredge Disposal Site H which is located from approximately river mile 8.5 to 9.5. The dike is on western side of the Calcasieu Ship Channel.

- Expansion of the backside of Dredge Disposal Site 17 into Lake Calcasieu and rock dike along western side of the Calcasieu Ship Channel from approximately river mile 18.5 to 20.

- Expansion of Dredge Disposal Sites D and E into Lake Calcasieu from approximately river mile 11.5 to 16.

The finite element mesh generated for the existing conditions hydraulic and sediment transport models was modified to include proposed modifications. Preliminary engineering drawings for modifications, provided by Gahagan & Bryant, Inc. (GBA), were converted into line files and imported into MIKE Zero to generate the modified finite element mesh. A few sections of the existing grid were refined to provide a smooth transition of elements around the modified sections of the Calcasieu system. Otherwise, the grid specifications for the system were identical to those used in the existing conditions mesh.

Based on the model results, the movement of sediment in the system is impacted by the addition of the expanded dredge disposal sites. However, it does not appear to drastically affect the existing sediment transport processes. The stone dikes on the margins of the channel from approximate river mile 11 to 16 and river mile 18.5 to 20 increase nearshore flow velocities and bed shears stresses; however, this influence is relatively localized, with no evidence of regional changes to sediment transport patterns. Due to the higher flow velocities along the proposed rock dikes, a reduction in sedimentation within these channel stretches can be anticipated. Portions of the CSC north and south of the proposed alterative can expect an increase in sedimentation rates; however, model results indicate that this influence is expected to be minor.

Expansion of the CDFs into the confined portion of the CSC will potentially alter sediment transport patterns within this frequently dredged region. As proposed, the expansion of the CDFs from river mile 11 to 16 and river mile 18.5 to 20 should only cause minor impacts to sediment transport patterns and channel shoaling. As presently designed, the expansion of Dredge Disposal Sites D and E into Lake Calcasieu may create areas of increased sedimentation of fine-grained material to the north and south of the containment dikes. A more gradual change in shoreline orientation will likely eliminate potential impacts on water circulation and sedimentation at the northern and southern ends of the proposed expansion. The improvements associated with Disposal Site H are minor and are anticipated to result in negligible changes to the system hydrodynamics and sediment transport patterns.

IX REFERENCES

Danish Hydraulics Institute (DHI) (2007). MIKE 21 Flow Model Mud Transport Module Scientific Background. DHI Water and Environment, Horsholm, Denmark.

Environmental Protection Agency (2002). Total Maximum Daily Load (TMDL) for suspended solids and turbidity for English Bayou (subsegment 030702) in the Calcasieu River Basin. US EPA Region 6.

Maynord, S.T. (2005). Evaluation of Ship Effects on Bank Recession in the Existing and Propsed Channels of the Sabine Neches Waterway, Texas. US Army Research and Development Center, Vicksburg, MS.

Ravens, T. (2007). "In Situ sediment erodibility testing in Calcasieu Lake, Louisiana on Dec. 16-17, 2006". Texas A&M University, Galveston.

US Army Corps of Engineers (2004). Calcasieu River and Pass Dredged Material Sedimentation Study. US Army Research and Development Center, Vicksburg, MS.

Yu-Chun S., J. Koutny, J. Benoliel, J. Mahmoud, M. Heaney (2005). "Sediment transport modeling of dredged disposal materials near Sabine Pass", Coastal Texas 2020 Technical Erosion Conference 2005.